Recherche de signaux de nouvelle physique en physique des particules et en cosmologie

J. -M. Virey

UNIVERSITE DE PROVENCE

Habilitation à Diriger des Recherches

présentée par

Jean-Marc VIREY

spécialité :

Physique Théorique : Particules et Cosmologie

RECHERCHE DE SIGNAUX DE NOUVELLE PHYSIQUE EN PHYSIQUE DES PARTICULES ET EN COSMOLOGIE

Soutenance le 14 Décembre 2007, devant le Jury composé de :

Mme	Anne	EALET
M.	Philippe	AMRAM (Rapporteur)
M.	Alain	BLANCHARD
M.	Jérôme	MARTIN (Raporteur)
M.	Patrick	PETER
M.	Jean-Marc	RICHARD (Rapporteur)
M.	Thomas	SCHUCKER
M.	Pierre	TAXIL

Cette Habilitation à Diriger des Recherches, ainsi que la plupart des travaux présentés, ont été réalisés au sein du Centre de Physique Théorique de Marseille et de l'Université de Provence. Je tiens à remercier toutes les personnes qui participent à l'existence de ces structures : enseignants-chercheurs, chercheurs, personnels administratifs et doctorants. Qu'elles soient ici profondément remerciées de leur disponibilité à mon égard.

A ma Famille et à mes Amis, qui m'ont toujours soutenu au cours de ces années de travail, et en particulier au moment de la rédaction où ils ont accepté mes changements de comportement et d'humeur.

Ma reconnaissance va à l'ensemble de mes collaborateurs scientifiques sans qui les travaux présentés n'auraient sans doute jamais vu le jour. En particulier, j'adresse un grand merci aux membres du groupe Renoir du CPPM (Anne Ealet, Charling Tao, André Tilquin, Dominique Fouchez et Alain Bonissent), aux membres du groupe Cosmologie du LAM et plus précisemment à Alain Mazure et Jean-Paul Kneib qui ont permis la mise en place d'une activité interdisciplinaire entre les trois laboratoires CPT-CPPM-LAM. Je salue chaleureusement les efforts de Diane Talon et de Sebastian Linden, doctorants avec qui j'ai le plaisir de travailler actuellement.

Je remercie profondément Anne Ealet, Alain Blanchard, Patrick Peter et Thomas Schucker qui, malgré leurs emplois du temps extrêmement bien fournis, ont accepté d'être dans mon Jury.

Mes remerciements vont encore à Jean-Marc Richard, Jérôme Martin et à Philippe Amram, qui ont accepté d'être mes rapporteurs et ceci malgré le court délai dont ils ont disposé et l'importante quantité de travail que cela a représenté.

Merci à Jacques Soffer, qui s'est révélé être un collaborateur inestimable par sa grande compétence, sa gentillesse et sa disponibilité. Je lui dois, en grande partie, les quelques notions que je possède de la Physique du Spin et je regrette qu'il n'ait pas pu faire partie du Jury.

Merci à Christian Marinoni pour nos nombreux échanges scientifiques qui ont gonflés mon enthousiasme pour la cosmologie. J'espère que cette collaboration naissante se poursuivra encore très longtemps.

Les mots sont insuffisants pour remercier Pierre Taxil, qui a su non-seulement me supporter mais aussi m'encourager tout au long de ces années de travail. Sans Pierre, ma vie serait autre et je ne serais pas là où j'en suis aujourd'hui.

Contents

Introduction

La recherche d'une unité cachée derrière l'immense diversité de la Nature a toujours passionné les physiciens. Aujourd'hui nous avançons de plus en plus vers une compréhension unifiée des lois de la physique gouvernant à la fois les grandes structures de l'Univers, comme les étoiles, les galaxies et les amas, et la structure intime de la matière, comme les atomes, les noyaux et les nucléons.

La précision expérimentale obtenue par les nombreuses expériences en physique des particules a permis de valider le Modèle Standard des interactions fortes et électro-faibles décrit dans le cadre de la théorie quantique des champs. Cependant de nombreuses questions restent encore ouvertes et on attend avec impatience les premiers résultats du LHC, d'ici deux à trois ans, pour connaître quelles manifestations de nouvelle physique permettent de décrire la voie que la Nature a choisie. A titre d'exemple de ce jeu fin entre expériences, modèles et théories, à la base de toute démarche scientifique, citons les prédictions du modèle standard électro-faible concernant les propriétés des bosons $W^{\pm}$ et Z^0. Celles-ci sont vérifiées par les expériences jusqu'au niveau des corrections radiatives, mais elles nécessitent l'introduction du boson de Higgs, une particule "scalaire" fondamentale, qu'il reste encore à découvrir. D'un point de vue théorique ce "modèle" pose de nombreux problèmes car la théorie quantique des champs fournit en général des prédictions divergentes en présence d'un champ scalaire fondamental (problèmes hiérarchique et de non-naturalité). On introduit alors des modèles ou théories allant au-delà du modèle standard permettant de s'affranchir des difficultés liées à la présence de ce champ scalaire. Les deux grandes possibilités sont l'existence soit d'une sous-structure (pour le Higgs et/ou les fermions fondamentaux (leptons, quarks)) soit d'une nouvelle symétrie liant bosons et fermions, appelée "supersymétrie" et qui peut intervenir dans le cadre plus général de la supergravité ou des théories des cordes. Avec ces dernières théories on entre dans une troisième voie qui tente d'élargir le cadre de la théorie des champs afin de pouvoir décrire l'interaction gravitationnelle. Les théories des cordes, ainsi que ses concurrents comme la géométrie non commutative ou la gravité quantique à boucles, établissent alors un lien naturel entre le monde microscopique et les plus grandes échelles de l'Univers.

Il est passionant de s'intéresser à ces questions particulièrement théoriques mais qui semblent plus mathématiques que physiques. Il est excitant de réaliser que les résultats du LHC ainsi que la grande précision des nombreuses observations qui vont être entreprises dans la prochaine décennie dans le domaine de la cosmologie vont permettre de tester certains modèles dérivés de ces différentes théories.

En effet, l'étude globale des caractéristiques de l'Univers à enregistré des progrés impressionnants depuis ces vingts dernières années et les projets observationnels en cours de discussions laissent entrevoir des perspectives très alléchantes. La cosmologie moderne repose sur trois piliers : la compréhension de l'expansion, la nucléosynthèse primordiale ainsi que la prédiction et l'observation du rayonnement cosmologique micro-onde. Le cadre est celui de la Relativité Générale et des lois de la physique microscopique et macroscopique. Ces diverses lois sont vérifiées à un très haut degré de précision localement, mais la cosmologie extrapole leurs applications à des distances très grandes et à des instants très lointains. Le Modèle Standard cosmologique repose sur de solides bases théoriques mais nécessite l'introduction de nouvelles composantes pour être en accord avec les diverses observations. Plus précisément, dans le modèle dit de "concordance", la matière ordinaire ne représente qu'environ 5% du contenu total de l'Univers qui semble posséder une géométrie plate. La matière noire entre dans une proportion de 25% et joue un role clé dans la dynamique des galaxies et des amas ainsi que dans les modèles de croissance des structures à partir des fluctuations primordiales de densité. L'énergie noire représente 70% du contenu énergétique et rend compte de l'accélération de l'expansion.

Les contraintes sur la matière noire indiquent que le fluide associé est sans collisions avec la matière ordinaire et donc que l'interaction serait purement gravitationnelle. Les modèles de microphysique, comme la supersymétrie, fournissent des candidats naturels que l'on cherche à détecter par des méthodes très diverses allant de la physique des collisionneurs à celles des astroparticules via l'étude des rayonnements cosmiques. Une autre possibilité, radicalement différente mais de plus en plus critiquée dans la communauté, serait de changer les lois de la dynamique gravitationnelle à l'échelle des galaxies et des amas. On espère que les futures données expérimentales et observationnelles permettront de séparer ces deux classes d'interprétation.

Concernant l'énergie noire, la situation est bien plus dramatique (ou intéressante !) car, d'une part, cela concerne la composante aujourd'hui dominante, et d'autre part, que de très nombreuses et diverses explications sont possibles. Les astronomes et les "relativistes" vont préférer une constante cosmologique qui peut être introduite naturellement dans les équations d'Einstein mais qui souffre alors du problème de "coïncidence" (pourquoi matière et énergie noire sont elles du même ordre de grandeur aujourd'hui bien que leurs dynamiques soient très différentes ?). Les "physiciens" vont alors proposer une origine microphysique à cette constante cosmologique en l'associant à l'énergie du vide. Ils sont alors confrontés au problème de son estimation qui est divergente en théorie quantique des champs : c'est le "problème de la constante cosmologique". Afin de résoudre ces problèmes, deux scénarios distincts sont envisagés: soit il faut effectivement rajouter une nouvelle composante, soit les équations de la dynamique sont à changer. Dans le premier cas et si on veut résoudre (partiellement) le problème de coïncidence, on introduit alors un champ scalaire (*e.g.* les modèles de quintessence). Dans le second cas on modifie ou on étend le cadre de la relativité générale (ou des seules équations de Friedmann).

Un autre aspect très incertain de la cosmologie standard concerne la periode d'inflation dans l'Univers primordial qui rendrait compte du problème de causalité mis en évidence par la très grande uniformité du fond diffus cosmologique, ainsi que de l'apparente plati-

tude spatiale de l'Univers. A nouveau les modèles d'inflation nécessitent soit l'introduction d'un champ scalaire soit une modification des équations de la dynamique.

On peut donc noter un certaine similitude entre ces trois grandes énigmes du modèle cosmologique standard que sont la matière noire, l'énergie noire et l'inflation. Il faut cependant remarquer que les domaines d'application de ces trois composantes sont extrêmement différents dans l'espace et dans le temps. Néanmoins, les physiciens théoriciens imaginent de nombreuses connexions possibles amenant à une trés grande diversités des modèles. Observationellement certaines quantités mesurées ne dependent que d'une (ou deux) de ces composantes, mais il est intéressant de réaliser que les modèles de formation de structures sont sensibles à l'ensemble de ces inconnues dont une meilleure connaissance est indispensable pour obtenir une vision plus complète et une meilleure compréhension.

Les nombreuses données de sources différentes et de très bonne qualité vont ainsi permettrent de relier des problèmes aux frontières de la physique théorique, de la physique des particules, des astroparticules, de la cosmologie et de l'astrophysique, en espérant qu'une vision plus unifiée des diverses interactions fondamentales et des différentes échelles de l'Univers en résulte.

Dans cette habilitation je vais aborder certains de ces problèmes en distinguant les travaux réalisés dans le domaine de la physique des particules de ceux effectués en cosmologie. J'ai entrepris des études de certains défauts de chaque "modèle standard" à travers des analyses phénoménologiques des diverses manifestations des modèles de nouvelle physique, en insistant particulièrement sur les effets expérimentaux et/ou observationnels.

La première partie concerne la recherche de signaux non-standards auprés de collisionneurs. Certaines de ces études font suite à mes travaux de thèse qui se concentraient sur la manifestation de nouvelles particules ou de nouvelles interactions lors de collisions avec faisceaux polarisés. Nous verrons qu'une nouvelle interaction purement hadronique (sous-structure ou nouveaux bosons de jauge), faible devant QCD, peut rester cachée et se manifester uniquement au travers d'observables décrivant les effets de polarisation (asymétries de spin). Nous étudierons aussi les informations cruciales et uniques que fournissent ces asymétries de spin sur la structure chirale et la structure scalaire des nouvelles interactions. Les modèles de nouvelles physiques concernés sont les manifestations "à basse énergie" relativement générique des modèles de sous-structures et de grande unification, ainsi que certains modèles plus spécifiques en supersymétrie ou dérivés des théories des cordes. En particulier, un article discutera les manifestations de la supersymétrie si la R-parité est brisée, dans le canal de production d'un seul quark top au LHC.

Dans la seconde partie je presente mes travaux en cosmologie, qui concernent essentiellement la détermination des paramètres cosmologiques avec un accent particulier sur les propriétes de l'énergie noire. Les premiers s'intéressent au problème des biais dûs aux hypothèses réalisées dans le processus d'interprétation des données. Nous verrons que des hypothèses sur les propriétés de l'énergie noire ont un fort impact sur la détermination des autres paramètres, et inversement. Les seconds concernent directement l'extraction de contraintes sur l'énergie noire à partir des données observationnelles combinant plusieurs

sondes cosmologiques. Un travail de prospective réalisé dans l'optique de l'optimisation de futurs projets est également présenté. La dernière partie propose un nouveau test de la cosmologie basé sur l'utilisation des propriétés cinématiques des galaxies (vitesses de rotation) afin de construire des "chandelles" et des "règles" standards.

Chapitre 1 : Au-delà du modèle standard de physique des particules : recherche de nouvelles particules et de nouvelles interactions

1.1 Introduction

Nous allons voir rapidement, d'une part, les raisons qui motivent l'existence de modèles de nouvelle physique allant au-delà du modèle standard à travers les limitations de ce dernier, et d'autre part, l'interêt d'utiliser divers collisionneurs et en particulier ceux avec faisceaux polarisés pour tester ces mêmes modèles. Ces deux aspects ont été largement discutés dans ma thèse et ne seront donc que succintement rappelés dans cette habilitation où j'insisterai surtout sur les dévellopements récents.

Le Modèle Standard, basé sur le groupe de jauge $SU(3)_c$ x $SU(2)_L$ x $U(1)_Y$ et brisé spontanément vers le groupe $SU(3)_c$ x $U(1)_{em}$ via le mécanisme de Higgs à une échelle d'énergie $v_{EW} = (\sqrt{2}G_F)^{-1/2} \approx 246\ GeV$, décrit de façon extrêmement précise les mesures expérimentales réalisées jusqu'à présent (à quelques exceptions près). Cependant, il est communément admis que ce Modèle Standard n'est en fait qu'une théorie effective à basse énergie d'une théorie plus étendue qui permettrait de résoudre de façon naturelle un grand nombre de problèmes inhérents au Modèle Standard dont une liste non exhaustive peut être la suivante :

- secteur scalaire du Modèle Standard : nature du Higgs et origine de la brisure électrofaible,
- origine de la hiérarchie des masses des fermions (*e.g.* $m_{e,u,d} \simeq 10^{-5} v_{EW}$ mais $m_t \approx v_{EW}$),
- grand nombre de paramètres laissés libres par la théorie et restant à fixer par l'expérience,
- origine de la violation de la parité des interactions faibles,
- origine des trois générations et donc de l'apparente duplication des quarks et leptons,

- quantification de la charge électrique,
- origine du confinement des quarks et du spin des nucléons.

A ces difficultés nous pouvons ajouter le désir, pour un grand nombre de physiciens, d'unifier les différentes interactions et/ou d'unifier les particules élémentaires (leptons et/ou quarks et/ou bosons). Avant de détailler les diverses pistes envisagées, insistons sur le premier point de la liste qui traite du problème de l'existence d'un champ scalaire massif en théorie quantique des champs.

Le potentiel du champ de Higgs H (doublet complexe) est supposé être donné par la relation suivante : $V(H) = m^2 H^\dagger H + \lambda (H^\dagger H)^2$. La symétrie $\mathrm{SU}(2)_L$ x $\mathrm{U}(1)_Y$ est brisée spontanément vers $\mathrm{U}(1)_{em}$ lorsque $m^2 < 0$ et que le champ de Higgs acquiert une valeur moyenne dans le vide non nulle ($\langle 0|H|0\rangle = (0, v/\sqrt{2})^T$). Concrètement, sur les quatre degrés de liberté initiaux, trois sont absorbés par les bosons $W^\pm$ et Z^0 afin de leur fournir une masse, le dernier correspond au boson de Higgs, qui a un spin 0 (scalaire) et une masse :

$$m_H = \sqrt{-2m^2} = \sqrt{2\lambda}\, v_{EW}. \tag{1.1}$$

Le fond du problème (dit de "naturalité") vient du comportement à haute énergie de cette masse, ou plus précisemment du couplage quadratique λ. Définissons le cut-off de notre théorie par Λ, qui dans le meilleur des cas (ou le pire !) peut être associé à l'échelle de Planck ($\Lambda = M_P \approx 10^{19}\, GeV$) et qui représente l'échelle d'énergie à partir de laquelle le modèle standard cesse d'être une bonne représentation effective de la réalité. Grâce aux corrections radiatives (controlées par les équations du groupe de renormalisation du modèle standard) qui font évoluer avec l'énergie les valeurs de l'autocouplage λ, on peut relier cette échelle de nouvelle physique Λ à la masse du Higgs m_H. La volonté d'avoir le modèle standard valide jusqu'à l'échelle Λ implique plusieurs critères comme la stabilité du vide et la perturbativité du modèle [1, 2].

La stabilité du vide du modèle jusqu'à une échelle d'énergie Q, requiert $\lambda(Q) > 0$ pour $Q < \Lambda$ et fournit une borne inférieure sur m_H qui est d'autant plus élevée que Λ est grand. Le critère dit de "perturbativité" du modèle standard correspond à la volonté de maintenir le couplage quadratique λ dans un régime perturbatif : $\lambda(Q) < 4\pi$ pour $Q < \Lambda$. On obtient ainsi une borne supérieure sur m_H qui est d'autant plus basse que Λ est grand. La figure 1.1 donne les zones permise et interdites pour les valeurs de m_H en fonction de l'échelle de nouvelle physique Λ, tirée de [2].

On en déduit donc que la découverte d'un Higgs lourd indique une échelle de nouvelle physique très proche. Un Higgs léger nous donne le moins d'information possible. Seul un higgs (léger) de masse comprise entre 150 et 190 GeV permet au modèle standard d'être parfaitement défini jusqu'à l'échelle de Planck. Une découverte dans cette gamme d'énergie serait le résultat le plus navrant car aucune piste vers la nouvelle physique ne nous serait fournie avec l'indication supplémentaire qu'elle n'est pas nécessaire avant 15 ordres de grandeur en énergie ! En revanche, l'absence de découverte du Higgs devrait

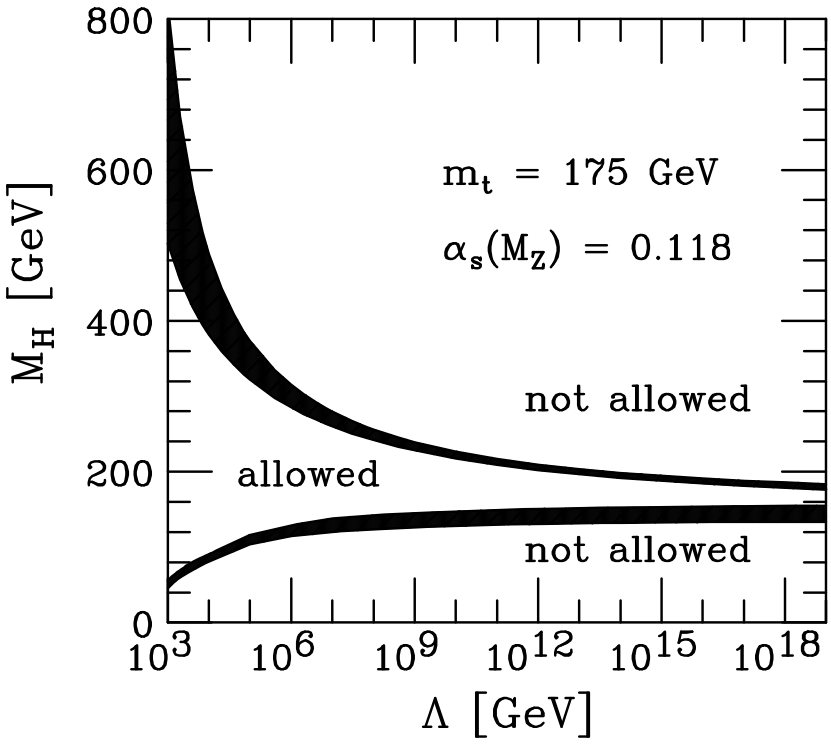

Figure 1.1: Limites théoriques sur la masse du Higgs, tirées de [2]

sonner le glas du modèle standard, ou au moins du mécanisme de Higgs ...

Dans le cas où $\Lambda = M_P$, il n'est pas nécessaire d'introduire de nouvelle physique (jusqu'à l'échelle de Planck où forcément les effets de gravité quantique doivent commencer à se faire sentir) mais on est alors confronté au problème hiérarchique. En effet, le modèle possède alors un grand désert entre l'échelle électrofaible et la masse de Planck. D'autre part, les corrections radiatives à m_H (ou λ) nécessitent un ajustement très fin à l'époque de Planck afin d'obtenir $m_H \approx v_{EW}$. On peut comprendre schématiquement le problème de la façon suivante [1]. Les corrections radiatives à la masse d'un boson (scalaire) sont quadratiquement divergentes. A l'ordre d'une boucle on a la relation $m_H^2(Q = v_{EW}) = m_H^2(Q = \Lambda) + a\Lambda^2$ où a est une constante. Avec $\Lambda = M_P$ le rapport $m_H(Q = \Lambda)/\Lambda$ doit être fixé à 17 décimales près ![1] Ce problème d'ajustement très fin, ou problème hiérarchique, nous fait penser que le modèle du grand désert jusqu'à l'échelle de Planck n'est pas un scénario réaliste. On s'attend donc très fortement à ce que le problème de l'existence d'un champ scalaire soit synonyme de l'existence d'une nouvelle physique à une certaine échelle (clairement indéterminée et non forcément à l'échelle du TeV ...).

Du point de vue expérimental les contraintes sur la masse du Higgs sont de nature directe ou indirecte. Tant que le LEP fonctionnait au pic du Z° la recherche du Higgs

était négative. Cependant, le Higgs influence les corrections radiatives. La contribution est de nature logarithmique, ainsi les contraintes sont assez faibles et sont contaminées par les incertitudes sur la masse du quark top dont les corrections sont quadratiques. Les mesures de haute précision au LEP sur de nombreux observables différents permettent de contraindres les effets des corrections radiatives et ainsi d'obtenir des contraintes sur m_H. Les résultats indirects obtenus sont donnés sur la figure 1.2 et indiquent un Higgs léger : $m_H = 97^{+53}_{-36}\, GeV$ (1σ) et $m_H < 194\, GeV$ à 95% CL [3].

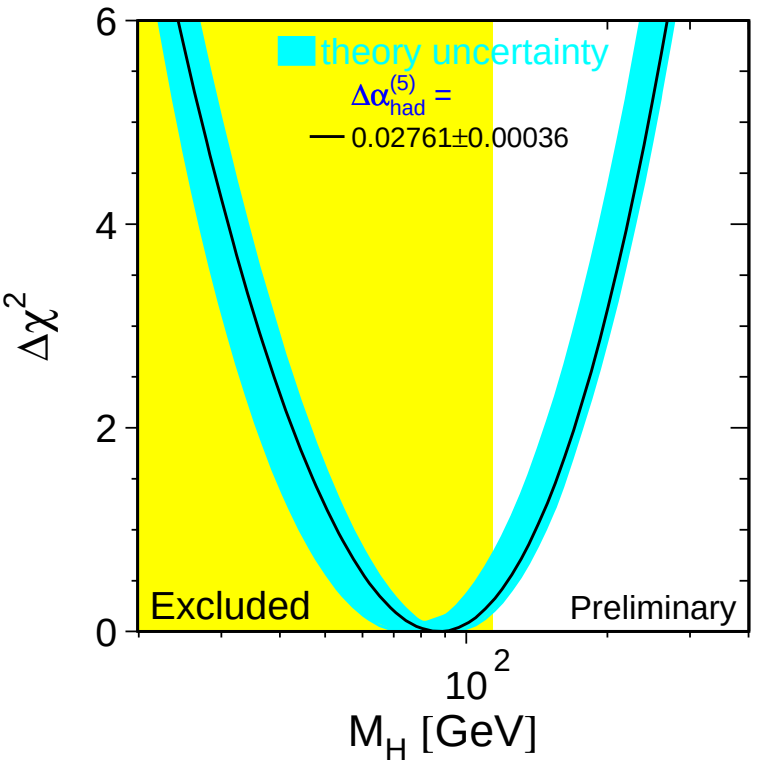

Figure 1.2: $\Delta\chi^2 = \chi^2 - \chi^2_{min}$ à partir d'un fit global de l'ensemble des données électrofaible de précision [4], en fonction de m_H. La bande bleue (ou grisée, qui suit la courbe des minimas) indique l'effet des incertitudes théoriques. La zone jaune (ou grisée, avec $m_H < 114.4\, GeV$) est exclue par les recherches directes à LEP2 [5].

La situation actuelle, issue des derniers résultats du LEP2 (caractérisé par $\sqrt{s} = 209\, GeV$) est assez ambigue. En effet, un Higgs avec $m_H < 114.4\, GeV$ est exclu à 95% CL mais il y a une légère indication de signal à 1.7σ pour le domaine $115 < m_H < 118\, GeV$. Cette estimation vient essentiellement de la collaboration travaillant sur le détecteur ALEPH qui, à elle seule, mesure un effet à 3σ[6]. Comme cet effet correspond à la limite cinématique du LEP2 et qu'une seule collaboration sur les quatres du LEP y est sensible, il a été décidé de stopper l'expérience fin 2000 pour pouvoir lancer la construction du LHC. Pour plus de détails à ce niveau on pourra consulter [6].

Les seules avancées récentes viennent du Tevatron qui contraint de mieux en mieux les propriétés du quark top et du boson W, ce qui permet un meilleur contrôle des corrections

radiatives et donc une meilleure estimation indirecte de la masse du Higgs. Les résultats les plus récents [7], schématisés sur la figure 1.3 et tenant compte des derniers calculs théoriques, indiquent toujours un Higgs relativement léger (même si le minimum a été augmenté et passe maintenant à $m_H \approx 168\,GeV$).

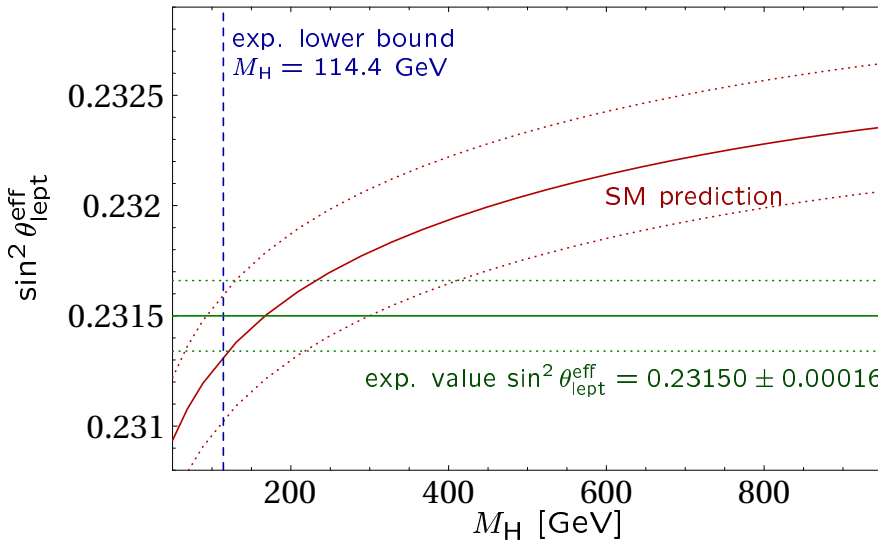

Figure 1.3: Prédictions pour $\sin^2\theta^{lept}_{eff}$ incluant les corrections à deux boucles en fonction de la masse du Higgs. La bande est obtenue en tenant compte des incertitudes expérimentales à 1σ. La droite pointillée verticale est la limite d'exclusion de LEP2.

Par ces quelques paragraphes nous avons voulu montrer que l'existence d'un champ scalaire massif fondamental et de nature quantique n'a toujours pas été confirmée et pose, par ailleurs, de sérieux problèmes à la théorie quantique des champs. De nombreuses solutions, plus ou moins satisfaisantes ont été proposées, mais une découverte expérimentale devient indispensable pour faire avancer notre compréhension. A ce niveau, réalisons que de nombreux problèmes en cosmologie sont (partiellement) résolus via l'introduction d'un champ scalaire "classique". On comprend donc que du point de vue de la physique microscopique ces modèles sont au mieux des descriptions effectives de la réalité. Cependant, l'ère de précision en cosmologie dans laquelle nous entrons à présent nous laisse espérer une meilleure compréhension de la nature de ces champs scalaires (ou des lois sous-jacentes) via l'étude de l'infiniment grand.

A présent, replongeons-nous dans le monde microscopique et les imperfections du modèle standard. Nous avons vu que ces dernières sont nombreuses et que les théories ou modèles alternatifs proposés le sont aussi. Pour de plus amples détails je renvoie le lecteur intéressé vers les introductions données dans ma thèse [8], dans la suite je ne décris que les points essentiels.

Il y a deux méthodes différentes pour tester les manifestations d'une nouvelle physique: soit on réalise un test direct des modèles en tenant compte de l'ensemble des détails

spécifiques à chaque modèle, soit on essaye d'établir une approche indépendante de tout modèle permettant de tester simultanément plusieurs classes de modèles. Mon travail étant plus phénoménologique que théorique, je me suis surtout penché sur la seconde approche.

Par exemple, un très grand nombre de théories et modèles prévoient l'existence de nouvelles interactions (*e.g.* théories de grande unification, supersymétrique ou non, modèles dérivés des théories des cordes, modèles de sous-structure). En général, chaque modèle possède des prédictions précises sur les couplages entre les nouveaux bosons de jauge et les particules élémentaires du modèle standard, fournissant ainsi certaines propriétés globales telle que les largeurs de désintégration par exemple. En revanche, d'autres propriétés (*e.g.* masses, angles de mélange) sont souvent des paramètres libres qui doivent être fixés par l'expérience. Cependant, les contraintes expérimentales que l'on obtient dépendent, bien entendu, des propriétés fixées par le modèle. Ainsi on dérive un ensemble de contraintes pour chaque modèle, mais au vu du nombre impressionnant de modèles possibles, on peut se poser la question de l'intéret de ces contraintes ... Une approche modèle indépendante, bien décrite dans [9] qui reprend directement les travaux pionniers de Fermi sur la description des interactions faibles dans les années 30, permet de réduire l'ensemble des paramètres du modèle à la seule énergie caractéristique (Λ) du nouveau phénomène. La description en terme de boson de jauge intermédiaire est remplacée par une interaction effective, dite "de contact", valable à des énergies inférieures à l'échelle d'énergie de la nouvelle physique Λ (*i.e.* $\sqrt{s} \ll \Lambda$). Concrètement, on ajoute un nouveau terme "effectif" au lagrangien du modèle standard, donné, par exemple, par l'expression suivante :

$$\mathcal{L}_{qq} = \frac{g^2}{2\Lambda_{qq}^2} \left(\eta_{LL}\, \bar{q}_L \gamma_\mu q_L . \bar{q}_L \gamma^\mu q_L \;+\; \eta_{RR}\, \bar{q}_R \gamma_\mu q_R . \bar{q}_R \gamma^\mu q_R \;+\; 2\eta_{LR}\, \bar{q}_L \gamma_\mu q_L . \bar{q}_R \gamma^\mu q_R \right) \qquad (1.2)$$

où g est la constante de couplage de la nouvelle interaction et est normalisé à $g^2 = 4\pi$. η_{ij} est tel que $|\eta_{ij}| \leq 1$, son signe caractérise le type, destructif ou constructif, des interférences entre les termes de contact et les amplitudes standards, le type dépendant du processus étudié. $q_{L,R}$ sont les composantes gauche et droite du quark q.

Une attention particulière a donc été portée sur les manifestations ou les contraintes que l'on pourrait obtenir sur ces interactions de contact, que ce soit dans le secteur des quarks uniquement ou dans le secteur commun aux quarks et aux leptons. Cependant, lorsque les énergies caractéristiques de l'expérience et de la nouvelle interaction se rapprochent, des effets subtils peuvent avoir lieu (*e.g.* résonance) et une description plus complète des modèles est préférable. Ainsi nous avons été amenés à étudier plus en détails les manifestations des bosons dits "leptophobes" (bosons de jauge ne couplant qu'aux quarks et étant ainsi très difficile à détecter), ou encore de "leptoquarks" (bosons couplant leptons et quarks directement au sein d'un même vertex). Les premiers ont été étudiés dans le cadre de l'expérience RHIC-Spin avec faisceaux de protons (et neutrons) polarisés, qui est en cours de fonctionnement. Ces résultats sont présentés dans la première partie de ce chapitre. Les seconds ont été étudiés dans le cadre de l'expérience HERA, dont un des projets était de polariser les faisceaux. Malheureusement, aujourd'hui, le projet a été

abandonné et l'experience arrétée, ce qui rend ces études obsolètes pour le moment. De fait, ces études seront présentées à la fin de ce chapitre.

En parallèle à ces travaux, j'ai participé à un travail commun entre les expérimentateurs du CPPM et les théoriciens du CPT sur la phénoménologie de la supersymétrie au LHC. Ce domaine étant très vaste, notre approche a été pragmatique. Nous nous sommes intéressés au processus de production d'un seul quark top ("single top production") qui a l'avantage de n'être sensible qu'à certaines manifestations de nouvelle physique (au premier ordre). Il est apparu que c'est un processus privilegié pour tester une symétrie propre à la supersymétrie appelée "R parité". En effet, si cette symétrie est brisée des effets nouveaux devraient être détectés dans la production d'un seul top. Le test de cette symétrie est, en fait, encore plus important pour la cosmologie car si elle se revèle être brisée c'est le candidat matière noire issu de la supersymétrie qui disparait .... Cette étude, qui ne fait absolument pas appel aux effets de polarisation, est présentée dans la deuxième partie de ce chapitre.

1.2 Nouvelle Physique auprès de RHIC-Spin

1.2.1 L'expérience RHIC-Spin et la crise du spin

Le "Relativistic Heavy Ion Collider" (RHIC) est en cours de fonctionnement depuis 2001 au Brookhaven National Laboratory (BNL-USA), et est voué essentiellement à l'étude de collisions d'ions lourds de très hautes énergies [10]. Cependant, ce collisionneur fonctionne entre 5 et 10 semaines par an, en mode proton-proton avec faisceaux polarisés. La Collaboration RHIC-Spin a ainsi vu le jour et essaye actuellement d'augmenter l'énergie caractéristique de l'expérience de $\sqrt{s} = 250\ GeV$ à $\sqrt{s} = 500\ GeV$. Des efforts très important sont entrepris pour atteindre les 70% de polarisation par faisceau escompté, ainsi que la luminosité intégrée de $L = 800\ pb^{-1}$.

Une autre particularité intéressante du RHIC, liée à sa nature de collisionneur d'ions lourds, est qu'il sera capable d'accélérer des faisceaux de hadrons, autres que des protons, en particulier des deutérons et des noyaux d'hélium 3. L'accélération de noyaux d' ^{3}He polarisés se révèle d'un grand intérêt, car le principe de Pauli nous indique que les spins des protons sont dans des directions opposées. Ainsi, la direction de la polarisation d'un noyau d'^{3}He est, à peu près, équivalente à celle d'un neutron [11, 12]. Cela nous permet de supposer que l'on bénéficiera également de faisceaux de neutrons polarisés de bonne qualité.

L'intérêt premier du RHIC [13] est la possibilité d'une étude de haute précision de QCD et de certains phénomènes électrofaibles. En particulier cela va permettre pour la première fois une bonne calibration des distributions partoniques polarisées [14], incluant celle des gluons, d'une façon radicalement différente de ce qui a été réalisé dans les expériences de diffusion inélastique polarisée. Avant de discuter des possibles effets de nouvelle physique, je voudrais dire quelques mots sur la crise du spin et les premiers résultats de RHIC-Spin,

relativement "inattendus" vu qu'ils confirment que l'on ne comprend pas grand chose à l'origine du spin du proton et de fait aux aspects (non perturbatifs) de QCD liés au confinement.

Le domaine de la physique du spin, controlé essentiellement par l'interaction forte à basse énergie, est toujours en pleine effervescence grâce aux résultats précis des expériences de diffusion profondément inélastique avec faisceaux de leptons et cibles hadroniques polarisés (pour une revue voir [15]) ainsi que ceux récents de RHIC-Spin (*e.g.* [16]). Le résultat le plus surprennant est que la contribution des quarks et antiquarks au spin du proton n'est que d'un quart ! On peut représenter ce résultat à l'aide de la règle de somme du spin du proton [17] :

$$\frac{1}{2} = \frac{1}{2}\Delta\Sigma(Q^2) + \Delta G(Q^2) + L_q(Q^2) + L_g(Q^2)\ , \tag{1.3}$$

et le fait qu'on obtient expérimentalement $\Delta\Sigma \approx 0.25$. Ceci implique qu'une contribution importante au spin du proton doit venir soit de la polarisation des gluons $\Delta G(Q^2)$ soit des moments orbitaux angulaires des quarks $L_q(Q^2)$ ou des gluons $L_g(Q^2)$. La dépendance de ces moments sur l'échelle d'énergie caractéristique de la collison Q a été incluse explicitement pour rappeler que les distributions partoniques ainsi que leurs moments peuvent difficilement être prédits théoriquement à cause des effets non perturbatifs de QCD. En revanche, les évolutions avec l'énergie de ces diverses quantitées sont parfaitement calculables (*e.g.* $\Delta G(Q^2) \approx \log(Q^2) \approx \alpha_s^{-1}(Q^2)$)[18]. Rappelons que les distributions partoniques sont définies par :

$$f^+ \ = \ f^+_+ \ = \ f^-_- \qquad\qquad f^- \ = \ f^-_+ \ = \ f^+_- \tag{1.4}$$

où l'invariance des interactions fortes sous la transformation de parité, permet de définir les distributions où le parton f a son spin parallèle (f^+) ou antiparallèle (f^-) au spin du hadron parent. On définit alors les distributions de partons :

- indépendantes du spin : $f(x,Q^2) \ = \ f_+(x,Q^2) + f_-(x,Q^2)$
- polarisées : $\Delta f(x,Q^2) \ = \ f_+(x,Q^2) - f_-(x,Q^2)$

où $f = q, \bar{q}, g$ et x représente la fraction d'impulsion emporté par le parton f. Les moments des distributions partoniques intervenant dans l'éq.(1.3) sont donnés par :

$$\Delta\Sigma(Q^2) \ = \ \int_0^1 \sum_q (\Delta q(x,Q^2) + \Delta\bar{q}(x,Q^2))\, dx \qquad \Delta G(Q^2) \ = \ \int_0^1 \Delta g(x,Q^2)\, dx. \tag{1.5}$$

La crise du spin a débutée en 1988 avec les résultats de la collaboration EMC [19] qui obtint $\Delta\Sigma(11\ GeV^2) = 0.01 \pm 0.29$. Depuis, les expériences de diffusion profondément inélastique polarisée de plus en plus précises ont amené la valeur centrale à 0.25 et l'erreur à quelques pour-cents. On a alors cherché à contraindre ΔG mais la diffusion lepton-hadron ne donne un accés à Δg qu'indirectement, à travers l'évolution des distributions ou via l'étude de processus rares. Jusqu'à l'avènement du RHIC-Spin les contraintes étaient

faibles, voire inexistantes. Du point de vue de la théorie, les estimations (sans parler des calculs) sont extrêmement difficiles à réaliser car dans le domaine non-perturbatif. A partir d'un raisonnement basé sur la très forte evolution en Q^2 de ΔG, on penchait plutôt [18, 20] vers une (très) forte polarisation des gluons ($\Delta G > 1.5$). En utilisant le "MIT bag model" ou des "modèles de quarks" non relativistes [21], on obtient des estimations de l'ordre du spin du proton ($\Delta G(1\ GeV^2) \approx 0.2 - 0.3$ [22, 23]). Très récemment et pour la première fois une estimation de la dépendance en x de Δg a été fournie [23].

Vu la profonde incertitude théorique et les résultats expérimentaux surprenants, il devenait urgent d'obtenir des mesures de la polarisation des gluons. C'est un des objectifs principaux du RHIC-Spin [13]. Plusieurs processus, comme la production de photons ("directs"), de jets, de π^0 ou encore de quarks lourds, donnent un accés direct à Δg. L'observable à utiliser est une double asymétrie de spin qui conserve la symétrie de Parité:

$$A_{LL} = \frac{\sigma^{++} - \sigma^{+-}}{\sigma^{++} + \sigma^{+-}} \tag{1.6}$$

où $\sigma^{\lambda_1 \lambda_2}$ est la section efficace du processus considéré pour une collision avec deux protons d'hélicités λ_1 et λ_2.

Les premiers résultats, présentés sur la figure 1.4, on été obtenus il y a un peu plus d'un an, dans le canal de production de π^0 pour la collaboration PHENIX, et pour la production de jets avec STAR. Les prédictions de plusieurs modèles phénoménologiques pour Δg sont aussi donnés sur la figure 1.4.

On constate qu'une forte polarisation des gluons est exclue. Les résultats sont en accord avec une polarisation des gluons nulle ou faible. Les gluons ne sont donc pas à l'origine du spin du proton ! Par conséquent, la crise du spin se renforce car il est difficile de croire que les moments angulaires orbitaux jouent un rôle important. (Pour une discussion intéressante qui a inspirée les lignes précédentes voir [16] ainsi que les deux premiers chapitres de ma thèse [8])

A priori, la nouvelle physique n'est pour rien dans cette crise du spin qui devrait trouver sa source dans notre très grande difficulté à réaliser des calculs et à avoir de l'intuition dans le domaine non perturbatif (de QCD). Cependant, les expériences avec faisceaux polarisés peuvent fournir des contraintes très intéressantes et des informations uniques sur la structure chirale d'une nouvelle interaction, à la condition de disposer d'une énergie et d'une luminosité suffisantes. C'est le cas de RHIC-Spin contrairement aux expériences sur cibles fixes.

Par ailleurs, la mise en évidence de nouvelle physique demande la distinction entre un phénomène non-standard et une fluctuation de la prédiction standard, liée à la faible connaissance de ces distributions partoniques. La calibration des distributions polarisées au RHIC [27, 14] nous laisse supposer que ces incertitudes seront fortement réduites dans un avenir proche. En effet, la collaboration RHIC-Spin a l'intention d'utiliser les runs de 2008, qui se feront pour la première fois à une énergie de $\sqrt{s} = 500\ GeV$, pour étudier les productions de bosons $W^{\pm}$ qui sont particulièrement sensibles aux distributions des quarks et

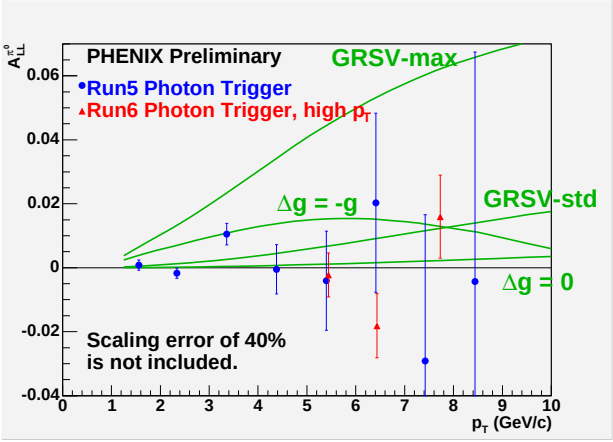

Figure 1.4: Données sur l'asymétrie à 2 spins A_{LL} pour la production inclusive de π^0 à $\sqrt{s} = 200\,GeV$ mesurées par la collaboration PHENIX [24] (gauche), et pour la production de jets mesurée par la collaboration STAR [25] (droite), comparées aux prédictions NLO pour plusieurs distributions polarisées des gluons décrites dans [26].

antiquarks. Une fois que ces distributions partoniques seront fortement contraintes il sera alors possible de se tourner vers le programme de recherche de signaux de nouvelle physique.

Les travaux qui vont suivre (ainsi que ceux présentés dans ma thèse sur ce sujet là) ont suscité un vif intérêt au sein de la collaboration RHIC-Spin, ce qui m'a permis de participer activement aux rencontres de la collaboration et à motiver plusieurs personnes d'étudier ces effets exotiques. Je donnerai en fin de section une rapide discussion des travaux réalisés dans la communauté depuis la parution des 3 articles qui sont présentés ici.

Avant de détailler chaque article il faut essayer de comprendre comment l'expérience RHIC-Spin avec $\sqrt{s} = 500\ GeV$ peut être compétitive pour decouvrir de nouveaux phénomènes avec des accélérateurs possédant des énergies plus élevées ($Sp\bar{p}S$ au CERN dans les années 1980-90 avec $\sqrt{s} = 630\ GeV$, Tevatron au Fermilab actuellement en service avec $\sqrt{s} = 2\ TeV$). Il apparaît que si des leptons sont produits (directement) et étudiés dans l'état final (*e.g.* processus de Drell-Yan), alors le Tevatron fournit les meilleures contraintes car les processus leptoniques sont "propres" expérimentalement. Dans ce cas c'est l'énergie qui prime (avec la luminosité en second plan) dans une optique de découverte. En revanche, si le processus est purement hadronique (*e.g.* production de jets) et donc controlé essentiellement par QCD, on recherche des événements à haute impulsion transverse mais on est alors confronté, expérimentalement, à des problèmes de reconstruction ce qui donne de forts bruits de fonds, et théoriquement, à des incertitudes dans l'estimation des sections

efficaces (fortes corrections des ordres supérieurs). Ces deux aspects déteriorent fortement les contraintes susceptibles d'être fournies.

C'est pour ce type de processus purement hadroniques que RHIC-Spin est particulièrement intéressant et plus performant que ses concurrents non polarisés plus énergétiques. Cette caractéristique vient de la présence de la polarisation qui permet de définir les nouveaux observables que sont les asymétries de spin, et en particulier l'asymétrie à 1 spin qui viole la Parité[1] :

$$A_L = \frac{\sigma^+ - \sigma^-}{\sigma^+ + \sigma^-} \tag{1.7}$$

La différence des sections efficaces au numérateur permet d'éliminer tous les bruits de fonds associés aux processus conservant la Parité gouvernés par QCD et QED. Le rapport de sections efficaces devrait permettre de limiter l'impact des corrections d'ordre supérieur. Cependant nous verrons dans notre cas d'étude que cet argument n'est pas correct (voir la discussion en fin de section sur l'estimation NLO des asymétries de spin).

Par conséquent, des effets de nouvelle physique pourront être détectés au RHIC-Spin si et seulement si les nouveaux phénomènes sont purement hadroniques et violent la Parité. Heureusement, de nombreux modèles théoriques satisfont ces deux critères. Pour plus de détails sur l'interêt de l'utilisation de faisceaux polarisés pour découvrir et étudier de la physique au-delà du modèle standard pour divers types de collisionneurs, je conseille le compte-rendu [29] où une telle revue m'avait été demandée.

Le premier article présenté ici traite de la manifestation de bosons leptophobes. Des modèles spécifiques sont étudiés, suivis d'une approche purement phénoménologique. Une attention particulière a été portée à la complémentarité entre collisionneurs. Il apparaît que dans les fenêtres de masse $M_{Z'} \approx 300\ GeV$ et $M_{Z'} < 100\ GeV$ seul RHIC-Spin peut découvrir de telles particules.

Le deuxième article a été rédigé suite à une demande des responsables de la collaboration RHIC-Spin qui voulaient connaitre l'impact d'une possible augmentation en énergie et/ou en luminosité de la machine. En effet, en utilisant au maximum les capacités du RHIC, il est possible d'atteindre $\sqrt{s} = 650\ GeV$ et $L = 20\ fb^{-1}$. Avec ces nouveaux paramètres nous avons calculé l'amélioration des contraintes en cas de présence de nouvelles interactions de contact ou de bosons leptophobes. Les résultats obtenus montrent qu'une telle amélioration de la machine augmente fortement ses capacités de découverte.

Le dernier article traite des informations que l'on peut obtenir sur les bosons leptophobes en utilisant à la fois des collisions polarisées proton-proton et neutron-neutron (via la polarisation de noyaux d'He^3). La structure chirale de l'interaction, mais aussi et de façon très intéressante, des informations sur la structure scalaire (type de couplage avec les bosons de Higgs) peuvent être obtenues.

[1] Dans les articles c'est l'asymétrie à 2 spins violant la Parité $A_{LL}^{PV} = \frac{\sigma^{++} - \sigma^{--}}{\sigma^{++} + \sigma^{--}}$ qui est discutée, mais il apparaît qu'elle est équivalente à l'asymétrie à 1 spin avec l'inconvenient d'avoir une expression relativement compliquée lorsque l'on tiend compte des degrés de polarisation partiels de chaque faisceau (voir [28] pour les formules et détails).

1.2.2 Recherche de Z' leptophobes

Article publié sous la référence : Phys. Lett. **B441** (1998) 376 .

A light leptophobic Z' in polarized hadronic collisions

P. Taxil and **J.-M. Virey**

Centre de Physique Théorique*, C.N.R.S. - Luminy, Case 907
F-13288 Marseille Cedex 9, France

and

Université de Provence, Marseille, France

Abstract

Theoretical and phenomenological arguments are in favor of an elusive new neutral vector boson Z' with a relatively low mass, chiral couplings to ordinary quarks and whose couplings to ordinary leptons are suppressed (leptophobia). We point out that this new particle could induce some parity violating spin asymmetries which could be measured soon at the Brookhaven Relativistic Heavy Ion Collider (RHIC), running part of the time as a polarized hadronic collider.

PACS Numbers : 12.60.Cn; 13.87.-a; 13.88.+e; 14.70.Pw
Key-Words : New Gauge bosons, Jets, Polarization.

Number of figures : 3

July 1998
CPT-98/P.3667

anonymous ftp or gopher : cpt.univ-mrs.fr

---

*Unité Propre de Recherche 7061
E-mail : Taxil@cpt.univ-mrs.fr ; Virey@cpt.univ-mrs.fr

1 Introduction

One of the simplest extensions of the Standard Model (SM) is the addition of an extra $U(1)'$ gauge factor to the $SU(3) \times SU(2) \times U(1)$ structure. If the symmetry breaking occurs at a scale not far from the electroweak scale, this leads to the existence of a new neutral gauge boson Z' at a mass accessible to forthcoming experiments.
In recent years, some discrepancies with respect with the Standard Model expectations observed at LEP and/or FNAL have triggered a lot of studies involving a possible Z' whose couplings to ordinary leptons could be very small (leptophobia).
Although the discrepancy in the $Z \to b\bar{b}$ sector has not completely disappeared, the improved agreement between the latest data [1] and the SM expectations has weakened the phenomenological motivations for that object (see e.g. [2]). However, the interest on such a leptophobic Z' goes far beyond the tentative for explaining the LEP and CDF data. Various models, based on Grand Unification and/or Superstring theory, display a parameter space which allows or favors a new neutral gauge boson with very small couplings to leptons. On the other hand, leptophobia still represents an attractive possibility allowing the existence of new physics at an accessible energy scale without any contradiction with the present data.

It has been emphasized in refs. [3, 4, 5, 6] that some non minimal SUSY models with an additional $U(1)'$ imply the presence of a relatively light Z' : $M_{Z'} < 1$ TeV$/c^2$. Indeed, a class of models, driven by a large trilinear soft SUSY-breaking term, prefers the range $M_Z \leq M_{Z'} \leq 400\,\mathrm{GeV}/c^2$ along with a very small mixing with the standard Z° . This opens some very interesting possibilities for phenomenology provided that this new vector boson displays leptophobic couplings to remain compatible with present data.

A leptophobic Z' is particularly elusive as far as conventional direct searches via Drell-Yan pair production at a $p\bar{p}$ collider are concerned. It is of some importance to consider other possible manifestations of this new boson.

If produced in hadronic collisions, the new Z' can decay into exotic fermions whose presence is necessary for anomaly cancellations [7]. Such decays can yield some anomalous events which are, however, difficult to interpret.
An other interesting feature has been pointed out by Rosner [7] : the direct Z' couplings to quarks (which can be generation dependent or not) often break chiral symmetry at a variance with QCD which is left-right symmetric. This can yield a substantial forward-backward asymmetry A_{FB} in $p\bar{p} \to Z' \to f\bar{f}$ events. Such measurements are particularly difficult in the absence of outgoing leptons (leptophobia) since it is mandatory to measure the charge of the outgoing particle or jet. Moreover, in some case like in the model described in [7], $A_{FB} = 0$ in the production of down(bottom)-type quarks which forbids the opportunity of using b-tagging.
There is an other way to be sensitive to chiral couplings, namely the measurement of a parity-violating (PV) spin effect in polarized hard collisions of hadrons, in particular in the production of jets [8]. In fact, within two years, the RHIC Spin Collaboration (RSC) [9] will start running the Relativistic Heavy Ion Collider at Brookhaven National

Laboratory part of the time in the $\vec{p}\vec{p}$ mode, with a high (70%) degree of polarization and with a very high luminosity $\mathcal{L} = 2.10^{32} cm^{-2} s^{-1}$. The physics goals of the collaboration have been discussed in a recent workshop [10].

As soon as one can find some arguments for *-i)* an extra $U(1)'$ gauge factor leading to a relatively light Z' , *-ii)* a parameter space which favors some very weak couplings of this Z' to conventional leptons, *-iii)* a model in which an asymmetry in the left and right-handed couplings to light quarks is preferred or at least allowed, then it is extremely interesting to explore the consequences on the spin observables which will be measured soon, with a high degree of precision, by the RHIC Spin Collaboration.

In the following section we will summarize the theoretical motivations for a light and leptophobic Z' with chiral couplings to quarks. We also give the parameter space which follows from the models we consider, along with the present experimental direct limits on the mass of the Z' and the strength of its coupling to light quarks. The effects of the new amplitudes on the spin asymmetries in inclusive jet production at the polarized RHIC collider are presented in Section 3, along with the bounds on the parameter space which could be obtained. We give our conclusions in Section 4.

2 Theoretical motivations and the parameter space

We will consider a new neutral vector boson Z' which couples to u- and d- type quarks with the following structure :

$$\mathcal{L}_{Z'} = \kappa \frac{g}{2\cos\theta_W} Z'^{\mu} \bar{q} \gamma_{\mu} [C_L^q (1-\gamma_5) \; + \; C_R^q (1+\gamma_5)] q \qquad (1)$$

for each given quark flavor q, the parameter $\kappa = g_{Z'}/g_Z$ being of order one.

We will not discuss any more the phenomenological models with strong couplings and $M_{Z'} = 1\mathrm{TeV}/c^2$ which were built [11] to explain the old LEP (+CDF) data. Spin asymmetries at RHIC for these particular models have been already discussed in Ref. [12].
A theoretically motivated leptophobic Z' with chiral couplings is present in many string inspired models : in particular we will consider a version due to Lopez and Nanopoulos [13] (model A) of the flipped-SU(5) model [14] and a generalized E_6 model with kinetic-mixing [15] (model B).

- In model (A), the particle content of the standard model is contained in the representations : $F = (\mathbf{10}, \frac{1}{2}) = \{Q, d^c, \nu^c\}$, $\bar{f} = (\bar{\mathbf{5}}, -\frac{3}{2}) = \{L, u^c\}$, $l^c = (\bar{\mathbf{1}}, \frac{5}{2}) = \{e^c\}$.

Leptophobia is achieved when $\bar{f}$ and l^c, which contain the standard model leptons, are uncharged under the new $U(1)'$. As a consequence (see [13]) the quark couplings verify $C_L^u = C_L^d = -C_R^d = 1/(2\sqrt{3})$ and $C_R^u = 0$. Therefore parity is maximally violated in the up-quark sector and is conserved in the down-quark sector since the resulting coupling is purely axial.

- Model (B) goes beyond the traditional parametrization in terms of the $U(1)$'s combination in E_6 models (for a review of E_6 models see [16]). In fact, it was noticed some years ago [17] that it was possible within E_6 models, to find a particular combination of charges leading to a suppression of the Z' couplings to ordinary leptons (see [7] for a recent discussion). In Ref.[15] one considers that kinetic mixing (KM) between the field strength of weak hypercharge $B_{\mu\nu}$ and the field strength of the new $U(1)'$ occurs. In the interesting case of KM between the so-called $U(1)_\eta$ and $U(1)_Y$, one gets leptophobia when, for each fermion f, the Z' couples to a combination $Q'^f = Q^f_\eta + \delta Y_W$ with $\delta = -1/3$. This yields the quark couplings : $C^u_L = C^d_L = C^d_R = -\frac{1}{2}C^u_R = -\frac{5}{18}\sin\theta_W$.
Note that to maintain κ of order one in eq.(1), the usual GUT factor $\sqrt{\frac{5}{3}}\sin\theta_W$ has been included in the $C^q_{L,R}$'s couplings.

Since a leptophobic Z' appears in several other string derived models [5, 18] it is valuable to consider a more general situation where the Z' couplings to ordinary quarks are less constrained. We will nevertheless assume $SU(2)_L$ invariance which imposes $C^u_L = C^d_L \equiv C_L$. Then, we are left with three parameters : C_L, C^u_R and C^d_R. Of course in some models the couplings are generation dependent : since we will be interested in ordinary jets, this point is not relevant for our analysis.
Non-SUSY leptophobic models have also been constructed [19, 20]. Again there is a large freedom in the precise values for the Z' couplings to light quarks. We will consider for illustration the special case introduced in Ref. [20] where the Z' is purely right-handed (model C) : $C_L = 0$, $C^u_R = C^d_R = 1/3$ (to be consistent with our notations we have divided the value given in [20] by a factor 3 to keep the corresponding $\kappa \approx 1$).

The constraints on models (A) and (B) which are coming from updated electroweak data have been studied very recently [21]. It turns out that for a small value of the Z° - Z' mixing angle ξ the Z' mass remains essentially an unconstrained parameter in case of pure leptophobia. From the theoretical side a very small mixing angle is natural in the scenario advocated in [4]. One gets the same behaviour when the new $U(1)'$ does not mix with the SM gauge group like within a class of models which can include model(A) [13]. As a consequence we have neglected the Z° - Z' mixing angle ξ which is in principle present in all the $C^q_{L,R}$ couplings and whose effect on the calculations described below would be very tiny.
Direct constraints on $M_{Z'}$ are coming from $p - \bar{p}$ collider experiments analyzing the dijet cross section : UA2 [22], CDF [23] and D0 [24]. These limits are usually displayed in term of the so-called "sequential standard model Z' " with $\kappa = 1$. It is not difficult to perform an extrapolation for a reasonable range of κ values and for a larger class of Z' models with various $C^q_{L,R}$ couplings. We have displayed the limits in Fig.1 for models (A) and (B) assuming a 100% branching ratio of the Z' into ordinary jets. One can notice that the Z' mass is not constrained in these models as soon as $\kappa < 0.95$. Also, and this is true in any leptophobic model, some windows are present around $M_{Z'} = 300$ GeV/c^2 and below $M_{Z'} = 100$ GeV/c^2.
Therefore, one can see that present data are not excluding a Z' as light as the one which is advocated in recent papers based on weak-scale supersymmetry [3, 4, 5, 6]. As discussed

by Lykken [5] this scenario could take place for model (A). This is also the case for model (B), according to Refs.[6], if additional matter from an extra **78** representation of E_6 is involved. Finally, we will also consider the very special case where the Z' is degenerate in mass with the SM Z° . This can be accepted in the framework of the trilinear scenario of Ref. [4] and it was stressed in Ref.[25] that such a leptophobic boson could explain the apparent discrepancy between the LEP and SLAC values of $\sin^2\theta_W$. To summarize, we will focus on a mass range $M_Z \leq M_{Z'} \leq 400$ GeV which could give spectacular effects in PV spin asymmetries at RHIC.

3 Calculation and results

At RHIC, running in the $\vec{p}\vec{p}$ mode, it will be possible to measure with a great precision the double helicity PV asymmetry :

$$A_{LL}^{PV} = \frac{d\sigma_{(-)(-)} - d\sigma_{(+)(+)}}{d\sigma_{(-)(-)} + d\sigma_{(+)(+)}} \tag{2}$$

where the signs $\pm$ refer to the helicities of the colliding protons. The cross section $d\sigma_{(\lambda_1)(\lambda_2)}$ means the one-jet production cross section in a given helicity configuration, $p_1^{(\lambda_1)} p_2^{(\lambda_2)} \to jet + X$, estimated at $\sqrt{s} = 500$ GeV for a given jet transverse energy E_T , integrated over a pseudorapidity interval $\Delta\eta = 1$ centered at $\eta = 0$.

The Z' will generate new amplitudes in quark-quark scattering which is the dominant subprocess in the E_T range we consider. At LO these amplitudes will interfere with the one-gluon exchange amplitude and also with the amplitudes due to SM gauge boson exchanges. This was described already in Ref. [12] and all the LO cross sections for the subprocesses can be found in Ref. [26].

In fact, 95% of the PV effect due to the new boson will come from Z' - gluon interference terms involving the scattering of u quarks in the t-channel.
In short notations :

$$A_{LL}^{PV}.d\sigma \simeq F \int \left((C_L^u)^2 - (C_R^u)^2\right) \Big[u(x_1,\mu^2)\Delta u(x_2,\mu^2) + \Delta u(x_1,\mu^2) u(x_2,\mu^2)\Big] \tag{3}$$

where F is a positive factor given by

$$F = \frac{32}{9}\alpha_s\, \alpha_Z \hat{s}^2 Re\left(\frac{1}{\hat{t} D_{Z'}^{\hat{u}}} + \frac{1}{\hat{u} D_{Z'}^{\hat{t}}}\right) \tag{4}$$

where $\alpha_Z = \alpha/\sin^2\theta_W \cos^2\theta_W$ and

$$D_{Z'}^{\hat{t}(\hat{u})} = (\hat{t}(\hat{u}) - M_{Z'}^2) + iM_{Z'}\Gamma_{Z'} \tag{5}$$

In eq.(3) $\Delta u(x,\mu^2) = u^+(x,\mu^2) - u^-(x,\mu^2)$ where $u^\pm(x,\mu^2)$ are the distributions of the polarized u quarks, either with helicity parallel (+) or antiparallel (-) to the parent proton

helicity. Summing u^+ and u^- one recovers the unpolarized distribution $u(x,\mu^2)$. Concerning these spin-dependent distributions (evaluated at $\mu = E_T$), we have used the ones of GRSV [27]. Note that the first part of the polarized RHIC Spin program itself [9] will greatly improve our knowledge of all the distributions Δq_i's and $\Delta\bar{q}_i$'s (see Ref. [28] for a recent analysis). In the present analysis, the Z' couplings to quarks remain in a "weak" range (of the same order as the SM Z° couplings) : this is at a variance with the phenomenological attempts of Refs.[11]. As a consequence the Z' width $\Gamma_{Z'}$ remains in the range of 1 - 10 GeV/c^2 (neglecting possible light exotica), the precise value having no influence on our results.

We present in Fig.2 the result of our calculation (taking all the terms, dominant or not, into account) for A_{LL}^{PV} versus E_T in $\vec{p}\vec{p}$ collisions at RHIC. For illustration we compare the SM asymmetry, which is due to small QCD-electroweak interference terms [29], to the non-standard one with a Z' of mass 90 or 200 GeV/c^2 for models (A) and (B) and 300 GeV/c^2 for model (C). The bump in the standard A_{LL}^{PV} at $E_T \approx M_{Z,W}/2$ corresponds to the vicinity of the corresponding "jacobian peak" in the production cross section. We observe the same behaviour at $E_T \approx 100$GeV for $M_{Z'} = 200$ GeV/c^2. Practically, it will be difficult to explore the E_T region below 45 GeV with the RHIC detectors due to experimental cuts [30]. However, above $E_T = 50$ GeV, on can see that a high precision measurement can be performed. The error bars correspond to the statistical error with an integrated luminosity $\mathcal{L}_1 = 800 pb^{-1}$ which can be achieved at RHIC in a few months running.

Clearly, if a deviation from the SM is seen in A_{LL}^{PV} , the sign of this deviation can allow to separate easily a model dominated by left-handed couplings to u quarks (like model (A)) from a model dominated by right-handed couplings like model (B) or (C). Of course the results are impressive because the mass of the leptophobic Z' is light. On the other hand, we have taken a value of κ around 1.5, when it is allowed by present data, or around 1 if not. Both values are compatible with "weak" Z' couplings to quarks (to be compared with the models in [11, 12]).

We have shown in Fig.1 the limits on the parameter space $(\kappa, M_{Z'})$ one can obtain from A_{LL}^{PV} with the integrated luminosities $\mathcal{L}_1 = 800\, pb^{-1}$ and $\mathcal{L}_2 = 3200\, pb^{-1}$ for models (A) and (B). One can see that the hole centered on $M_{Z'} \approx 300$GeV/c^2 is now fully covered, along with the low mass or "degenerate" case $M_{Z'} \approx M_Z$. Fig.3 is more general since it is model independent. It represents some exclusion contours at 95% C.L. in the plane ($\kappa.C_L$, $\kappa.C_R^u$) for two values of the Z' mass. The circles represent some estimates of the present experimental constraints on this parameter space assuming some simple additional relations ($(C_R^d)^2 = (C_R^u)^2$) between the couplings entering the dijet cross section. This assumption is not necessary to get the contours obtained from A_{LL}^{PV} since the d-quark couplings have a very small influence on this asymmetry.
The particular models (A), (B) and (C) are represented by some particular points on the same plot for $\kappa = 1$. Moving away from this κ value results in a translation along a straight line as shown. One can see that the measurement of A_{LL}^{PV} at RHIC will strongly reduce the allowed parameter space, in particular in the region around $M_{Z'} = 300$ GeV/c^2

which is poorly constrained up to now. Only when parity is restored, that is along the diagonals, this kind of measurement cannot provide us some useful information.

4 Conclusions

Interest is growing on the potentialities offered by the polarized RHIC collider to get a handle on new phenomena thanks to precision measurements of spin asymmetries [10]. We had first investigated in Ref. [12] the influence on A_{LL}^{PV} in $\vec{p}\vec{p}$ collisions of a purely phenomenological Z' with strong couplings to quarks and a mass around 1 TeV/c^2. Now it turns out that various theoretical models are in favor of a lighter and leptophobic new neutral gauge boson displaying chiral couplings to quarks. We have checked in this paper that it is particularly relevant to search for some effects in the experimental conditions of RHIC. In particular, the quite poor information available from the $p\bar{p}$ dijet experiments could be complemented for a wide part of the parameter space. Moreover, in case of a positive signal it is possible to get immediately an information on the chiral structure of the new interaction. However it is still not possible to discriminate between a SUSY or a non-SUSY origin of the new Z' .
Finally, it is interesting to note that a general prediction of all the leptophobic models we have investigated (which assume a trilinear Yukawa term for u-type quarks) is that $C_L^u \neq C_R^u$ since the Higgs doublet H_U is assumed to be charged under the group $U(1)'$. This implies that parity is violated in the u-quark sector except for the very special axial case : $C_L^u = -C_R^u$. On the other hand, parity is conserved for d-quark couplings in the minimal two- Higgs doublets models [15], which is not a priori the case for non-minimal models (see e.g. Refs.[4, 20]). Unfortunately, as we have said before, d-quark interactions are essentially masked in $\vec{p}\vec{p}$ collisions. It will be mandatory to perform polarized neutron-neutron collisions to get a complementary information : at RHIC this could be realized with polarized ^3He beams as discussed recently [31]. Motivated by these arguments, and also by our earlier work on the charged gauge boson sector [32], we are strongly in favor of a complete polarization program at RHIC.

Acknowledgments
J.M.V. acknowledges the warm hospitality at the RIKEN-BNL Research center where part of this work has been performed. Thanks are due to G. Bunce, G. Eppley, B. Kamal, N. Saito, M. Tannenbaum and W. Vogelsang for fruitful discussions. P.T. wishes to thank Yves Bigot for kind referencing.

References

[1] The LEP Collaborations Aleph, Delphi, L3, Opal, the LEP Electroweak Working Group and the SLD Heavy Flavor Group, CERN-PPE/97-154.

[2] M.L. Mangano, proceedings of the Warsaw Conference ICHEP96, p. 1332.

[3] M. Cvetič and P. Langacker, Phys. Rev. **54** (1996) 3570.

[4] M. Cvetič, D.A. Demir, J.R. Espinosa, L. Everett and P. Langacker, Phys. Rev. **56** (1997) 2861.

[5] J. D. Lykken in Snowmass 1996, ed. D.G. Cassel, L. Trindle Gennari and R.H. Siemann, p. 891.

[6] P. Langacker and J. Wang, hep-ph/9804438, see also P. Langacker hep-ph/9805486.

[7] J.L. Rosner, Phys. Lett. **B387** (1996) 113.

[8] M. Tannenbaum, in *Polarized Collider Workshop*, J. Collins, S.F. Heppelmann and R.W. Robinett eds, AIP Conf. Proceedings **223**, AIP, New York, 1990, p. 201.

[9] G. Bunce et al. (RHIC Spin Collaboration), *Polarized protons at RHIC*, Particle World, **3** (1992) 1 ; RSC, Letter of intent, April 1991 and RSC (STAR/PHENIX) letter of intent update, August 1992, BNL Reports, unpublished.

[10] Proceedings of the RIKEN-BNL research center workshop, april 1998, BNL Report 65615.

[11] G. Altarelli et al., Phys. Lett. **B375** (1996) 292 ; P. Chiappetta et al., Phys. Rev. **D54** (1996) 789.

[12] P. Taxil and J.-M. Virey, Phys. Lett. **B383**, 355 (1996).

[13] J.L. Lopez and D.V. Nanopoulos, Phys. Rev. **D55** (1997) 397.

[14] I. Antoniadis, J. Ellis, J.S. Hagelin and D.V. Nanopoulos, Phys. Lett. **B194** (1987) 321.

[15] K.S. Babu, C. Kolda and J. March-Russell, Phys. Rev. **D54** (1996) 4635 ; **D57** (1998) 6788.

[16] J.L. Hewett and T.G. Rizzo, Phys. Reports, **183**, 193 (1989).

[17] F. del Aguila, G. Blair, M. Daniel and G.G. Ross, Nucl. Phys. **B283** (1987) 50.

[18] A.E. Faraggi and M. Masip., Phys. Lett. **B388** (1996) 524.

[19] K. Agashe, M. Graesser, I. Hinchliffe and M. Suzuki, Phys. Lett. **B385** (1996) 218.

[20] H. Georgi and S.L. Glashow, Phys. Lett. **B387**, 341 (1996).

[21] Y. Umeda, G.C. Cho and K. Hagiwara, hep-ph/9805447, hep-ph/9805448.

[22] J. Alitti et al., Zeit. f. Phys. **C49** (1991), 17 ; Nucl. Phys. **B400** (1993), 3.

[23] F. Abe et al., Phys. Rev. **D55** (1997) R5263.

[24] B. Abbott et al., FERMILAB-Conf-97/356-E.

[25] F. Caravaglios and G.G.Ross, Phys. Lett. **B346** (1995), 159.

[26] C. Bourrely, J. Ph. Guillet and J. Soffer, Nucl. Phys. **B361** (1991) 72.

[27] M. Glück, E. Reya, M. Stratman and W. Vogelsang, Phys. Rev. **D53** (1996), 4775.

[28] J. Soffer and J.-M. Virey, Nucl. Phys. **B509** (1998) 297.

[29] M. Abud, R. Gatto and C.A. Savoy, Ann. Phys. (NY) **122** (1979) 219 ; U. Baur, E.W.N. Glover and A.D. Martin, Phys. Lett. **B232** (1989) 519.

[30] G. Eppley in Ref.[10], p. 301.

[31] E. Courant in Ref.[10], p. 275.

[32] P. Taxil and J.-M. Virey, Phys. Lett. **B404**, 302 (1997); J.-M. Virey in Ref.[10], p. 293.

Figure captions

Fig. 1 Bounds on the parameter space $(\kappa, M_{Z'})$ in models A and B. Contours are from the dijet cross section analysis in $p\bar{p}$ collisions at CERN (UA2) (90% C.L.) and FNAL (CDF,D0) (95% C.L.). The dotted (dashed) line corresponds to the predicted limit at (95% C.L.) from A_{LL}^{PV} in polarized pp collisions at RHIC with a c.m. energy of 500 GeV and an integrated luminosity $\mathcal{L}_1 = 800pb^{-1}$ ($\mathcal{L}_2 = 3200pb^{-1}$).

Fig. 2 A_{LL}^{PV} for one-jet inclusive production, versus E_T, for polarized pp collisions at RHIC. The plain curve is the SM expectation, the dotted curves correspond to the "degenerate" case $M_{Z'} = M_Z$ in model (A) (upper curve) and model (B) (lower curve). Same for the dashed curves with $M_{Z'} = 200$ GeV/c^2. The dash-dotted curve corresponds to model (C) with $M_{Z'} = 300$ GeV/c^2. The error bars correspond to the statistical error with the luminosity $\mathcal{L}_1$.

Fig. 3 Contour plots at 95%C.L. in the plane $(\kappa.C_L,\ \kappa.C_R^u)$ from A_{LL}^{PV} measured with the integrated luminosity $\mathcal{L}_2$. Plain (dashed) curves are for $M_{Z'} = 200(300)$ GeV/c^2. The circles correspond to exclusion limits from present collider data. The black triangle, square and disk correspond to models (A), (B) and (C) respectively for $\kappa = 1$.

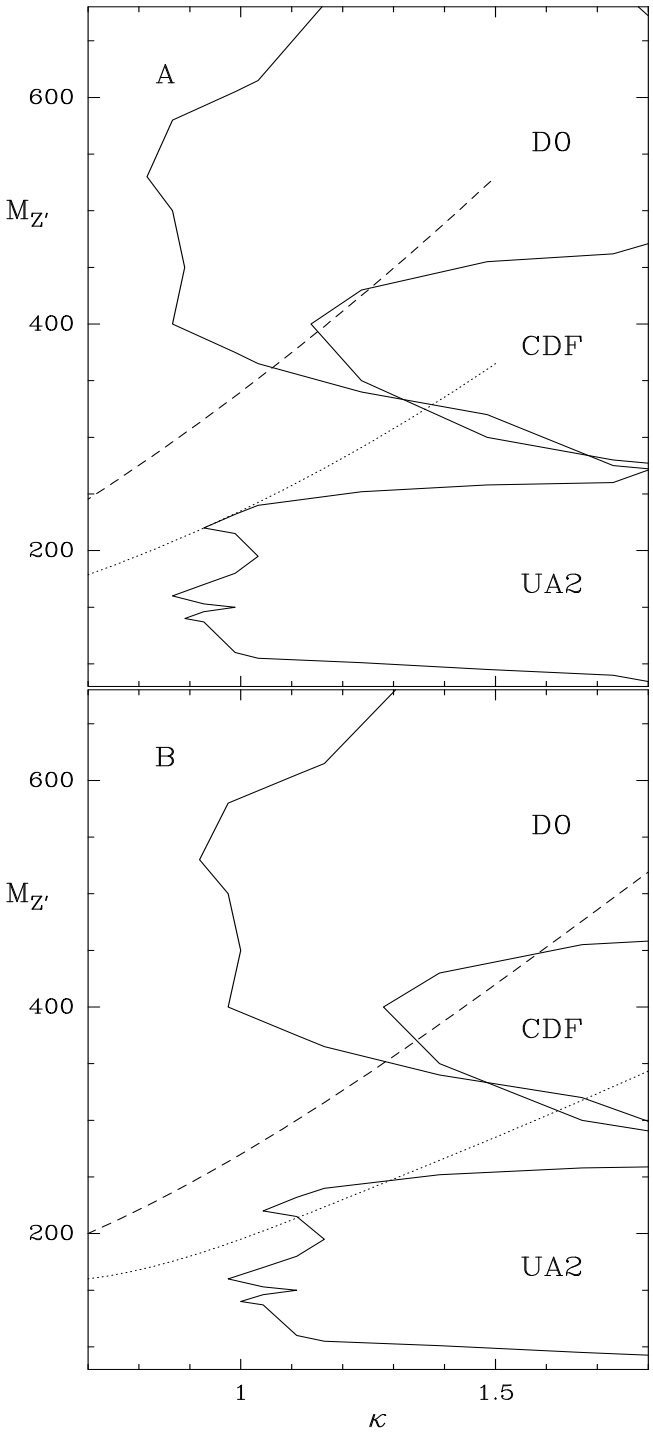

Fig 1

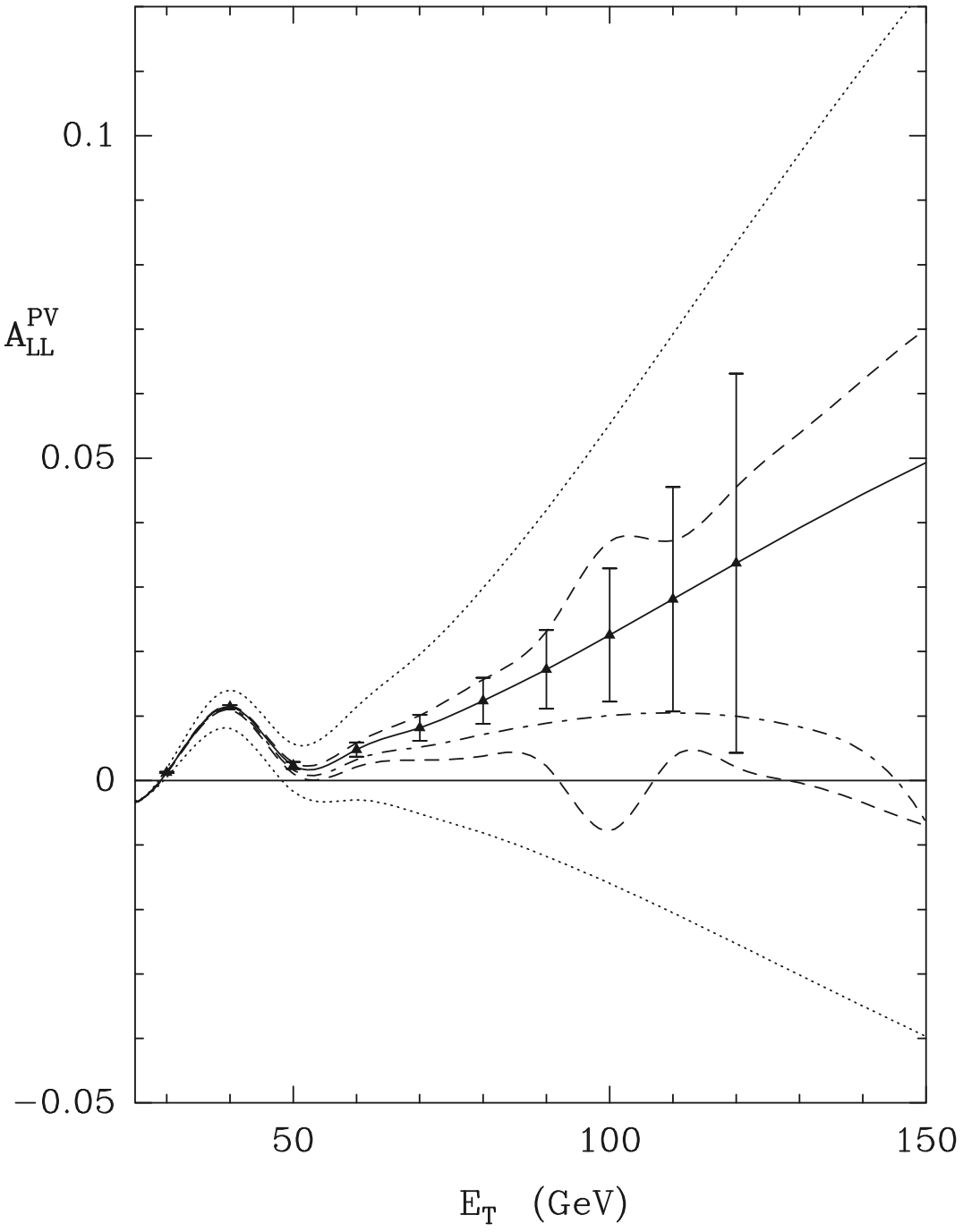

Fig 2

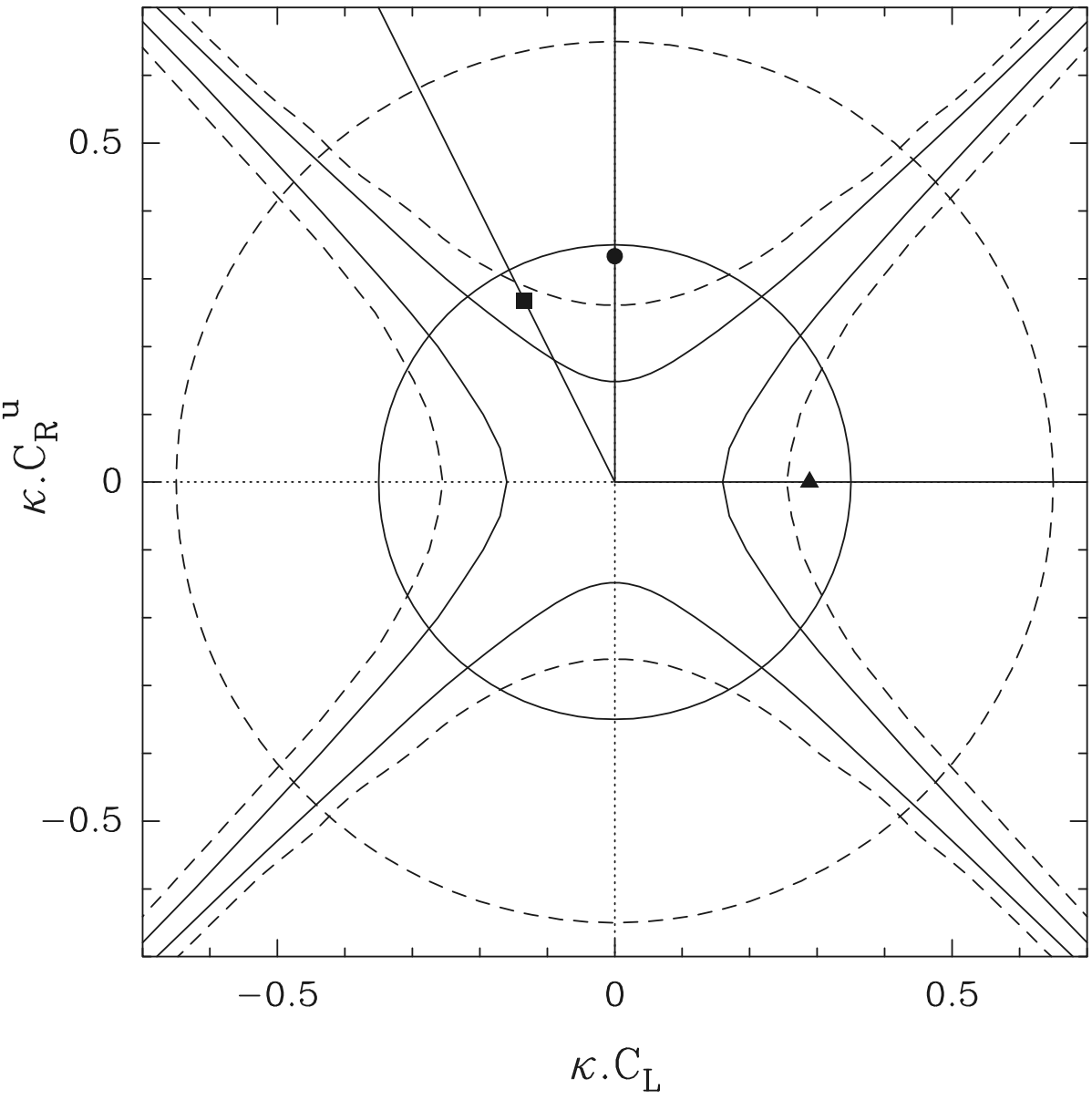

Fig 3

1.2.3 Interaction de contact et nouveaux bosons pour RHIC-Spin amélioré

Article publié sous la référence : Phys. Lett. **B522** (2001) 89 .

Discovery potential for New Physics

in view of the RHIC-Spin upgrade

P. Taxil and **J.-M. Virey**

Centre de Physique Théorique*, C.N.R.S. - Luminy, Case 907
F-13288 Marseille Cedex 9, France

and

Université de Provence, Marseille, France

Abstract

In view of a possible upgrade of the RHIC-Spin program at BNL, concerning both the machine and the detectors, we give some predictions concerning the potentialities of New Physics detection with polarized proton beams. We focus on parity-violating asymmetries in one-jet production due to contact terms or to a new leptophobic neutral gauge boson. We comment on the main uncertainties and we compare with unpolarized searches at Tevatron.

PACS Numbers : 12.60.Cn; 13.87.-a; 13.88.+e; 14.70.Pw
Key-Words : New Gauge bosons, Jets, Polarization.

Number of figures : 1

September 2001
CPT-01/P.4224

anonymous ftp or gopher : cpt.univ-mrs.fr

---

*Unité Propre de Recherche 7061
E-mail : taxil@cpt.univ-mrs.fr ; virey@cpt.univ-mrs.fr

1 Introduction

There is a growing interest on the physics program which will be achieved at RHIC-Spin, that is at the Brookhaven National Laboratory Relativistic Heavy Ion Collider (RHIC), running in the polarized $\vec{p}\vec{p}$ mode.

Actually, during the year 2001 the RHIC-Spin Collaboration (RSC) will perform the first polarized run at a c.m. energy of $\sqrt{s} = 200$ GeV and a luminosity of a few $10^{30} cm^{-2} s^{-1}$.

The nominal energy of $\sqrt{s} = 500$ GeV and luminosity $\mathcal{L} = 2.10^{32} cm^{-2} s^{-1}$ should be reached in the early months of 2003, allowing an exposure of 800 pb^{-1} in four months of running.

Physics at RHIC-Spin has been extensively covered in a recent review paper [1], where many references can also be found (see also [2]). The first part of the program will include precise measurements of the polarization of the gluons, quarks and sea-antiquarks in a polarized proton. This will be done thanks to well-known Standard Model processes : direct photon, W and Z production, Drell-Yan pair production, heavy-flavor production and the production of jets. The helicity structure of perturbative QCD will be thoroughly tested at the same time with the help of Parity Conserving (PC) double spin asymmetries.

It has been first noticed more than ten years ago [3] that the production of high E_T jets from polarized protons could allow to pin down a possible new interaction, provided that parity is violated in the subprocess.

Since QCD is parity conserving and dominates the process, according to the Standard Model (SM), the expected Parity Violating (PV) spin asymmetry in jet production should come from tiny electroweak effects. Hence, a net deviation from the small expected Standard Model asymmetry could be a clear signature of the presence of New Physics.

Due to the energy reach of the machine the New Physics scale should not be too high to yield a contribution : fortunately some scenarios are still allowed by present data, in particular the existence of a new weak force belonging uniquely to the quark sector.

In previous papers, we have explored the very phenomenological case of a PV contact interaction between quarks [4], various situations with a new Z' with nearly zero couplings to leptons (the so-called leptophobic Z') [5] and also a scenario with a right-handed W' decaying into quarks in the case of a very massive right-handed neutrino [6].

In this letter we will explore the potentialities of RHIC-Spin in view of the two kinds of possible upgrades [7]. The improved machine could reach $\sqrt{s} = 650$ GeV with an integrated luminosity $L = 20 fb^{-1}$ in a few months running and the STAR detector could greatly improve the angular coverage with new end-caps. We compare also with the limits which could be obtained with the (unpolarized) Tevatron in Run-II. Concerning theoretical uncertainties, we comment the situation on higher-order calculations when they are available.

2 Sources of PV effects in jet production

The production of high E_T jets is dominated by QCD, in particular by quark-quark scattering. The existence of W and Z° adds a small standard contribution to the cross section [8]. On the other hand the interference of weak amplitudes with QCD amplitudes will be the main Standard source of PV helicity asymmetries in this process. A peak in the asymmetries at $E_T \approx M_{W,Z}/2$ is also the main signature for a pure electroweak contribution.

All the tree-level polarized cross sections for these standard subprocesses can be found in Ref. [9]. Predictions using updated polarized partonic distributions can be found in [5] or [1].

The effects of some possible Non Standard PV interactions have been studied in recent years :

- First [4] one can think to a simple phenomenological contact interaction which could represent the consequences of quark compositeness. Such (color singlet and isoscalar) terms are usually parametrized following Eichten et al. [10] :

$$\mathcal{L}_{qqqq} = \epsilon \frac{g^2}{8\Lambda^2} \bar{\Psi}\gamma_\mu(1-\eta\gamma_5)\Psi.\bar{\Psi}\gamma^\mu(1-\eta\gamma_5)\Psi \tag{1}$$

where Ψ is a quark doublet, ϵ is a sign and η can take the values ± 1 or 0. g is a new strong coupling constant usually normalized to $g^2 = 4\pi$ and Λ is the compositeness scale.

In the following we will consider the LL^- case with Left-handed chiralities ($\eta = 1$) and constructive interference with QCD amplitudes which corresponds to $\epsilon = -1$.

- Second, we can consider some new neutral gauge bosons with general Left and Right-handed couplings to each given quark flavor q:

$$\mathcal{L}_{Z'} = \kappa \frac{g}{2\cos\theta_W} Z'^\mu \bar{q}\gamma_\mu[C_L^q(1-\gamma_5) \; + \; C_R^q(1+\gamma_5)]q \tag{2}$$

the parameter $\kappa = g_{Z'}/g_Z$ being of order one. For a recent review on Z' phenomenology (in the context of e^+e^- collisions), one can consult [11]. A particular class of models, called leptophobic Z' , is poorly constrained by present data since they evade the LEP constraints. Such models appear in several string-inspired scenarios [12, 13]. Non supersymmetric models can also be constructed [14]. Other references can be found in [5]. In addition, it was advocated in [15] that such a boson could appear with a mass close to the electroweak scale and a mixing angle to the standard Z° close to zero.

In this letter we will focus for illustration on the flipped-SU(5) model of Lopez and Nanopoulos [12] (model A of [5]) in which parity is maximally violated in the up-quark sector. Therefore the couplings in eq.(2) take the following values : $C_L^u = C_L^d = -C_R^d = 1/(2\sqrt{3})$ and $C_R^u = 0$, the ratio κ being a free parameter. In this scenario, 95% of the new PV effect will come from the interference between the Z' exchange and the one-gluon exchange amplitudes in the scattering of u quarks in the t-channel.

3 Results

For Spin experiments, the most important quantities in practice are not the polarized cross sections themselves, but the spin asymmetries.

At RHIC, running in the $\vec{p}\vec{p}$ mode, it will be possible to measure with a great precision the single PV asymmetry A_L :

$$A_L \;=\; \frac{d\sigma_{(-)} - d\sigma_{(+)}}{d\sigma_{(-)} + d\sigma_{(+)}} \tag{3}$$

where only one of the proton is polarized, or the double helicity PV asymmetry :

$$A_{LL}^{PV} = \frac{d\sigma_{(-)(-)} - d\sigma_{(+)(+)}}{d\sigma_{(-)(-)} + d\sigma_{(+)(+)}} \tag{4}$$

where both polarizations are available. In the above quantities the signs $\pm$ refer to the helicities of the colliding protons. The cross section $d\sigma_{(\lambda_1)(\lambda_2)}$ means the one-jet production cross section in a given helicity configuration, $p_1^{(\lambda_1)} p_2^{(\lambda_2)} \to jet + X$, estimated at some $\sqrt{s}$ for a given jet transverse energy E_T , integrated over a pseudorapidity interval $\Delta\eta$ centered at $\eta = 0$. In fact, both quantities will exactly yield the same amount of information. From now we will discuss only the single PV asymmetry.

All the present calculations use polarized parton distribution functions $\Delta f_i(x, Q^2)$'s which have been parametrized from deep-inelastic data e.g. GRSV distributions [16]. The polarized quark distributions $\Delta q(x, Q^2)$ which play a dominant role in our calculation at high E_T are the most reliable : in any case they will be much better measured soon thanks to the first part of the RHIC-Spin program itself.

We give in Table 1 the 95 % C.L. limits on $\Lambda \equiv \Lambda_{LL^-}$ (eq.1) one gets, at lowest order, from a comparison between the SM asymmetry A_L and the Non-Standard one. We have taken into account the statistical error, which for small asymmetries is given by :

$$\Delta A_L = \frac{1}{P}\frac{1}{\sqrt{N}} \tag{5}$$

where P is the degree of polarization of the beams, expected to be $P = 0.7$. Systematics are assumed to be low [1] (see comments below), and we have taken the conservative value $\delta_{syst} \equiv (\Delta A)_{syst}/A = 10\%$.

One can compare the bounds at $\sqrt{s} = 500$ GeV and $L = 0.8 fb^{-1}$ with the ones after the energy and/or luminosity upgrade. $4 fb^{-1}$ ($100 fb^{-1}$) represents 5×4 months running with the presently designed (future) nominal luminosity. On the other hand, the cross section being essentially flat in rapidity in the interval which is accessible to experiment, an increase in rapidity from $\Delta\eta = 1$ to 2.6 is equivalent to a substantial increase in luminosity.

Since the statistical error goes like $(1/P)(1/\sqrt{N})$, reducing the degree of polarization P by a factor ϵ is equivalent to a factor ϵ^2 in luminosity. In practice, varying the designed value $P = 0.7$ by 10% will change the limits by roughly 6%.

$\sqrt{s}$ (GeV)	L (fb^{-1})	$\Lambda(\Delta\eta = 1)$	$\Lambda(\Delta\eta = 2.6)$
500	0.8	3.2	4.0
500	4	4.55	5.5
500	20	6.15	7.0
500	100	7.55	8.30
650	4	5.2	6.3
650	20	7.05	8.10
650	100	8.75	9.5

Table 1 : Limits on Λ_{LL^-}, in TeV, at 95% CL with $\delta_{syst} = 10\%$, $P = 0.7$.

This table can be compared with the last published analysis of the D0 experiments at Tevatron [17]: $\Lambda > 2.2$ TeV (95% C.L.) from the dijet mass cross section. From these figures we have extrapolated a limit at Tevatron of 3.2 TeV (3.7 TeV) with a 1 fb^{-1} (10 fb^{-1}) exposure.

Turning now to the case of a leptophobic Z' , we present in Fig.1 the constraints on the parameter space $(\kappa, M_{Z'})$ obtained from A_L in the flipped SU(5) model. The dotted curves correspond to $\sqrt{s} = 500$ GeV and the dashed curves to $\sqrt{s} = 650$ GeV. From bottom to top they correspond to an integrated luminosity $L = 1, 10, 100 fb^{-1}$. It appears that the increase in luminosity is more efficient than the increase in energy. Therefore the high luminosity scenario has to be supported even if the RHIC pp c.m. energy remains at its "low" value.

We display also in Fig.1 the inferred constraints coming from the published results of UA2 [18], CDF [19] and D0 [20] experiments. The form of the forbidden areas result from a combination of statistical and systematic errors. For high $M_{Z'}$ one looks for some unexpected high-E_T jet events and the main uncertainty is statistical in nature. For instance, the upper part of the "CDF area" is well below the one of D0 because of the well-known excess observed by CDF at high-E_T. In the future (run II) the increase in statistics will improve the bounds in the $(\kappa, M_{Z'})$ plane by enlarging the upper part of the CDF and D0 areas (or will lead to a discovery). For relatively low $M_{Z'}$ values, the main problem comes from the large systematic errors for "low" E_T jets. Due to these systematics, at Tevatron, even with a high statistics it will be difficult to probe the low κ region for $M_{Z'} \leq 400$ GeV or to close the windows around $M_{Z'} \simeq 300$ and 100 GeV. In this respect, as can be seen from Fig.1, the RHIC-Spin measurements at high luminosity should allow to cover this region and to get definite conclusions, if the new interaction violates parity.

4 Comments

Concerning experimental uncertainties, with a good knowledge of the beam polarization ($\pm 5\%$) and a very good relative luminosity measurement (10^{-4}), the systematic scale of uncertainty for a single spin measurement should be of the order of 5% [1]. Hence

we have been conservative in taking $\delta_{syst} = 10\%$. For instance, one should get higher limits with the former figure : $\Lambda = 9.0(10.35)$ TeV with 100 fb^{-1} at 500 (650) GeV, with $\Delta\eta = 1$. The consequences of a smaller systematical error are more sizeable at high luminosity where the statistical error becomes very small.

On the theoretical side, the current prejudice is that spin asymmetries are much less affected than simple cross sections by higher order corrections. Indeed, recent calculations confirm this simple behaviour.

Concerning SM PV effects, their precise knowledge is mandatory to extract any signal of New Physics. It has been stressed in Ref.[21] that corrections to the QCD-Electroweak interfence terms, at the order $\alpha_s^2\alpha_W$, might be important in the quark-quark channel and also that there were some new contributions from this order in quark-gluon scattering. Recently, the authors of Ref.[22] have carried out the calculation of the one-loop weak corrections to polarized $q-g$ scattering and the corresponding crossed channels. It appears that the PV effects involving gluons are relatively small, i.e. at most 10% of the tree-level contribution. Moreover, any effect at the partonic level will not be enhanced by a possibly large polarization of the gluons, ΔG, because in the large x region which is of interest here the gluon distributions are small. We have implemented the NLO amplitudes of Ref.[22] in our code, and we have verified that the corrections on A_L are of the order of 5% (7%) on the whole E_T spectrum at a c.m. energy of 500 GeV (650 GeV). It was also straightforward to add the effect of the presence of a new Z' in the one-loop amplitude : it turns out that the contribution is negligeable.

Concerning $q - q$ scattering, the NLO calculations are not available but we hope to have them in a not too distant future [23]. However, as shown recently by Vogelsang [24], a relatively good estimate of the size of these corrections can be obtained by performing some gluon resummations. Results of a calculation on A_L at RHIC, after resummation at the Leading-Log level, indicate a relatively small correction, of the order of 10% at high E_T. However more precise calculations at the Next-to-Leading-Log level are necessary to get a definite conclusion.

5 Conclusions

Qualitatively new measurements will be allowed by the RHIC-Spin experiment. Parity violation searches for physics beyond the Standard Model will be competitive with unpolarized searches at the Fermilab Tevatron, in particular in the upgraded version of the machine and of the detector(s). It is worth stressing that an increase in luminosity of the RHIC $\vec{p}\vec{p}$ machine and/or an improvement of the angular coverage of the detectors seem more efficient than an increase in energy above $\sqrt{s} = 600$ GeV.

From now the precise amount of systematic uncertainties is not accurately known. However experts at RHIC are confident in the capacities of polarimetry and luminosity calibrations. On the other hand, some recent theoretical results indicate that the tree-level prediction for the SM parity-violating asymmetry is quite stable. Hence definite results could be obtained from the measurement of A_L : in particular it has to be emphasized

that the existence of a new weak force between quarks only is not in contradiction with present data. It might also explain the small discrepancies which still exists between leptonic and hadronic observables in LEP and SLC results.

Concerning an other possible step for the program, the possibility of colliding polarized protons against polarized (or unpolarized) ^3He nuclei has been discussed. This could allow to measure some spin asymmetries in $\vec{p}$-n and/or $\vec{p}$-$\vec{n}$ collisions and also possibly in $\vec{n}$-$\vec{n}$ collisions via polarized ^3He-^3He collisions. In this case a new charged vector boson (e.g. a massive right-handed W_R) could also mediate some visible effects (see Ref.[6]).

Acknowledgments
J.M.V. acknowledges the warm hospitality at the RIKEN-BNL Research center where part of this work has been performed. Thanks are due to G. Bunce, G. Eppley, S. Moretti, D.A. Ross, N. Saito, J. Soffer and W. Vogelsang for fruitful discussions.

References

[1] G. Bunce, N. Saito, J. Soffer and W. Vogelsang, Ann. Rev. Nucl. Part. Sci. **50** (2000) 525.

[2] Proceedings of the 14th International Spin Physics Symposium, Osaka, 2000, K. Hatanaka et al. eds., AIP Conf. Proceedings **570**, AIP, New York, 2001.

[3] M. Tannenbaum, in *Polarized Collider Workshop*, J. Collins, S.F. Heppelmann and R.W. Robinett eds, AIP Conf. Proceedings **223**, AIP, New York, 1990, p. 201.

[4] P. Taxil and J.-M. Virey, Phys. Lett. **B364** (1995) 181.

[5] P. Taxil and J.-M. Virey, Phys. Lett. **B441** (1998) 376.

[6] P. Taxil and J.-M. Virey, Phys. Lett. **B404** (1997) 302.

[7] N. Saito in Ref.[2] and references therein.

[8] M. Abud, R. Gatto and C.A. Savoy, Ann. Phys. (NY) **122** (1979) 219 ; U. Baur, E.W.N. Glover and A.D. Martin, Phys. Lett. **B232** (1989) 519.

[9] C. Bourrely, J. Ph. Guillet and J. Soffer, Nucl. Phys. **B361** (1991) 72.

[10] E. Eichten, K.Lane and M. Peskin, Phys. Rev. Lett. **50**, 811 (1983), E. Eichten, et al., Rev. Mod. Phys. **56** (1984) 579.

[11] A. Leike, Phys. Rept. **317** (1999) 143.

[12] J.L. Lopez and D.V. Nanopoulos, Phys. Rev. **D55** (1997) 397.

[13] J.D. Lykken in Snowmass 1996, ed. D.G. Cassel, L. Trindle Gennari, R.H. Siemann, p.891; K.S. Babu, C. Kolda and J. March-Russell, Phys. Rev. **D54** (1996) 4635 ; **D57** (1998) 6788.

[14] K. Agashe, M. Graesser, I. Hinchliffe and M. Suzuki, Phys. Lett. **B385** (1996) 218; H. Georgi and S.L. Glashow, Phys. Lett. **B387**, 341 (1996).

[15] M. Cvetič et al, Phys. Rev. **D56** (1997) 2861.

[16] M. Glück, E. Reya, M. Stratman and W. Vogelsang, Phys. Rev. **D53** (1996) 4775.

[17] B. Abbott et al.(D0 Collaboration), Phys. Rev. **D64** (2001) 032003.

[18] J. Alitti et al., Zeit. f. Phys. **C49** (1991), 17 ; Nucl. Phys. **B400** (1993), 3.

[19] F. Abe et al., Phys. Rev. **D55** (1997) R5263.

[20] B. Abbott et al., FERMILAB-Conf-97/356-E.

[21] J.-M. Virey in *Predictions and uncertainties for RHIC Spin Physics and event generators for RHIC Spin Physics III*, Proceedings of the RIKEN-BNL Workshop, March 2000, Brookhaven, p. 111.

[22] J. Ellis, S. Moretti and D.A. Ross, JHEP **06** (2001) 043.

[23] D.A. Ross, private communication.

[24] W. Vogelsang in *Spin Physics at RHIC in year-1 and beyond*, Proceedings of the RIKEN-BNL Workshop, May 2001, Brookhaven; and in *The Spin Structure of the Proton and Polarized Collider Physics*, Proceedings of the ECT* workshop, July 2001, Trento, Italy, to appear.

[25] J. Soffer and J.-M. Virey, Nucl. Phys. **B509** (1998) 297.

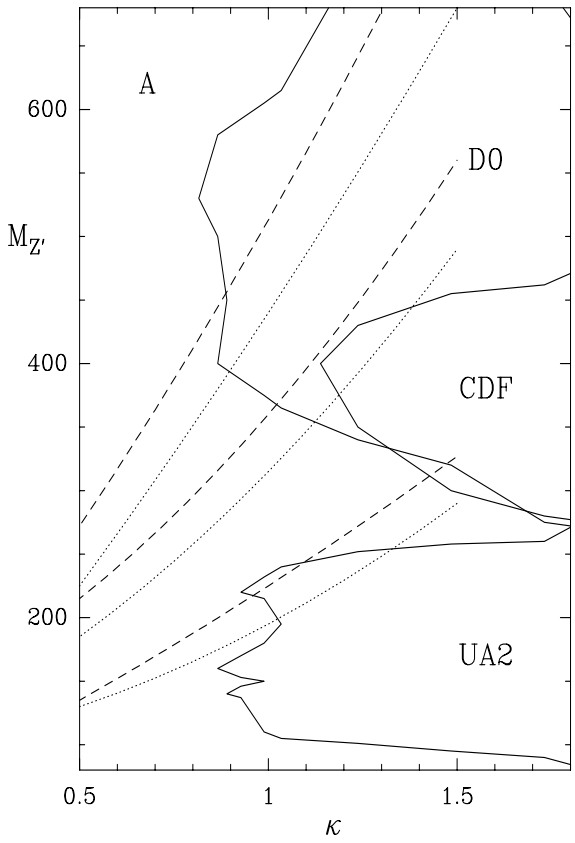

Figure 1: Bounds on the parameter space for leptophobic flipped SU(5) Z' models (see text).

1.2.4 Contraintes sur le secteur scalaire avec des neutrons

Article publié sous la référence : Eur. Phys. J. **C24** (2002) 149.

Constraints on leptophobic gauge bosons with polarized neutrons and protons at RHIC

P. Taxil[a], **E. Tuğcu**[b] and **J.-M. Virey**[a]

[a]Centre de Physique Théorique*, C.N.R.S. - Luminy, Case 907
F-13288 Marseille Cedex 9, France

and

Université de Provence, Marseille, France

[b]Galatasaray University, Çırağan Cad. 102, Ortaköy 80840-İstanbul, Turkey

Abstract

We explore the sensitivity and the physics interest of the measurement of parity-violating spin asymmetries in one-jet production in the presence of a new leptophobic neutral gauge boson $Z^{'}$, within polarized hadronic collisions at the BNL RHIC. We focus on polarized neutron collisions which could be achieved in a realistic upgrade of the RHIC-Spin program. We show that, in case of a discovery, a compilation of the information coming from both polarized $\vec{p}\vec{p}$ and $\vec{n}\vec{n}$ collisions should constrain the number of Higgs doublets and the presence or absence of trilinear fermion mass terms in the underlying model of New Physics.

PACS Numbers : 12.60.Cn; 13.87.-a; 13.88.+e; 14.70.Pw
Key-Words : New Gauge bosons, Jets, Polarization, Neutron Collisions.

Number of figures : 4

November 2001
CPT-2001/P.4263

anonymous ftp or gopher : cpt.univ-mrs.fr

---

*Unité Propre de Recherche 7061
E-mail : taxil@cpt.univ-mrs.fr ; tugcu@gsunv.gsu.edu.tr ; virey@cpt.univ-mrs.fr

1 Introduction

The addition of an extra $U(1)'$ gauge factor to the $SU(3) \times SU(2) \times U(1)$ structure is one of the simplest extensions of the Standard Model (SM). When the symmetry breaking of this extra factor occurs at a scale close to the electroweak scale, one obtains a new neutral gauge boson Z' in the particle spectrum, at a mass accessible to forthcoming experiments.

The strongest experimental constraints on such Z' models come from experiments which analyze some processes involving leptons, either in the initial state or/and in the final state. For instance, the constraints coming from LEP, HERA or the Drell-Yan process at Tevatron are complementary and provide some bounds on the Z' mass of the order of $600 - 700\ GeV$ for canonical models [1], the precise values depending on the specific model and the relevant process involved in the analysis. However, when the Z' has zero or very small direct couplings to leptons (leptophobia), the above processes are irrelevant and one has to turn to pure hadronic channels to provide some constraints [1].

The existence of relatively light leptophobic gauge bosons is an attractive possibility, both for phenomenology and from theoretical arguments. Recent papers advocated a weak-scale supersymmetry (SUSY) scenario in non-minimal SUSY models with an additional extra $U(1)^{'}$. The corresponding Z' could be "light" : $M_{Z'} < 1.5\,TeV$. More precisely, a class of models driven by a large trilinear soft SUSY breaking term, prefer the range $M_Z < M_{Z'} < 400\,GeV$, along with a very small mixing with the standard Z. This particular scenario is only allowed if the model exhibits leptophobic couplings [2]. On the other hand, other models display or can accommodate leptophobia : some are string inspired [3, 4, 5], others are non-SUSY [6, 7] (for a more complete set of references one can consult our paper [8]). Furthermore, in many models an asymmetry in the left and right-handed couplings of the $Z^{'}$ to light quarks is preferred or at least allowed. Finally, a small $Z - Z^{'}$ mixing angle is generated in these models, in agreement with electroweak precision data.

In a previous paper [8], we have shown that the measurement of Parity Violating (PV) spin effects in the production of jets from hard collisions of polarized hadrons, could be a way to get a handle on this elusive leptophobic Z' boson.
The situation of interest is the one at Brookhaven National Laboratory where the RHIC machine is operating mainly as a heavy-ion collider but will be used part of the time as a polarized proton-proton ($\vec{p}\vec{p}$) collider. The RHIC Spin Collaboration (RSC) has performed a first run during the year 2001 , with polarized protons, an energy $\sqrt{s} =$ 200 GeV and a luminosity of a few $10^{30} cm^{-2} s^{-1}$. Around 2003, it is expected to reach $\sqrt{s} = 500$ GeV and $\mathcal{L} = 2.10^{32} cm^{-2} s^{-1}$ [9] allowing an exposure of 800 pb^{-1} in only four months of running. The physics program of the collaboration has been reviewed recently in ref.[10] where many references can also be found (see also [9]). This program will allow first some precise measurements of the polarization of the gluons, quarks and sea-antiquarks in a polarized proton. This will be done thanks to well-known Standard Model processes : direct photon, W and Z production, Drell-Yan pair production, heavy-flavor

production and the production of jets. The helicity structure of perturbative QCD will be thoroughly tested at the same time with the help of Parity Conserving (PC) double spin asymmetries.

Concerning new physics, it has been noticed that non-zero CP-violating asymmetries can be generated from various mechanisms going beyond the SM [11, 12, 13]. On the other hand, the production of high E_T jets from polarized protons could allow to pin down a possible new weak interaction between quarks, provided that parity is violated in the subprocess [14, 15, 16, 8, 17]. In the case of a simple phenomenological PV Contact Term, a search strategy based on the polarized RHIC can be competitive with conventional searches at the Tevatron, or even better [18, 17].

Indeed, the production of jets is largely dominated by QCD, which is a parity conserving theory. However a Standard PV spin asymmetry in jet production should be present from tiny QCD-Electroweak interference effects, namely the interference between the one-weak boson exchange amplitude and the one-gluon exchange amplitude since, at high E_T, the process is dominated by qq scattering. The magnitude and sign of this Standard PV asymmetry can be safely estimated from well-known subprocess amplitudes and from our knowledge of the polarized quark distributions in a polarized proton. Note that polarized gluons distributions (which are poorly known) are irrelevant in this process at least at Leading Order (LO). Therefore, a net deviation from the small expected Standard Model asymmetry could be a clear signature of the presence of a new force belonging to the quark sector with a peculiar chiral structure.

Models with leptophobic Z's are obviously good candidates to consider in this context. The study presented in [8] has shown that, in order to detect a non standard effect in $\vec{p}\vec{p}$ collisions at RHIC, besides the necessity of leptophobia plus a low mass, the Z' boson must exhibit an asymmetry in the left and right couplings to u quarks since u quarks dominate in $\vec{p}\vec{p}$ collisions. Fortunately, the existence of such PV couplings for u quarks is a prediction of several leptophobic models constructed up to now [4, 5, 6, 7].

Conversely, the PV nature of the Z' couplings to d quarks is much more model dependent. Indeed, it depends on the symmetry breaking scenarios and on the scalar potential assumed for the models. More precisely, we will see that the PV properties of the d couplings are directly connected to the number of Higgs doublets involved in the model and to the presence or absence of tri-linear fermion mass terms in the Yukawa lagrangian. So, in case of a discovery, the measurements of these d couplings, or at least the test of their PV nature, should provide a unique information on the scalar sector of the underlying theoretical model of New Physics.

Unfortunately, within $\vec{p}\vec{p}$ collisions at RHIC the Z' amplitudes involving d quarks in the initial and final states are completely hidden by the u quark contributions. However, a particular feature of the RHIC as a heavy ion collider, is to be able to accelerate polarized ^3He nuclei, which could mimic high energy polarized neutrons. Indeed, the Pauli exclusion principle implies that the polarized ^3He nuclei carries essentially the spin of the neutron since the spins of the protons are in opposite directions.

This possibility has been considered by the RSC and it is expected to get some polarized beams of "neutrons" of relatively good quality [19]. Therefore, in the following, we consider polarized $\vec{n}\vec{n}$ collisions at RHIC in order to explore which kind of information could be obtained on the d-couplings and on the scalar sector of the new theory.

In section two, we present the models and the different scalar structures which are considered in our analysis. In section three, we present the definition of the spin dependent observable that we consider, we summarize our calculations and we give the limits on the parameter space which could be achieved at RHIC in the case of the various models, within $\vec{n}\vec{n}$ collisions. In the last section, we show a combined analysis of the information which could be provided by both $\vec{p}\vec{p}$ and $\vec{n}\vec{n}$ collisions, in case of a discovery, and therefore the constraints that might be obtained on the Higgs sector of the theory .

2 Classification of the models

The interactions between a new neutral vector gauge boson $Z^{'}$ and up and down-type quarks are described by the following lagrangian:

$$\mathcal{L}_{Z'} \;=\; \kappa \frac{g}{2cos\theta_W} \sum_q Z^{'\mu} \bar{q} \gamma_\mu \left[C_L^q \left(1-\gamma_5\right) + C_R^q \left(1+\gamma_5\right) \right] q \qquad (1)$$

where $C_{L,R}^q$ are the couplings to left and right handed quarks for each given quark flavor q and the parameter $\kappa = g_{Z'}/g_Z$ being of order one. We restrict our discussion to the light quark flavors u and d since only a Z' which couples to these light quarks may give some observable effects at RHIC energies.
In what follows, we will concentrate on leptophobic $Z^{'}$ models of relatively light masses with chiral couplings to quarks. We refer the reader to ref.[8] and to the original literature for more details on the theoretical motivations and on the underlying structures of each model.

At first, we consider an approach similar to the one of Georgi and Glashow [7] to determine the general conditions imposed by gauge invariance, leptophobia and symmetry breaking on the $U(1)'$ charges. Then, each different general situation will be illustrated by a specific model.
First of all, gauge invariance under the SM group $SU(2)_L$ imposes the universality of the left-handed couplings :

$$C_L^u \;=\; C_L^d \;\equiv\; C_L \qquad (2)$$

Therefore, in the following, we will suppress the flavour indice on the left-handed couplings.

Initially we can assume that all SM fermions acquire their masses via the trilinear mass terms present in the Yukawa lagrangian :

$$\mathcal{L}_Y \;=\; h_u \bar{Q} H_u u_R \;+\; h_d \bar{Q} H_d d_R \;+\; h_l \bar{L} H_l e_R \tag{3}$$

where Q is a quark doublet, L a lepton doublet, u_R, d_R and e_R are right-handed singlets. $H_{u,d,l}$ represent the corresponding Higgs doublets and $h_{u,d,l}$ are Yukawa coupling matrices. For supersymmetric models, the structure is formally the same on condition that one replaces the potential by the superpotential and the fields by the superfields.

Gauge invariance under the new $U(1)^{'}$ gauge group associated with the Z', imposes that the sum of the $U(1)^{'}$ charges $Q^{'}$ for each term is zero :

$$Q^{'}(H_u) \;-\; Q^{'}(Q) \;+\; Q^{'}(u_R) \;=\; 0 \tag{4}$$

$$Q^{'}(H_d) \;-\; Q^{'}(Q) \;+\; Q^{'}(d_R) \;=\; 0 \tag{5}$$

$$Q^{'}(H_l) \;-\; Q^{'}(L) \;+\; Q^{'}(e_R) \;=\; 0 \tag{6}$$

The $U(1)'$ charges of the fermions are directly related to their chiral couplings : $Q^{'}(Q) = C_L$, $Q^{'}(L) = C_L^{e,\nu}$ and $Q^{'}(f_R) = C_R^{f}$.

From eq.(6) the condition of leptohobia[1] $Q^{'}(e_L) = Q^{'}(e_R) = 0$, forces the charge of the Higgs doublet coupling to the lepton field to be zero :

$$Q^{'}(H_l) \;=\; 0 \tag{7}$$

Given these assumptions, we will describe now three different scalar structures implying different properties for the right-handed couplings of d quarks to the $Z^{'}$. Of course, one may be surprised by this particular approach where the Q' charges seem to be put by hand instead of taking a specific model where these charges are fixed and where anomaly cancellation is fulfilled thanks to the presence of exotics. Here we are not interested in these exotics since we can assume safely that their masses are sufficiently high to avoid detection at existing colliders, including RHIC. Moreover, we want to choose an approach which is as most as possible model independent. Since, at RHIC, we can test the PV structure of d quark couplings, we just quote which choice of scalar structure, independently of the choice of a particular new gauge theory, implies a modification in this PV structure.

• Structure I : 2HDM

A first interesting case appears when the Higgs doublet H_d which generates the masses of d-type quarks is identical to the one which yields (charged) lepton masses. This structure corresponds to the Two Higgs Doublets Models (2HDM) and it can be achieved for

[1]In case of gauge kinetic mixing, the Z' actually couples to an effective charge which is a linear combination of Q' and Y (*e.g.* see [4]). To simplify, we have kept the notation Q' for these effective charges.

special values of the Q' charges [7]. In this case, $H_l \equiv H_d$ and we have from eq.(7) :

$$Q^{'}(H_d) = 0 \tag{8}$$

This implies from eq.(5) $Q^{'}(Q) = Q^{'}(d_R)$ or, in terms of the couplings :

$$C_R^d \;=\; C_L \tag{9}$$

We see that the d quark couplings are *vector-like* which means that Parity is conserved in this quark sector. This is the main characteristic of the models displaying this structure that we call *structure I* from now.

Conversely, if we want the remaining Higgs doublet H_u to play a role in the symmetry breaking of the $U(1)'$ symmetry, then it must be charged under $U(1)'$ in order to acquire a vacuum expectation value that breaks the $U(1)'$ symmetry. So, we take $Q'(H_u) \neq 0$ which implies for the couplings (see eq.(4)) :

$$C_R^u \;\neq\; C_L \tag{10}$$

From this equation, we see that the u quark couplings cannot be vector-like. Hence, Parity will be violated, except for the peculiar axial case where $C_R^u \;=\; -C_L$.

This remark and eq.(10) are also valid for the remaining structures that we will consider, *i.e.* we always assume that H_u is playing a role in the breaking of the $U(1)'$ symmetry. Note that additional scalars, singlets of $SU(2)_L$, can also be present in the breaking scenario but they have no impact on the PV nature of the d couplings.

An explicit model which can be an illustration of this *structure I* is the supersymmetric "η-kinetic model" of Babu, Kolda and March-Russell [4], whose properties are Parity Conservation for d quarks and PV for u quarks. We call it *Model B* to remain coherent with reference [8]:

$$Model\ B\ :\qquad C_L^u \;=\; C_L^d \;=\; C_R^d \;=\; -\frac{1}{2}C_R^u \;=\; -\frac{5}{18}sin\theta_W \tag{11}$$

Note that, at a variance with the notations of ref.[4] the usual factor of Grand Unification Theories ($\sqrt{\frac{5}{3}}sin\theta_W$) has been included in the $C_{L,R}^q$ couplings to maintain κ of order one.

• Structure II :

The first extension of the previous scalar structure is achieved when we allow the third Higgs doublet H_l to be different from H_d. In this case, leptophobia does not provide anymore a direct relation among the couplings C_L and C_R^d, since eq.(5) and eq.(6) are now completely disconnected. For *structure II* we still consider that eq.(5) is valid, *i.e.* that d quarks acquire their masses from a trilinear mass term. Conversely, we don't make any assumption on the form of the (charged) lepton mass term which plays no role in the

following discussion.

Nevertheless, in many extensions of the SM, particularly in most of the leptophobic $Z^{'}$ models, it is assumed that the symmetry breaking is driven by the two vacuum expectation values of the H_u and H_d Higgs doublets which are of the same order ($v_{H_u} \simeq v_{H_d}$) [7]. Indeed, the constraints from the electroweak precision data impose that the $Z-Z^{'}$ mixing angle, $\theta_{Z-Z'}$ should be very small. This requires that [7]:

$$g_{Z'}^2 \left| \, v_{H_u}^2 Q^{'}(H_u) \, - \, v_{H_d}^2 Q^{'}(H_d) \, \right| \, << \, g_Z^2 v^2 \tag{12}$$

With $v_{H_u} \simeq v_{H_d}$, this expression leads us to assume that $Q^{'}(H_u)$ and $Q^{'}(H_d)$ are also of the same order and have the same sign :

$$Q^{'}(H_u) \simeq Q^{'}(H_d) \tag{13}$$

Using the condition of $U(1)'$gauge invariance of the trilinear u and d mass terms (eq.(4) and eq.(5)), we get the following relation among the chiral couplings :

$$C_L \, - \, C_R^u \, \simeq \, C_L \, - \, C_R^d \tag{14}$$

Thanks to the $SU(2)_L$ gauge invariance this gives :

$$C_R^u \simeq C_R^d \tag{15}$$

It clearly means that the left or right handed dominance is the same for u quarks and for d quarks. An example of such models, is given by the following right-handed model we call *Model C* [2] :

$$Model\, C \; : \qquad C_L \, = \, 0, \quad C_R^u \, = \, C_R^d \, = \, \frac{1}{3} \tag{16}$$

Note that some authors consider eq.(14) and eq.(15) simply as orders of magnitude. For example, the model presented in [6] (which is also the first model of [7]) fits into this scalar *stucture II* , but the $U(1)'$ charges are : $Q'(H_u) = -3$, $Q'(H_d) = -2$, $Q'(Q) = C_L = -1$, $Q'(u_R) = C_R^u = 2$, and $Q'(d_R) = C_R^d = 1$. Therefore, we get PV couplings for u quarks but axial couplings for d quarks.
Then, in order to be conservative, one can say that a characteristic of the models with the scalar *stucture II* is that they cannot yield a left handed (right handed) dominance for u quarks and a right handed (left handed) dominance for d quarks at the same time.

• Structure III :

Finally, we can consider the non-minimal scalar structure provided by string derived models as the ones considered by Cvetič, Langacker and collaborators [2]. A peculiarity

[2] This model is analogous to the second model of [7], but we have changed the precise values of the $U(1)'$ charges in order to have $\kappa \simeq 1$.

of these string derived models is that trilinear mass terms appear naturally for u or d-type quarks but not for both [20]. A correct prediction for the top quark mass is done [21] if one takes a trilinear mass term for the top quark [20]. This choice is made in [2]. In these scenarios, d-type quarks and charged leptons acquire their mass thanks to nonrenormalizable terms (*i.e* not trilinear).

If there is no trilinear mass term in the theory for d-quarks, eq.(5) is no longer valid. Therefore, the chiral couplings of the d quarks are completely free. It means that we can have PC couplings (vector-like as in *structure I*, or axial), or PV couplings with a left-handed or a right-handed dominance, the same as for u quarks (this is similar to *structure II*), or on the contrary in opposition to the case of u quarks. This situation will characterize *structure III*.

We have chosen the following phenomenological *Model D* to illustrate this last possibility :

$$Model\ D\ :\qquad C_L\ =\ \frac{1}{3},\quad C_R^u\ =\ 0,\quad C_R^d\ =\ \frac{2}{3} \tag{17}$$

In addition, the flipped $SU(5)$ model of Lopez and Nanopoulos [5] is another good example of *structure III*, but now with axial couplings for d quarks. This model, that we call *Model A* from reference [8], is characterized by :

$$Model\ A\ :\qquad C_L\ =\ -\ C_R^d\ =\ \frac{1}{2\sqrt{3}},\quad C_R^u\ =\ 0 \tag{18}$$

These couplings imply that Parity is maximally violated in the u-quark sector whereas it is conserved in the d quark sector because of the purely axial character of the couplings.

3 Observables and Results

We concentrate on the inclusive single jet production process $\vec{n}n \rightarrow jet + X$, where the polarization of only one neutron is necessary to define the single helicity PV asymmetry :

$$A_L\ =\ \frac{d\sigma_{(-)} - d\sigma_{(+)}}{d\sigma_{(-)} + d\sigma_{(+)}} \tag{19}$$

where the signs $\pm$ refer to the helicity of the polarized neutron. The cross section $d\sigma_{(\lambda)}$ means the one-jet production cross section estimated at some $\sqrt{s}$ for a given jet transverse energy E_T, integrated over a pseudorapidity interval $\Delta\eta$ centered at $\eta\ =\ 0$.

In fact, both ^3He beams could be polarized in principle, giving access to doubly polarized neutron collisions $\vec{n}\vec{n} \rightarrow jet + X$ and to double-helicity asymmetries (for a review on definitions and calculations of spin observables one can consult ref.[22]). Then the statistical significance is increased but a similar amount of information is obtained on the chiral and scalar structures. We prefer to be conservative considering that only one beam

will be polarized.

Concerning the value of $\sqrt{s}$, at RHIC, the charged nucleons (protons) of a nuclei are accelerated up to energies of $E_p = 250 - 300\ GeV$ per nucleon. At first, the machine will run with $E_p = 250\ GeV$, it is the reason why we have taken a center mass energy $\sqrt{s} = 500\ GeV$ for $\vec{p}\vec{p}$ collisions [8]. A ^3He nuclei, being accelerated, will get the total energy of its two protons. The neutron will be able to reach only one third of this energy, which means that the center of mass energy will be reduced for $n - n$ collisions. To be sensitive to a possible New Physics effect, it is necessary to run at the highest possible energy (*i.e.* $E_p = 300\ GeV$). Hence, we have $E_{^3He} = 600\ GeV$ and $E_n = 200\ GeV$, $\vec{n}\vec{n}$ (or $\vec{n}n$) collisions reaching an energy $\sqrt{s} = 400\ GeV$ in the center of mass, value that we take in the following. Concerning the integrated luminosities, we have taken the same values as in [8], namely $L_1 = 800\, pb^{-1}$ and $L_2 = 3.2\, fb^{-1}$ for practical comparison with the $\vec{p}\vec{p}$ results, even if these values are certainly a little bit optimistic. However, if we take seriously the possibility of some luminosity upgrades at RHIC in the future [23], these numbers become perfectly realistic.

The dominant subprocess in the E_T range that we consider, is quark-quark scattering. Concerning the Standard contribution, A_L is given by the expression (in short notations):

$$A_L \simeq \frac{1}{d\sigma} \sum_{i,j} \sum_{\alpha,\beta} \int \left(T^{--}_{\alpha,\beta}(i,j) - T^{++}_{\alpha,\beta}(i,j) \right) \left[q_i(x_1) \Delta q_j(x_2) + \Delta q_i(x_1) q_j(x_) + (i \leftrightarrow j) \right] \quad (20)$$

The $T^{\lambda_1,\lambda_2}_{\alpha,\beta}(i,j)$'s are the matrix element squared with α boson and β boson exchanges in a given helicity configuration for the involved partons i and j. The expressions for the relevant $T_{\alpha,\beta}$'s at leading order (LO) are well-known, they can be found e.g. in ref.[24]. $\Delta q_i = q_{i+} - q_{i-}$ where $q_{i\pm} \equiv q_{i\pm}(x, \mu^2)$ are the distributions of the polarized quark of flavor i, either with helicity parallel $(+)$ or antiparallel $(-)$ to the parent proton helicity. Summing the two states one recovers $q_{i+} + q_{i-} = q_i(x, \mu^2)$. All these distributions are evaluated at the scale $\mu = E_T$. The unpolarized cross section $d\sigma$ is dominated by QCD and must also include all the relevant Electroweak and $Z^{'}$ terms and their interference with QCD terms when it is allowed by color rules. Of course, the non-dominant $q(\bar{q})g$ and gg scattering subprocesses have to be included in the part of the cross section which is purely QCD. The resulting standard A_L is positive and increases with the jet transverse energy E_T as soon as E_T is larger than the range $E_T \approx M_{W,Z}/2$ (see the figures below). This is due to the increasing importance of quark-quark scattering with respect to other subprocesses involving gluons.

If present, the leptophobic $Z^{'}$ contributes to the quark-quark scattering process via new amplitudes which interfere with the single gluon exchange amplitude. It is straightforward to get these amplitudes from the Standard ones involving the standard Z. One has also to add the very tiny Electroweak-$Z^{'}$ interference which will not yield an observable effect. As it was already pointed out in reference [8], 95% of the effect due to the new boson comes from $Z'.g$ interference terms involving the scattering of identical quarks in

the t,u-channels. In the case of $\vec{n}n$ collisions it corresponds essentially to the scattering of d quarks. This dominant contribution can be written as follows :

$$A_L \cdot d\sigma \;\simeq\; F \int \left[C_L^2 - C_R^{d\,2}\right] \left[d\left(x_1,\mu^2\right)\Delta d\left(x_2,\mu^2\right) + \Delta d\left(x_1,\mu^2\right) d\left(x_2,\mu^2\right)\right]_{neutron} \quad (21)$$

where F is a positive factor given by

$$F \;=\; \frac{32}{9}\alpha_s\alpha_z\hat{s}^2 Re\left(\frac{1}{\hat{t}D_{Z'}^{\hat{u}}} + \frac{1}{\hat{u}D_{Z'}^{\hat{t}}}\right) \quad (22)$$

where $\alpha_z = \alpha/sin^2\theta_W cos^2\theta_W$ and $D_{Z'}^{\hat{t}(\hat{u})} = \left(\hat{t}(\hat{u}) - M_{Z'}^2\right) + iM_{Z'}\Gamma_{Z'}$.

Note that the partonic part of eq.(21) corresponds to the polarized and unpolarized d quark distributions in a *neutron*. So, if we want to use an expression with the more familiar definitions of quark distributions in a *proton*, from isospin symmetry, we have to replace $d_{neutron}(x,\mu^2)$ and $\Delta d_{neutron}(x,\mu^2)$ by the functions $u(x,\mu^2)$ and $\Delta u(x,\mu^2)$, defined for a proton. It means that the partonic part of eq.(21) is positive since Δu_{proton} is positive as well-known.

We can remark that eq.(21) allows us to predict easily the behaviour of the spin asymmetry A_L in the presence of a new $Z^{'}$ contribution. Given the positivity of the factor F and of the partonic part, the direction of a possible deviation from the SM A_L asymmetry will be determined directly by the chiral couplings $C_{L,R}^d$, more precisely by the difference $C_L^2 - C_R^{d\,2}$. Consequently, a model whose d chiral couplings present a left (right) dominance will provide a positive (negative) deviation to the SM A_L asymmetry.

In our LO calculations, all the contributions, dominant or not are included. Concerning the partonic part we have used the GRSV polarized parton distribution functions (pdf) [25] along with the associated unpolarized pdf's. Remember that the uncertainties due to the imperfect knowledge of the polarized pdf's will be reduced soon thanks to the first part of the RHIC-Spin program itself [10].

On the theoretical side some systematic uncertainties are coming from the existence of higher order corrections to the SM prediction for A_L and to the $Z^{'}$ contribution itself. Indeed, at NLO, several new contributions appear [26]. However, the current prejudice is that spin asymmetries which are ratios of cross sections, are much less affected than simple cross sections by higher order corrections. This behaviour has been confirmed recently by some calculations who have provided some precise results on the small influence of gluons on the standard QCD-Electroweak interference term at NLO [27]. A first estimate of the size of NLO corrections to qq scattering is in favor of a relatively small correction, of the order of 10% of the asymmetry itself [28].
Concerning experimental uncertainties, a good knowledge of the beam polarization ($\pm 5\%$) and a very good relative luminosity measurement (10^{-4}), should allow to get a systematic

uncertainty for a single spin measurement of the order of 5% [10]. For the time being, we have taken into account all the present uncertainties by using a global systematic error on the spin asymmetry $(\Delta A)_{syst}/A = 10\%$.

In figures 1 and 2 we compare the non-standard asymmetries $A_L(\vec{p}p)$ and $A_L(\vec{n}n)$ to the Standard one in each case, focusing on models C and D. We ignore here models A and B which don't give any effect on $A_L(\vec{n}n)$ since in these models parity is conserved in the interactions between the corresponding $Z^{'}$ and d quarks (axial for Model A and vector-like for Model B). The result of our calculation for these models in the case of $\vec{p}\vec{p}$ collisions has been already displayed in ref. [8].

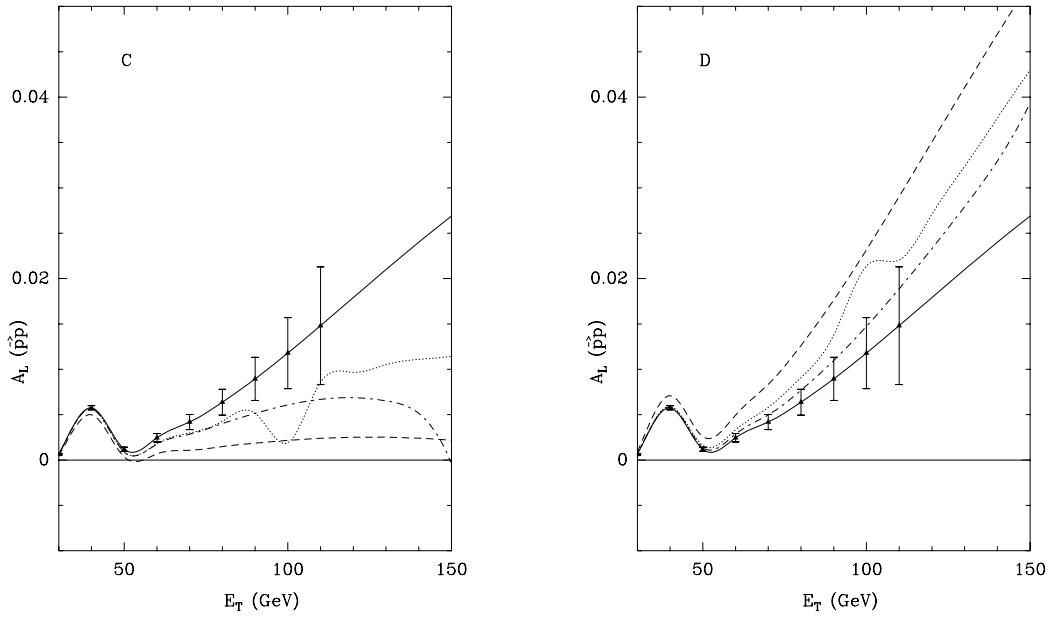

Figure 1: A_L versus E_T for models C (left) and D (right) with $\vec{p}p$ collisions at RHIC at $\sqrt{s} = 500$ GeV. The plain curves represent the SM predictions. The dashed, dotted and dash-dotted curves correspond to the cases where the masses are $M_{Z'} = 90,\ 200$ et 300 GeV respectively. The error bars correspond to the integrated luminosity $L_2 = 3.2\ fb^{-1}$. $\kappa = 1$ for all cases except for the model C with $M_{Z'} = 300\ GeV$ and $\kappa = 1.5$.

Concerning the standard asymmetry, one can notice that, in spite of the smaller center of mass energy the $A_L(\vec{n}n)$ is larger than the one calculated for $\vec{p}\vec{p}$ collisions in ref. [10, 17] This is due to the larger parity violation in the d quark sector compared to the u quark sector for the SM (*i.e.* $|C_L^2 - C_R^{d\,2}| >> |C_L^2 - C_R^{u\,2}|$). However, the influence of the reduced energy shows itself on the error bars which are larger than for the ones on $A_L(\vec{p}p)$ for the same E_T bin. The bumps in the curves correspond to the jacobian peaks due to real W and Z exchanges around $E_T \approx M_{W,Z}/2$, or Z' exchange at $E_T \approx M_{Z'}/2$. The remaining effects on the whole E_T spectrum are due to $Z.g$ and $Z'.g$ interference terms.

One can see that, in the framework of the Models C and D the effects of the $Z^{'}$ are

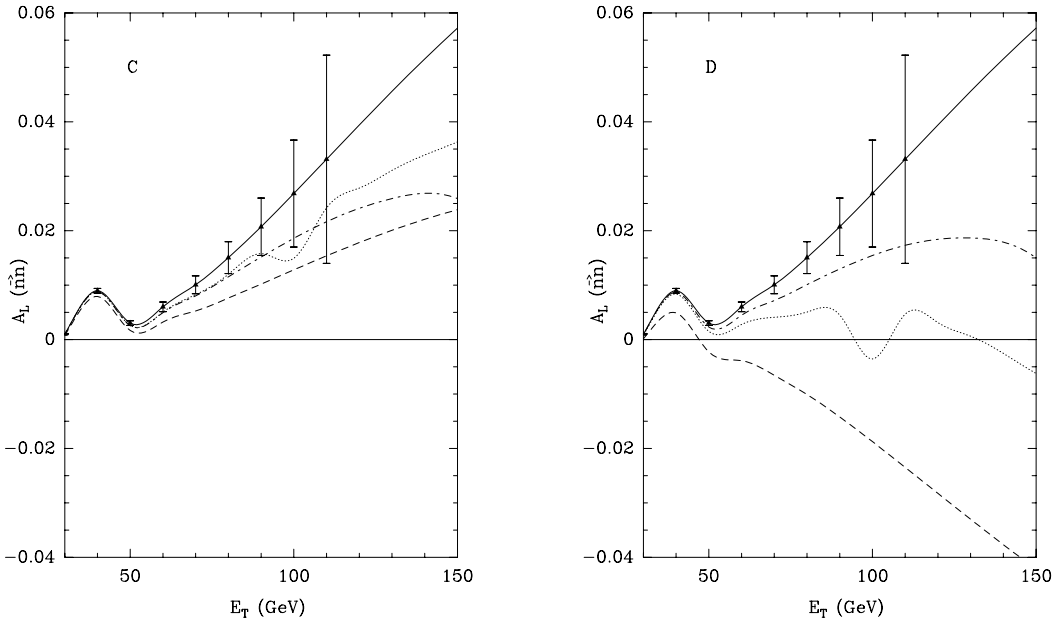

Figure 2: Same as fig.1 for $\vec{n}n$ collisions at $\sqrt{s} = 400$ GeV.

spectacular provided its mass is not too high, hence RHIC should not miss them if they are present.

The deviations from the SM expectations are negative in Model C in fig.1 and fig.2 in accordance with the right-handed dominance of both u and d quark couplings. On the other hand, in the case of Model D which is dominantly left-handed for u quarks and right-handed for d quarks, the deviation is positive in $\vec{p}p$ collisions and negative in $\vec{n}n$ collisions.

Finally, in the case of $\vec{n}n$ collisions, if we compare the effects on A_L coming from Models C and D for the same Z' mass, we see that Model D implies some larger deviations from the SM predictions. This difference is due to the larger parity violation in the d quark sector for Model D compared to Model C. Indeed, the difference $C_L^2 - {C_R^d}^2$ appearing in eq.(21) is equal to $1/9$ for Model C and to $1/3$ for Model D, implying roughly a three times larger deviation for model D.

In figure 3, we present the limits on the parameter space $(\kappa, M_{Z'})$ that both $A_L(\vec{n}n)$ and $A_L(\vec{p}p)$ should provide with the integrated luminosities $L_1 = 800\ pb^{-1}$ and $L_2 = 3200\ pb^{-1}$ for models C and D. We also display the inferred constraints coming from the dijet cross section studies by the $p\bar{p}$ collider experiments UA2 [29], CDF [30] and D0 [31]. In fact the published results were restricted to the so-called Z' "sequential standard model" (SSM) with $\kappa = 1$. We have easily extrapolated these results to models C and D by changing the couplings appropriately for a reasonable range of κ values. One can see that these unpolarized collider studies are not constraining a $Z^{'}$ mass as soon as κ is small enough. Also, and this is true in any leptophobic model, some windows were still

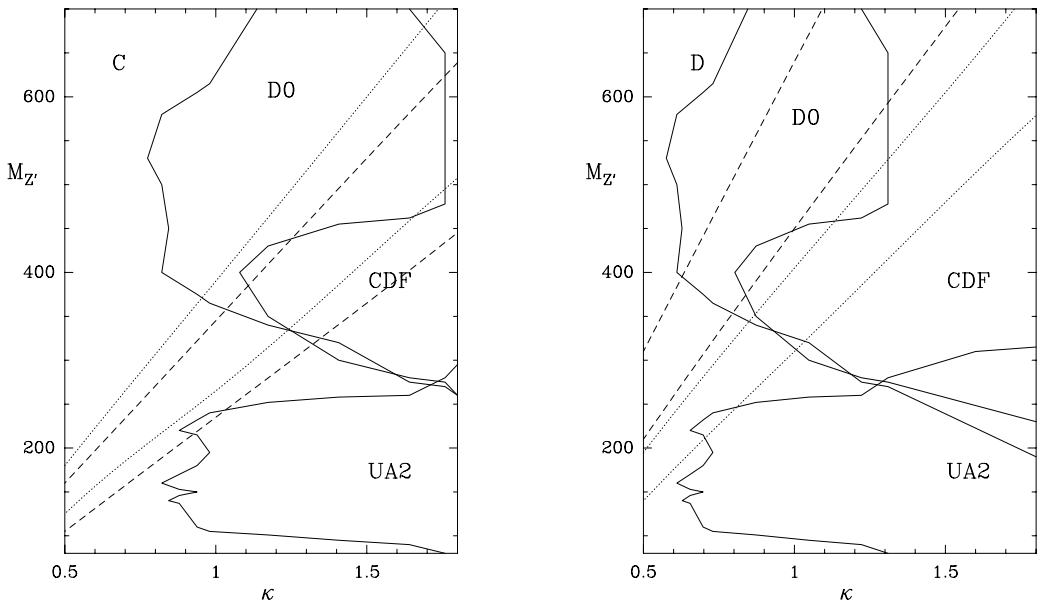

Figure 3: Bounds on the parameter space $(\kappa, M_{Z'})$ for models C and D. The dotted and dashed curves correspond respectively to the predicted limits at 95% C.L. from $A_L(\vec{p}\vec{p})$ and $A_L(\vec{n}\vec{n})$ at RHIC with $\sqrt{s} = 500\,GeV$ for $\vec{p}\vec{p}$, $\sqrt{s} = 400\,GeV$ for $\vec{n}\vec{n}$ collisions, and with $L_1 = 800\,pb^{-1}$ (lower curves) and $L_2 = 3200\,pb^{-1}$ (upper curves).

present around $M_{Z'} = 300$ GeV/c^2 and below $M_{Z'} = 100$ GeV/c^2. With the help of polarized hadronic beams the situation could be greatly improved : in particular the hole centered on $M_{Z'} \approx 300$GeV/c^2 should be covered provided κ is greater than ≈ 0.7. One gets the same behaviour for the bounds in the framework of Models A and B (see ref. [8]).

We remark that $A_L(\vec{p}p)$ is slightly more sensitive than $A_L(\vec{n}n)$ for model C. This difference can be explained simply by the reduced center of mass energy for $\vec{n}\vec{n}$ collisions. Indeed for the model C, the parity violation is equal in strength for both the u and d quark sectors, *i.e.* $C_L^2 - {C_R^u}^2 = C_L^2 - {C_R^d}^2$. Conversely, for Model D, we see that the sensitivity is clearly in favour of $A_L(\vec{n}n)$ which can be understood thanks to the relation $|C_L^2 - {C_R^d}^2| = 3|C_L^2 - {C_R^u}^2|$.

To conclude, the analysis of PV spin asymmetries measured within $\vec{n}n$ collisions is able to constrain the presence of a new weak hadronic interaction in the d quark sector. In the case of a discovery, the deviations from the SM expectations indicate the chirality of the new interaction in respect of d quarks.

4 Constraints on the scalar structure

In this part, we want to analyze which kind of information could be provided by the precise measurements of both spin asymmetries at RHIC, namely $A_L(\vec{p}p)$ and $A_L(\vec{n}n)$. In particular, are we able to discriminate between the three scalar structures we have described in Section 2.

At this stage it is worth recalling our assumptions :
i) the condition of leptophobia plus a small $Z - Z'$ mixing angle,
ii) the gauge invariance under $U(1)^{'}$ of the fermion mass terms,
iii) $SU(2)_L$ invariance,
iv) we assume that some PV effects due to a leptophobic $Z^{'}$ have been detected through the measurement of $A_L(\vec{p}p)$ in the "first" phase of the RHIC operations with polarized proton beam(s) : This means that parity is violated in the u quark sector of the new $U(1)^{'}$.

In figure 4, we present $A_L(\vec{p}p)$ versus $A_L(\vec{n}n)$ for a transverse energy $E_T = 70 \pm 5\ GeV$. We have chosen this particular interval since its contribution to the χ^2 function involved in the analysis is maximal. Of course, a full integration over the E_T range accessible experimentally will reduce the error bars. However, to be realistic, this integration should take into account the details of the jet reconstruction of the RHIC detectors, an analysis which is far beyond the scope of this paper.
In this figure, the central point represents the SM prediction. The error bars correspond to the integrated luminosity $L_2 = 3200\ pb^{-1}$. The models A, B, C and D, which were introduced to illustrate the different scalar structures, are represented each one by a shaded ellipse. Each point inside an ellipse corresponds to a precise value of κ and $M_{Z'}$, these values are taken as to satisfy the present experimental constraints presented in fig.3 and in fig.1 of ref.[8].
Concerning the shapes of the ellipses, there is no simple dependence on the two parameters κ and $M_{Z'}$ in this plane. However, a point close to the "SM cross" obviously means that one has a small κ and/or a large $M_{Z'}$. Conversely, the biggest effect (that is the farthest from the SM point) is obtained for $M_{Z'} = M_Z$ (which is our lowest $M_{Z'}$ value) and for the highest experimentally allowed value of κ within each model.

Remember that *structure I* is characterized by a vector-like coupling of the d quark to the $Z^{'}$. Models belonging to *Structure II* should exhibit the same left-handed or right-handed dominance for u and d quarks. It means that the deviations from SM expectations for $A_L(\vec{p}p)$ and for $A_L(\vec{n}n)$ go in the same direction. In the framework of *structure III*, corresponding to highly non-trivial scalar structures, no predictions are made for the d quark couplings, hence they can be located anywhere in the plane ($A_L(\vec{p}p)$,$A_L(\vec{n}n)$). However, it is only for this structure that we can have an opposite chirality for u and d quarks couplings. On fig.4 we call "X" the two regions which correspond to the latter case, in the upper-left and lower-right sectors. Model D is an illustration of this situation. A first conclusion is that experimental results belonging to zone "X" should allow to eliminate both *structure I* (i.e. the 2HDM) and *structure II* whose common property

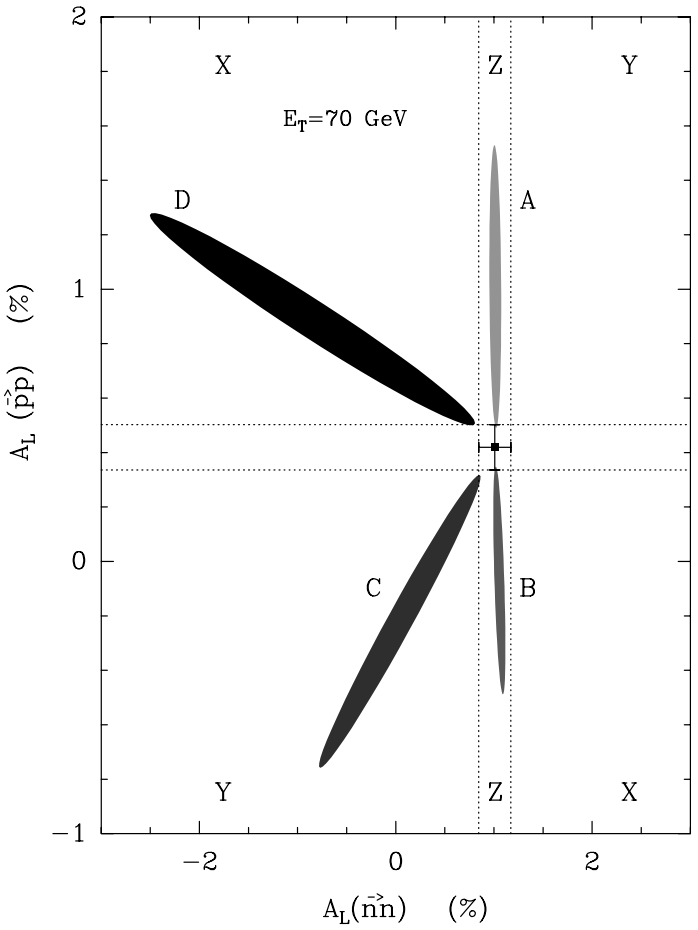

Figure 4: Predictions of the various models (see text) in the plane $A_L(\vec{p}p)$ versus $A_L(\vec{n}n)$ for $E_T = 70\ GeV$. The error bars on the SM point correspond to the integrated luminosity $L_2 = 3.2\ fb^{-1}$.

is the presence of trilinear mass terms for u and d quarks .

Secondly, we define sector "Y" which is accessible by models from *structure II* or *structure III* but wich excludes *structure I*. Concerning *structure II*, the fact that the points belong to zone "Y" is related to the common property of left-handed dominance (right-handed dominance) for u and d couplings, corresponding to the upper-right (lower-left) sector of the plane. Model C belongs to this category with a right-handed dominance.

Finally, for the models of *structure I*, like model B, the d quarks have some vector-like couplings to the $Z^{'}$ and we don't expect any deviation on $A_L(\vec{n}n)$. So, they should be located on the vertical line passing through the SM point. Taking into account the experimental conditions, this line is replaced by the band "Z" whose width is determined by the error on the standard $A_L(\vec{n}n)$. Of course models belonging to the two other structure can fall into this band (Model A is an illustration from *structure III*). Conversely models from *structure I*, which characterize the 2HDM with trilinear mass terms for all fermions, will be ruled out by the RHIC $\vec{p}p$ and $\vec{n}n$ collision experiments if any effect is observed outside this band.
On the other hand, if for some other phenomenological or theoretical reason, it turns out that models from *structure III* have to be rejected, then the "Z" band should be a clear signature of the simplest 2HDM's of *structure I*. The only drawback is the case of axial couplings of the d quarks which is forbidden by these models but is allowed as a very particular case of the models of *structure II* and which contaminates the "Z" band.

5 Conclusion

The existence of a new weak force between quarks at a not too high energy scale is an attractive possibility which is not ruled out by present data. If a new neutral gauge boson $Z^{'}$ owns the property of leptophobia plus a small $Z - Z^{'}$ mixing angle, it evades the bounds coming from previous experiments and it must be looked for in purely hadronic processes.

The polarized proton beams which are available at RHIC allow the precise measurement of the PV spin asymmetry A_L in the production of jets. As pointed out in our previous papers, and also stressed by some authors [5], such measurements could really lead to a discovery if the new $Z^{'}$ exhibits some handed couplings to u quarks, since u quarks play a dominant role in the collision process. In addition, as usual, measuring a spin asymmetry allows to get a handle on the chiral structure of the underlying interaction. More precisely, the sign of the deviation from the expected standard value of A_L should allow to pin down the chiral structure of the new interaction, still in the u quark sector.
In spite of its relatively low center of mass energy (500 - 600 GeV) the RHIC machine should be a remarkable tool, in particular thanks to the very high luminosity which is expected. Hence, in some models a mass as high as $M_{Z'} = 400$ GeV could give a measurable effect.

Since the acceleration and storage of high intensity polarized ^3He ions, which means polarized neutrons, will be a real possibility in a second phase of RHIC, it is valuable to investigate what could be obtained on the d quark sector.

We had already checked that polarized *proton-neutron* collisions could only give access to the effects of a new charged current [16]. For testing the d quark sector of a new $U(1)'$, the use of both "neutron beams" is mandatory.

In this paper, we have checked first that it would be possible to get some valuable information on the chirality of the $Z'd\bar{d}$ vertex thanks to the measurement of the asymmetry $A_L(\vec{n}n)$. This could be done with a precision which is comparable to what can be hoped from the measurement of $A_L(\vec{p}p)$.

Moreover, getting in the same time an information on the u and the d couplings is a way of testing the scalar structure of the underlying model. We have seen that the property of leptophobia, plus some general assumptions like gauge invariance under the standard $SU(2)_L$ and under the new $U(1)'$, constrains the Higgs sector of the model.

The simplest case of 2-Higgs Doublet Models, with trilinear mass terms and the traditional property $H_d \equiv H_l$, exhibits the interesting consequence of vector-like couplings of the $Z^{'}$ to d quarks along with PV violation in the u quark sector in general. Other models exhibit a more elaborated scalar structure, in particular the scalar sector which gives masses to ordinary quarks could be decoupled from the corresponding sector for leptons. This is the case in our models from *structure II* where we have considered two Higgs doublets giving masses to u and d quarks along with some phenomenological constraints, without any assumptions on the leptons. In this case parity is violated in general in both the u and d sectors. Measuring $A_L(\vec{p}p)$ and $A_L(\vec{n}n)$ should allow to separate the two structures, if an even more general possibility was not present. Conversely, if one does not assume anymore the presence of trilinear mass terms for the quarks (*structure III*), the situation is more open in the plane ($A_L(\vec{p}p)$,$A_L(\vec{n}n)$). Therefore, some definite conclusions could be yielded only if the measurements are in favor of the "sector X" described in section 4 : In this case *structures I and II* are forbidden. Similarly an effect observed outside the "Z band" rules out the 2HDM's (*structure I*) without any ambiguity.

Our conclusion is that the implementation of polarized "neutron beams" at RHIC should greatly complement the program of New Physics searches with polarized proton beams, since a non trivial piece of information could be obtained on the scalar sector of the underlying theory.

Acknowledgments

E.T acknowledges Prof. Y. Yayla, previous president of the Galatasaray University, to have supported his studies at the Centre de Physique Théorique, CNRS-Marseille.

J.M.V. acknowledges the warm hospitality at the RIKEN-BNL Research Center where part of this work has been performed. Thanks are due to G. Bunce, G. Eppley, N. Saito, J. Soffer, M. Tannenbaum and W. Vogelsang for fruitful discussions.

References

[1] Particle Data Group, Eur. Phys. J. **C15**, 1 (2000).

[2] M. Cvetič et al, Phys. Rev. **D56**, 2861 (1997) ; see also M. Cvetič and P. Langacker, Phys. Rev. **D54**, 3570 (1996) and P. Langacker and J. Wang, Phys. Rev. **D58**, 115010 (1998).

[3] J.D. Lykken in Snowmass 1996, ed. D.G. Cassel, L. Trindle Gennari, R.H. Siemann, p.891; A.E. Faraggi and M. Masip, Phys. Lett. **B388**, 524 (1996).

[4] K.S. Babu, C. Kolda and J. March-Russell, Phys. Rev. **D54**, 4635 (1996) ; **D57**, 6788 (1998).

[5] J.L. Lopez and D.V. Nanopoulos, Phys. Rev. **D55**, 397 (1997).

[6] K. Agashe, M. Graesser, I. Hinchliffe and M. Suzuki, Phys. Lett. **B385**, 218 (1996).

[7] H. Georgi and S.L. Glashow, Phys. Lett. **B387**, 341 (1996).

[8] P. Taxil and J.-M. Virey, Phys. Lett. **B441**, 376 (1998).

[9] Proceedings of the RIKEN-BNL Workshop, *Spin Physics at RHIC in year-1 and beyond*, May 2001, Brookhaven, BNL Report 52635.

[10] G. Bunce, N. Saito, J. Soffer and W. Vogelsang, Ann. Rev. Nucl. Part. Sci. **50**, 525 (2000).

[11] S. Kovalenko, I. Schmidt and J. Soffer, Phys. Lett. **B503**, 313 (2001).

[12] B. Grzadkowski in [9], p.75.

[13] D. Atwood in [9], p.29.

[14] M. Tannenbaum, in *Polarized Collider Workshop*, J. Collins, S.F. Heppelmann and R.W. Robinett eds, AIP Conf. Proceedings **223**, AIP, New York, 1990, p. 201.

[15] P. Taxil and J.-M. Virey, Phys. Lett. **B364**, 181 (1995).

[16] P. Taxil and J.-M. Virey, Phys. Lett. **B404**, 302 (1997).

[17] P. Taxil and J.-M. Virey, hep-ph/0109094, to appear in Phys. Lett. B.

[18] P. Taxil and J.-M. Virey, Phys. Rev. **D55**, 4480 (1997).

[19] E. Courant, *Proceedings of the RIKEN-BNL research center workshop, april 1998*, BNL Report 65615 p.275.

[20] A.E. Faraggi, Phys. Lett. **B377**, 43 (1996).

[21] A.E. Faraggi, Phys. Lett. **B274**, 47 (1992).

[22] C. Bourrely, F.M. Renard, J. Soffer and P. Taxil, Phys. Reports **177**, 319 (1989).

[23] N. Saito in the proceedings of the 14th International Spin Physics Symposium, Osaka, 2000, K. Hatanaka et al. eds., AIP Conf. Proceedings **570**, AIP, New York, 2001.

[24] C. Bourrely, J.-Ph. Guillet and J. Soffer, Nucl. Phys. **B361**, 72 (1991).

[25] M. Glück, E. Reya, M. Stratmann and W. Vogelsang, Phys. Rev. **D53**, 4775 (1996).

[26] J.-M. Virey in *Predictions and uncertainties for RHIC Spin Physics and event generators for RHIC Spin Physics III*, Proceedings of the RIKEN-BNL Workshop, March 2000, Brookhaven, p.111.

[27] J. Ellis, S. Moretti and D.A. Ross, JHEP **06**, 043 (2001); and S. Moretti in [9], p.57.

[28] W. Vogelsang in [9], p.63; and in *The Spin Structure of the Proton and Polarized Collider Physics*, Proceedings of the ECT* workshop, July 2001, Trento, Italy, to appear.

[29] J. Alitti et al., Zeit. f. Phys. **C49**, 17 (1991); Nucl. Phys. **B400**, 3 (1993).

[30] F. Abe et al., Phys. Rev. **D55**, R5263 (1997).

[31] B. Abbott et al., FERMILAB-Conf-97/356-E.

.

1.2.5 Discussion et prospective

Les analyses proposées précédemment seront réalisées prochainement au RHIC. Néanmoins, ces études ont été réalisées à l'ordre le plus bas de la théorie des perturbations. Dans un contexte hadronique il est clair que les corrections QCD sont très importantes et doivent être prises en compte. L'utilisation d'asymétries de spin réduit ce problème comparativement à toute analyse basée sur l'étude de sections efficaces non polarisées. Cependant, il faut réaliser que les contributions non nulles à ces asymétries de spin violant la parité proviennent d'interférences entre les diagrammes avec échange de gluons et ceux faisant intervenir l'échange des autres bosons de jauge, et en particulier les neutres (Z^0 et Z'). Remarquons que les bosons Z^0 et W fournissent une contribution directe (résonance) ce qui se traduit par le petit pic à $E_T \approx 40 - 45\ GeV$ dans la figure 2 du premier article présenté précédemment. Il en sera de même du Z' leptophobe si $M_{Z'} < 300\,GeV$. En d'autres termes, si on néglige les résonances, les contributions dominantes (LO) viennent à l'ordre $\mathcal{O}(\alpha_s\alpha_W)$(des processus à 4 quarks).

A l'ordre suivant $\mathcal{O}(\alpha_s^2\alpha_W)$ (NLO) on constate que de très nombreux diagrammes vont intervenir [30, 31] (voir aussi [32] pour la fastidieuse liste de diagrammes !). En effet, il faut tenir compte, d'une part, des corrections QCD ($\mathcal{O}(\alpha_s)$) aux interférences précédentes ($\mathcal{O}(\alpha_s\alpha_W)$), mais aussi d'autre part, des corrections faibles ($\mathcal{O}(\alpha_W)$) à tous les processus QCD ($\mathcal{O}(\alpha_s^2)$). Ce dernier type de corrections va faire entrer dans le jeu les gluons. D'autres corrections à prendre en compte sont celles concernant le dénominateur de l'asymétrie. Le terme dominant est d'ordre $\mathcal{O}(\alpha_s^2)$ mais les corrections d'ordre $\mathcal{O}(\alpha_s^3)$ peuvent atteindre 60 à 80% d'augmentation (facteur K) selon l'énergie considérée. Ces corrections au dénominateur vont donc avoir un effet important sur la normalisation de l'asymétrie mais heureusement aucun sur sa forme (car QCD conserve la parité).

Par conséquent, au vu de l'explosion du nombre de diagrammes (plus d'un facteur 10), de la nouvelle contribution des gluons, des effets de dénominateur et en réalisant que les corrections NLO font intervenir seulement un facteur $\alpha_s \approx 0.1$ supplémentaire, il devenait extrêmement difficle d'estimer intuitivement la véritable importance de ces corrections. La proximité des mesures et la volonté d'obtenir des résultats aussi précis que possible imposait donc la nécessité de réaliser les calculs à l'ordre suivant.

J'ai ainsi discuté des différentes corrections à calculer avec Werner Vogelsang (BNL), Daniel de Florian (Université de Buenos Aires) et Marco Stratmann (RIKEN). Finalement c'est Stefano Moretti et Douglas Ross de l'Université de Southampton qui ont entrepris ces calculs [33, 31]. Les principaux résultats pour la production de jets au RHIC [31] sont donnés sur la figure 1.5.

On constate ainsi que les corrections sur l'asymétrie varient de +100% à -70% selon l'énergie transverse considérée pour le jet ! Cependant, la figure 1.5 donne ces prédictions pour deux ensembles de distributions partoniques polarisées différents (Ghermann-Stirling-A [34] et GRSV-standard [26]) et on peut réaliser que les corrections changent beaucoup d'une paramétrisation à l'autre.

Ceci nous montre donc qu'afin d'étudier d'éventuels signaux de nouvelle physique au RHIC-Spin, il est fondamental de tenir compte des corrections d'ordre supérieur mais aussi de réduire considérablement les incertitudes sur les distributions partoniques, ce qui est heureusement au programme de la collaboration RHIC-Spin.

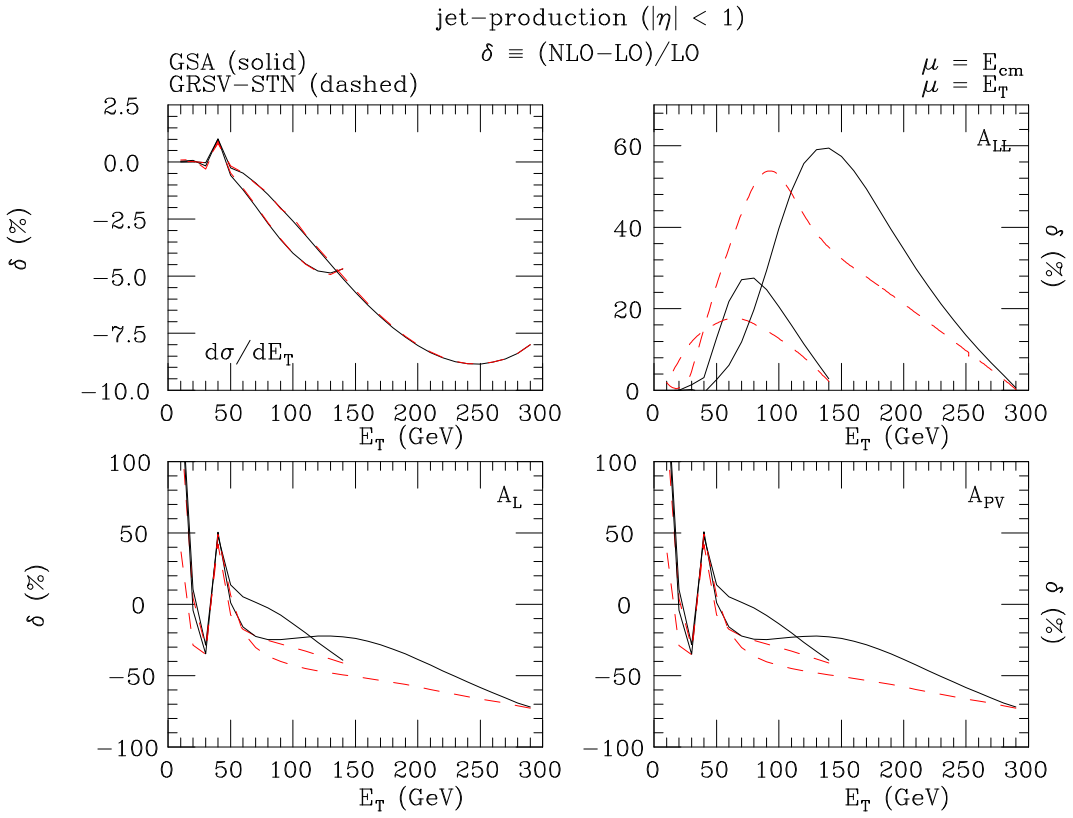

Figure 1.5: Corrections à l'ordre $\mathcal{O}(\alpha_s^2\alpha_W)$ en fonction de l'énergie transverse pour la production de jets au RHIC-Spin avec $\sqrt{s} = 600\,GeV$ (courbes s'étendant jusqu'à $E_T = 300\,GeV$) et $\sqrt{s} = 300\,GeV$ (courbes s'étendant jusqu'à $E_T = 150\,GeV$). Les 4 plots correspondent à quatre observables distincts : section efficace, asymétrie conservant la parité, asymétries violant la parité à 1 et 2 spins (label sur les figures), et ceci pour deux types de distributions partoniques polarisées. Source [31]

1.3 Recherche de la supersymétrie violant la R parité au LHC

L'étude qui suit concerne la recherche de signaux supersymétriques violant la R Parité auprès du collisionneurs LHC dans le canal de production d'un seul top ($pp \to t\bar{b} + X$).

Le LHC est un collisionneur proton-proton qui devrait entrer en fonction très prochainement (2008). L'énergie des faisceaux (non-polarisés) sera de 7 TeV donnant ainsi un énergie caractéristique ($\sqrt{s} = 14\ TeV$) supérieure d'un ordre de grandeur à celle du collisionneur actuel le plus puissant. Avec une luminosité intégrée de $L = 10\ fb^{-1}$ attendue au bout d'un an dans le cas le plus défavorable, le LHC représente le meilleur espoir de nouvelles découvertes pour la communauté.

Le processus de production d'un seul quark top semble prometteur pour tester des modèles violant les nombres leptonique (L) et baryonique (B), ce qui est le cas des modèles supersymétriques avec R parité brisée. Un autre avantage de ce processus est que les prédictions du modèle standard sont relativement bien étudiées [35, 36]. D'autre part la contamination du signal par d'autres processus est très bien simulée par les différents générateurs d'événements.

Article publié sous la référence : Phys. Rev. **D61** (2000) 115008.

Single top production at the LHC as a probe of R parity violation.

P. Chiappetta
Centre de Physique Théorique, UPR7061, CNRS-Luminy, Case 907, F-13288 Marseille Cedex 9, France

A. Deandrea
Theoretical Physics Division, CERN, CH-1211 Geneva 23, Switzerland

E. Nagy and S. Negroni
Centre de Physique des Particules de Marseille, Université de la Méditerranée, Case 907, F-13288 Marseille Cedex 9, France

G. Polesello
INFN, Sezione di Pavia, via Bassi 6, I-27100 Pavia Italy

J.M. Virey
Institut für Physik, Universität Dortmund, D-44221 Dortmund, Germany and, Centre de Physique Théorique, UPR7061, CNRS-Luminy, Case 907, F-13288 Marseille Cedex 9, France and Université de Provence, Marseille, France

(October 1999)

We investigate the potential of the LHC to probe the R parity violating couplings involving the third generation by considering single top production. This study is based on particle level event generation for both signal and background, interfaced to a simplified simulation of the ATLAS detector.

I. INTRODUCTION

The conservation of the baryon B and lepton L number is a consequence of the gauge invariance and renormalizability of the Standard Model. In supersymmetric extensions of the Standard Model, gauge invariance and renormalizability do not imply baryon and lepton number conservation. We shall consider in what follows the Minimal Supersymmetric Standard Model (MSSM) together with baryon or lepton number violating couplings. These Yukawa-type interactions are often referred to as R-parity violating couplings. They can mediate proton decay to an unacceptable level and for this reason a discrete symmetry R was postulated [1] that acts as 1 on all known particles and as -1 on all the superpartners:

$$R = (-1)^{3B+L+2S} \tag{1}$$

where S is the spin of the particle. In the MSSM with a conserved R-parity the lightest supersymmetric particle (LSP) cannot disintegrate into ordinary particles and is therefore stable. The superpartners can be produced only in pairs so that one needs usually to wait for high energy colliders.

In models [2] not constrained by the ad-hoc imposition of R-parity one can still avoid proton decay and the experimental signatures can be quite interesting: single production of supersymmetric particles and modification of standard decays and cross-sections due to the exchange of these sparticles, which could be observed at lower energies compared to the R-parity conserving model. In the following we shall investigate top quark production taking into account R-parity violating effects. The top quark being heavy with a mass close to the electroweak symmetry breaking scale, it is believed to be more sensitive to new physics than other quarks. The mechanism we plan to study is single top quark production at LHC, which is complementary to top quark pair production and reliably well known in the Standard Model.

Two basic ways to probe new physics can be investigated. The first one is a model independent analysis, in which the effects of new physics appear as new terms in an effective Lagrangian describing the interactions of the third family with gauge bosons and Higgs [3–5]. The effects due to the interactions between quarks and gauge bosons will be visible at LEP2, e^+e^- next linear colliders and the Tevatron whereas dimension 6 CP violating operators affect the transverse polarisation asymmetry of the top quark. The second way is to consider a new theory which contains

the Standard Model at low energies. A possible framework is supersymmetry. In the Minimal Supersymmetric Model with R parity conservation, the single top production at Tevatron is enhanced by a few percent due to gluino, squarks, higgs, charginos and neutralinos corrections, the magnitude being sensitive to $\tan\beta$ [6]. The decays $t \to cV$ with $V = g, Z, \gamma$, which are small in magnitude in the Standard Model (BR $\simeq 10^{-10} - 10^{-12}$), may be enhanced by a few orders of magnitude in the MSSM [7]. If the stop and the charged Higgs are light enough new top decays are possible [8]. Our purpose is to investigate the effects of R parity violation. The superpotential contains three types of new terms:

$$W_{\not R} = \lambda_{ijk} L_i L_j \bar{E}_k + \lambda'_{ijk} L_i Q_j \bar{D}_k + \lambda''_{ijk} \bar{U}_i \bar{D}_j \bar{D}_k \tag{2}$$

the first two terms violating the leptonic number and the last the baryonic one. Here L and E are isodoublet and isosinglet lepton, Q and D are isodoublet and isosinglet quark super-fields, the indices i, j and k run for the three lepton and quark families. In the following we shall assume that R-parity violation arises from one of these terms only.

The feasibility of single top quark production via squark and slepton exchanges to probe several combinations of R parity violating couplings at hadron colliders has been studied [9–11]. The LHC is better at probing the B violating couplings λ'' whereas the Tevatron and the LHC have a similar sensitivity to λ' couplings. We perform a complete and detailed study including for the signal all channels using a Monte Carlo generator based on Pythia 6.1 [12], taking into account all the backgrounds and including the ATLAS detector response using ATLFAST 2.0 [13].

The paper is organised as follows. Section II is devoted to an evaluation of the different subprocesses contributing to single top production (standard model, squark, slepton and charged Higgs exchanges). The potential of the LHC to discover or put limits on R-parity violating interactions is given in section III.

II. SUBPROCESSES CONTRIBUTING TO SINGLE TOP PRODUCTION

The R-parity violating parts of the Lagrangian that contribute to single top production are:

$$L_{\not R} = \lambda'_{ijk} \tilde{e}^i_L \bar{d}^k_R u^j_L - \lambda''_{ijk} (\tilde{d}^k_R \bar{u}^i_L d^j_L + \tilde{d}^j_R (\bar{d}^k_L)^c u^i_L) + h.c. \tag{3}$$

The superscript c corresponds to charge conjugation. There are altogether 27 and 9 λ'_{ijk} and λ''_{ijk} Yukawa couplings, respectively. The most suppressed couplings are $\lambda'_{111} \leq 3.5 \times 10^{-4}$, $\lambda'_{133} \leq 7 \times 10^{-4}$, $\lambda''_{112} \leq 10^{-6}$, $\lambda''_{113} \leq 10^{-5}$ (for bounds see [14]). In order to fix the kinematical variables, the reaction we consider is

$$u_i(p_1) + d_j(p_2) \to t(p_3) + b(p_4) \ , \tag{4}$$

the p_k being the 4-momenta of the particles and the indices i and j refer to the generations of the u and d-type quarks.

We first discuss valence-valence (VV) or sea-sea (SS) subprocesses (this notation refers to the proton-proton collisions at the LHC, but the calculation is valid in general). The SM squared amplitude due to W exchange in $\hat{u}$-channel [1] is suppressed by the Kobayashi-Maskawa matrix elements $V_{u_i b} V_{t d_j}$:

$$|M^{VV}_{WW}|^2 \ = \ g^4 \, |V_{u_i b}|^2 \, |V_{t d_j}|^2 \, \frac{1}{(\hat{u} - m^2_W)^2 + m^2_W \Gamma^2_W} \ p_1 \cdot p_2 \; p_3 \cdot p_4, \tag{5}$$

where g, m and Γ denote the weak coupling constant, the mass and the width of the exchanged particle. The $H^\pm$ exchange in $\hat{u}$-channel is included in the calculation but numerically suppressed by the quark masses and the mixing matrix elements for the charged Higgs sector $K_{u_i b} K_{t d_j}$(under the assumption $K = V$):

$$\begin{aligned} |M^{VV}_{H^\pm H^\pm}|^2 \ = \ & \frac{g^4}{16\, m^4_W} \, |K_{u_i b}|^2 \, |K_{t d_j}|^2 \, \frac{1}{(\hat{u} - m^2_{H^\pm})^2 + m^2_{H^\pm} \Gamma^2_{H^\pm}} \\ & [(v^2_{b u_i} + a^2_{b u_i}) \, p_1 \cdot p_4 \ + \ (v^2_{b u_i} - a^2_{b u_i}) \, m_b m_{u_i}][(v^2_{d_j t} + a^2_{d_j t}) \, p_2 \cdot p_3 \ + \ (v^2_{d_j t} - a^2_{d_j t}) \, m_{d_j} m_t], \end{aligned} \tag{6}$$

v_{ud} and a_{ud} are respectively the vector and axial vector couplings of $H^\pm$ to quarks:

[1] The "hat" symbol refers to the usual Mandelstam variables for the process at the parton level

$$v_{ud} = m_d \tan\beta + m_u \cot\beta \qquad a_{ud} = m_d \tan\beta - m_u \cot\beta \tag{7}$$

The interference term between the W and $H^\pm$ is:

$$\begin{aligned} 2\,\mathcal{R}e(M^{VV}_{WH^\pm}) \;=\; & -\frac{g^4}{8\,m_W^2}\,|V_{u_ib}|\,|V_{td_j}|\,|K_{u_ib}|\,|K_{td_j}|\,\frac{(\hat u - m_W^2)(\hat u - m_{H^\pm}^2) + m_W\Gamma_W m_{H^\pm}\Gamma_{H^\pm}}{[(\hat u - m_W^2)^2 + m_W^2\Gamma_W^2][(\hat u - m_{H^\pm}^2)^2 + m_{H^\pm}^2\Gamma_{H^\pm}^2]} \\ & \times [(v_{bu_i} + a_{bu_i})(v_{d_jt} + a_{d_jt})\,m_b m_{d_j}\; p_1\cdot p_3 \;+\; (v_{bu_i} + a_{bu_i})(v_{d_jt} - a_{d_jt})\,m_b m_t\; p_1\cdot p_2 \\ & + (v_{bu_i} - a_{bu_i})(v_{d_jt} + a_{d_jt})\,m_{u_i} m_{d_j}\; p_3\cdot p_4 \;+\; (v_{bu_i} - a_{bu_i})(v_{d_jt} - a_{d_jt})\,m_{u_i} m_t\; p_2\cdot p_4]. \end{aligned} \tag{8}$$

The scalar slepton exchange in $\hat u$-channel is taken into account but appears to be suppressed within our assumptions on the λ' couplings (see below). It reads:

$$|M^{VV}_{\tilde e^k_L \tilde e^k_L}|^2 \;=\; \lambda'^2_{ki3}\;\lambda'^2_{k3j}\,\frac{1}{(\hat u - m^2_{\tilde e^k_L})^2 + m^2_{\tilde e^k_L}\Gamma^2_{\tilde e^k_L}}\;\; p_1\cdot p_4\; p_2\cdot p_3. \tag{9}$$

The interference term between scalar slepton and W reads:

$$2\,\mathcal{R}e(M^{VV}_{W\tilde e^k_L}) = -\,g^2\,|V_{u_ib}|\,|V_{td_j}|\,\lambda'_{ki3}\;\lambda'_{k3j}\,\frac{(\hat u - m_W^2)(\hat u - m^2_{\tilde e^k_L}) + m_W\Gamma_W m_{\tilde e^k_L}\Gamma_{\tilde e^k_L}}{[(\hat u - m_W^2)^2 + m_W^2\Gamma_W^2][(\hat u - m^2_{\tilde e^k_L})^2 + m^2_{\tilde e^k_L}\Gamma^2_{\tilde e^k_L}]}\; m_d\, m_b\; p_1\cdot p_3. \tag{10}$$

The interference term between scalar slepton and $H^\pm$, which is suppressed, reads:

$$\begin{aligned} 2\,\mathcal{R}e(M^{VV}_{\tilde e^k_L H^\pm}) = & \frac{g^2}{4\,m_W^2}\,\lambda'_{ki3}\;\lambda'_{k3j}\;|K_{u_ib}|\,|K_{td_j}|\,\frac{(\hat u - m^2_{H^\pm})(\hat u - m^2_{\tilde e^k_L}) + m_{H^\pm}\Gamma_{H^\pm} m_{\tilde e^k_L}\Gamma_{\tilde e^k_L}}{[(\hat u - m^2_{H^\pm})^2 + m^2_{H^\pm}\Gamma^2_{H^\pm}][(\hat u - m^2_{\tilde e^k_L})^2 + m^2_{\tilde e^k_L}\Gamma^2_{\tilde e^k_L}]} \\ & \times [(v_{bu_i} + a_{bu_i})(v_{d_jt} + a_{d_jt})\; p_1\cdot p_4\; p_2\cdot p_3 \;+\; (v_{bu_i} + a_{bu_i})(v_{d_jt} - a_{d_jt})\,m_{d_j} m_t\; p_1\cdot p_4 \\ & + (v_{bu_i} - a_{bu_i})(v_{d_jt} + a_{d_jt})\,m_{u_i} m_b\; p_2\cdot p_3 \;+\; (v_{bu_i} - a_{bu_i})(v_{d_jt} - a_{d_jt})\,m_{u_i} m_{d_j} m_b m_t]. \end{aligned} \tag{11}$$

The down type squark exchange in $\hat s$-channel squared amplitude is dominant and given by:

$$|M^{VV}_{\tilde d^k_R \tilde d^k_R}|^2 \;=\; \frac{4}{3}\;16\;\lambda''^2_{ijk}\;\lambda''^2_{33k}\,\frac{1}{(\hat s - m^2_{\tilde d^k_R})^2 + m^2_{\tilde d^k_R}\,\Gamma^2_{\tilde d^k_R}}\;\; p_1\cdot p_2\; p_3\cdot p_4. \tag{12}$$

The corresponding interference terms are:

$$2\,\mathcal{R}e(M^{VV}_{W\tilde d^k_R}) = -\frac{2}{3}\;8\,g^2\,|V_{u_ib}|\,|V_{td_j}|\,\lambda''_{ijk}\;\lambda''_{33k}\,\frac{(\hat u - m_W^2)(\hat s - m^2_{\tilde d^k_R}) + m_W\Gamma_W m_{\tilde d^k_R}\Gamma_{\tilde d^k_R}}{[(\hat u - m_W^2)^2 + m_W^2\Gamma_W^2][(\hat s - m^2_{\tilde d^k_R})^2 + m^2_{\tilde d^k_R}\Gamma^2_{\tilde d^k_R}]}\; p_1\cdot p_2\; p_3\cdot p_4, \tag{13}$$

and:

$$\begin{aligned} 2\,\mathcal{R}e(M^{VV}_{\tilde d^k_R H^\pm}) = & \frac{2}{3}\,\frac{g^2}{2\,m_W^2}\,\lambda''_{ijk}\;\lambda''_{33k}\;|K_{u_ib}|\,|K_{td_j}|\,\frac{(\hat u - m^2_{H^\pm})(\hat s - m^2_{\tilde d^k_R}) + m_{H^\pm}\Gamma_{H^\pm} m_{\tilde d^k_R}\Gamma_{\tilde d^k_R}}{[(\hat u - m^2_{H^\pm})^2 + m^2_{H^\pm}\Gamma^2_{H^\pm}][(\hat s - m^2_{\tilde d^k_R})^2 + m^2_{\tilde d^k_R}\Gamma^2_{\tilde d^k_R}]} \\ & \times [(v_{bu_i} + a_{bu_i})(v_{d_jt} + a_{d_jt})\,m_b m_{d_j}\; p_1\cdot p_3 \;+\; (v_{bu_i} + a_{bu_i})(v_{d_jt} - a_{d_jt})\,m_b m_t\; p_1\cdot p_2 \\ & + (v_{bu_i} - a_{bu_i})(v_{d_jt} + a_{d_jt})\,m_{u_i} m_{d_j}\; p_3\cdot p_4 \;+\; (v_{bu_i} - a_{bu_i})(v_{d_jt} - a_{d_jt})\,m_{u_i} m_t\; p_2\cdot p_4]. \end{aligned} \tag{14}$$

Let us now take into account the subprocesses involving valence-sea (VS) quarks. The SM squared amplitude due to W exchange in the $\hat s$-channel, being proportional to $(V_{u_id_j}V_{tb})^2$ is dominant for quarks of the same generation. It reads:

$$|M^{VS}_{WW}|^2 \;=\; g^4\,|V_{u_id_j}|^2\,|V_{tb}|^2\,\frac{1}{(\hat s - m_W^2)^2 + m_W^2\Gamma_W^2}\;\; p_1\cdot p_4\; p_2\cdot p_3. \tag{15}$$

The charged Higgs contribution in the $\hat s$-channel is suppressed by the quark masses of the initial state. The squared amplitude is:

$$\begin{aligned} |M^{VS}_{H^\pm H^\pm}|^2 \;=\; & \frac{g^4}{16\,m_W^4}\,|K_{u_id_j}|^2\,|K_{tb}|^2\,\frac{1}{(\hat s - m^2_{H^\pm})^2 + m^2_{H^\pm}\Gamma^2_{H^\pm}} \\ & \times [(v^2_{d_ju_i} + a^2_{d_ju_i})\,p_1\cdot p_2 \;-\; (v^2_{d_ju_i} - a^2_{d_ju_i})\,m_{d_j} m_{u_i}][(v^2_{bt} + a^2_{bt})\;p_3\cdot p_4 \;-\; (v^2_{bt} - a^2_{bt})\,m_b m_t]. \end{aligned} \tag{16}$$

The interference term between W and $H^{\pm}$ is:

$$
\begin{aligned}
2\,\mathcal{R}e(M^{VS}_{WH^{\pm}}) = & -\frac{g^4}{8\,m^2_W}\,|V_{u_id_j}|\,|V_{tb}|\,|K_{u_id_j}|\,|K_{tb}|\,\frac{(\hat{s}-m^2_W)(\hat{s}-m^2_{H^{\pm}})+m_W\Gamma_W m_{H^{\pm}}\Gamma_{H^{\pm}}}{[(\hat{s}-m^2_W)^2+m^2_W\Gamma^2_W][(\hat{s}-m^2_{H^{\pm}})^2+m^2_{H^{\pm}}\Gamma^2_{H^{\pm}}]} \\
& \times[(v_{d_ju_i}+a_{d_ju_i})(v_{bt}+a_{bt})\,m_b m_{d_j}\;p_1\cdot p_3\;-\;(v_{d_ju_i}+a_{d_ju_i})(v_{bt}-a_{bt})\,m_{d_j}m_t\;p_1\cdot p_4 \\
& -(v_{d_ju_i}-a_{d_ju_i})(v_{bt}+a_{bt})\,m_b m_{u_i}\;p_2\cdot p_3\;+\;(v_{d_ju_i}-a_{d_ju_i})(v_{bt}-a_{bt})\,m_{u_i}m_t\;p_2\cdot p_4\;]. \qquad (17)
\end{aligned}
$$

Concerning R parity violating terms, slepton exchange in $\hat{s}$-channel and down type squark exchange in the $\hat{u}$-channel contribute:

$$
\begin{aligned}
|M^{VS}_{\tilde{e}^k_L\,\tilde{e}^k_L}|^2 &= \lambda'^2_{kij}.\lambda'^2_{k33}\frac{1}{(\hat{s}-m^2_{\tilde{e}^k_L})^2+m^2_{\tilde{e}^k_L}\Gamma^2_{\tilde{e}^k_L}}\;\;p_1\cdot p_2\;p_3\cdot p_4 \\
|M^{VS}_{\tilde{d}^k_R\tilde{d}^k_R}|^2 &= \frac{4}{3}\;16\;\lambda''^2_{i3k}\;\lambda''^2_{3jk}\frac{1}{(\hat{u}-m^2_{\tilde{d}^k_R})^2+m^2_{\tilde{d}^k_R}\Gamma^2_{\tilde{d}^k_R}}\;\;p_1\cdot p_4\;p_2\cdot p_3. \qquad (18)
\end{aligned}
$$

The interference terms involving the scalar lepton are:

$$
2\,\mathcal{R}e(M^{VS}_{W\tilde{e}^k_L}) \;=\; -\,g^2\,|V_{u_id_j}|\,|V_{tb}|\,\lambda'_{kij}\;\lambda'_{k33}\frac{(\hat{s}-m^2_W)(\hat{s}-m^2_{\tilde{e}^k_L})+m_W\Gamma_W m_{\tilde{e}^k_L}\Gamma_{\tilde{e}^k_L}}{[(\hat{s}-m^2_W)^2+m^2_W\Gamma^2_W][(\hat{s}-m^2_{\tilde{e}^k_L})^2+m^2_{\tilde{e}^k_L}\Gamma^2_{\tilde{e}^k_L}]}\;m_d\;m_b\;p_1\cdot p_3, \qquad (19)
$$

and:

$$
\begin{aligned}
2\,\mathcal{R}e(M^{VS}_{\tilde{e}^k_L H^{\pm}}) = & \frac{g^2}{4\,m^2_W}\,\lambda'_{kij}\;\lambda'_{k33}\,|K_{u_id_j}|\,|K_{tb}|\,\frac{(\hat{s}-m^2_{H^{\pm}})(\hat{s}-m^2_{\tilde{e}^k_L})+m_{H^{\pm}}\Gamma_{H^{\pm}}m_{\tilde{e}^k_L}\Gamma_{\tilde{e}^k_L}}{[(\hat{s}-m^2_{H^{\pm}})^2+m^2_{H^{\pm}}\Gamma^2_{H^{\pm}}][(\hat{s}-m^2_{\tilde{e}^k_L})^2+m^2_{\tilde{e}^k_L}\Gamma^2_{\tilde{e}^k_L}]} \\
& \times[(v_{d_ju_i}+a_{d_ju_i})(v_{bt}+a_{bt})\;p_1\cdot p_2\;p_3\cdot p_4\;-\;(v_{d_ju_i}+a_{d_ju_i})(v_{bt}-a_{bt})\;m_t m_b\;p_1.p_2 \\
& -(v_{d_ju_i}-a_{d_ju_i})(v_{bt}+a_{bt})\,m_{d_j}m_{u_i}\;p_3\cdot p_4\;+\;(v_{d_ju_i}-a_{d_ju_i})(v_{bt}-a_{bt})\,m_{u_i}m_{d_j}m_b m_t]. \qquad (20)
\end{aligned}
$$

The interference terms involving the scalar quark are:

$$
2\,\mathcal{R}e(M^{VS}_{W.\tilde{d}^k_R}) \;=\; -\frac{2}{3}\;8\,g^2\,|V_{u_id_j}|\,|V_{tb}|\,\lambda''_{i3k}\;\lambda''_{3jk}\frac{(\hat{s}-m^2_W)(\hat{u}-m^2_{\tilde{d}^k_R})+m_W\Gamma_W m_{\tilde{d}^k_R}\Gamma_{\tilde{d}^k_R}}{[(\hat{s}-m^2_W)^2+m^2_W\Gamma^2_W][(\hat{u}-m^2_{\tilde{d}^k_R})^2+m^2_{\tilde{d}^k_R}\Gamma^2_{\tilde{d}^k_R}]}\;p_1\cdot p_4\;p_2\cdot p_3 \qquad (21)
$$

and:

$$
\begin{aligned}
2\,\mathcal{R}e(M^{VS}_{\tilde{d}^k_R.H^{\pm}}) = & \frac{2}{3}\,\frac{g^2}{2\,m^2_W}\,\lambda''_{i3k}\;\lambda''_{3jk}\,|K_{u_id_j}|\,|K_{tb}|\,\frac{(\hat{s}-m^2_{H^{\pm}})(\hat{u}-m^2_{\tilde{d}^k_R})+m_{H^{\pm}}\Gamma_{H^{\pm}}m_{\tilde{d}^k_R}\Gamma_{\tilde{d}^k_R}}{[(\hat{s}-m^2_{H^{\pm}})^2+m^2_{H^{\pm}}\Gamma^2_{H^{\pm}}][(\hat{u}-m^2_{\tilde{d}^k_R})^2+m^2_{\tilde{d}^k_R}\Gamma^2_{\tilde{d}^k_R}]} \\
& \times[(v_{d_ju_i}+a_{d_ju_i})(v_{bt}+a_{bt})\,m_b m_{d_j}\;p_1\cdot p_3\;-\;(v_{d_ju_i}+a_{d_ju_i})(v_{bt}-a_{bt})\,m_{d_j}m_t\;p_1\cdot p_4 \\
& -(v_{d_ju_i}-a_{d_ju_i})(v_{bt}+a_{bt})\,m_b m_{u_i}\;p_2.p_3\;+\;(v_{d_ju_i}-a_{d_ju_i})(v_{bt}-a_{bt})\,m_{u_i}m_t\;p_2.p_4\;]. \qquad (22)
\end{aligned}
$$

The dominant terms are the squared amplitude due to $\tilde{e}$ exchange, and for initial quarks of the same generation ($i=j$), the interference between W and $\tilde{d}$. The result is sensitive to the interference term only if the product of λ'' couplings is large (around 10^{-1}). For subprocesses involving quarks of different generations in the initial state the situation is more complex and all amplitudes have to be taken into account.

The resonant $\hat{s}$-channel processes have been studied in [11], for first family up and down quarks. For the B-violating couplings, the study of $\hat{s}$-channels $cd\to\tilde{s}$ and $cs\to\tilde{d}$ can also be found in [11]. The $\hat{u}$-diagram has been studied at the Tevatron for the first family of up and down quarks [10].

In the present note we have improved previous calculations for LHC because we have included all contributions to single top production. Since the dominant terms are those considered in the literature, our complete evaluation validates the approximations done in previous papers.

III. DETECTION OF SINGLE TOP PRODUCTION THROUGH R-PARITY VIOLATION AT THE LHC

We have carried out the feasibility study to detect single top production through R-parity violation at the LHC by measuring the $l\nu bb$ final state using the following procedure.

First, we have implemented the partonic $2 \to 2$ cross sections calculated using Eqs. (5)–(22) in the PYTHIA event generator. Providing PYTHIA with the flavour and the momenta of the initial partons using a given parton distribution function (p.d.f.)[2] it then generates complete final states including initial and final state radiations and hadronization.

The generated events were implemented in ATLFAST to simulate the response of the ATLAS detector. In particular, isolated electrons, photons were smeared with the detector resolution in the pseudo-rapidity range of $|\eta| < 2.5$. In the same way and the same η region the measured parameters of the isolated and non-isolated muons were simulated. Finally, a simple fixed cone algorithm (of radius $R = 0.4$) was used to reconstruct the parton jets. The minimum transverse energy of a jet was set at 15 GeV. According to the expected b-tagging performance of the ATLAS detector [15] for low luminosity at the LHC we have assumed a 60% b-tag efficiency for a factor 100 of rejection against light jets.

The same procedure was applied to the SM background with the exception that we used besides PYTHIA also the ONETOP [16] event generator.

The integrated luminosity for one year at low luminosity at the LHC is taken to be 10 fb^{-1}.

The number of signal events depends on the mass and the width of the exchanged sparticle, and on the value of the Yukawa couplings (see Section II). We assume that only one type of Yukawa coupling is nonzero, i.e. either sleptons ($\lambda' \neq 0$) or squarks ($\lambda'' \neq 0$) are exchanged. The width of the the exchanged sparticle is a sum of the widths due to R-parity conserving and R-parity violating decays:

$$\Gamma_{tot} = \Gamma_R + \Gamma_{\not R} \tag{23}$$

where $\Gamma_{\not R}$ is given by

$$\Gamma_{\not R}(\tilde{q}^i_R \longrightarrow q^j q^k) = \frac{(\lambda''_{ijk})^2}{2\pi} \frac{(M^2_{\tilde{q}^i_R} - M^2_{top})^2}{M^3_{\tilde{q}^i_R}} \tag{24}$$

for the squarks, and it is given by

$$\Gamma_{\not R}(\tilde{l}^i_L \longrightarrow q^j \bar{q}^k) = \frac{3(\lambda'_{ijk})^2}{16\pi} \frac{(M^2_{\tilde{l}^i_L} - M^2_{top})^2}{M^3_{\tilde{l}^i_L}} \tag{25}$$

for the sleptons. The number of signal events depends also on the flavour of the initial partons through their p.d.f. In Table I we display the total cross section values for different initial parton flavours in the case of exchanged squarks of mass of 600 GeV and of R-parity conserving width $\Gamma_R = 0.5$ GeV. We took for all $\lambda'' = 10^{-1}$, which yields a natural width of the squark which is smaller than the experimental resolution. Table II contains the same information for slepton exchange ($\lambda' = 10^{-1}$, for a slepton of mass of 250 GeV and a width of $\Gamma_R = 0.5$ GeV). Other processes are not quoted because the small value of the limits of their couplings prevents their detection.

In order to study the dependence of the signal on the mass and the width of the exchanged particle we have fixed the couplings to 10^{-1} and have chosen three different masses for the exchanged squarks: 300, 600 and 900 GeV, respectively. For each mass value we have chosen two different Γ_R: 0.5 and 20 GeV, respectively. For the first case $\Gamma_{\not R}$ dominates, whereas in the last one, when $\Gamma_{tot} \approx \Gamma_R$, the single top-production cross section decreases by a factor ~ 10. We have considered here the ub parton initial state, since this has the highest cross section value. Besides, we have also generated events with a cd initial partonic state and an exchanged $\tilde{s}$-quark of mass of 300 GeV, for comparison with the simulation presented in Ref. [11].

In order to study the dependence on the parton initial state we have fixed the mass of the exchanged squark to 600 GeV and its width with $\Gamma_R = 0.5$ GeV and varied the initial state according to the first line of Table I.

Finally, for the exchanged sleptons we have studied only one case, namely the $u\bar{d}$ initial state with a mass and width of the exchanged slepton of 250 GeV and 0.5 GeV, respectively. In each case we have generated about 10^5 signal events.

The different types of background considered are listed in Table III together with their estimated cross sections. The irreducible backgrounds are single top production through a virtual W (noted W^*), or through W-gluon fusion.

[2]We have used the CTEQ3L p.d.f.

W-gluon fusion is the dominant process (for a detailed study see [17]). A Wbb final state can be obtained either in direct production or through Wt or $t\bar{t}$ production. Finally, the reducible background consists of W-nj events where two of the jets are misidentified as b-jets.

We have used the ONETOP [16] event generator to simulate the W-gluon fusion process. For the other backgrounds we have used PYTHIA. We have generated from one thousand (W^*) to several million events ($t\bar{t}$) depending on the importance of the background.

The separation of the signal from the background is based on the presence of a resonant structure of the tb final state in the case of the signal. The background does not show such a structure as it is illustrated in Fig 1.

In the process to reconstruct the tb final state first we reconstruct the top quark. The top quark can be reconstructed from the W and from one of the b-quarks in the final state, requiring that their invariant mass satisfy

$$150 \leq M_{Wb} \leq 200\text{GeV}.$$

The W is in turn reconstructed from either of the two decay channels:

$$W \to u\bar{d}$$
$$W \to l\nu.$$

Here we have considered only the latter case which gives a better signature due to the presence of a high p_t lepton and missing energy. The former case suffers from multi-jets event backgrounds. As we have only one neutrino, its longitudinal momentum can be reconstructed by using the W and top mass constraints. The procedure used is the following :
- we keep events with two b-jets of $p_t \geq 40$ GeV, with one lepton of $p_t \geq 25$ GeV, with $E_t^{miss} \geq 35$ GeV and with a jet multiplicity ≤ 3,
- we reconstruct the longitudinal component (p_z) of the neutrino by requiring $M_{l\nu} = M_W$. This leads to an equation with twofold ambiguity on p_z.
- More than 80% of the events have at least one solution for p_z. In case of two solutions, we calculate $M_{l\nu b}$ for each of the two b-jets and we keep the p_z that minimises $|M_{top} - M_{l\nu b}|$.
- we keep only events where $150 \leq M_{l\nu b} \leq 200$ GeV.

Next, the reconstructed top quark is combined with the b quark not taking part in the top reconstruction. An example of the invariant mass distribution of the tb final state is shown in Fig. 2.

In order to reduce the the $t\bar{t}$ background to a manageable level, we need to apply a strong jet veto on the third jet by requiring that its p_t should be ≤ 20 GeV.

The invariant mass distribution of the tb final state after having applied this cut is shown in Fig. 3. The signal to background ratio is clearly increased in comparison to Fig. 2.

Once an indication for a signal is found, we count the number of signal (N_s) and background (N_b) events in an interval corresponding to 2 standard deviations around the signal peak for an integrated luminosity of 30 fb^{-1}. Then we rescale the signal peak by a factor α such that

$$N_s/\sqrt{N_b} = 5.$$

By definition the scale-factor α determines the limit of sensitivity for the lowest value of the λ'' (λ') coupling we can test with the LHC:

$$\lambda''_{ijk} \cdot \lambda''_{lmn} \leq 0.01 \cdot \sqrt{\alpha}.$$

In Table IV we show the limits obtained for the combinations of $\lambda''_{132}\lambda''_{332}$ for different masses and widths of the exchanged $\tilde{s}$-quark. Also shown are the current limit assuming assuming a mass for $\tilde{m}_f = 100$ GeV, the number of signal and background events, as well as the experimentally observable widths of the peak (Γ_{exp}). In Fig. 4 we compare our results with those obtained in Ref. [11] for $m_{\tilde{s}} = 300$ GeV, and a cd initial state, using parton-level simulation. We ascribe the lower efficiency of this analysis to the more detailed and realistic detector simulation employed.

In Table V we compile the sensitivity limit of the bilinear combination of the different Yukawa couplings one can obtain after 3 years of LHC run with low luminosity, if the exchanged squark has a mass of 600 GeV. For its width we consider $\Gamma_R = 0.5$ GeV and a component $\Gamma_{\not R}$ given by Eq.(24).

For the exchanged sleptons (cf Table II) we have calculated the sensitivity limit of the bilinear combination of the different Yukawa couplings only for the most favourable case, i.e. for the $u\bar{d}$ partonic initial state. We obtain

4.63×10^{-3} for the limits on $\lambda'_{11k}\lambda'_{k33}$ (in comparison with the limit of 2.8×10^{-3} obtained by Oakes *et al.*). For those cases where the exchanged squark (slepton) might be discovered at the LHC we have made an estimate on the precision one can determine its mass. For this purpose, we have subtracted the background under the mass peak and fitted a Gaussian curve on the remaining signal. This procedure is illustrated in Fig. 5 for the case of 600 GeV squark mass and ub partonic initial state. For the assumed value of the coupling constant, the error on the mass determination is dominated by the 1% systematic uncertainty on the jet energy scale in ATLAS [15].

IV. CONCLUSIONS

We have studied single top production through R-parity violating Yukawa type couplings, at the LHC.

We have considered all $2 \to 2$ partonic processes at tree-level, including interference terms. The calculated $2 \to 2$ partonic cross sections have been implemented in PYTHIA to generate complete particle final states. A fast particle level simulation was used to obtain the response of the ATLAS detector. We have taken into account all important SM backgrounds.

We have studied the signal-to-background ratio as a function of the initial partonic states, the exchanged sparticle mass and width, and of the value of the Yukawa couplings.

At the chosen value of the coupling constants ($\sim 10^{-1}$), significant signal-to-background ratio was obtained only in the $\hat{s}$-channel, in the tb ($l\nu bb$) invariant mass distribution, around the mass of the exchanged sparticle, if

(i) the exchanged sparticle is a squark, and

(ii) its width due to R-parity conserving decay is of the order of a GeV.

In this case we obtain a significance of $S = N_s/\sqrt{N_b} > 5$ for the whole mass range investigated (300 – 900 GeV) for an integrated luminosity of 30 fb^{-1}. This means, that squarks ($\tilde{d}$ or $\tilde{s}$) with narrow width might be discovered at the LHC. The experimental mass resolution would permit to measure the squark mass in this case with a precision of $\sim 1\%$.

Conversely, if no single top production above the SM expectation is observed at the LHC, after 3 years of running at low luminosity, the experimental limit on the quadratic combination of the λ'' couplings can be lowered by at least one order of magnitude, for narrow width squarks. In the case of the exchanged sleptons significant signal-to-background ratio can be obtained in the case of $u\bar{d}$ partonic initial state, i.e. for the combination of the $\lambda'_{11k}\lambda'_{k33}$ couplings. Due to the lower rate, as compared to squark exchange, in the absence of a signal the current limit can be improved only by a factor 2. The difference between the significance in our study and the one in Ref. [11] can be explained by the different degree of detail in the simulation process.

ACKNOWLEDGEMENTS.

We thank S. Ambrosanio and S. Lola for useful comments on the manuscript. A.D. acknowledges the support of a "Marie Curie" TMR research fellowship of the European Commission under contract ERBFMBICT960965 in the first stage of this work. J.-M. V. thanks the "Alexander von Humboldt Foundation" for financial support.

---

[1] P. Fayet Phys. Lett. **B69** (1977) 489; G. Farrar and P. Fayet, Phys. Lett. **B76** (1978) 575.

[2] F. Zwirner, Phys. Lett. **B132** (1983) 103; L. Hall and M. Suzuki, Nucl. Phys. **B231** (1984) 419; J. Ellis et al, Phys. Lett. **B150** (1985) 142; G. Ross and J. Valle, Phys. Lett. **B151** (1985) 375; S. Dawson, Nucl. Phys. **B261** (1985) 297; R. Barbieri and A. Masiero, Nucl. Phys. **B267** (1986) 679; S. Dimopoulos and L.J. Hall, Phys. Lett. **B207** (1987) 210; L.E. Ibanez and G.G. Ross Nucl. Phys. **B368** (1992) 3; S. Lola, G.G. Ross, Phys. Lett. **B314** (1993) 336; J. Ellis, S. Lola and G.G. Ross Nucl. Phys. **B526** (1998) 115.

[3] G.J Gounaris, D.T. Papadamou and F.M. Renard, Z. Phys. **C76** (1997) 333.

[4] K. Whisnant, J.M. Yang, B.L. Young and X. Zhang, Phys. Rev. **D56** (1997) 467.

[5] J.M. Yang and B.L. Young, Phys. Rev. **D56** (1997) 5907.

[6] C.S. Li, R.J. Oakes, J.M. Yang and H.Y. Zhou, Phys. Rev. **D57** (1998) 2009.

[7] G. Couture, C. Hamzaoui and H. Konig, Phys. Rev. **D52** (1995) 171; J.L. Lopez, D.V. Nanopoulos and R. Rangarajan, Phys. Rev. **D56** (1997) 3100; G. Couture, M. Frank and H. Konig, Phys. Rev. **D56** (1997) 4213; G.M. de Divitiis, R. Petronzio and L. Silvestrini, Nucl. Phys. **B504** (1997) 45.
[8] M. Hosch, R.J. Oakes, K. Whisnant, J.M. Yang, B.L. Young and X. Zhang, Phys. Rev. **D58** (1998) 4002; S. Mrenna and C.P. Yuan, Phys. Lett. **B367** (1996) 188; J. Guasch and J. Sola, Phys. Lett. **B416** (1998) 353.
[9] H. Dreiner and G.G. Ross, Nucl. Phys. **B365** (1991) 597.
[10] A. Datta, J.M. Yang, B.L. Young and X. Zhang, Phys. Rev. **D56** (1997) 3107.
[11] R.J. Oakes, K. Whisnant, J.M. Yang, B.L. Young and X. Zhang, Phys. Rev. **D57** (1998) 534.
[12] T. Sjöstrand, Comput. Commun. 82 (1994) 74.
[13] E.Richter-Wąs, D.Froidevaux, L.Poggioli, ATLAS Internal Note Phys-No-79, 1996.
[14] G. Bhattacharyya, Nucl. Phys. Proc. Suppl. **52A** (1997) 83; H. Dreiner, hep-ph/9707435, in Perspectives on Supersymmetry, ed. G. Kane, World Scientific; Report of the R-parity group of GDR SUSY, hep-ph/9810232, available at http://www.in2p3.fr/susy/ and references therein.
[15] The ATLAS Collaboration, Detector and Physics Performance Technical Design Report, CERN/LHCC/99-14, ATLAS TDR 14, 25 may 1999.
[16] Onetop, C.P. Yuan, D. Carlson, S. Mrenna, Barringer, B. Pineiro, R. Brock, http://www.pa.msu.edu/~brock/atlas-1top/EW-top-programs.html
[17] T. Stelzer, Z. Sullivan, S. Willenbrock, Phys. Rev. **D58** (1998) 094021.

FIGURES

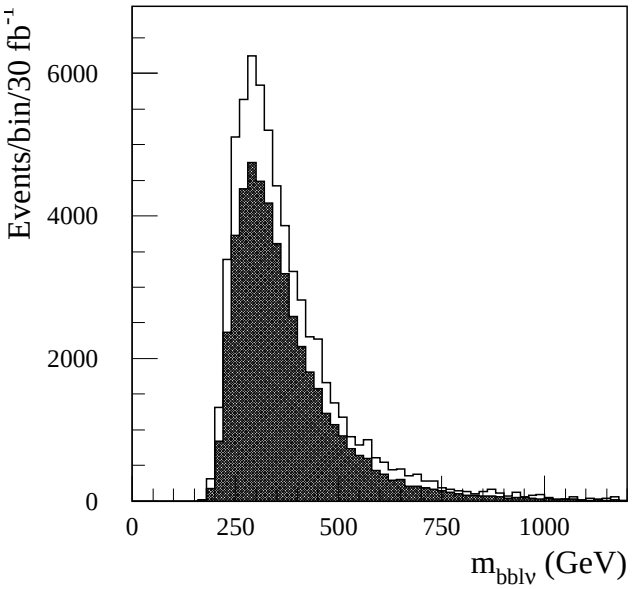

Fig. 1 - Invariant mass distribution of $l\nu bb$ for the backgrounds after three years at LHC at low luminosity. The $t\bar{t}$ background dominates (dashed histogram).

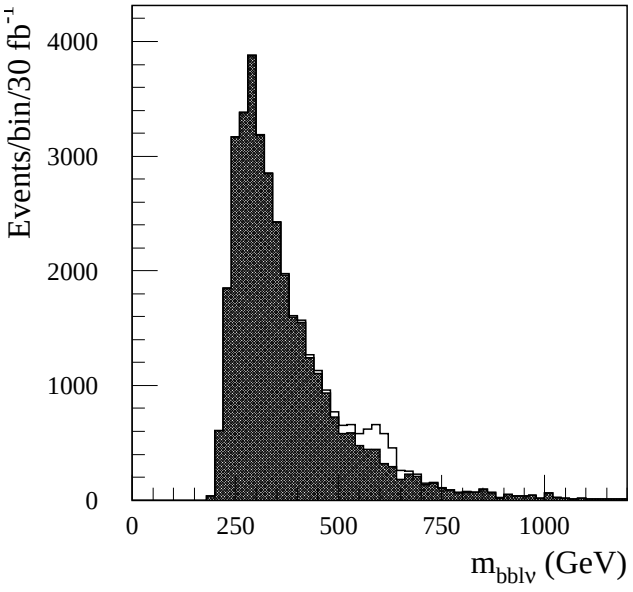

Fig. 2 - Invariant mass distribution of $l\nu bb$ combination for the signal and backgrounds (dashed histogram) after three years of LHC run at low luminosity. The signal corresponds to an exchanged $\tilde{s}$-quark of 600 GeV mass and 0.5 GeV width. The initial partons are ub and the λ'' couplings are set to 10^{-1}.

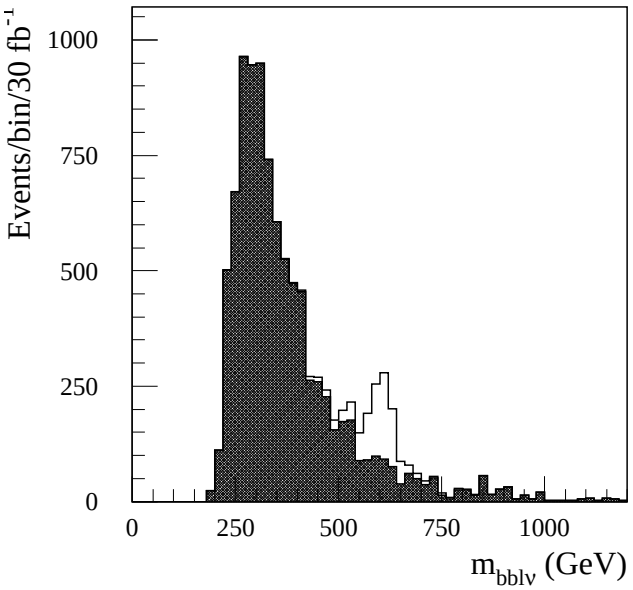

Fig. 3 - Invariant mass distribution of $l\nu bb$ for the signal and backgrounds (dashed histogram) after three years at LHC at low luminosity after having applied the cuts.

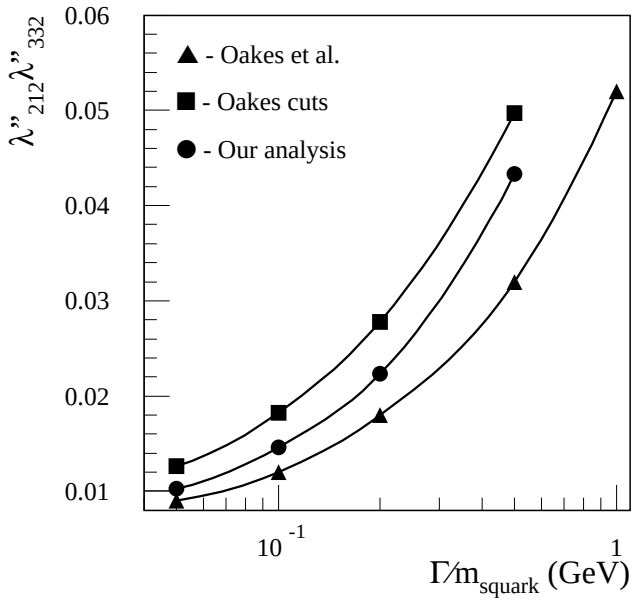

Fig. 4 - Sensitivity limits for the values of the $\lambda''_{212}\lambda''_{332}$ Yukawa couplings we obtain for the *cd* initial state at the LHC after 1 year with low luminosity, for an exchanged $\tilde{s}$-quark of mass of 300 GeV (circles). The result obtained by Oakes *et al.*, is also shown (triangles). The squares indicate a result obtained by applying the cuts used by Oakes *et al.* on our sample.

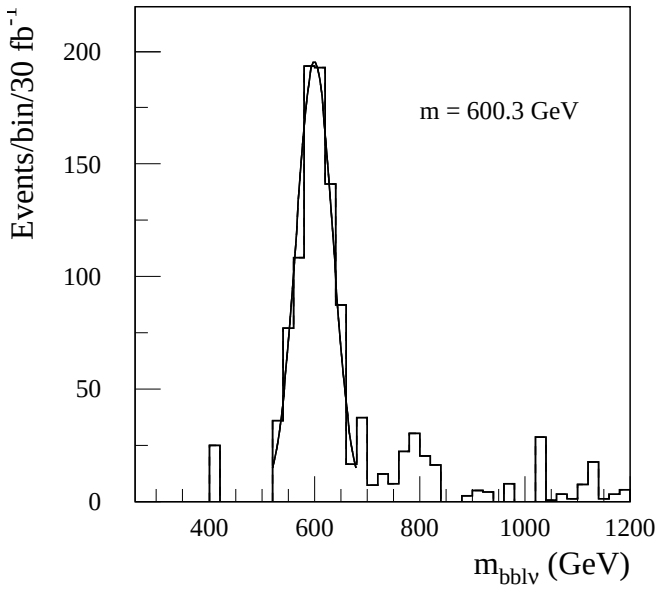

Fig. 5 - The background subtracted mass distribution fitted with a Gaussian in case of an exchanged $\tilde{s}$-quark of 600 GeV for a *ub* initial parton state. It corresponds to 3 years of LHC run with low luminosity.

TABLES

Initial partons	cd	cs	ub	cb	
Exchanged particle	$\tilde{s}$	$\tilde{d}$	$\tilde{s}$	$\tilde{d}$	$\tilde{s}$
Couplings	$\lambda''_{212}\lambda''_{332}$	$\lambda''_{212}\lambda''_{331}$	$\lambda''_{132}\lambda''_{332}$	$\lambda''_{231}\lambda''_{331}$	$\lambda''_{232}\lambda''_{332}$
Cross section in pb	3.98	1.45	5.01	0.659	

TABLE I. Total cross-section in pb for squark exchange in the $\hat{s}$-channel for a squark of mass of 600 GeV assuming $\Gamma_R = 0.5$ GeV.

Initial partons	$u\bar{d}$	$u\bar{s}$	$c\bar{d}$	$c\bar{s}$	$u\bar{b}$	$c\bar{b}$
Couplings	$\lambda'_{11k}\lambda'_{k33}$	$\lambda'_{12k}\lambda'_{k33}$	$\lambda'_{21k}\lambda'_{k33}$	$\lambda'_{22k}\lambda'_{k33}$	$\lambda'_{13k}\lambda'_{k33}$	$\lambda'_{23k}\lambda'_{k33}$
Cross section in pb	7.05	4.45	2.31	1.07	2.64	0.525

TABLE II. Total cross-section in pb for slepton exchange in the $\hat{s}$-channel for a slepton of mass of 250 GeV assuming $\Gamma_R = 0.5$ GeV.

Background	$\sigma \times BR$ (pb)
W^*	2.2
gluon fusion	54
Wt	17
$t\bar{t}$	246
Wbb	66.6
Wjj	440

TABLE III. $\sigma\times$ Branching Ratio for backgrounds.

$m_{\tilde{s}}$ (GeV)	300		600		900	
Γ_R (GeV)	0.5	20	0.5	20	0.5	20
N_s	6300	250	703	69	161	22
N_b	4920	5640	558	1056	222	215
Γ_{exp} (GeV)	24.3	30.5	37.5	55.6	55.4	62.1
Limits on $\lambda'' \times \lambda''$	2.36×10^{-3}	1.21×10^{-2}	4.10×10^{-3}	1.51×10^{-2}	6.09×10^{-3}	2.09×10^{-2}

TABLE IV. Sensitivity limits for the values of the $\lambda''_{132}\lambda''_{332}$ Yukawa couplings for an integrated luminosity of 30 fb^{-1}. For the other quantities see the text. Current limit is 6.25×10^{-1}.

Initial partons	cd	cs	ub	cb	
Exchanged particle	$\tilde{s}$	$\tilde{d}$	$\tilde{s}$	$\tilde{d}$	$\tilde{s}$
Couplings	$\lambda''_{212}\lambda''_{332}$	$\lambda''_{212}\lambda''_{331}$	$\lambda''_{132}\lambda''_{332}$	$\lambda''_{231}\lambda''_{331}$	$\lambda''_{232}\lambda''_{332}$
N_s	660	236	703	96	
N_b	558				
Γ_{exp} (GeV)	38.5	31.3	37.5	40.1	
Limits on $\lambda'' \times \lambda''$	4.26×10^{-3}	7.08×10^{-3}	4.1×10^{-3}	1.11×10^{-2}	

TABLE V. Sensitivity limit of the Yukawa couplings for an exchanged squark of mass of 600 GeV assuming $\Gamma_R = 0.5$ GeV, for an integrated luminosity of 30 fb^{-1}. Current limit is 6.25×10^{-1}.

1.4 Nouvelle Physique auprès de HERA polarisé

Le collisionneur HERA était dédié à l'étude de la diffusion profondément inélastique via des collisions entre protons et électrons (ou positrons). L'énergie caractéristique était de $\sqrt{s} = 300\ GeV$ et la luminosité intégrée a fini par atteindre quelques centaines de pb^{-1} ($\approx 0.5\, fb^{-1}$). La polarisation des faisceaux de positrons et d'électrons pouvait être obtenue sans trop de difficulté. En revanche, le faisceau de proton était non polarisé mais il a été considéré très sérieusement de le polariser lorsque les responsables du collisionneur et des expériences pensaient au futur d'HERA. J'ai ainsi été contacté par Albert de Roeck (DESY/CERN) qui m'a demandé de réaliser des études sur l'intérêt de polariser le faisceau de protons pour analyser d'éventuels signaux de nouvelle physique. Plus tard, Yves Sirois (Polytechnique) et Abbhay Deshpande (Yale/BNL) m'ont demandé des études similaires pour des projets, aujourd'hui avortés, de collisionneurs ep avec différentes énergies, tels que TESLAxHERA qui aurait pu avoir $\sqrt{s} = 1\ TeV$ ou eRHIC avec $\sqrt{s} = 100\ GeV$ mais une très forte luminosité.

Les types de nouvelle physique testables à HERA (et autres collisionneurs ep) doivent faire intervenir de nouveaux couplages entre électrons et quarks. Ces même modèles peuvent induire des effets dans le processus de Drell-Yan dans le cadre des collisions du Tevatron ($p\bar{p} \to l^+l^- + X$). Au vu de la très grande différence d'énergie entre les deux machines, il est assez clair que le Tevatron avait la plus grande chance de découverte. Une étude plus attentive a montré que les contraintes étaient plutôt complémentaires et à peu près comparables mais qu'il fallait tenir compte aussi d'autres résultats comme les limites venant du LEP ou de la violation de parité dans les atomes de Cesium. Par conséquent, la question la plus intéressante pour HERA n'etait pas ce qui pouvait y être découvert mais plutôt, en cas de découverte d'un nouveau couplage électron-quark auprès d'une quelconque expérience, quelles informations auraient pu être obtenues à partir des divers observables mesurables à HERA.

Les modèles que j'ai considérés sont les interactions de contact entre électrons et quarks ainsi que les nouvelles interactions dues à la présence de leptoquarks. En ce qui concerne les interactions de contact, un article a été publié en 1999 [28] mais les principaux résultats ont été donnés dans ma thèse. Par conséquent, je ne reporte pas cette analyse dans cette habilitation.

L'article qui suit traite des possibles manifestations de leptoquarks. Les leptoquarks trouvent une origine théorique dans les théories de grande unification où ils sont associés à des bosons de jauge (leptoquarks vectoriels), dans les théories supersymétriques violant la R parité où ils sont associés aux super-partenaires des quarks (leptoquarks scalaires/squarks), et enfin dans certains modèles de sous-structure. L'approche suivie est purement phénoménologique et ne tiens compte que de l'invariance de jauge. Le résultat important obtenu est que la polarisation des faisceaux permet une identification de la nature du leptoquark, ce qui semble beaucoup plus difficile voire impossible sans polarisation.

Malheureusement, ces études sont obsolètes car le collisionneur HERA ne fonctionne

plus. Il faut également souligné qu'aucun signal n'a indiqué sérieusement la présence d'une nouvelle interaction entre électrons et quarks jusqu'à présent.

Article publié sous la référence : Eur. Phys. J. **C14** (2000) 165.

Search and identification of Scalar and Vector Leptoquarks at HERA with polarization

P. Taxil[1], **E. Tuğcu**[1,2] **and J.-M. Virey**[1,3,⋆]

[1]Centre de Physique Théorique[†], CNRS-Luminy, Case 907, F-13288 Marseille Cedex 9, France and Université de Provence, Marseille, France
[2] Galatasaray University, Çırağan Cad. 102, Ortaköy 80840-İstanbul, Turkey
[3]Institut für Physik, Universität Dortmund, D-44221 Dortmund, Germany

Abstract

We analyze the effects of Scalar and Vector Leptoquarks on various observables in electron (positron) - proton deep inelastic scattering. In view of the future program of the HERA collider, with a high luminosity and also with polarization, we present the constraints that can be reached using this facility for several Leptoquark scenarios. We address the question of the identification of the nature of a discovered Leptoquark. We emphasize the relevance of having polarized lepton and proton beams in order to disentangle completely the various Leptoquark models. This study is also relevant in the context of the TESLA×HERA project.

PACS Numbers : 12.60.-i; 13.88.+e; 13.85.Qk; 13.85.Rm
Key-Words : Deep Inelastic Scattering, Leptoquarks, Polarization.

Number of figures : 8

December 1999
DO-TH 99/15
CPT-99/P.3831

[†]Unité Propre de Recherche 7061

⋆ Fellow of the "Alexander von Humboldt" Foundation, present address: 1, email: virey@cpt.univ-mrs.fr

1 Introduction

Many extensions of the Standard Model (SM), like for instance Supersymmetry (SUSY) or Grand Unified Theories (GUT), predict the existence of Leptoquarks (LQs), which are particles that couple directly to quark-lepton pairs. In general there is no particular prediction for the masses of these LQs, which can range from the electroweak (EW) scale to the GUT scale. However an interesting possibility is the case of SUSY models where the R_{Parity} symmetry [1] is violated (for a recent review on this subject see [2]). Then some $\not{R}_p$ -squarks have direct couplings to electron-quark pairs and are completely analogous to some of the LQs considered here. The equivalence between $\not{R}_p$ -squarks and LQs is described, for instance, in [3]. An interesting feature of the SUSY models with $\not{R}_p$-squarks is that the squarks could have some relatively low masses (between the EW and the TeV scales) since SUSY is believed to be broken at the TeV scale.

In this paper we will not consider any precise $\not{R}_p$-squarks model but we rather adopt the "model independent" approach of Buchmüller-Rückl-Wyler (BRW)[4], where the LQs are classified according to their quantum numbers and have to fulfill several assumptions like B and L conservation (to avoid rapid proton decay) and $SU(3)$x$SU(2)$x$U(1)$ invariance. We refer to [4] for more details. The interaction lagrangian for scalar leptoquarks is given by :

$$\begin{aligned}\mathcal{L}_{scal} &= (g_{1L}\,\bar{q}_L^c i\tau_2 \ell_L + g_{1R}\,\bar{u}_R^c e_R)\,.\,\mathbf{S_1} + \tilde{g}_{1R}\,\bar{d}_R^c e_R\,.\,\tilde{\mathbf{S}}_\mathbf{1} + g_{3L}\,\bar{q}_L^c i\tau_2 \tau \ell_L\,.\,\mathbf{S_3} \\ &+ (h_{2L}\,\bar{u}_R \ell_L + h_{2R}\,\bar{q}_L i\tau_2 e_R)\,.\,\mathbf{R_2} + \tilde{h}_{2L}\,\bar{d}_R \ell_L\,.\,\tilde{\mathbf{R}}_\mathbf{2}\ , \end{aligned} \tag{1}$$

where the scalar LQs S_1, $\tilde{S}_1$ are singlets and S_3 is a triplet, all with fermionic number $(F = 3B + L)$ $F = 2$. R_2 and $\tilde{R}_2$ are doublets with $F = 0$. ℓ_L, q_L (e_R, d_R, u_R) are the usual lepton and quark doublets (singlets).
For vector LQs the lagrangian is :

$$\begin{aligned}\mathcal{L}_{vect} &= \left(h_{1L}\,\bar{q}_L \gamma^\mu \ell_L + h_{1R}\,\bar{d}_R \gamma^\mu e_R\right)\,.\,\mathbf{U_{1\mu}} + \tilde{h}_{1R}\,\bar{u}_R \gamma^\mu e_R\,.\,\tilde{\mathbf{U}}_{\mathbf{1}\mu} + h_{3L}\,\bar{q}_L \tau \gamma^\mu \ell_L\,.\,\mathbf{U_{3\mu}} \\ &+ \left(g_{2L}\,\bar{d}_R^c \gamma^\mu \ell_L + g_{2R}\,\bar{q}_L^c \gamma^\mu e_R\right)\,.\,\mathbf{V_{2\mu}} + \tilde{g}_{2L}\,\bar{u}_R^c \gamma^\mu \ell_L\,.\,\tilde{\mathbf{V}}_{\mathbf{2}\mu}\ , \end{aligned} \tag{2}$$

where the vector $U_{1\mu}$, $\tilde{U}_{1\mu}$ are singlets and $U_{3\mu}$ is a triplet, all with $F = 0$, and $V_{2\mu}$, $\tilde{V}_{2\mu}$ are doublets with $F = 2$.
Therefore, if one takes into account the left and right-handed chiralities $\mathcal{L}_{scal} + \mathcal{L}_{vect}$ yields 14 independent models of LQs. From these two lagrangians one can deduce some properties of the LQ models which are compiled in Table 1 of [3]. A point which is important to notice is that the LQ couplings are flavor dependent. In what follows we denote generically by λ any LQ coupling and by M the associated mass.
In addition, in order to simplify the analysis, we make the following assumptions : *i*) the LQ couples to the first generation only, *ii*) one LQ multiplet is present at a time, *iii*) the different LQ components within one LQ multiplet are mass degenerate, *iv*) there is no mixing among LQs.

The LQs are severely constrained by several different experiments, and we refer to [5, 6, 7] for some detailed discussions. Here we only quote the most important facts :

1) Leptonic pion decays and $(g-2)_\mu$ measurements indicate that the LQs must be chiral [5, 6] (*e.g.* S_1 and R_2 could have Left-handed or Right-handed couplings but not both).

2) To avoid the stringent constraints from FCNC processes the simplest assumption is to impose "family diagonal" couplings for the LQs, namely they couple to only one generation [5].

3) There are some collider constraints coming from Tevatron through the searches for LQ pair production. This process, which involves the color properties of the LQs, yields some bounds on the mass of the LQs independently of the λ coupling and of the particular scalar or vector LQ model. However, these mass bounds are strongly dependent on the branching ratio $BR(LQ \to eq)$, and the values quoted below correspond to the maximal case $BR = 1$.
For the scalar LQ models, the CDF and D0 collaborations at the Tevatron have combined their data to provide [8] the constraint : $M > 242\,GeV$ $(BR = 1)$. The dependence of these limits on BR is presented in [8].
For the vector LQ models the situation is more complex since, in general, the experimental bounds depend on two new parameters : κ_g and λ_g. These two parameters correspond to the possible anomalous couplings present at vertices involving gluon(s) plus vector LQ(s) [9]. The value of the cross sections depends on these two parameters. In particular, the smallest cross sections do not correspond in general to the ones obtained for "pure" gauge boson couplings (i.e. $\kappa_g = 0$, $\lambda_g = 0$).
The D0 collaboration has published some mass bounds for vector LQs for several values of (κ_g,λ_g) [10]. They obtained $M > 340\,GeV$ $(BR = 1)$ for ($\kappa_g = 0$,$\lambda_g = 0$), but the weakest constraint, corresponding to the minimal cross section, $M > 245\,GeV$ $(BR = 1)$ is obtained for ($\kappa_g = 1.3$,$\lambda_g = -0.2$).
To conclude this part, we remark that the minimal mass bound for vector LQs is close to the mass bound for scalar LQs, and we recall that these bounds are strongly dependent on BR. For instance, the $\not{R}_p$-squarks models mentioned above are not coupled to $e-q$ pairs only but also to some superpartners (R_p conserving decays) which means that $BR < 1$. As a consequence, for some particular models, BR can be relatively small, giving much lower LQs mass limits.

4) Low Energy Neutral Current data, in particular from Atomic Parity Violation on Cesium atoms (APV) experiments, give in general the strongest bounds on the ratio M/λ. In fact, the last experimental results on the measurements of $Q_W(Cs)$, the weak charge for Cesium atoms, give [11]: $Q_W^{exp} = -72.06 \pm (0.28)_{exp} \pm (0.34)_{th}$. For the SM we expect [12]: $Q_W^{th} = -72.84 \pm 0.13$. This means that the SM is excluded at the 1.8σ level. However this discrepancy is not huge and even if the experimental errors have strongly decreased compared with preceding experiments, they are still sizable. Then we take these results

with some caution.
Nevertheless, we have used the formula from [6] to compute the constraints on the LQ models taking these new data into account.

In fact, since the Q_W experimental value does not exactly correspond to the SM prediction, we need some new physics effects to fit the data. Consequently, on the one hand, if a particular LQ model gives a deviation for Q_W which is in the wrong direction with respect with the measured value, then it is simply excluded for any value of M/λ. On the other hand, if the deviation of the LQ model is on the right direction, this LQ model helps to fit the data and we get not only an upper bound for M/λ but a window of "presence", namely the LQ should have a ratio M/λ in this window to make agreement between data and theory. The figures we obtain for the BRW LQ models considered here are given in Table 1 :

Leptoquark	**Limits**	**Leptoquark**	**Limits**
S_{1L}	1600-3900	U_{1L}	$\times$
S_{1R}	$\times$	U_{1R}	2400-5800
$\tilde{S}_{1R}$	$\times$	$\tilde{U}_{1R}$	2300-5500
S_{3L}	2900-7000	U_{3L}	$\times$
R_{2L}	$\times$	V_{2L}	2400-5800
R_{2R}	2350-5650	V_{2R}	$\times$
$\tilde{R}_{2L}$	$\times$	$\tilde{V}_{2L}$	2300-5500

Table 1: Limits on M/λ in GeV at 95% CL from APV.

In this table a cross indicates that the model is excluded.

Note that similar bounds have been obtained for LQ models from the GUT group E_6 [13]. These constraints can be relaxed if there are some compensating contributions coming from more than one source of new physics [14].
Adopting a conservative attitude we do not consider the last measurement of Q_W as a clear evidence for new physics, and in the following we will consider that *all* the LQ models can still exist at low energy scales and can induce some effects in deep inelastic scattering (DIS).

5) Finally, there are also some collider constraints coming from LEP [15] and HERA [16]. In fact, depending on the particular LQ model involved the limits obtained at these facilities cover in general a small part of the parameter space (M,λ).

The analysis of LQ effects at present or future ep machines is of particular relevance since such particles could be produced in the s-channel [4].
In this paper, we complete and extend the analysis which has been presented recently [17] on the effects of Scalar LQs in the Neutral Current (NC) and Charged Current (CC) channels at HERA.

We will concentrate on the HERA collider with high integrated luminosities and also with a slightly higher energy in the center of mass. Namely we take $\sqrt{s} = 380\,GeV$ in order to increase the domain of sensitivity for the LQ models. This value for the energy could be reached in the future at HERA [18]. However, we consider also the case $\sqrt{s} = 300\,GeV$ in order to test the impact of the energy value on the capabilities of the HERA collider to discover LQs. In addition, we are also concerned with a possible new ep collider running at much higher energies $\sqrt{s} = 1\,TeV$, like the TESLAxHERA project [19].

An other important point of our analysis is that we consider the case where polarized beams are available. Indeed, thanks to the progress which have been performed by the RHIC Spin Collaboration [20] at Brookhaven, the acceleration of polarized proton beams up to high energies is becoming a true possibility. Adding this opportunity to the fact that high intensity polarized lepton beams will certainly be available soon at HERA, and also at a future linear accelerator, some new windows could be opened with $\vec{e}\vec{p}$ collisions. The resulting potentialities for HERA physics have been discussed in several recent workshops [21, 22, 23, 24].

This paper is organized as follows : In section 2, we estimate the constraints on the parameter space that can be reached in the future at HERA for several Leptoquark scenarios and we compare these results with the present bounds. In section 3, we propose a strategy for the identification of the various LQ models. In particular, we show that both electron and proton polarizations $(\vec{e} + \vec{p})$ are necessary to disentangle the different models. Finally we summarize our results and we conclude in section 4. The details of the formulas we have used are given in the Appendix.

2 Discovery limits from future ep experiments

We consider the HERA collider with e^- or e^+ beams but with some high integrated luminosities, namely $L_{e^-} = L_{e^+} = 500\,pb^{-1}$. The other parameters for the analysis being : $\sqrt{s} = 380\,GeV$, $0.01 < y < 0.9$, $(\Delta\sigma/\sigma)_{syst} = 2\,\%$ and we use the GRV partonic distribution functions (pdf) set [25].

We present in Fig. 1 the discovery limits at 95% CL for the various LQ models that we obtain from a χ^2 analysis performed on the unpolarized NC cross sections $d\sigma/dQ^2$ for $ep \to eX$ at leading order (see the Appendix).
Next-to-leading order (NLO) QCD corrections to the production cross-section have been estimated recently [26, 27]. In the mass range we consider, $K-$factors increase the cross section by up to 30-50% according to two different calculations [26, 27]. This means that our bounds are somewhat pessimistic. On the other hand, we expect that the asymmetries we will present later will be less affected by NLO corrections since $K-$factors should cancel in the ratios.

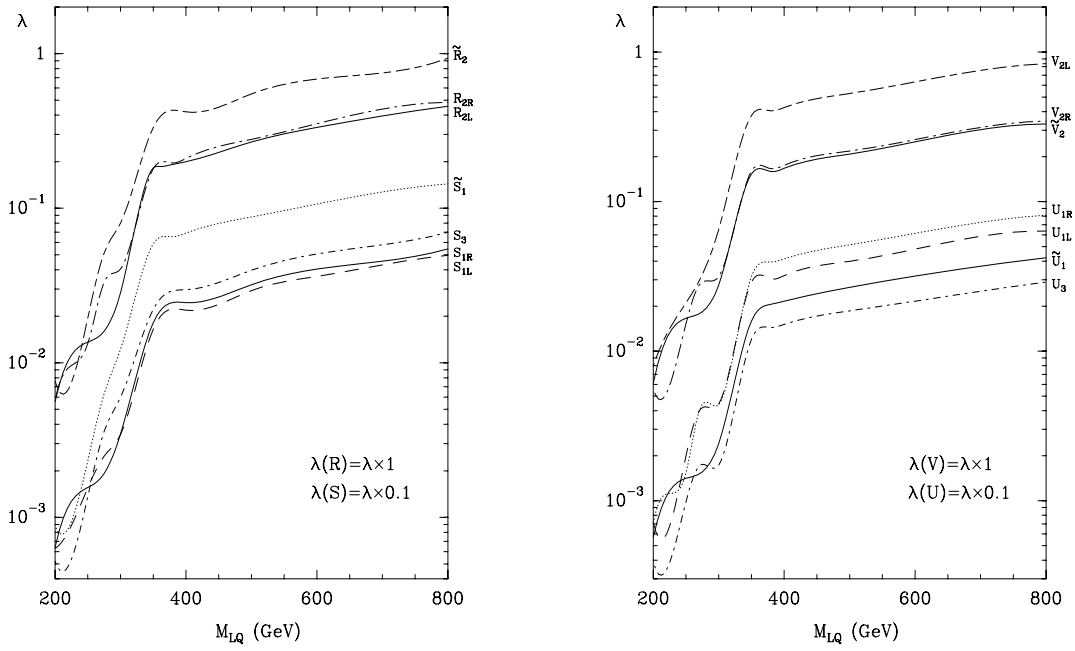

Figure 1: Discovery limits at 95% CL for the various LQ models at HERA.

From these plots we see that there are clearly two different domains of constraints in the plane (M, λ). In the "real domain", $(M < 380\,GeV)$, production in the s-channel is by far dominant due to the resonance. The "virtual domain" for masses above 380 GeV corresponds to the production or exchange of an off-shell LQ and the SM cross-section is less affected. As a consequence the bounds are weaker. In addition we see on this figure that the LQs which couple preferentially to d-quarks ($\tilde{S}_1$, $\tilde{R}_2$) and (V_{2L},U_{1R}) are less constrained compared to the others since u quarks are dominant in the proton. Isospin symmetry implies that we would need en collisions (with the same values for $\sqrt{s}$ and L) to constrain these two LQs at the same level.

Besides the discovery bounds obtained from the unpolarized NC cross sections, it is interesting to examine which sensitivity could be obtained from other observables like the unpolarized CC cross sections, the single or double polarized cross sections (in NC or CC processes) or some spin asymmetries.

• *Charged Current cross sections :*

Concerning the CC channel, in DIS the SM process corresponds to W exchanges : $ep \to \nu X$. The LQs which have both couplings to eq and $e\nu$ pairs should also induce some effects in CC processes. Note that within our assumptions (no mixing) only S_{1L} , S_3, U_{1L} and U_3 could induce some effects in the CC sector.

The effects in CC at HERA have been analyzed some time ago in [28] in the framework of some specific models based on superstring-inspired E_6. More recently they were considered again, essentially in the context of the so-called HERA anomaly problem (for a review and references, see [29]). Then, the CC process was considered to analyze the origin of the LQ rather than in the purpose of discovery. Here we can confirm this strategy since our χ^2 analysis shows that the sensitivity of the CC unpolarized cross section to the presence of the LQs is well below the one of the NC unpolarized cross section. Therefore, in the following of this section we do not consider anymore the CC processes.

• *Polarized cross sections :*

When polarized beams are available, the basic observables are the helicity-dependent (=polarized) cross sections. Polarization adds several types of systematic errors to the unpolarized case (see [30] for example). Then, in general, with polarized beams one prefers to use some spin asymmetries rather than the individual polarized cross sections. Indeed, most of the systematics cancel in the differences between the cross sections in various helicity states (numerator) and also in the ratio. However, at HERA, one can expect relatively small systematics for the polarized cross sections themselves. In particular one expects [31]:

$$(\frac{\Delta\sigma^{h_e}}{\sigma^{h_e}})_{syst} = 2-5\% \qquad and \qquad (\frac{\Delta\sigma^{h_e,h_p}}{\sigma^{h_e,h_p}})_{syst} = 5-10\% \tag{3}$$

where h_e, h_p are the helicities of the electron and of the proton (protons are not polarized in the first case).

Therefore, we have computed the sensitivities of the polarized cross sections using the most favorable values for the systematics. For the calculations we have assumed a degree of polarization $P = 70\%$ and used the GRSV polarized pdf set [32].

In comparison with the unpolarized NC cross sections we find, on the one hand, that the double polarized NC cross sections have a sensitivity of the same order and, on the other hand, that the single polarized NC cross sections have a slightly better sensitivity by roughly $2-10$ % (the precise value depending on the model). These conclusions are only indicative because the sensitivity of the cross sections (polarized or not) are strongly dependent on the systematics.

• *Spin asymmetries :*

Finally, we have also computed the constraints that can be reached by studying some Parity Violating (PV) spin asymmetries (definitions below). Concerning the systematic errors, we have considered $(\Delta A/A)_{syst} = 10$ % which is the expected value [30]. It appears that when both lepton and proton beams are polarized, the limits are very close to the ones obtained in the unpolarized case. When lepton polarization only is available the bounds are slightly weaker.

In conclusion, for the purpose of discovery the most simple way to proceed at HERA

is to consider the NC unpolarized cross sections.

In figure 2 we present a comparison in the plane (M, λ) between the present constraints and what could be achieved in the future in ep collisions.
We have shown the cases of two different scalars and two different vectors for illustration. The situation is very similar for the 10 remaining models. For future experiments one considers, on the one hand, the HERA collider with a higher energy of $\sqrt{s} = 380\ GeV$ but also with $\sqrt{s} = 300\ GeV$ and, on the other hand, the very interesting project TESLA(e)xHERA(p) where an energy of $\sqrt{s} = 1\,TeV$ could be reached [19]. The integrated luminosities are $L_{e^-} = L_{e^+} = 500\,pb^{-1}$ in all cases.

We can remark the followings : 1) For most of the models, LEP limits are already covered by present HERA data [16]. 2) Concerning the constraints from APV experiments, we show the allowed windows which are obtained by taking seriously into account the recent results on Q_W and their interpretation in terms of a New Physics due to a LQ. Then, in the virtual domain, the expected sensitivity of the future HERA program would not give better insights than the APV experiments with their present sensitivity. In the real domain the situation is different. 3) Tevatron data cover an important part of the parameter space in the real domain. However, we recall that the bounds obtained from LQ pair production at Tevatron are strongly sensitive to $BR(LQ \to eq)$. This is the case for R-parity violating squarks in SUSY models [3]. 4) To increase the window of sensitivity in the real domain, it is more important to increase the energy than the integrated luminosity. 5) The TESLAxHERA project will give access to a domain (both real and virtual) which is unconstrained presently. However, if this project is achieved, it will run at a time where the LHC will be running too. Then, there will be some important constraints on M from LQ pair production at LHC, but again those constraints will be strongly model dependent (*i.e.* BR dependent).

We conclude that there are still some windows for discovery at HERA and at future ep machines, in complementarity with the constraints coming from LQ pair production at pure hadronic colliders. We now turn to the problem of the identification of the nature of the LQ, a problem which is much more difficult and where polarization will be of great help.

3 Strategy for the identification of the various LQ models

3.1 Observables in a future HERA program

Besides the unpolarized differential cross sections $d\sigma_\pm/dy$ and $d\sigma_\pm/dQ^2$ in both the e^+ and e^- channels, we have considered a large set of polarized observables like the spin asym-

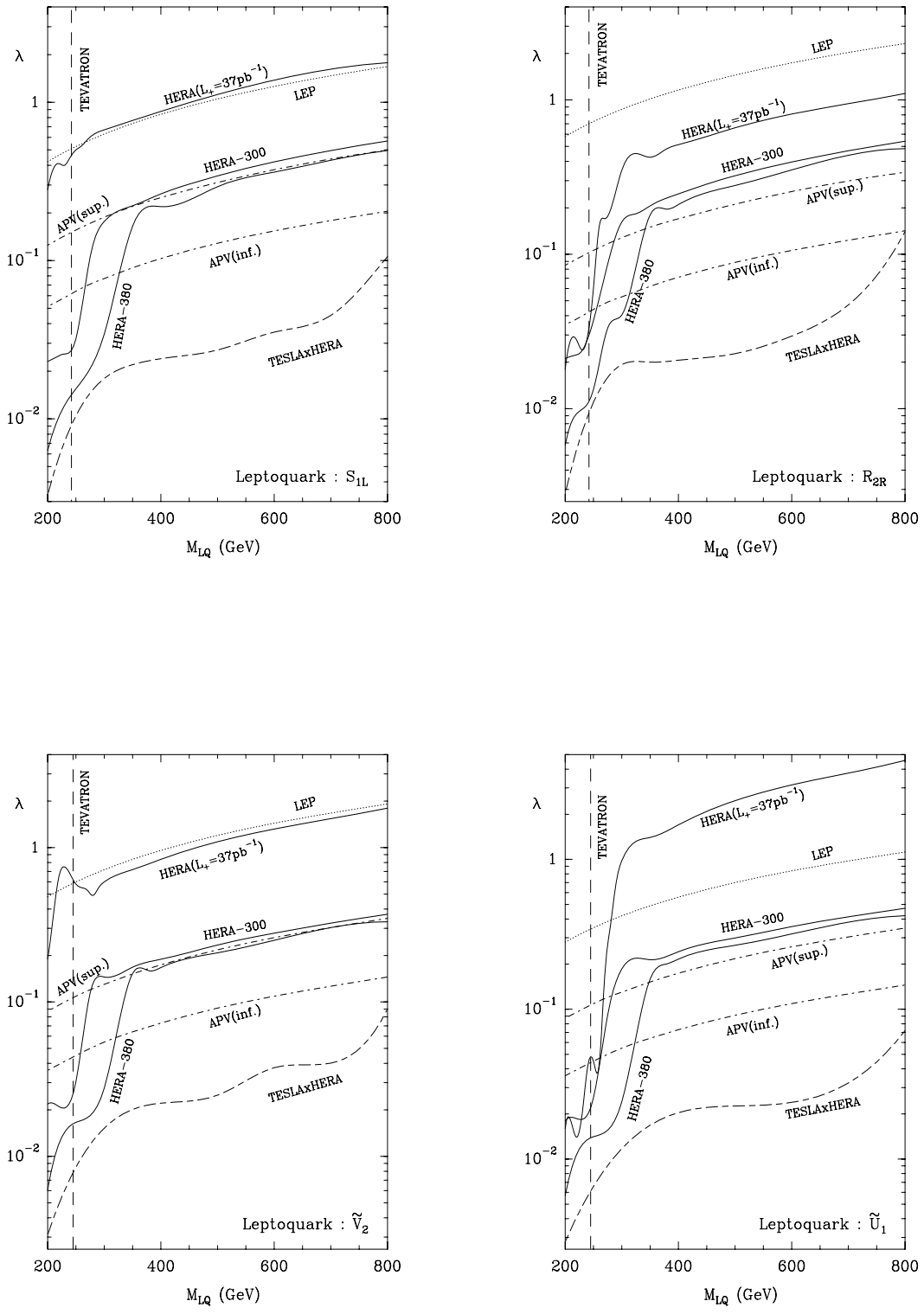

Figure 2: Constraints at 95% CL for various present and future experiments for R_{2R}, S_{1L}, $\tilde{V}_2$ and $\tilde{U}_1$.

metries. Indeed, since the LQs are chiral one can expect that the most important effects will appear on the Parity Violating (PV) spin asymmetries which can be defined when both beams are polarized or when there is lepton polarization only. Parity Conserving (PC) spin asymmetries will also be of great help as well as some charge asymmetries.

We will only define and discuss below the quantities which turned out to be the best ones to pin down the nature of the LQ and which have the stronger sensitivity to this kind of new physics. We will start by recalling the definitions of the relevant asymmetries.

If one beam is polarized (in practice, the lepton beam) one can define the single-spin parity-violating longitudinal asymmetry $A_L(e^t)$: ($t = \pm$ according to the electric charge of the lepton)

$$A_L(e^t) \;=\; \frac{\sigma_t^- \,-\, \sigma_t^+}{\sigma_t^- \,+\, \sigma_t^+} \;\;, \tag{4}$$

where $\sigma_t^{h_e} \equiv (d\sigma_t/dQ^2)^{h_e}$ and h_e is the helicity of the lepton. In addition, when both lepton and proton beams are polarized, some double-spin PV asymmetries can be defined [33]. For instance A_{LL}^{PV} is defined as :

$$A_{LL}^{PV}(e^t) \;=\; \frac{\sigma_t^{--} \,-\, \sigma_t^{++}}{\sigma_t^{--} \,+\, \sigma_t^{++}} \;\;, \tag{5}$$

where $\sigma_t^{h_e h_p} \equiv (d\sigma_t/dQ^2)^{h_e h_p}$, and h_e, h_p are the helicities of the lepton and the proton, respectively.

On the other hand, with longitudinally polarized beams, one needs two polarizations to define some parity-conserving (PC) asymmetries A_{LL}^{PC}. These well-known quantities have been extensively used in polarized DIS to determine the spin structure of the nucleon [34]. Here we will use the following :

$$A_1^{PC} \;=\; \frac{\sigma_-^{--} \,-\, \sigma_-^{-+}}{\sigma_-^{--} \,+\, \sigma_-^{-+}} \;\;, \tag{6}$$

$$A_2^{PC} \;=\; \frac{\sigma_-^{++} \,-\, \sigma_-^{+-}}{\sigma_-^{++} \,+\, \sigma_-^{+-}} \;\;, \tag{7}$$

and

$$A_3^{PC} \;=\; \frac{\sigma_+^{++} \,-\, \sigma_+^{+-}}{\sigma_+^{++} \,+\, \sigma_+^{+-}} \;\;, \tag{8}$$

Finally, since e^- as well as e^+ (polarized) beams will be available at HERA, one can define a large set of (polarized) charge asymmetries [35]. Among this set, only the following turned out to be relevant for our purpose :

$$B_U \;=\; \frac{\sigma_-^{--} - \sigma_-^{++} + \sigma_+^{++} - \sigma_+^{--} + \sigma_-^{-+} - \sigma_-^{+-} + \sigma_+^{-+} - \sigma_+^{+-}}{\sigma_-^{--} + \sigma_-^{++} + \sigma_+^{++} + \sigma_+^{--} + \sigma_-^{-+} + \sigma_-^{+-} + \sigma_+^{-+} + \sigma_+^{+-}} \;=\; \frac{\sigma_-^{-0} - \sigma_-^{+0} + \sigma_+^{0+} - \sigma_+^{0-}}{\sigma_-^{-0} + \sigma_-^{+0} + \sigma_+^{0+} + \sigma_+^{0-}} \;\;, \tag{9}$$

and

$$B_V \;=\; \frac{\sigma_-^{--}-\sigma_-^{++}+\sigma_+^{--}-\sigma_+^{++}+\sigma_-^{+-}-\sigma_-^{-+}+\sigma_+^{-+}-\sigma_+^{+-}}{\sigma_-^{--}+\sigma_-^{++}+\sigma_+^{--}+\sigma_+^{++}+\sigma_-^{+-}+\sigma_-^{-+}+\sigma_+^{-+}+\sigma_+^{+-}} \;=\; \frac{\sigma_-^{0-}-\sigma_-^{0+}+\sigma_+^{-0}-\sigma_+^{+0}}{\sigma_-^{0-}+\sigma_-^{0+}+\sigma_+^{-0}+\sigma_+^{+0}} \;, \tag{10}$$

where the index 0 means unpolarized and the order h_e, h_p has been respected. Note that both lepton and proton polarizations are necessary if one wants to measure these quantities.

3.2 Unpolarized case

We consider first the case of neutral currents.
If a LQ is present in an accessible kinematic range at HERA, it will be discovered from the analysis of $d\sigma_t/dQ^2$ which have the greatest "discovery" potential. However, if one starts trying to pin down the various models, both $d\sigma_t/dy$ and $d\sigma_t/dQ^2$ have to be analyzed simultaneously.

As is well known [4] the use of e^- or e^+ beams allows the separation of the 14 models of LQs into two classes according to the value of the fermionic number F. This comes from the dominant (LQ mediated) interaction between a valence quark and an e^- (F = 2) or an e^+ (F = 0).

Hence, a deviation from $d\sigma_-^{SM}/dQ^2$ indicates the class (S_{type} *or* V_{type}), whereas a deviation from $d\sigma_+^{SM}/dQ^2$ corresponds to the class (R_{type} *or* U_{type}).

Then, the y dependence, which is obtained from the two $d\sigma_t/dy$, is the best way to discriminate between a scalar and a vector interaction. Indeed, the SM background displays $d\sigma_t/dy \sim 1/y^2$ when the pure vector LQ case goes as y and the pure scalar LQ is constant in y. It is straightforward to obtain these behaviours from the formulas given in [4, 3] and in the Appendix.
We illustrate this pattern in Fig. 3 for two different choices of scalar and vector LQs, with parameters allowed by the present limits. Since the separation is easy, in the following we will treat scalar and vectors as two distinct species. Now the LQ models are separated in four distinct classes :(S_{type}), (R_{type}), (V_{type}) and (U_{type}).

On the other hand, Charged Current (CC) processes could in principle allow to go further into the distinction procedure. We have seen previously that only S_{1L} and S_3 for scalars, U_{1L} and U_3 for vectors, can induce a deviation from SM expectations (if we do not assume LQs mixing[1]). This means that the analysis of $\sigma_{e^-p}^{CC}$ allows to split the (S_{type}) class into (S_{1L},S_3) and (S_{1R},$\tilde{S}_1$), while the (U_{type}) class is split into (U_{1L},U_3) and (U_{1R},$\tilde{U}_1$).

In addition, it appears that when LQ exchange interferes with W exchange, S_{1L} and S_3 display some opposite patterns (see Appendix), and this is also the case between U_{1L} and U_3. However this interference term is too small to be measurable from unpolarized

[1] We refer to [36] for a discussion on scalar LQs mixings.

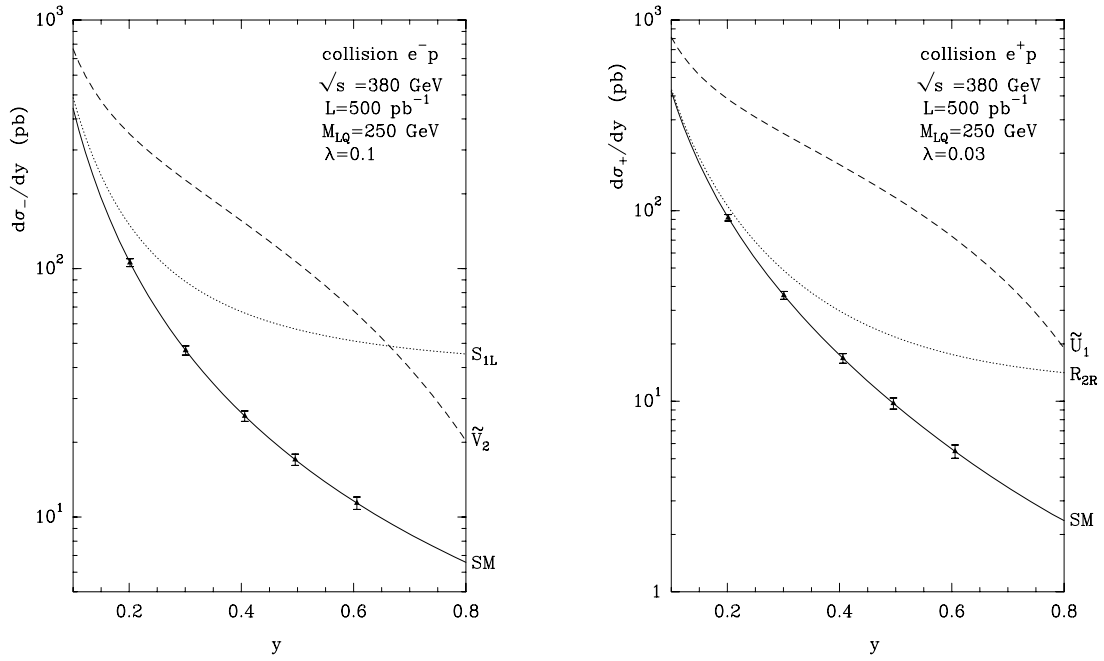

Figure 3: $d\sigma_-/dy$ for S_{1L} and $\tilde{V}_2$, and $d\sigma_+/dy$ for R_{2R} and $\tilde{U}_1$.

CC processes at HERA within the allowed parameters.

Then, if we want to go further into the identification of the LQs we need to separate "eu" from "ed" interactions, which seems to be impossible within ep collisions except if the number of anomalous events is huge [37]. If en collisions were available, the analysis of the respective ep and en production rates should allow this separation [17].

In conclusion, the ep unpolarized studies should allow the separation of the 14 LQ models into the six following classes : (S_{1L},S_3), $(S_{1R},\tilde{S}_1)$, $(R_{2L},R_{2R},\tilde{R}_2)$, (U_{1L},U_3), $(U_{1R},\tilde{U}_1)$ and $(V_{2L},V_{2R},\tilde{V}_2)$.

3.3 Polarized case

In a first step, we have tried to pin down the spin asymmetries which should allow to disentangle the chiral structure of the new interaction. Following our previous experience [38, 35] we know that the PV spin asymmetries (A_L or A_{LL}^{PV}) should fulfill this purpose.

Since their interactions are chiral, the LQs will induce some effects in these PV asymmetries, and the directions of the deviations from the SM expectations allow the distinction between several classes of models. For instance, a positive deviation for $A_L(e^-p)$ pins down the class (S_{1L},S_3) (or $(V_{2L},\tilde{V}_2)$) and, a negative one, the class $(S_{1R},\tilde{S}_1)$ (or V_{2R}). Similarly, an effect for $A_L(e^+p)$ makes a distinction between the model R_{2R} (or $(U_{1R},\tilde{U}_1)$)

and the class (R_{2L},$\tilde{R}_2$) (or (U_{1L},U_3)). These properties are illustrated in Fig. 4 which display A_L for e^-p and e^+p collisions with separated plots for scalar and vector LQs. The HERA and LQ parameters are given in the figure. The statistical and the 10% systematic errors are added in quadrature.

Therefore, the PV asymmetries separate the 14 BRW models into the following eight classes : (S_{1L},S_3), (S_{1R},$\tilde{S}_1$), (R_{2R}), (R_{2L},$\tilde{R}_2$), (U_{1L},U_3), (U_{1R},$\tilde{U}_1$), (V_{2L},$\tilde{V}_2$) and (V_{2R}).
It appears that the sensitivity of the two-spin PV asymmetry A_{LL}^{PV} is only slightly better than the one of A_L. Therefore, at this step, polarized protons are not mandatory.

The final step is to distinguish between an eu and an ed interaction, i.e. to obtain the flavor of the valence quark involved in the dominant interaction. With a polarized lepton beam and unpolarized protons, this flavor separation is not easy since only the different electric charges or partonic weights of u and d quarks can be used. Conversely, when polarized protons are available, it is possible to use a peculiarity of the polarized valence quark distributions, namely $\Delta u > 0$ and $\Delta d < 0$ (see e.g. [34] for a recent review). Indeed, if we pin down a spin asymmetry which is directly proportional to the Δq's, the flavor separation will be obtained from the sign of the deviation with respect with the SM value for this asymmetry. The double spin asymmetries A_{LL}^{PC}'s and the polarized charge asymmetries B_U and B_V defined above share this property.
At this point we need to discuss separately the scalar case and the vector case.

• *Scalar case :*

The three A_{LL}^{PC}: A_1^{PC}, A_2^{PC}, A_3^{PC} are the useful observables to separate the scalar LQs within the remaining classes. In Fig. 5 they are displayed for real LQ production. With the values we have chosen for the LQ parameters the separation is clear.

In fact the situation is a little bit more complex. Indeed, at this stage, we need to know if the LQ is real or virtual in order to pin down the dominant amplitude.
1) If the LQ is on-shell, the dominant term is the squared amplitude for LQ production. This information is known from the observation of the x distribution of the events [4].
2) If the LQ is off-shell, the dominant term is now the $\gamma.LQ$ interference term. This information is known from the non-observation of the s-resonance.
The dominant term controls the behaviour of the asymmetries. Since it depends on the mass of the LQ, we deduce that the behaviour of the asymmetries may be also M dependent. In fact we should have a change of behaviour for the LQ models which induce a destructive interference with standard γ exchange. For scalar LQs this happens for $\tilde{S}_1$, R_{2R} and R_{2L} (see Appendix).
At HERA the window for LQ discovery falls essentially in the real domain. At the TESLAxHERA facility, however, this distinction between real or virtual LQ exchange will be mandatory.

In the following we will consider only the LQs in the real domain, at HERA.

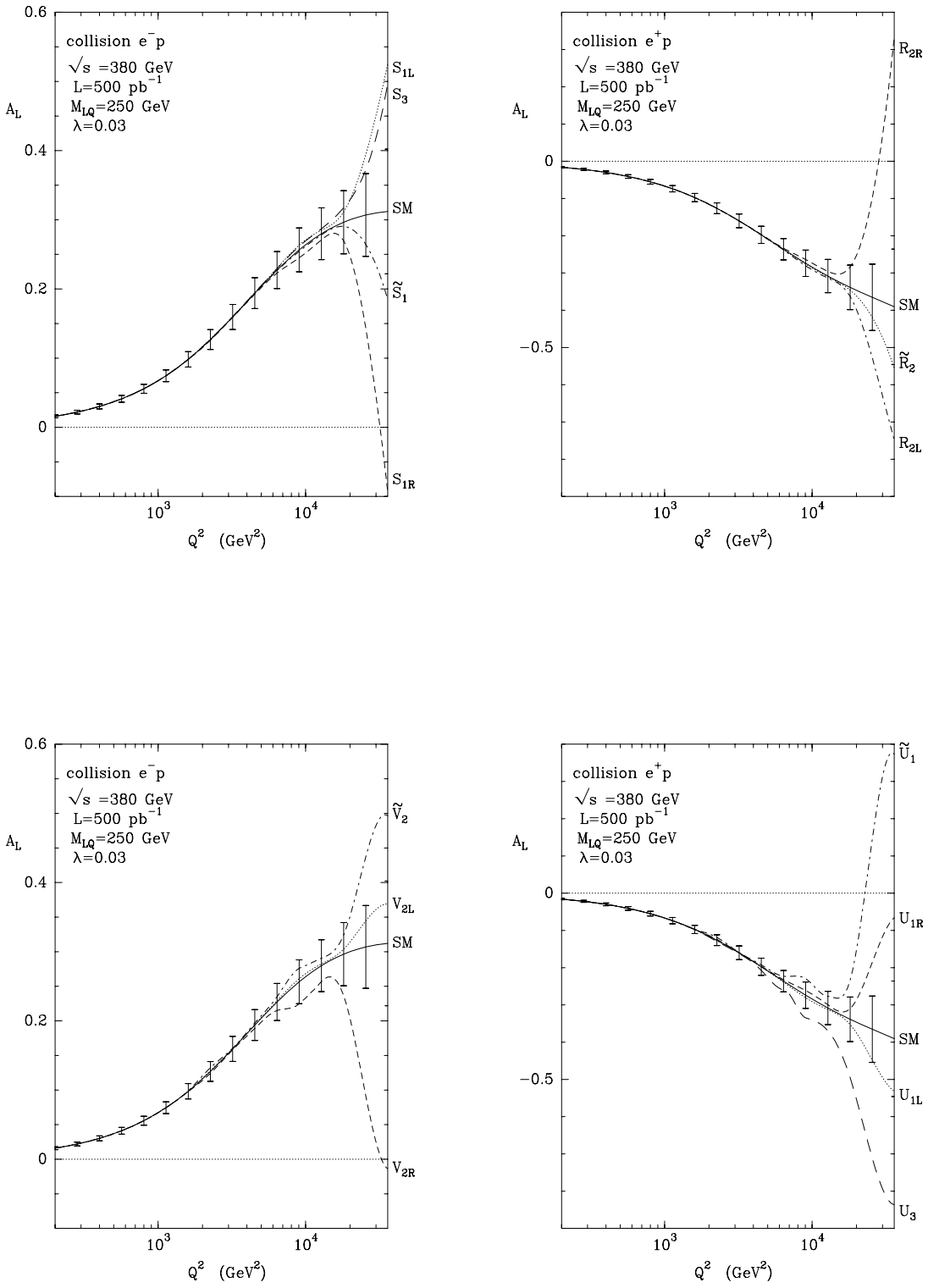

Figure 4: A_L vs Q^2 for the BRW models.

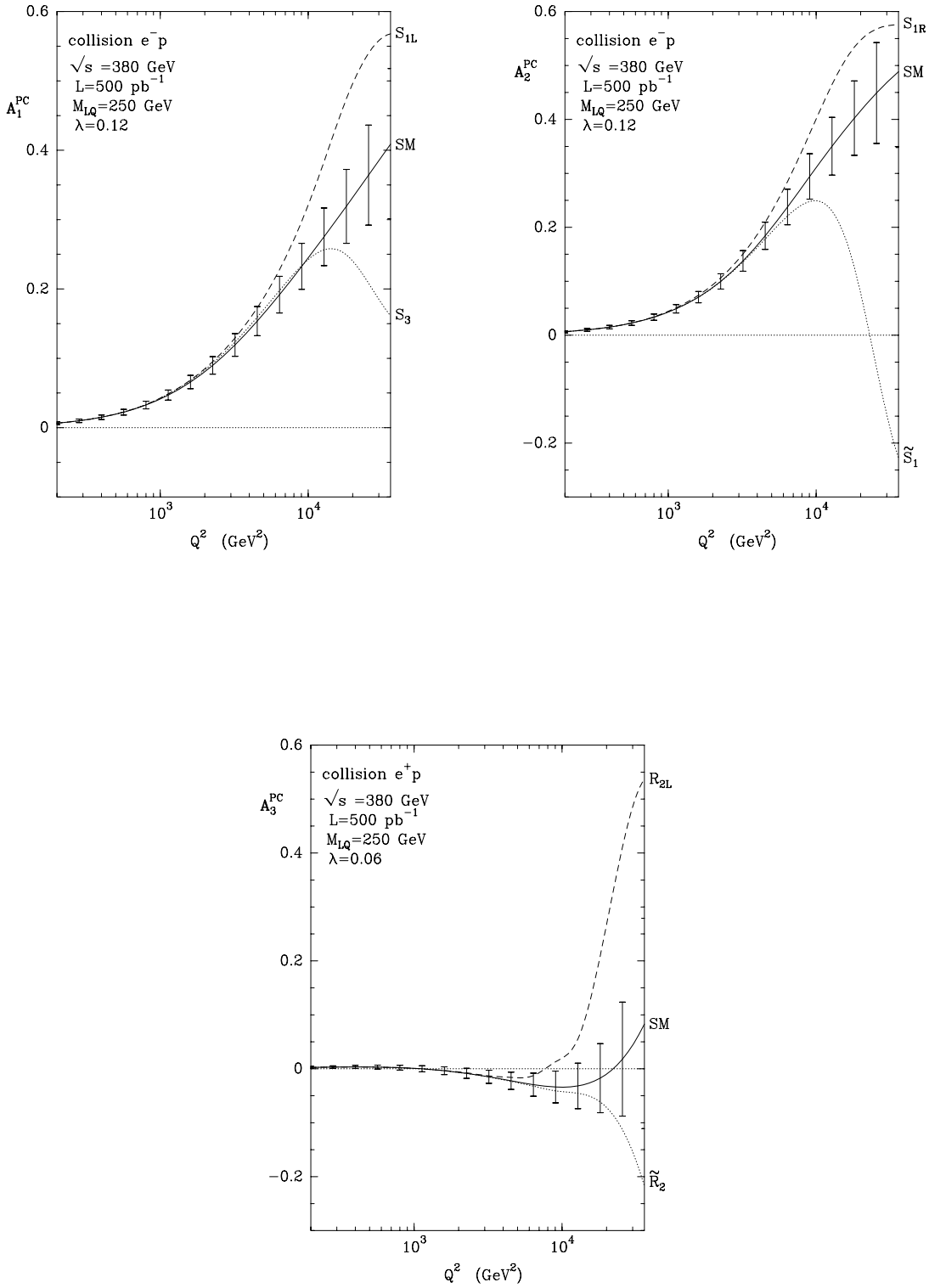

Figure 5: A_{LL}^{PC}'s vs Q^2 for the scalar BRW models.

Therefore, adding the information which should be obtained from $A_L(e^-p)$ (or from $A_{LL}^{PV}(e^-p)$), we get now a non-ambiguous separation of the LQ scalar models. This is shown by the different "deviation signatures" for all the different models presented on table 2.

	S_{1L}	S_{1R}	$\tilde{S}_1$	S_3	R_{2L}	R_{2R}	$\tilde{R}_2$
$A_L(e^-)$	+	−	−	+	0	0	0
$A_L(e^+)$	0	0	0	0	−	+	−
A_{LL}^{PC}	+	+	−	−	+	0	−

Table 2: "Deviation signatures" for the BRW scalar LQ models (real domain).

In this table, "0 deviation" means that the effect of a LQ on a particular quantity is contained into the error bar centered on the SM expectation. On the other hand, positive and negative deviations should be clearly visible thanks to the high integrated luminosities.

- *Vector case :*

Concerning vector LQs, the most sensitive quantities allowing the flavor separation are the polarized charge asymmetries. In the real domain the relevant charge asymmetries are B_U and B_V.
These asymmetries are shown in Fig. 6. We have separated the effects of the classes (U_{1L},U_3) and (U_{1R},$\tilde{U}_1$) on B_U since these two classes are already distinguished thanks to the PV asymmetries.

The deviation signatures for vector LQs are displayed in table 3.

	U_{1L}	U_{1R}	$\tilde{U}_1$	U_3	V_{2L}	V_{2R}	$\tilde{V}_2$
$A_L(e^-)$	−	+	+	−	0	0	0
$A_L(e^+)$	0	0	0	0	+	−	+
$B_{U\,or\,V}$	+	−	+	−	+	0	−

Table 3: "Deviation signatures" for the BRW vector LQ models (real domain).

3.4 Identification domains

Finally, it is possible to estimate the domains in the plane (M, λ) where a non-ambiguous identification of the nature of a LQ should be possible. We present in Fig. 7 these "identification domains" for some representative examples.

The upper curves correspond to the present discovery limits from Tevatron, HERA and LEP. Constraints from APV have been omitted. The lower curves represent the constraints coming from the PV spin asymmetries. They are better, in general, than the ones from the PC or charge asymmetries (dashed curves). Note that, for $\tilde{V}_2$ the sensitivities from both types of asymmetries are equivalent.
The regions in the parameter space where a complete identification of the chiral structure

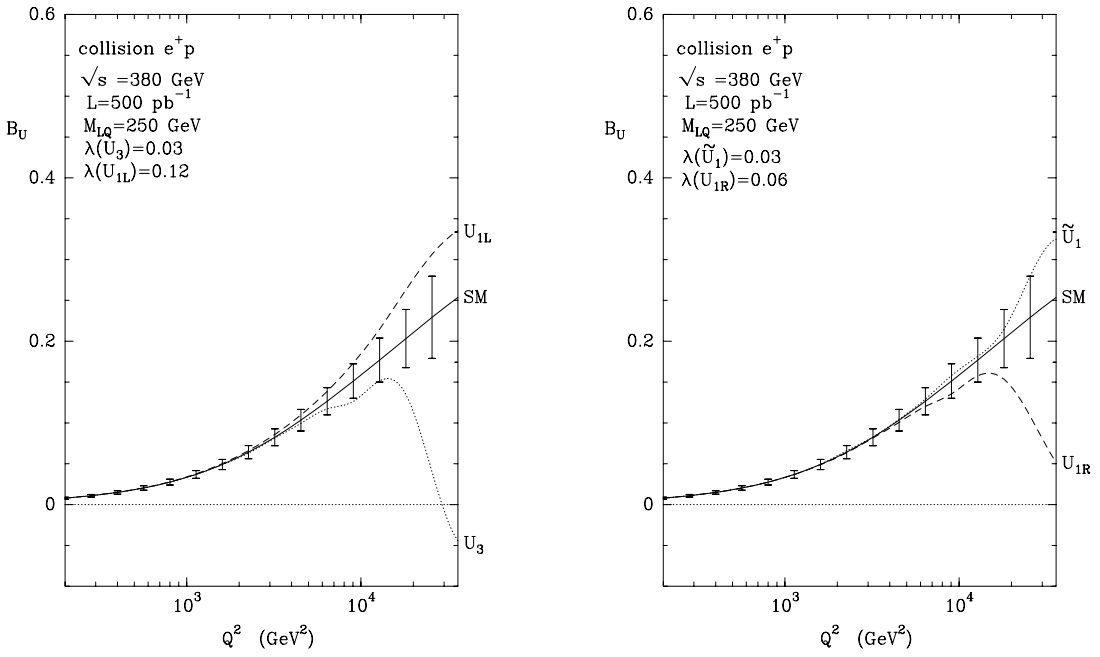

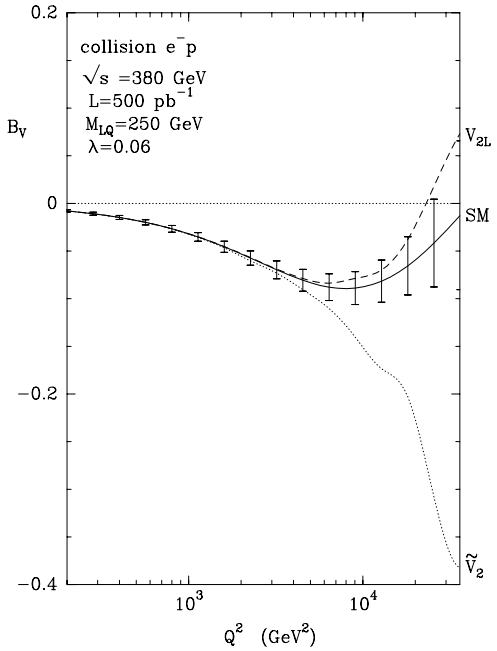

Figure 6: B_U and B_V vs Q^2 for the vector BRW models.

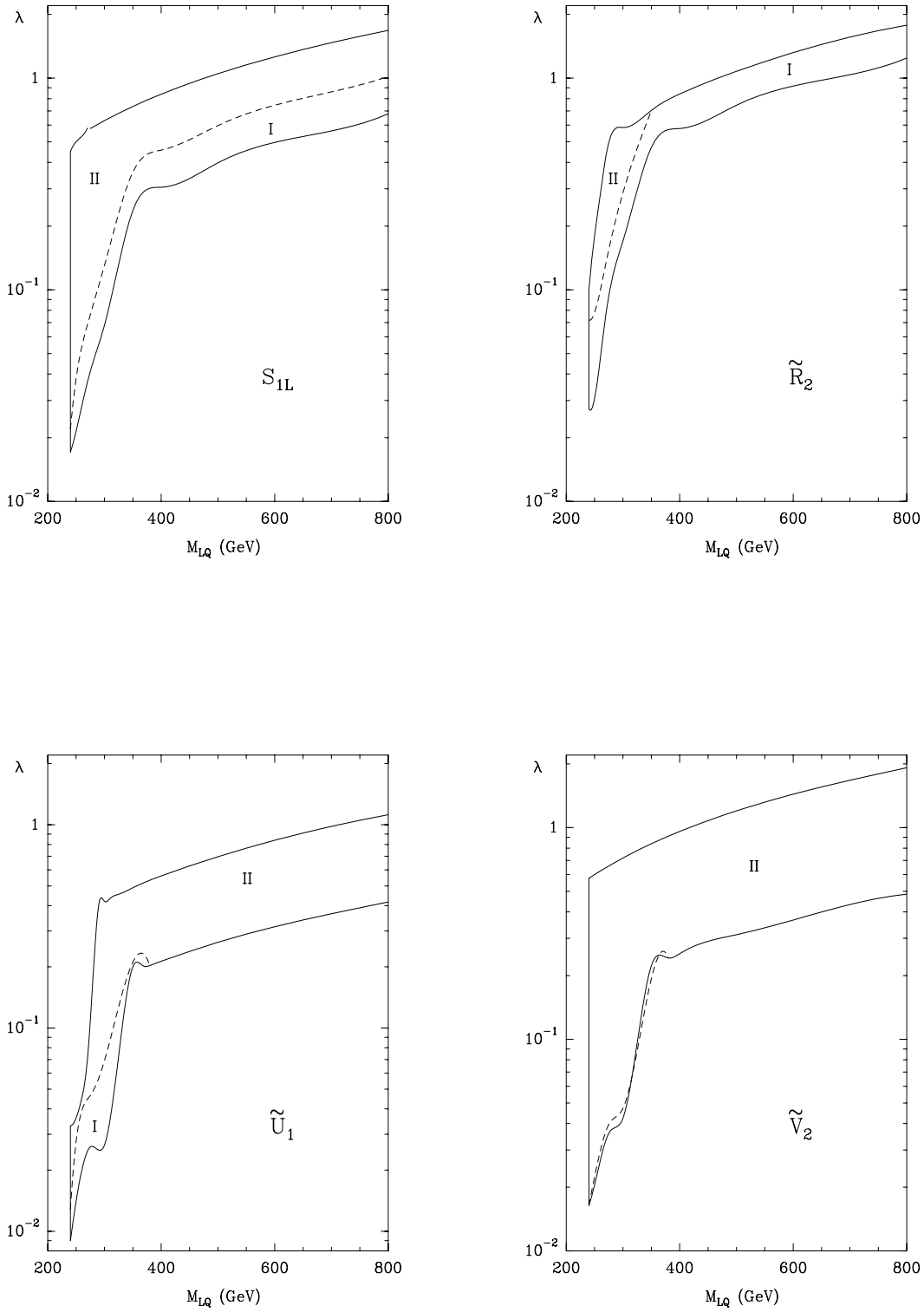

Figure 7: Identification domain at 95% CL for S_{1L}, $\tilde{R}_2$, $\tilde{U}_1$ and $\tilde{V}_2$.

is possible are given by the domains I+II. In domain I no effect will appear on the A^{PC}'s nor B's and one misses the flavor separation. In the domain II it is possible to identify the nature of the LQ without ambiguity.

4 Conclusion

Concerning the chances of discovery of Leptoquark states in the future HERA program (with a high integrated luminosity), we have seen that there are still some windows that are not covered by present data, in particular in the real domain ($M < \sqrt{s}$). Measurements of the integrated unpolarized cross section in NC processes, at the highest possible energy, should present the best opportunity. At this stage, polarized beams would not yield better results.
Our purpose was mainly to explore the possibilities of disentangling the various LQ models. We present in Fig. 8 a schematic view of what can be done from the precise measurements of the various observables we have discussed.
The first two steps are well known : with unpolarized e^- and e^+ beams it is easy to get in the same time the separation between scalars and vectors (from the y distributions) and between $F = 0$ and $F = 2$ LQs (from $d\sigma_\pm/dQ^2$).

The next steps are more difficult to perform. However, it is mandatory to try to pin down the chiral structure of a newly discovered LQ-like particle. For example it is worth recalling here that, due to SUSY, the R-parity breaking squarks have universal left-handed couplings to leptons.

We have shown that polarization of the lepton beam should yield this information thanks to the precise measurement of A_L in both e^- and e^+ collisions. At this step the polarization of the proton beams is not necessary. Note also that the sensitivities of the PV asymmetry and of the unpolarized cross sections are comparable. This means that, if polarized lepton beams are available in the same run, as soon as a LQ is discovered in e^+ or e^- collisions (via $d\sigma/dQ^2$), one gets almost simultaneously his scalar or vector nature (via $d\sigma/dy$) and the chiral structure of its couplings (via A_L) .
Now, the next step is to try to get the flavor separation within the remaining classes of models, which is the most difficult task. Indeed, CC processes with unpolarized beams do not seem to be sufficient to fulfill this program, as long as "neutron" beams, through the use of ionized Deuterium or ^3He atoms, are not available. On the other hand, the behaviours of the polarized valence quark distributions Δu and Δd in a polarized proton should allow to do this job. In the case of scalar LQs, measuring the PC double spin asymmetries is sufficient. In the case of the remaining vectors, it is necessary to measure some polarized charge asymmetries to obtain the separation at the same level of sensitivity. In both cases, the price to pay is a proton beam with a high degree of polarization ($P = 70\%$).

We feel that it was important to get an answer to the following question : are both (lepton and proton) polarizations mandatory to completely disentangle the various LQ

models present in the BRW lagrangians ? According to our analysis the answer is yes. This conclusion holds certainly also for the TESLA×HERA project.

Finally, if we relax the working assumptions *i-iv* (see Section 1), the LQs can have a more complex structure and the analysis should be less easy. In this case, like in the more general context of Contact Interactions [35], the use of additional asymmetries, that one can also define with lepton plus proton polarizations, should be very useful.

Moreover, polarized electron-neutron collisions could be performed with polarized ^3He beams : this option has been seriously considered in the framework of the RHIC-Spin program at Brookhaven and also at HERA [22]. This could be the final goal of an ambitious polarization program at HERA.

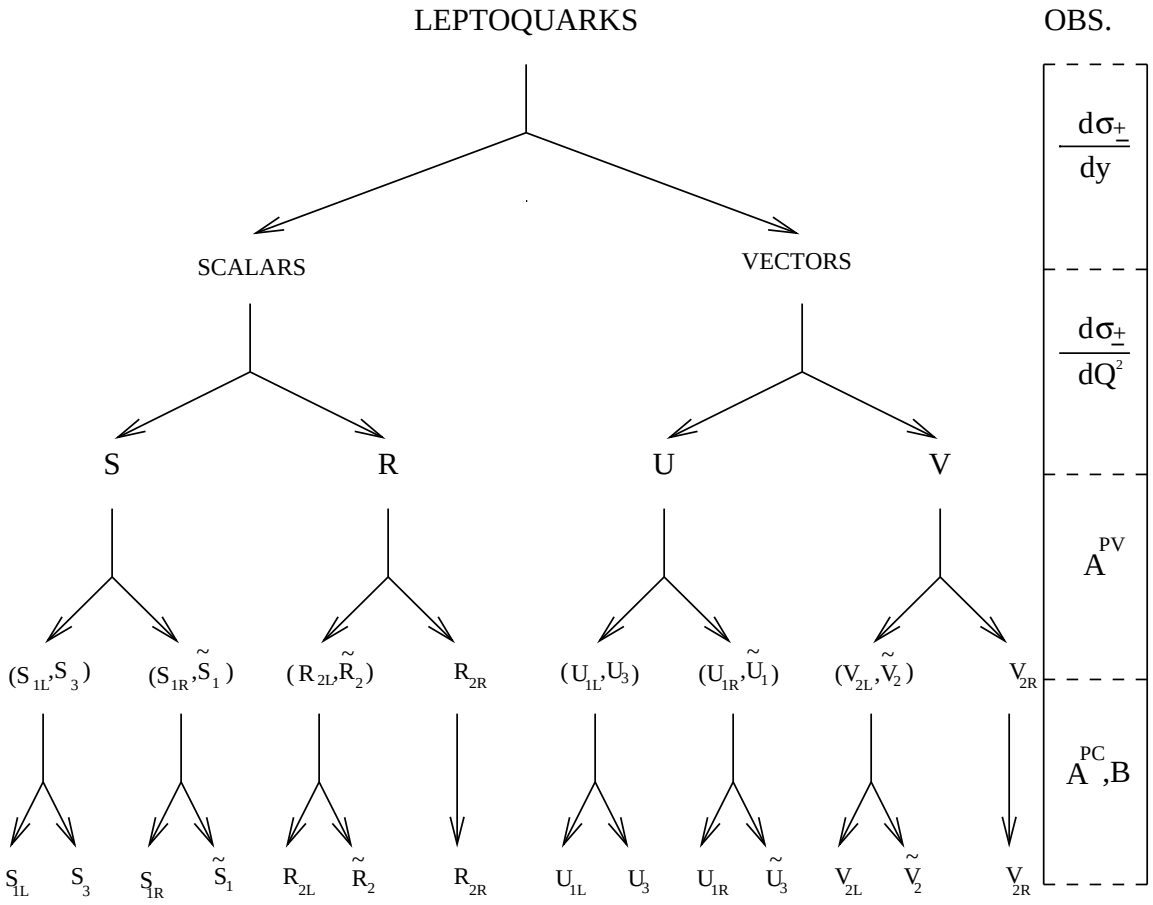

Figure 8: Schematic view for LQ identification.

Acknowledgements
We are indebted to A. De Roeck, J. Kalinowski, E. Reya, Y. Sirois, J. Soffer and W. Vogelsang for many interesting discussions and informations. JMV has the pleasure to thank the theoreticians of the "Institut für Physik" in Dortmund for helpful conversations and the excellent atmosphere, and finally, Susanne Laurent for her kindness and efficiency. The Alexander von Humboldt foundation is acknowledged for financial support.

A Appendix : Cross sections

We present in this appendix, the set of formulas necessary to calculate the double polarized cross sections, the spin and charge asymmetries involved in the present analysis.

A.1 Neutral Current

• *Process*

The single polarized cross sections are given in [4, 3]. Here we give the cross sections in the (s, t, u) notations.
The collisions between charged leptons and protons, in the neutral current channel, correspond to the process : $\vec{e}^{\pm}\,\vec{p} \longrightarrow e^{\pm}\,X$, whose cross section is given by :

$$\frac{d\sigma_t}{dxdQ^2}^{h_e h_p} = \sum_{h_q} \frac{d\hat{\sigma}_t}{d\hat{t}}^{h_e h_q} q_{h_p}^{h_q}(x, Q^2) \tag{A.1}$$

where h_e, h_p and h_q are the helicities of the charged lepton, proton and parton (quark or antiquark), respectively. The label $t = \pm$ corresponds to the electric charge of the colliding lepton. $\sum_q$ represent the sum over all the quark and antiquark flavors present inside the proton. The subprocess invariants $\hat{s}$, $\hat{t}$ and $\hat{u}$ are given by :

$$\hat{s} = x\,s \quad , \tag{A.2}$$

$$\hat{t} = -Q^2 \quad , \tag{A.3}$$

$$\hat{u} = x\,u = -x(1-y)\,s\,, \tag{A.4}$$

where the usual variable y is defined by $y = Q^2/xs$.

We denote by $q_{h_p}^{h_q}(x, Q^2)$ the parton distribution for the parton q inside a proton of helicity h_p, with momentum fraction x and helicity h_q, at the energy scale Q^2. These distributions are related to the parallel and anti-parallel distributions by : $q_+ = q_+^+ = q_-^-$, $q_- = q_+^- = q_-^+$, which are related to the usual unpolarized and polarized parton distributions by : $q = q_+ + q_-$ and $\Delta q = q_+ - q_-$.

• *Subprocesses*

Using the notations of [39], the cross section of the elementary subprocess $\vec{e}\,\vec{q} \to e\,q$ is given by :

$$\frac{d\hat{\sigma}_t}{d\hat{t}}^{h_e h_q} = \frac{\pi}{\hat{s}^2} \sum_{\alpha,\beta} T_{\alpha,\beta}^{h_e h_q}(e^t, q)\,, \tag{A.5}$$

where $T^{h_e h_q}_{\alpha,\beta}(e^t, q)$ is the squared matrix element for α and β boson exchange. q is a quark or an antiquark. The $T^{h_e h_q}_{\alpha,\beta}(e^t, q)$ for the SM (i.e. for $\alpha, \beta = \gamma,\ Z$) are given in [35]. The $T^{h_e h_q}_{\alpha,\beta}(e^t, q)$ for LQ production, exchange and interferences with γ or Z, are given below. We have omitted the hat symbol of the variables $\hat{s}$, $\hat{t}$ and $\hat{u}$, for clarity.

Subprocess $\quad e^- \, q \longrightarrow e^- \, q$:

$$T_{SS} = F^2 \frac{1}{64\pi^2} \frac{s^2}{s_S^2 + M_S^2 \Gamma_S^2} \left[\lambda_L^4 (1 - h_e)(1 - h_q) + \lambda_R^4 (1 + h_e)(1 + h_q) \right] \tag{A.6}$$

$$T_{VV} = F^2 \frac{1}{16\pi^2} \frac{u^2}{s_V^2 + M_V^2 \Gamma_V^2} \left[\lambda_L^4 (1 - h_e)(1 + h_q) + \lambda_R^4 (1 + h_e)(1 - h_q) \right] \tag{A.7}$$

$$T_{RR} = F^2 \frac{1}{64\pi^2} \frac{u^2}{u_R^2} \left[\lambda_L^4 (1 - h_e)(1 + h_q) + \lambda_R^4 (1 + h_e)(1 - h_q) \right] \tag{A.8}$$

$$T_{UU} = F^2 \frac{1}{16\pi^2} \frac{s^2}{u_U^2} \left[\lambda_L^4 (1 - h_e)(1 - h_q) + \lambda_R^4 (1 + h_e)(1 + h_q) \right] \tag{A.9}$$

$$T_{\gamma S} = -F \frac{\alpha Q_e Q_q}{4\pi t} \frac{s^2 s_S}{s_S^2 + M_S^2 \Gamma_S^2} \left[\lambda_L^2 (1 - h_e)(1 - h_q) + \lambda_R^2 (1 + h_e)(1 + h_q) \right] \tag{A.10}$$

$$T_{\gamma V} = -F \frac{\alpha Q_e Q_q}{2\pi t} \frac{u^2 s_V}{s_V^2 + M_V^2 \Gamma_V^2} \left[\lambda_L^2 (1 - h_e)(1 + h_q) + \lambda_R^2 (1 + h_e)(1 - h_q) \right] \tag{A.11}$$

$$T_{\gamma R} = F \frac{\alpha Q_e Q_q}{4\pi t} \frac{u^2}{u_R} \left[\lambda_L^2 (1 - h_e)(1 + h_q) + \lambda_R^2 (1 + h_e)(1 - h_q) \right] \tag{A.12}$$

$$T_{\gamma U} = F \frac{\alpha Q_e Q_q}{2\pi t} \frac{s^2}{u_U} \left[\lambda_L^2 (1 - h_e)(1 - h_q) + \lambda_R^2 (1 + h_e)(1 + h_q) \right] \tag{A.13}$$

$$T_{ZS} = -F \frac{\alpha_Z}{4\pi t_Z} \frac{s^2 s_S}{s_S^2 + M_S^2 \Gamma_S^2} [\lambda_L^2 C_{eL} C_{qL} (1 - h_e)(1 - h_q) + \lambda_R^2 C_{eR} C_{qR} (1 + h_e)(1 + h_q)] \tag{A.14}$$

$$T_{ZV} = -F \frac{\alpha_Z}{2\pi t_Z} \frac{u^2 s_V}{s_V^2 + M_V^2 \Gamma_V^2} [\lambda_L^2 C_{eL} C_{qR} (1 - h_e)(1 + h_q) + \lambda_R^2 C_{eR} C_{qL} (1 + h_e)(1 - h_q)] \tag{A.15}$$

$$T_{ZR} = F \frac{\alpha_Z}{4\pi t_Z} \frac{u^2}{u_R} [\lambda_L^2 C_{eL} C_{qR} (1 - h_e)(1 + h_q) + \lambda_R^2 C_{eR} C_{qL} (1 + h_e)(1 - h_q)] \tag{A.16}$$

$$T_{ZU} = F \frac{\alpha_Z}{2\pi t_Z} \frac{s^2}{u_U} [\lambda_L^2 C_{eL} C_{qL} (1 - h_e)(1 - h_q) + \lambda_R^2 C_{eR} C_{qR} (1 + h_e)(1 + h_q)] \tag{A.17}$$

where α is the electromagnetic coupling, $\alpha_Z = \alpha / \sin^2\theta_W \cos^2\theta_W$, $t_Z = t - M_Z^2$. C_{fL} and C_{fR} are the usual Left-handed and Right-handed couplings of the Z to the fermion f, given by $C_{fL} = I_3^f - e_f \sin^2\theta_W$, $C_{fR} = -e_f \sin^2\theta_W$ with $I_3^f = \pm 1/2$. For LQs, $s_{LQ} = s - M_{LQ}^2$ and $u_{LQ} = u - M_{LQ}^2$. The values for λ_L^2, λ_R^2 and the factor F are given in table 4 for scalar LQs and in table 5 for vector LQs. The factor F, given in term of combinations of kronecker products, is relevant only when we convolute subprocess cross sections with pdfs.

	S_{1L}	S_{1R}	$\tilde{S}_1$	S_3	R_{2L}	R_{2R}	$\tilde{R}_2$
λ_L^2	λ^2	0	0	λ^2	λ^2	0	λ^2
λ_R^2	0	λ^2	λ^2	0	0	λ^2	0
F	δ_{qu}	δ_{qu}	δ_{qd}	$\delta_{qu}+2\delta_{qd}$	δ_{qu}	$\delta_{qu}+\delta_{qd}$	δ_{qd}
$\lambda_{eq}.\lambda_{\nu q'}$	$-\lambda^2$	0	0	$+\lambda^2$	0	0	0

Table 4: Parameters for the BRW scalar LQ models.

	U_{1L}	U_{1R}	$\tilde{U}_1$	U_3	V_{2L}	V_{2R}	$\tilde{V}_2$
λ_L^2	λ^2	0	0	λ^2	λ^2	0	λ^2
λ_R^2	0	λ^2	λ^2	0	0	λ^2	0
F	δ_{qd}	δ_{qd}	δ_{qu}	$2\delta_{qu}+\delta_{qd}$	δ_{qd}	$\delta_{qu}+\delta_{qd}$	δ_{qu}
$\lambda_{eq}.\lambda_{\nu q'}$	$+\lambda^2$	0	0	$-\lambda^2$	0	0	0

Table 5: Parameters for the BRW vector LQ models.

Subprocess $e^+\,q \longrightarrow e^+\,q$:

The squared matrix elements $T_{\alpha,\beta}$ are obtained from the twelve preceding equations with the following changes : $h_e \longleftrightarrow -h_e$, $s \longleftrightarrow u$, $1/(s_{LQ}^2+M_{LQ}^2\Gamma_{LQ}^2) \longleftrightarrow 1/u_{LQ}^2$ and $s_{LQ}/(s_{LQ}^2+M_{LQ}^2\Gamma_{LQ}^2) \longleftrightarrow 1/u_{LQ}$.

Subprocess $e^\pm\,\bar{q} \longrightarrow e^\pm\,\bar{q}$:

The $T_{\alpha,\beta}$ are obtained from the ones for $e^\mp q$ scattering after the same transformations as above plus $h_q \longleftrightarrow -h_q$.

A.2 Charged Current

The process for CC is : $\vec{e}^{\pm}\,\vec{p} \longrightarrow \nu(\bar{\nu})\,X$
All the preceding formulas hold for CC processes with the following substitutions : $Q_{e,q} \to 0$, $C_L \to 1$, $C_R \to 0$, $\alpha_Z \to \alpha_W = \alpha_Z \cos^2\theta_W$, $M_Z \to M_W$ and $t_Z \to t_W$. Concerning factor F, we have $F = \delta_{qu}$ (δ_{qd}) for S_{1L} and S_3 (U_{1L} and U_3). Finally, for $W.LQ$ interferences one has now two different vertices in the diagram for LQ exchange (i.e. $e.q.LQ + \nu.q'.LQ$ vertices). Then the squared coupling $\lambda^2 \equiv \lambda_{eq}^2$ appearing in NC, is changed to the product $\lambda_{eq}\lambda_{\nu q'}$. From eqs.1,2 or from table 1 of [3] we have $\lambda_{eq} = \pm\lambda_{\nu q'} = \pm\lambda$. The product $\lambda_{eq}\lambda_{\nu q'}$ is given in the last row of tables 4 and 5.

References

[1] P. Fayet, Phys. Lett. **B69**, 489 (1977); G. Farrar and P. Fayet, Phys. Lett. **B76**, 575 (1978).

[2] Report of the R_{parity} group of the CNRS-GDR SUSY Working group, hep-ph/9810232.

[3] J. Kalinowski et al., Z. Phys. **C74**, 595 (1997).

[4] W. Buchmüller, R. Rückl and D. Wyler, Phys. Lett. **B191**, 442 (1987).

[5] S. Davidson et al., Z. Phys. **C61**, 613 (1994).

[6] M. Leurer, Phys. Rev. **D50**, 536 (1994), Phys. Rev. **D49**, 333 (1994).

[7] J. Hewett and T. Rizzo, Phys. Rev. **D56**, 5709 (1997), Phys. Rev. **D58**, 055005 (1998); A. Deandrea, Phys. Lett. **B409**, 277 (1997).

[8] Leptoquark Limit Combination Working Group, hep-ex/9810015.

[9] J. Blümlein et al., Z. Phys. **C76**, 137 (1997); hep-ph/9811271; and references therein.

[10] D0 Collaboration, ICHEP98, Vancouver, Canada;
http://www-d0.fnal.gov/public/new/new_public.html#conferences.

[11] S.C. Bennett and C.E. Wieman, Phys. Rev. Lett. **82**, 2484 (1999).

[12] Particle Data Group, Eur. Phys. J. **C3**, 1 (1998).

[13] R. Casalbuoni et al., Phys. Lett. **B460**, 135 (1999).

[14] V. Barger et al., Phys. Rev. **D57**, 3833 (1998).

[15] K. Ackerstoff et al., OPAL Collaboration, Eur. Phys. J. **C2**, 441 (1998).

[16] H1 Collaboration, hep-ex/9907002 submitted to Eur. Phys. J. C; T. Matsushita, E. Perez and R. Rückl, in the proceedings of [23]; J. Phys. **G25**, 1418 (1999).

[17] J.-M. Virey, E. Tuğcu and P. Taxil, in Proceedings of the 7th Workshop on "Deep Inelastic Scattering and QCD", DESY-Zeuthen, Germany, April 1999, Nucl. Phys. B (Proc. Suppl.)**79**, 617 (1999); P. Taxil et al., in Proceedings of [24].

[18] M. Botje and G. Wolf, DESY 98-140, hep-ex/9809027.

[19] Y. Sirois, in Proceedings of the 7th Workshop on "Deep Inelastic Scattering and QCD", DESY-Zeuthen, Germany, April 1999.

[20] RHIC Spin Collaboration, Letter of intent, April 1991; G. Bunce et al., *Polarized protons at RHIC*, Particle World **3** (1992) 1; Proceedings of the RSC annual meeting, Marseille, September 1996, preprint CPT-96/P.3400; Proceedings of RIKEN-BNL Research Center Workshop, "RHIC Spin Physics", April 1998, preprint BNL-65615.

[21] 1996 HERA Workshop, "Future Physics at HERA", Eds. G. Ingelman, A. De Roeck and R. Klanner.

[22] "1997 Workshop on Physics with Polarized Protons at HERA", Eds. A. De Roeck and T. Gehrmann; desy-proceedings-1998-01.

[23] "3^{rd} UK Phenomenology Workshop on HERA Physics", Durham, UK, September 1998, Eds. R. Devenish et al.; J. Phys. **G25**, 1269 (1999).

[24] "Workshop on Polarized Protons at High Energies - Accelerator Challenges and Physics Opportunities", DESY-Hamburg, Germany, May 1999, Eds. D. Barber et al.

[25] M. Glück, E. Reya and A. Vogt, Z. Phys. **C67**, 433 (1995).

[26] T. Plehn, H. Spiesberger, M. Spira and P.M. Zerwas, Z. Phys. **C74**, 611 (1997)

[27] Z. Kunszt and W.J. Stirling, Z. Phys. **C75**, 453 (1997)

[28] M.A. Doncheski and J.L. Hewett, Z. Phys. **C56**, 209 (1992).

[29] G. Altarelli, Nucl. Phys. Proc. Suppl. **62**, 3 (1998) and references therein.

[30] R.D. Ball et al., p.777 of [21]; A. De Roeck et al., Eur. Phys. J. **C6**, 121 (1999).

[31] A. De Roeck, private communication.

[32] M. Glück, E. Reya, M. Stratman and W. Vogelsang., Phys. Rev. **D53**, 4775 (1996).

[33] C. Bourrely et al., Phys. Rep. **177**, 319 (1989); J. Soffer and J.-M. Virey Nucl. Phys. **B509**, 297 (1998).

[34] B. Lampe and E. Reya, hep-ph/9810270, to appear in Physics Reports.

[35] J.-M. Virey, Eur. Phys. J. **C8**, 283 (1999).

[36] K.S. Babu et al., Phys. Lett. **B408**, 261 (1997).

[37] Y. Sirois, private communication.

[38] P. Taxil and J.-M. Virey, Phys. Lett. **B441**, 376 (1998) and references therein.

[39] C. Bourrely, J. Ph. Guillet and J. Soffer Nucl. Phys. **B361**, 72 (1991).

Chapitre 2 : Détermination des paramètres cosmologiques et propriétés de l'énergie noire

Fin 2001, j'ai entrepris avec Pierre Taxil une reconversion thématique. La première année je me suis intéressé à la physique des astroparticules, et en particulier à la physique des neutrinos ou plutôt des télescopes à neutrinos (ANTARES, AMANDA, ICECUBE), ainsi qu'à la problématique des rayons cosmiques d'extrêmement haute énergie. En parallèle, l'ancien groupe ALEPH (LEP) du CPPM étudiait de plus en plus la physique et la cosmologie associés aux supernovae de type Ia (SNIa) considérées comme chandelles standard. Il est apparu que les perspectives en cosmologie étaient très alléchantes, et c'est ainsi qu'à partir de 2002/2003 je me suis concentré sur la cosmologie en liaison avec des expérimentateurs.

Le moteur de mes recherches est l'étude des propriétés de l'énergie noire, la composante principale de l'Univers qui est à la source de l'accélération récente de l'expansion et qui n'est plus vraiment remise en cause depuis 1998 grâce aux analyses des SNIa.

Ces études étant à la frontière de nombreux domaines différents de la physique fondamentale (voir l'introduction), je vais essayer de donner une vision claire de la problématique en détaillant dans l'introduction de ce chapitre les divers éléments essentiels. Les articles, relativement techniques, suivent.

Dans cette introduction, nous rappellerons rapidement les bases théoriques du modèle standard de la cosmologie ce qui nous permettra d'introduire les paramètres cosmologiques. Ensuite nous présenterons les résultats expérimentaux les plus marquants qui sont liés aux études qui suivront. Nous détaillerons alors les différents modèles d'énergie noire qui sont un des ponts entre cosmologie et physique (théorique) des particules. Enfin, une analyse critique de l'extraction des paramètres cosmologiques sera donnée. Nous discuterons, en particulier, le problème de la dégénérescence géométrique et des très fortes corrélations qui existent entre les divers paramètres.

La seconde section est constituée de 4 articles qui traitent de l'extraction des paramètres cosmologiques à partir des SNIa. Les 3 premiers s'intéressent aux biais de certains paramètres qui peuvent amener à une interprétation erronée des résultats. Ces biais trouvent leur origine, du point de vue théorique, dans les fortes dégénérescences entre paramètres, et du

point de vue expérimental, dans le grand nombre d'hypothèses qu'il faut faire au niveau de l'analyse pour extraire les paramètres. Nous avons donc entrepris d'étudier les effets de ces différentes hypothèses d'analyse. Dans le quatrième article, nous négligeons les problèmes de biais et nous nous concentrons sur l'optimisation des projets d'observation de SNIa. Plus précisément, nous essayons de répondre à la question suivante : "Vaut-il mieux un sondage profond ou un sondage large pour extraire des informations sur la dynamique de l'énergie noire ?" En d'autres termes, nous tentons d'optimiser la profondeur en redshift ainsi que le nombre total de SNIa à découvrir, quantités caractérisant le sondage.

Afin d'éviter le problème des biais, et afin de fournir les meilleures contraintes possibles, il apparaît indispensable de réaliser des analyses de données combinant plusieurs sondes cosmologiques. Cet exercice est relativement difficile car il faut analyser les diverses sondes dans un même cadre théorique et avec les même hypothèses, ce qui techniquement nécessite la fusion et la compréhension de plusieurs codes numériques en général assez complexes. La troisième partie du chapitre est dévouée à ce type d'analyses dites "combinées". Le premier travail a été réalisé en 2005 en collaboration avec des équipes du CPPM et de Saclay. Nous avons combiné les données les plus récentes (à cette époque) venant de l'étude des SNIa et du rayonnement de fond cosmologique (CMB) pour contraindre l'équation d'état (dynamique) de l'énergie noire. Nous avons réalisé également un travail de prospective sur les contraintes que l'on pourrait obtenir sur l'équation d'état en combinant les SNIa et le CMB avec les mesures de cisaillement gravitationnel (WL). Un second travail a été réalisé, fin 2006, en collaboration avec une équipe chinoise de l'institut des hautes énergies de Pékin. Nous avons combiné les données les plus récentes des SNIa, du CMB mais aussi des grands sondages de galaxies (spectre de puissance des galaxies mesuré par SDSS). Pour la première fois cette analyse tentait de contraindre simultanément l'équation d'état dynamique de l'énergie noire et la courbure de l'Univers.

La dernière partie présente un nouveau test cosmologique à partir des propriétés cinématiques des galaxies. L'idée originale, essentiellement due à Christian Marinoni, est d'utiliser les vitesses particulières des galaxies afin de construire des "règles" standard ainsi que des "chandelles" standard. Le premier article, relativement théorique, présente l'idée de base. Le second applique cette idée aux mesures faites par la collaboration VVDS qui a réalisé un sondage profond de galaxies avec une spectroscopie très précise.

2.1 Introduction

2.1.1 Le Modèle Cosmologique Standard

Les équations de base

Le modèle cosmologique standard repose sur la théorie de la relativité générale et sur le principe cosmologique. Ce dernier stipule que l'on peut considérer l'univers comme homogène et isotrope aux grandes échelles. L'origine de cette hypothèse, du point de vue

théorique, remonte à Copernic et au refus de supposer l'existence d'une région (et d'une direction) particulière dans l'univers, et a été rendu populaire par Einstein au début du XX^{eme} siècle. Du point de vue observationnel, il est confirmé par l'apparente homogénéité constatée à des échelles supérieures à $100\,Mpc$.

Si on considère un univers maximalement symétrique on est alors amené à utiliser la métrique de Friedmann-Robertson-Walker (FRW) donnée par :

$$ds^2 = -dt^2 + a^2(t)\left[\frac{d^2r}{1-kr^2} + r^2(d\theta^2 + \sin^2\theta d\phi^2)\right] \tag{2.8}$$

où k, l'indice de courbure, est tel que $k = 1, 0, -1$ correspondant à un univers ouvert, plat et fermé, respectivement. $a(t)$ est le facteur d'échelle, qui peut être considéré comme "étalon de longueur", et dont la valeur aujourd'hui a_0 est normalisée à 1 pour un univers plat, ou $a_0^2 = k/(H_0^2|\Omega_T - 1|)$ pour une courbure non-nulle (H_0 et Ω_T sont des paramètres cosmologiques mesurables dont les définitions suivent). Les variations du facteur d'échelle sont mesurables grâce à la mesure du redshift z qui est une mesure relative de la dilatation de l'espace entre deux instants, et qui est associé, pour un phénomène lumineux, à la variation de la longueur d'onde du photon. On a ainsi la relation :

$$\frac{a(t)}{a_0} = \frac{\lambda(t)}{\lambda_0} \equiv \frac{1}{1+z} \tag{2.9}$$

Le paramètre de Hubble $H(t)$ décrit l'expansion et est définit par :

$$H(t) = \frac{\dot{a}}{a} \tag{2.10}$$

Au temps présent on définit $H_0 = 100\,h\,kms^{-1}Mpc^{-1}$ avec la contrainte observationnelle $0.4 < h < 0.9$.

La dérivée seconde du facteur d'échelle est relié au paramètre de décélération $q(t)$:

$$q(t) = -\frac{\ddot{a}a}{\dot{a}^2} \tag{2.11}$$

La valeur de ce paramètre aujourd'hui, q_0, est négative ce qui implique la présence d'une énergie noire lorsque l'on tient compte de la dynamique tirée des équations d'Einstein. Avant de rentrer dans ces détails, continuons la description de la cinématique en introduisant les diverses notions de distances spécifiques à la cosmologie.

La distance comobile est donnée par :

$$r(z) = a_0\mathcal{S}_k\left(\frac{1}{a_0}\int_0^z \frac{1}{H(z')}dz'\right) \tag{2.12}$$

où $\mathcal{S}_k(x) = \sinh(x),\ x,\ \sin(x)$ pour $k = 1, 0, -1$, respectivement.

Cette distance va servir de base à la définition d'autres distances en cosmologie dont les interprétations sont beaucoup plus intuitives. La mesure de ces distances est au coeur de la détermination des paramètres cosmologiques détaillée dans ce chapitre.

La distance lumineuse $d_L(z)$ relie le flux L émis par un objet de redshift z au flux observé par unité de surface aujourd'hui Φ :

$$\Phi \equiv \frac{L}{4\pi d_L^2} \tag{2.13}$$

On peut alors montrer que :

$$d_L(z) = r(z)(1+z) \tag{2.14}$$

La distance angulaire $d_A(z)$ relie la distance propre d'un objet prise perpendiculairement à la direction radiale (de propagation des photons) $\delta l_\perp$, à l'angle sous-tendu $\delta\theta$:

$$\delta l_\perp \equiv d_A\, \delta\theta \tag{2.15}$$

De cette définition on obtient :

$$d_A(z) = \frac{r(z)}{(1+z)} = d_L(z)/(1+z)^2 \tag{2.16}$$

A présent, nous allons tenir compte de la dynamique décrite par les équations d'Einstein[2]:

$$R_{\mu\nu} - \frac{R}{2} g_{\mu\nu} = 8\pi G\, T_{\mu\nu} \tag{2.17}$$

Ces équations relient la dynamique de la métrique (et donc du facteur d'échelle $a(t)$) via le tenseur de Ricci $R_{\mu\nu}$ et le scalaire de Ricci R, au contenu énergétique de l'univers (représenté par le tenseur énergie-impulsion $T_{\mu\nu}$). En utilisant la métrique FRW et en supposant que les éléments constitutifs de l'univers peuvent être décris par un fluide parfait, nous obtenons les équations de Friedmann :

$$H^2 = \left(\frac{\dot{a}}{a}\right)^2 = \frac{8\pi G}{3} \sum_i \rho_i - \frac{k}{a^2} \tag{2.18}$$

et

$$\frac{\ddot{a}}{a} = \frac{4\pi G}{3} \sum_i (\rho_i + 3p_i) \tag{2.19}$$

où ρ_i et p_i sont les densité et pression du fluide de nature i.

La première équation relie le facteur d'échelle et la courbure aux densités des divers éléments de l'univers. On introduit alors la densité critique $\rho_c = 8\pi G/3H^2$ qui permet de définir les paramètres cosmologiques $\Omega_i = \rho_i/\rho_c$ qui sont des rapports de densités. La première équation de Friedmann se simplifie alors grandement :

$$\Omega_T = \sum_i \Omega_i = 1 - \Omega_k, \tag{2.20}$$

ce qui permet de définir le paramètre $\Omega_k = -k/(a^2H^2)$ pour représenter le terme de courbure.

[2]L'éventuelle présence d'une constante cosmologique sera discutée dans la prochaine section.

En général, on considère 3 composantes distinctes, la matière ($i \equiv M$, qui peut se décomposer en baryons et matière noire), la radiation ($i \equiv R$, qui peut se décomposer en photon et neutrino, *i.e.* les particules relativistes), et l'énergie noire ($i \equiv X$). Ces trois composantes ont des évolutions temporelles radicalement différentes. L'évolution d'un fluide parfait dans un univers en expansion est soumise à l'équation suivante :

$$\dot{\rho}_i + 3H(\rho_i + p_i) = 0 \tag{2.21}$$

qui donne la relation intégrale suivante :

$$\frac{\rho_i(z)}{\rho_i(0)} \;=\; \exp\left[3\int_0^z \,(1+w_i(z'))\;d\;\ln(1+z')\right] \tag{2.22}$$

où $w_i = p_i/\rho_i$ est l'équation d'état du fluide i. On peut alors définir le paramètre de Hubble en fonction des valeurs actuelles des paramètres Ω_i et de l'équation d'état de l'énergie noire $w_X(z)$:

$$E^2(z) \;=\; \left(\frac{H(z)}{H_0}\right)^2 \;=\; (1+z)^3\,\Omega_m + \frac{\rho_X(z)}{\rho_X(0)}\,\Omega_X + (1+z)^2\,\Omega_k \tag{2.23}$$

On a utilisé le fait que la matière est telle que $w_M = 0$ (impliquant une évolution de la densité en a^{-3}), et que la radiation correspond à $w_R = 1/3$ ($\rho_R \simeq a^{-4}$). Ceci implique que la radiation a dominé la dynamique de l'univers avant celle de la matière. L'équation d'état de l'énergie noire est inconnue et c'est la quantité physique qui va fortement nous occuper par la suite. Remarquons seulement que si l'énergie noire est associée à une constante cosmologique alors $w_X = w_\Lambda = -1$, la densité ρ_Λ est une constante et il apparaît alors que le destin de l'univers est controlé par cette composante inconnue. Cependant, avant de détailler les divers modèles d'énergie noire, nous allons présenter succinctement les contraintes observationnelles existantes sur ces paramètres cosmologiques.

Notons que le modèle présenté est parfaitement homogène et isotrope, il ne permet donc qu'une description simplifiée de l'Univers, on parle de description du "fond". Si on veut tenter d'expliquer l'origine des différentes structures peuplant l'univers, il faut aller plus loin dans notre description. Les modèles de formation des structures nécessitent de perturber les équations d'Einstein afin d'étudier la croissance des fluctuations de densité. Nous verrons que de nombreuses sondes cosmiques sont sensibles à cette physique, et que l'obtention d'informations fiables sur les propriétés de l'énergie noire nécessitent la prise en considération de ces sondes. Cependant, l'ensemble des travaux présentés dans cette habilitation ne s'intéressent principalement qu'à des contraintes venant du fond. Nous ne détaillerons donc pas cette physique de la croissance des perturbations. Néanmoins, lors de l'étude des analyses combinées nous inclurons par exemple le CMB, ou l'analyse du spectre de puissance des galaxies ou encore les effets de cisaillement gravitationnel, qui impliquent cette physique de la croissance des fluctuations primordiales. Cependant l'introduction à cette physique reste assez lourde et je préfère laisser le lecteur intéressé consulter les références suivantes [37, 38, 39] plutôt que de surcharger ce manuscrit. Nous allons nous

concentrer sur les paramètres cosmologiques suivants :
Pour le fond :

- les densités Ω_i pour les baryons ($i = b$), la matière ($i = M$, incluant baryons et matière noire froide), la radiation ($i = R$), l'énergie noire ($i = X$) et une eventuelle courbure spatiale pour l'univers ($i = k$);
- les paramètres décrivant une équation d'état dynamique pour l'énergie noire, *e.g.* w_0 et w_a (définis dans la section suivante);
- la constante de Hubble, *e.g.* H_0 ou h;
- un paramètre de normalisation du diagramme de hubble, *e.g.* M_S pour les SNIa (qui inclut H_0 mais aussi la magnitude absolue des SNIa, relativement mal connue) .

Pour décrire les inhomogénéités et en particulier les physiques du CMB, du WL et de la formation des structures on introduit au moins les paramètres suivants :

- l'indice spectral du spectre de puissance primordial n_s;
- un paramètre de normalisation du spectre de puissance, *e.g.* σ_8 ou A selon les définitions utilisées;
- la profondeur optique de réionisation τ.

Les contraintes observationnelles

Nous discutons à présent les mesures qui ont eu le plus d'impact récemment et qui sont en lien direct avec les études des propriétés de l'énergie noire.

L'étude des SNIa donne des contraintes fortes sur le phénomène d'accélération. Les SNIa sont des objets rares (≈ 1/siècle/galaxie) mais très brillants. On les considère comme des chandelles standard car il apparaît que leurs luminosités (intrinsèques) sont comparables. Théoriquement, on le comprend en associant aux SNIa un mécanisme d'explosion qui change peu d'une SN à l'autre. Plus précisemment, on suppose qu'une SNIa résulte de l'implosion d'une naine blanche qui vient juste d'atteindre la masse de Chandrasekhar ($\approx 1.4 M_\odot$). On imagine un système double où une étoile, devenue une naine blanche, accrète la matière de son étoile compagnon jusqu'à l'instant critique du début de la supernovae.

Observationnellement, on distingue les SNIa des autres types de SN grâce à leurs propriétés photométriques et spectrales. En effet, la courbe de lumière (évolution de la luminosité dans le temps) des SNIa est caractérisée par une croissance initiale relativement lente, et le spectre présente une raie d'absorption pour le Silicium à $\approx 600\, nm$. Concrètement, les SNIa peuvent avoir des variations en luminosité très importantes, mais il existe plusieurs procédures expérimentales dites de "standardisation" qui permettent de réduire fortement la dispersion de l'échantillon (au maximum de 15% aujourd'hui).

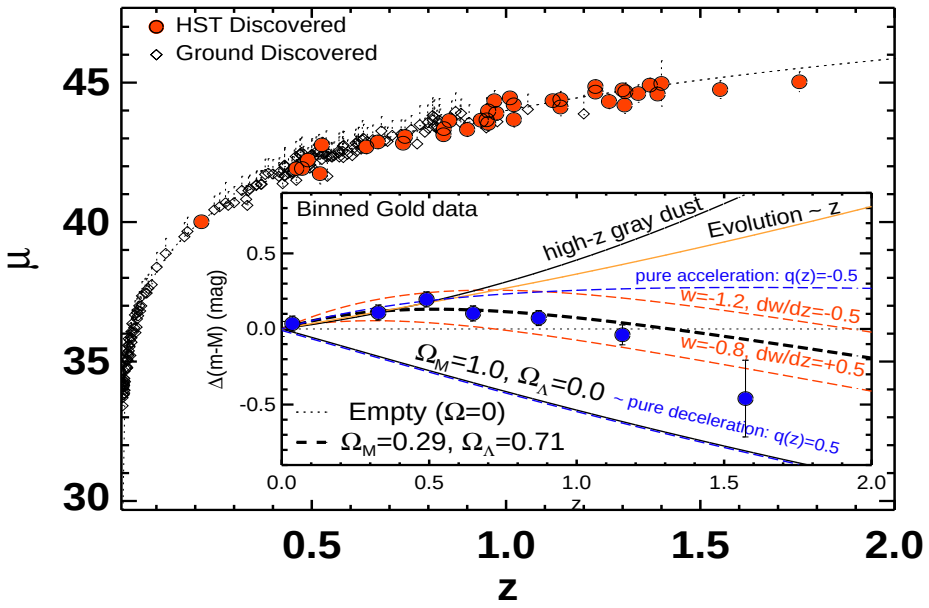

Figure 2.6: Diagramme de Hubble à partir des SNIa les plus récentes [53]. La courbe en pointillée correspond au best-fit en supposant un univers plat caractérisé par $\Omega_M = 0.27$. La figure insérée correspond au diagramme de Hubble "résiduel" obtenu en soustrayant aux données et à différents modèles théoriques, un modèle d'univers vide [53].

Une fois ces étapes franchies, on peut alors construire un diagramme de Hubble qui relie la magnitude effective de la SNIa à son redshift. La magnitude apparente effective, m, est reliée à la magnitude absolue des SNIa, M, et à la distance lumineuse d_L par :

$$\mu = m - M = 5\log_{10}\left(\frac{d_L}{\text{Mpc}}\right) + 25 \tag{2.24}$$

où les facteurs numériques viennent des conventions choisies pour définir m et M en astronomie. Techniquement, pour ne pas trop détériorer la détermination des paramètres cosmologiques, on définit un paramètre de normalisation (ou de nuisance) M_S qui englobe les incertitudes sur M et sur H_0 :

$$m(z) = 5\log_{10}(D_L) + M - 5\log_{10}(H_0/c) + 25 = M_S + 5\log_{10}(D_L) \tag{2.25}$$

où $D_L(z) \equiv (H_0/c)\ d_L(z)$ est la distance lumineuse indépendante de H_0. La figure 2.6 donne le diagramme de Hubble avec les données les plus récentes. De ce diagramme on extrait des contraintes sur les paramètres cosmologiques.

Cependant, dès que l'on veut extraire des contraintes sur la courbure et/ou sur les propriétés de l'énergie noire on est confronté au problème des dégénérescences entre paramètres ce qui nous oblige à contraindre à la main certains paramètres (*i.e.* utilisation de "priors") ou à réaliser des analyses combinées.

Une sonde cosmologique fréquemment utilisée est le CMB. La mesure des anisotropies du fond diffus, réalisées par COBE en 1992 puis par WMAP depuis 2003, et bientôt par Planck, permet de contraindre un grand nombre de paramètres associés à des physiques très différentes (expansion/géométrie, inflation, réionisation, normalisation du spectre de puissance des grandes structures ...). En ce qui concerne l'expansion, le CMB fournit d'excellentes contraintes sur la courbure de l'Univers (paramètre Ω_T), mais n'est sensible qu'à une moyenne de l'équation d'état de l'énergie noire donnée par [40] :

$$\bar{w} \approx \int dz\, \Omega_X(z) w_X(z) / \int dz\, \Omega_X(z) \tag{2.26}$$

Afin de contraindre $w_X(z)$ il est également fondamental d'avoir de très bonnes informations sur Ω_M. Les sondages de galaxies sont alors fréquemment utilisés. Plusieurs types d'observables de nature très différente peuvent être définis comme les comptages d'amas, la mesure du spectre de puissance des galaxies, les effets de cisaillement gravitationnels (WL) ou encore la mesure des oscillations baryoniques acoustiques (BAO). Chaque observable a ses avantages et inconvénients, et en particulier, est plus ou moins sensible aux modèles de formation des structures et d'énergie noire. Nous ne rappellerons pas ici les caractéristiques et propriétés de chaque type de mesure qui sont bien détaillée dans les revues suivantes [41, 42, 43].

En combinant ces différentes sondes cosmologiques on obtient des contraintes plus ou moins précises. La figure 2.7 donne les contraintes sur Ω_X (et la courbure $\Omega_T = \Omega_M + \Omega_X$) lorsque l'on suppose que l'énergie noire est une constante cosmologique (*i.e.* $X = \Lambda$).

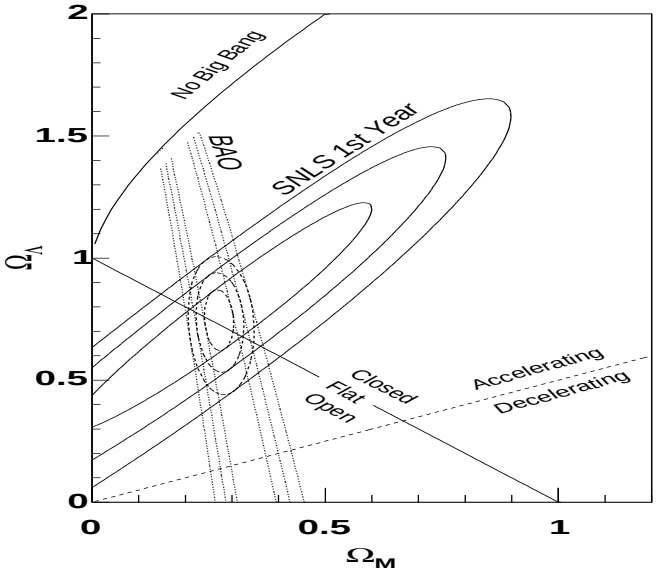

Figure 2.7: Contours dans le plan Ω_M-Ω_Λ à partir des observations de SNIa et des BAO. Les contraintes sont données pour chaque sonde séparément ou en les combinant, pour des degés de confiance de 68.3%, 95.5% et 99.7% [44].

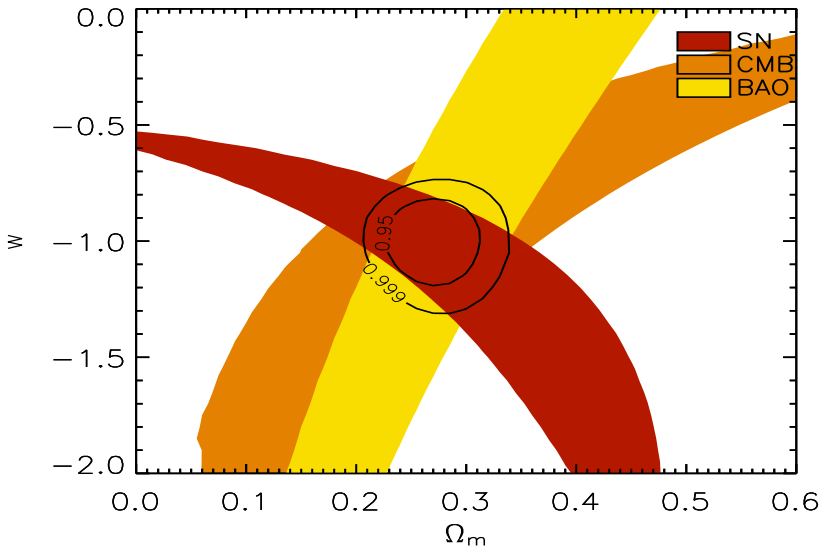

Figure 2.8: Contours dans le plan w-Ω_M à partir des observations de SNIa[45], du CMB[49] et des BAO[50]. Les contraintes sont données pour chaque sonde séparément (labels portés sur la figure, contours à 95%CL) ou en les combinant (traits pleins, contours à 95%CL et 99%CL), tirées de [45].

Si on suppose maintenant que l'énergie noire n'est pas forcément une constante cosmologique mais un fluide avec une équation d'état constante (*i.e.* $w_X(z) = w = cste$), on obtient alors les contraintes données sur la figure 2.8.

Enfin, si on veut avoir une description plus générale des modèles d'énergie noire, on doit considèrer une équation d'état dynamique. A cette fin, la paramétrisation [46, 47] $w_X(z) = w_0 + w_a z/(1+z)$ est souvent utilisée. On peut alors obtenir des contraintes dans le plan (w_0,w_a), ce qui est illustré par la figure 2.9 qui donne les contraintes pour chaque sonde séparément ou en les combinant[45]. Bien qu'il ait été supposé que l'univers était plat, on constate que les contraintes sur l'équation d'état de l'énergie noire sont encore assez faibles, ce qui nous demande d'avoir une grande ouverture d'esprit lorsque l'on va considérer les divers modèles d'énergie noire.

A partir des 3 figures précédentes on réalise que chaque sonde fournit des contraintes assez "faibles" mais qui indiquent des directions de dégénérescence différentes. Raison pour laquelle les analyses combinées sont aussi puissantes en fournissant des contraintes relativement fortes.

Si maintenant on s'intéresse aux résultats de ces contraintes on s'apercoit qu'elles tendent vers un modèle particulier, appelé "modèle de concordance", ou ΛCDM, qui est caractérisé par un univers plat avec constante cosmologique tel que $\Omega_M \approx 0.3$ et $\Omega_X \approx 0.7$. Une étude plus attentive, en considérant une énergie noire avec équation d'état dynamique, montre que le modèle ΛCDM est au bord des contours à 1σ. Si on essaye alors de reconstruire l'évolution en redshift de $w_X(z)$ on obtient le résultat surprenant que $w_X(z)$

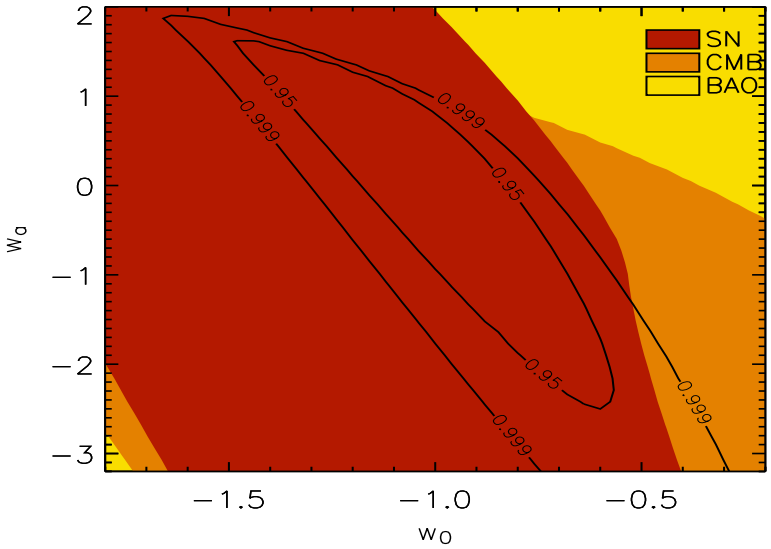

Figure 2.9: Contraintes dans le plan (w_0,w_a) à partir des données les plus récentes de SNIa[45], du CMB[49] et des BAO[50], en supposant que l'univers est plat. Les contraintes sont données pour chaque sonde séparément (labels portés sur la figure, contours à 95%CL) ou en les combinant (traits pleins, contours à 95%CL et 99%CL), tirées de [45].

franchit la barrière problématique $w = -1$ [52] comme montré sur la figure 2.10.

2.1.2 Modèles d'énergie noire

La nouvelle composante "énergie noire" doit rendre compte de l'accélération de l'expansion (pour des revues consulter [42, 54, 55, 56]). Si on suppose qu'un seul fluide est présent, il doit être tel que $w_X < -1/3$ (si on néglige la radiation mais en tenant compte de la matière cette relation devient $w_X < -\Omega_T/(3\Omega_X)$). On constate donc que l'énergie noire doit avoir une équation d'état négative, ce qui correspond à un fluide relativement exotique.

Le candidat le plus simple est une constante cosmologique ou l'énergie du vide, selon le point de vue adopté. Le modèle de concordance, en accord avec les données, correspond à cette hypothèse. Cependant, il souffre de deux difficultés : le problème de la constante cosmologique, fondamental pour les physiciens des particules mais négligeable ou infondé pour les astronomes, ainsi que le problème de coïncidence.

Une constante cosmologique est un terme supplémentaire dans les équations d'Einstein qui deviennent :

$$R_{\mu\nu} - \frac{R}{2} g_{\mu\nu} - \Lambda g_{\mu\nu} = 8\pi G\, T_{\mu\nu} \tag{2.27}$$

Historiquement, ce terme a été introduit par Einstein pour construire un univers statique. Supprimée par la suite grâce à la découverte de l'expansion et de la notion d'un univers dynamique, elle fut réintroduite récemment pour expliquer l'apparente platitude de l'univers et l'accélération récente. Dans les équations de Friedmann on voit apparaître alors le

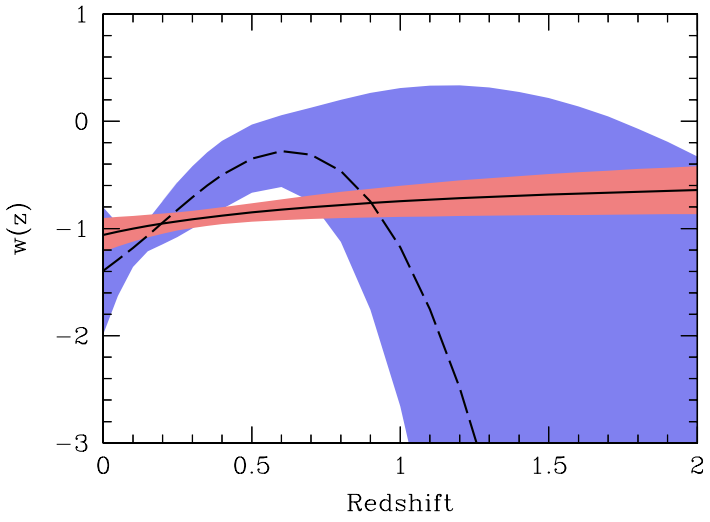

Figure 2.10: Evolution en redshift de $w_X(z)$ à partir des observations les plus récentes de SNIa[53], du CMB[49] et des BAO[50], tirée de [53]. La courbe pleine est associée à la paramétrisation 2.35, et la courbe en pointillée à un developpement de Taylor du quatrième ordre.

terme $\Lambda/3$ dans le membre de droite, nous permettant de définir le paramètre Ω_Λ. Les contraintes observationnelles actuelles indiquent $\Omega_\Lambda \approx 0.7$ ce qui se traduit en terme de densité d'énergie par $\rho_\Lambda^{1/4} \approx 10^{-3}\, eV$.

Pour les astronomes et les spécialistes de la relativité générale ce terme est de nature géométrique et il n'est pas nécessaire de lui trouver une origine plus fondamentale. Cependant, pour les physiciens des particules et les experts de théorie quantique des champs, il apparaît que l'état fondamental de la théorie, qu'on appelle aussi le vide, est un invariant de Lorentz. Sa description mathématique est équivalente à la présence d'un fluide parfait dont l'équation d'état vaut $w_{vide} = -1$. On obtient alors une correspondance entre cette énergie du vide et la constante cosmologique ($\Lambda = 8\pi G \rho_{vide}$). Pour la cosmologie, la différence est surtout technique et il importe peu de savoir si on ajoute dans les équations d'Einstein un terme à gauche (partie géométrique) ou à droite (partie constitutive). Du point de vue physique, la différence est fondamentale, mais la distinction est elle possible? Aujourd'hui il est difficle de répondre à cette question ...

Le problème de la constante cosmologique [56, 57, 58] apparaît lorsqu'on essaye d'estimer la densité d'énergie du vide dans le cadre de la théorie quantique des champs. En fait, le vide souffre des mêmes problèmes que les particules scalaires à savoir que les corrections radiatives sont quadratiquement divergentes. On a discuté ce point dans la section 1.1 à travers le problème dit hiérarchique où l'on a vu que $m_H \approx \Lambda_{cut}^2$ avec Λ_{cut} le cut-off de notre théorie. Pour la densité d'énergie du vide on obtient $\rho_{vide} \approx \Lambda_{cut}^4$, on parle aussi de catastrophe ultraviolette. Vu les échelles impliquées en physique des particules ($M_{EW} \approx 100\, GeV$, $M_{SUSY} \geq 1\, TeV$ ou $M_P \approx 10^{19}\, GeV$) on constate que les estimations de $\rho_{vide}^{1/4}$ sont entre 10^{15} et 10^{30} trop élevées par rapport à $\rho_\Lambda^{1/4}$. Moralité, de grands progrès

restent à faire pour calculer la densité d'énergie du vide en théorie quantique des champs. Peut-être la solution sortira-t-elle des théories quantique de la gravitation, mais nous n'en sommes pas encore là !

Nous adopterons donc le point de vue de l'astronome par la suite en faisant abstraction de ce problème et en parlant de constante cosmologique et non d'énergie du vide.

Venons en à présent au problème de coïncidence qui est à l'origine d'un grand nombre de modèles d'énergie noire : on constate que les densités de matière (noire) et de constante cosmologique sont du même ordre de grandeur aujourd'hui ($\rho_\Lambda \approx 0.7\rho_c$ et $\rho_M \approx 0.3\rho_c$) alors que les évolutions temporelles de ces deux composantes sont très différentes ($\rho_\Lambda = cste$ et $\rho_M \approx a^{-3}$). C'est donc une coïncidence très surprenante qui a motivé la construction d'un grand nombre de modèles d'énergie noire tentant de donner une origine dynamique à ce phénomène.

Les modèles d'énergie noire se décomposent en deux grandes classes. Soit on considère que nos hypothèses de travail sont justes, et il est alors indispensable de rajouter une nouvelle composante dans l'univers, l'énergie noire proprement dite qui est en général décrite par un nouveau champ scalaire (classique). Soit on considère qu'une de nos hypothèses est fausse ce qui se traduit par une modification de nos équations de base. Il n'est alors plus nécessaire d'introduire une nouvelle composante, mais la nouvelle dynamique interprétée dans un cadre standard se traduit par un nouveau fluide "effectif", que l'on nomme toujours énergie noire. Nous verrons que la simple distinction entre ces deux classes d'interprétation demande déjà un programme de recherche très ambitieux.

• Modèles avec champ scalaire :

Cette approche est la plus simple car elle conserve nos équations de base. La dynamique de l'énergie noire est représentée par celle d'un champ scalaire, ce qui nécessite l'introduction d'un potentiel $V(\phi)$ de forme inconnue. La description à l'aide d'un lagrangien canonique correspond aux modèles dits de quintessence. Afin de rendre compte des contraintes observationnelles qui indiquent une équation d'état plutôt exotique ($w < -1$ récemment), des modèles modifiant le lagrangien canonique sont apparus. Nous détaillons dans la suite ces divers modèles.

Les modèles de quintessence trouvent leurs origines dans les travaux de Ratra-Peebles [59] et de Wetterich [60], qui reprenaient les idées développées pour les modèles d'inflation (qui correspond à une accélération de l'expansion mais dans les instants primordiaux de l'univers). On suppose que le champ scalaire ϕ couple minimalement, c'est à dire qu'il ressent la gravité à travers la courbure de l'espace-temps et qu'il possède un auto-couplage représenté par le potentiel $V(\phi)$. La dynamique du champ est alors décrite par le lagrangien canonique suivant :

$$\mathcal{L}_\phi = \frac{1}{2}\partial_\mu\phi\partial^\mu\phi - V(\phi). \tag{2.28}$$

où le terme cinétique est canonique et le plus simple possible (*i.e.* linéaire et positif). A partir du théorème de Noether on en déduit la forme du tenseur énergie impulsion :

$$T_{\mu\nu} = \frac{2}{\sqrt{-g}} \frac{\delta(\sqrt{-g}\mathcal{L})}{\delta g^{\mu\nu}} \tag{2.29}$$

où g est le déterminant de la métrique.

On peut relier les propriétés du champ scalaire à celles d'un fluide parfait, ce qui simplifiera les discussions ultèrieures :

$$\rho_\phi = \frac{1}{2}\dot{\phi}^2 + V(\phi)\ (+\frac{1}{2}(\nabla\phi)^2) \tag{2.30}$$

$$p_\phi = \frac{1}{2}\dot{\phi}^2 - V(\phi)\ (-\frac{1}{6}(\nabla\phi)^2) \tag{2.31}$$

Afin d'expliquer une accélération récente il faut que le champ scalaire roule encore vers le minimum de son potentiel, ce qui se traduit par une masse du champ extrêmement faible ($\approx 10^{-30}\, eV$). La longueur d'onde Compton du champ est alors de l'ordre du rayon de Hubble ce qui nous laisse supposer que le champ a une distribution spatiale très douce dans l'univers observable. On négligera donc le gradient du champ dans les deux équations précédentes.

On définit alors l'équation d'état du champ par $w_X = p_\phi/\rho_\phi$ qui est dynamique dans le cas général *i.e.* $w_X \equiv w_X(z)$. On constate que si le terme cinétique est faible devant le potentiel alors la dynamique se rapproche fortement de celle d'une constante cosmologique (*i.e.* $w_X \to -1$). Dans tous les cas on peut réaliser que cette équation d'état est bornée entre -1 et 1 ($-1 \leq w_X \leq 1$).

L'équation du mouvement du champ scalaire est l'équation de Klein-Gordon :

$$\ddot{\phi} + 3H\dot{\phi} = -dV/d\phi \tag{2.32}$$

qui est équivalente à l'équation de continuité (éq.(2.21)).

Grâce à ces formules d'équivalence on peut facilement passer d'une description en terme de champ scalaire à celle en terme d'un fluide parfait. Par la suite nous nous concentrerons sur ce dernier type de description. Ce choix est renforcé [55] par la difficile reconstruction du potentiel scalaire à partir des données. Notons que la description en terme d'un fluide effectif peut englober l'ensemble des modèles d'énergie noire.

La dynamique du champ scalaire peut alors se résumer à la connaissance des trois quantités suivantes [55] : Ω_X, $w_X(z)$ et $w'_X(z) = dw_X/d\ln a$. Les deux dernières fonctions permettent de définir un espace des phases pour la dynamique de l'énergie noire. A titre d'exemple, on peut décomposer les modèles de quintessence en deux sous-classes [61] appelé modèles "freezing" ou "thawing", qui diffèrent par le signe de w'_X comme montré sur la figure 2.11.

Différents modèles issus de la physique des hautes énergies se placent dans ces deux sous-classes. Par exemple des modèles avec axions, dilatons, modulis ou encore avec des

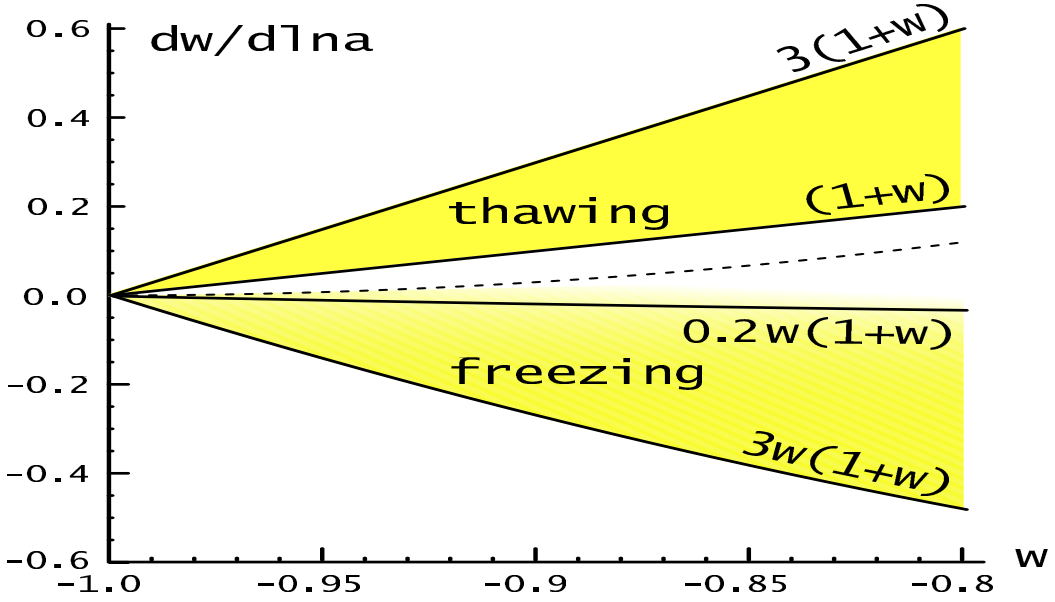

Figure 2.11: Trajectoires des modèles de quintessence, "freezing" et "thawing", dans l'espace de phase $(w_X(z),w'_X(z))$, tiré de [61].

pseudo bosons de Nambu-Goldstone, rentrent dans la classe "thawing". Les modèles de supergravité [62] ou des modèles avec brisure dynamique de la supersymétrie, rentrent dans la classe "freezing". D'autres modèles de nature plus phénoménologique peuvent aussi être placés dans ces sous-classes. Par exemple, les modèles "tracker[3]" [63] grâce à un choix judicieux du potentiel permettent d'obtenir des solutions avec accélération récente quelque soit les conditions initiales du champ (ϕ_{ini},ϕ'_{ini}), et rentrent dans la classe "freezing". Notons que les définitions de ces classes de modèles ne sont pas absolues et que certains modèles de quintessence peuvent être situés en dehors (voir *e.g.* [64].

Comme une alternative aux modèles de quintessence qui semblent peu en accord avec les données, un autre ensemble de modèles a été construit. Les modèles de "k-essence" [65] sont construits à partir d'un lagrangien non canonique (*e.g.* $\mathcal{L} = K(\partial_\mu\phi)V(\phi)$) où le rôle du terme cinétique est renforcé, voir dominant. Ces modèles rentrent, en général, dans la classe "thawing" [66]. Les modèles "phantom"[67], particulièrement exotiques, possèdent la propriété $w_X < -1$ et sont construits à l'aide d'un terme cinétique négatif. Leurs trajectoires dans le plan $(w_X(z),w'_X(z))$ se distinguent aisément de celles des modèles précédents. Enfin, une dernière classe de modèles où le champ scalaire possède des couplages aux neutrinos [68] semblent intéressante. Beaucoup plus de détails et de références peuvent être trouvés dans [54].

[3]Les modèles de supergravité [62] rentrent aussi dans cette classe.

• **Modèles avec modification des équations de base :**

Afin d'éviter d'inclure directement une nouvelle composante dans le modèle cosmologique standard, on peut changer les équations de Friedmann ou directement les équations d'Einstein. Dans le premier cas, ce sont les hypothèses d'isotropie et d'homogénéité qui sont remises en cause. Des modèles très intéressants, dits de "back-reaction" des inhomogénéités [69, 70, 71], relient l'accélération présente à la formation des structures qui sont le résultat des inhomogénéités primordiales et de l'instabilité gravitationnelle. Les premiers modèles apparus [69] ont été fortement critiqués [72], en revanche des développements récents [70, 71] semblent prometteurs.

De nombreux modèles phénoménologiques [73, 74] ont aussi été construits dans lesquels on postule une nouvelle forme pour l'équation de Friedmann, où la relation entre H^2 et les densités n'est plus linéaire. Des modèles dérivés des théories des cordes et des modèles où la matière noire possède des auto-couplages tombent dans cette catégorie.

Les extensions de la relativité générale sont nombreuses, et je ne citerai ici que les modèles suivants ayant obtenus quelques succès :
i) Les théories tenseur-scalaire [75] où un champ scalaire fondamental couple directement à la courbure. Ces théories sont très souvent les manifestations à basse énergie des modèles avec dimensions suplémentaires.
ii) Les modèles qui modifient l'action d'Hilbert/Einstein par l'ajout de nouveaux termes de courbure [76, 77].
iii) Les modèles dérivés des théories des cordes comme le modèle DGP [78] ou de Deffayet [79] peuvent prédire l'existence de phénomènes très surprenants comme une auto-accélération.

Plutôt que de détailler ces divers modèles théoriques, à notre niveau il est plus important de réaliser que ces modèles, interprétés dans un cadre standard (*i.e.* avec les équations de Friedmann), sont équivalents à la présence d'un fluide aux propriétés non standard. En effet, on peut définir une équation d'état effective [55] :

$$w_{eff} \equiv -1 - \frac{1}{3}\frac{d\ln \delta H^2}{d\ln a} \tag{2.33}$$

où δH^2 représente la variation du taux d'expansion entre le nouveau modèle et le modèle standard sans énergie noire :

$$\delta H^2 \equiv (H/H_0)^2 - \Omega_M(1+z)^3 \quad (-\Omega_k(1+z)^2) \tag{2.34}$$

Par conséquent, il est aussi possible de définir des trajectoires dans le plan $(w_X(z), w'_X(z))$ où $w_X(z)$ et $w'_X(z)$ sont à présent effectifs. Par exemple, la figure 2.12 donne quelques trajectoires de modèles phénoménologiques modifiant les équations de Friedmann de la façon

suivante $\delta H^2 \approx H^\alpha$ [74]. Les modèles avec $\alpha = 0.5$ et $\alpha = 1$ sont représentés [55]. Remarquons que ce dernier modèle correspond au modèle DGP [78] dérivé des théories des cordes.

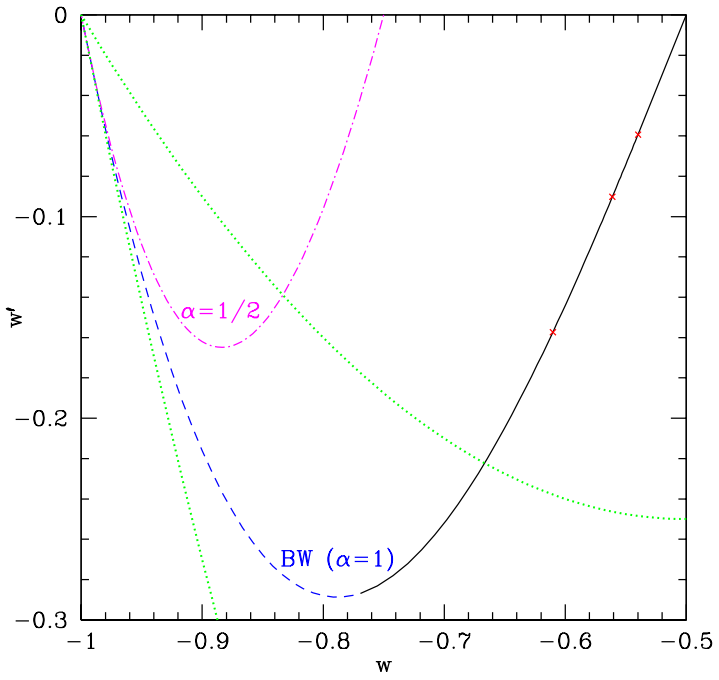

Figure 2.12: Trajectoires des modèles du type $\delta H^2 \approx H^\alpha$ avec $\alpha = 0.5$ et $\alpha = 1$ (équivalent au modèle DGP), dans l'espace de phase $(w_X(z), w'_X(z))$, tiré de [55]. Les lignes pointillées délimitent la zone de la classe "freezing". La courbe du modèle DGP est continue jusqu'à $z = 0$, les croix indiquent les valeurs à $z = 1, 2, 3$.

• **Les problèmes :**

Utiliser une approche basée sur la détermination de l'équation d'état pour distinguer les divers modèles d'énergie noire est pertinent car cela permet de définir une méthode indépendante de tout modèle spécifique. Cependant les problèmes sont nombreux dont voici une liste minimale :

* Nécéssité de définir une paramétrisation :
La caractérisation de l'énergie noire passe, au moins, par la connaissance d'un nombre (Ω_X) et de deux fonctions $w_X(z)$ et $w'_X(z)$. Malheureusement, les données observationnelles ne peuvent pas contraindre un nombre élevé de paramètres. Des études récentes montrent que l'on peut espérer contraindre au plus deux paramètres caractérisant $w_X(z)$ [80]. Avec les analyses combinées ce chiffre peut sans doute augmenter un peu mais cela reste à étudier. Il faudrait donc avoir une intuition physique pour imaginer grossièrement la forme de ces

fonctions, ce qui est très audacieux aujourd'hui vu le grand nombre de modèles proposés. Cependant, un consensus se forme autour de l'utilisation de la paramétrisation suivante [46, 47]:

$$w_X(z) = w_0 + w_a \frac{z}{1+z} \tag{2.35}$$

qui semble posséder des propriétés intéressantes et en particulier reproduit correctement bon nombre de modèles (voir [55] pour plus de détails). En particulier, w_0 est la valeur de l'équation d'état aujourd'hui, et w_a est une mesure de la variation temporelle w'_X :

$$w_a \equiv (-w'_X/a)|_{z=1} = -2w'_X(z=1). \tag{2.36}$$

Bien-entendu, cette description à deux paramètres ne peut pas décrire toutes les dynamiques possibles. Par exemple, la forme donnée par l'éq.(2.35) impose une relation linéaire dans l'espace de phase ($w_X(z)$,$w'_X(z)$), car on a la relation $w'_X = w_X - w_\infty$ où $w_\infty = w_X(z \to \infty) = w_0 + w_a$.

D'autres paramétrisations ont été proposées, voir [81] pour une liste récente, mais aucune ne semble plus adaptée que la paramétrisation de l'éq.(2.35). Par exemple, un simple développement de Taylor en z a tout d'abord été proposé : $w_X(z) = w_0 + w_1 z$, mais dès que l'on tiend compte du CMB on a besoin de calculer w_X à très haut redshift (*i.e.* $z_{CMB} \approx 1089$) et on s'apercoit que w_X devient très grand (si $w_1 > 0$) ce qui fait diverger la densité d'énergie noire. Il est donc indispensable de faire attention au comportement à haut z de toute paramétrisation. En particulier, le CMB impose $w_\infty = w_X(z \to \infty) < 0$ [82].

Il est aussi possible de définir des approches n'utilisant aucune paramétrisation, comme l'analyse en composantes principales [83], la "dérivation" des données [84, 85] ou encore des techniques par itération adaptative [86]. Il apparaît que ces méthodes ont leurs propres avantages et inconvénients, ce qui ne les rend pas compétitives par rapport à l'approche paramétrique mais plutôt complémentaires.

* Dégénérescence des paramètres cosmologiques :
Une fois une paramétrisation de $w_X(z)$ choisie on peut définir l'ensemble des paramètres cosmologiques intervenant dans le paramètre de Hubble $H(z)$ (voir éq.(2.23)), à savoir Ω_M, Ω_X, w_0 et w_a. Les distances, qui sont mesurées expérimentalement, sont reliés au niveau de la théorie au paramètre de Hubble $H(z)$ à travers une relation intégrale (éq.(2.14) et éq.(2.12)). Cette relation intégrale va produire de très fortes dégénérescences entre les divers paramètres [87, 88], ce qui rend leur détermination difficile. Nous allons détailler ce point dans la prochaine section car il est à l'origine de l'existence de nombreux biais d'analyse ce qui motive la réalisation des analyses combinées afin de rendre moins sévère ce problème.

* Nécessité de tenir compte de la croissance des structures et/ou d'autres tests :
Il apparaît que plusieurs modèles d'énergie noire issus de classes différentes peuvent correspondre exactement aux mêmes équations d'état effectives. Par exemple, les théories

tenseur-scalaire sont équivalentes aux modèles avec termes de courbure supplémentaires [76]. De même certains modèles de backreactions sont équivalents aux modèles de quintessence [70]. L'équation d'état et sa dérivée ne sont donc plus suffisant pour caractériser les modèles d'énergie noire. Il faut utiliser d'autres observables qui vont aller plus loin dans la distinction entre modèles. De grands espoirs se fondent sur les contraintes que l'on peut obtenir à travers l'étude de la croissance des structures. Par exemple, Linder a montré récemment [89] qu'une paramétrisation du facteur de croissance pourrait être utile à la distinction des modèles respectant ou non la relativité générale. Pour certains modèles, en particulier ceux issus de la physique des hautes énergies, il sera nécessaire de tenir compte de nombreux tests différents, comme les résultats du LHC sur l'existence de nouvelles particules, forces ou symétries, les tests locaux de la relativité générale, la vérification de la relation de dualité entre distances (*i.e.* relation entre $d_L(z)$ et $d_A(z)$, voir éq.(2.16)), le test de l'équation de Poisson ou encore le test du principe d'équivalence .... Cette problématique est relativement bien décrite dans [90, 91].

2.1.3 La dégénérescence géométrique

Initialement la dégénérescence géométrique a été traitée dans le cadre de l'étude des anisotropies du CMB, mais en fait elle est générique à l'utilisation de distances (lumineuses ou angulaires) en cosmologie. Le cœur du problème vient de la relation intégrale entre les distances et le paramètre de Hubble $d \approx \int 1/H(z)$ (voir les équations (2.14) et (2.16)).

La dégénérescence géométrique est telle que l'on peut avoir des spectres de puissance des anisotropies du CMB identiques pour des évolutions du bruit de fond très différentes [92, 93, 87, 40]. Pour cela il faut satisfaire trois conditions :
* contenus en baryons et en matière noire identiques,
* spectre de fluctuations primordiales identiques,
* paramètres de décalage R ("CMB shift parameter") identiques.

Le paramètre R est defini par :

$$R = \frac{\sqrt{\Omega_M}}{\sqrt{|\Omega_k|}} \mathcal{S}_k \left(\sqrt{|\Omega_k|} \int_0^{z_{CMB}} \frac{1}{E(z')} dz' \right) \tag{2.37}$$

$$= (1+z) H_0 \sqrt{\Omega_M}\, d_A(z_{CMB}) \tag{2.38}$$

où $z_{CMB} = 1089$ [49], $\mathcal{S}_k(x) = \sinh(x),\ x,\ \sin(x)$ pour $\Omega_k > 0$ $(k = 1, \Omega_T < 1)$, $\Omega_k = 0$ $(k = 0, \Omega_T = 1)$, $\Omega_k < 0$ $(k = -1, \Omega_T > 1)$ respectivement, et

$$E(z)^2 = \left(\frac{H(z)}{H_0} \right)^2 = (1+z)^3 \Omega_m + \frac{\rho_X(z)}{\rho_X(0)} \Omega_X + (1+z)^2 \Omega_k, \tag{2.39}$$

où $\frac{\rho_X(z)}{\rho_X(0)}$ est donné par l'éq.(2.22) qui avec la paramètrisation donnée par l'éq.(2.35) fournit:

$$\frac{\rho_X(z)}{\rho_X(0)} = (1+z)^{3(1+w_0+w_a)} e^{-3w_a z/(1+z)}. \tag{2.40}$$

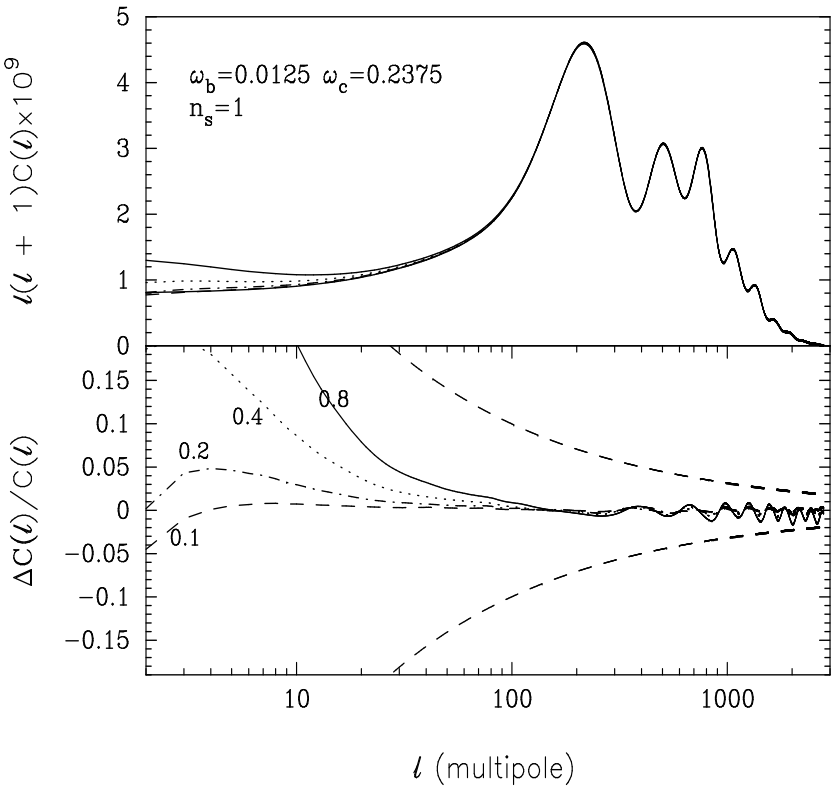

Figure 2.13: Haut : Spectre de puissance du CMB pour les modèles représentés par les 5 points de la figure 2.14. Bas : effets résiduels de chaque modèle par rapport à un univers plat avec $\Omega_M = 1$, les valeurs près de chaque courbe donnent $\Omega_\Lambda h^2$. Les deux lignes externes hachurées donnent les déviations standard duent à la variance cosmique, indiquant donc que les divers modèles sont indistinguables. Figure tirée de [87].

Dans le cadre de la théorie linéaire des perturbations, aucune mesure des anisotropies du CMB, quelque soit leur précision, ne permet de briser cette dégénérescence[87]. Cela impose des limites fondamentales sur la reconstruction de la courbure, du paramètre de Hubble H_0 et sur les propriétés de l'énergie noire [87, 40]. Pour illustrer ceci la figure 2.13 donne le spectre de puissance des anisotropies du CMB pour des modèles différents représentés par les 5 points de la figure 2.14 mais vérifiant les 3 conditions de dégénérescence géométrique. Ces modèles diffèrents uniquement par leurs valeurs de Ω_k et Ω_Λ mais possèdent la même valeur de R ce qui est illustré sur la figure 2.14. Ces modèles sont donc dégénérés du point de vue du CMB. La figure 2.14 donne les dégénérescences pour plusieurs valeurs de R, montrant ainsi que pour des valeurs de R raisonnables on a une infinité de modèles dégénérés. Cette dégénérescence entre la courbure et une constante cosmologique, *i.e.* entre Ω_k et Ω_Λ, a été étudiée en détails dans [87] où il est montré que sans information extérieure les erreurs sur Ω_k et Ω_Λ sont de l'ordre de 0.1 et 1, respectivement, et ce quelque soit la précision des mesures du CMB.

Si on élargit notre espace des paramètres pour aller au-delà d'une constante cosmologique, comme par exemple en supposant des modèles d'énergie noire avec $w_X = cste$

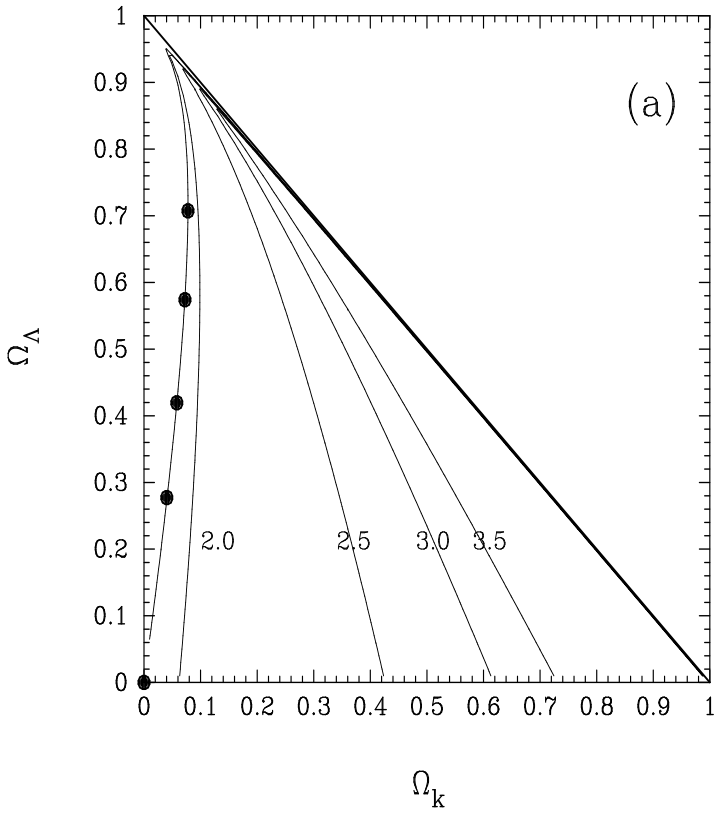

Figure 2.14: Lignes de dégénérescence avec R constant dans le plan (Ω_k,Ω_Λ). Les valeurs de R sont données près de chaque courbe. Les 5 points donnent les positions de chaque modèle ayant un spectre de puissance indistinguable des autres. Le poin à l'origine correspond au modèle SCDM tel que $\Omega_T = \Omega_M = 1$. Figure tirée de [87].

ou avec une équation d'état dynamique, on renforce ce problème de dégénérescence. On pourra consulter [40] qui donne les lignes de dégénérescence dans le plan (Ω_M,w) pour un univers plat. La figure 2.15 donne les modèles dégénérés dans le plan (w_0,w_a) pour différentes valeurs des paramètres de densité.

Chaque point du plan (w_0,w_a) correspond à un modèle particulier pour lequel on calcule R. Afin de voir quels modèles sont dégénérés, les contours sont obtenus en demandant $R = 1.70 \pm 0.03$, qui est la valeur actuelle[94] déduite des dernières mesures de WMAP[49]. On peut remarquer que cette valeur est obtenue sous de nombreuses hypothèses (*e.g.* univers plat avec constante cosmologique) et que cela peut avoir un fort impact sur le résultat [95], mais cela importe peu pour nos propos.

A partir de la figure 2.15, on constate que la position et la taille de la zone dégénérée varient beaucoup avec les paramètres de densité :

- Pour les modèles ouverts (plot en haut à gauche avec $\Omega_M = 0.3$ et $\Omega_X = 0.6$) la zone dégénérée se réduit à une ligne très fine.

- Pour les modèles plats (plot en haut à droite avec $\Omega_M = 0.3$ et $\Omega_X = 0.7$) on obtient

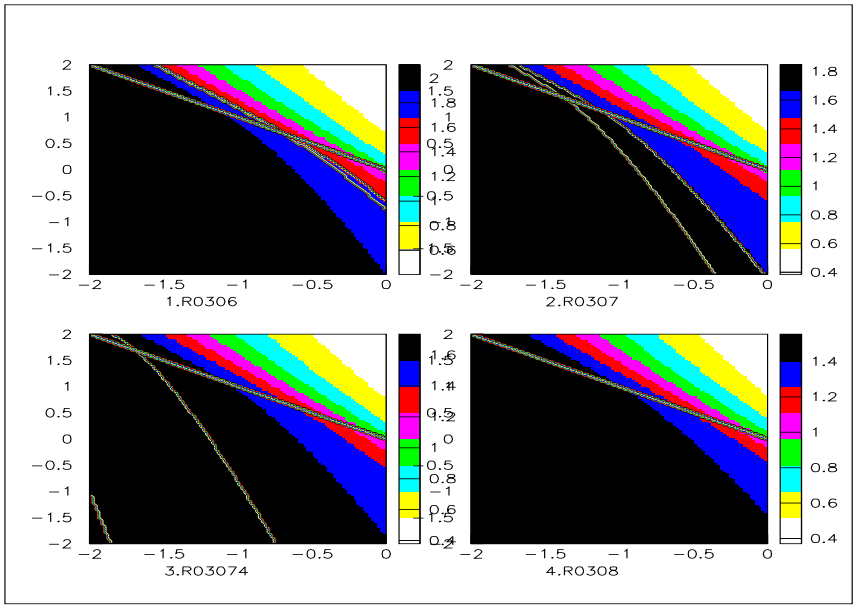

Figure 2.15: Dégénérescence géométrique dans le plan (w_0,w_a) pour $\Omega_M = 0.3$ et $\Omega_X = 0.6$ (en haut à gauche); $\Omega_M = 0.3$ et $\Omega_X = 0.7$ (en haut à droite); $\Omega_M = 0.3$ et $\Omega_X = 0.74$ (en bas à gauche); $\Omega_M = 0.3$ et $\Omega_X = 0.8$ (en bas à droite). Les contours correspondent à $R = 1.70 \pm 0.03$, est la limite CMB $w_\infty = w_0 + w_a > 0$ est donnée.

une ligne très fine pour les modèles phantom mais la zone dégénérée augmente dans la partie $w_0 > -1$.

- Pour les modèles légèrement fermés tels que $1 < \Omega_T \leq 1.06$ (plot en bas à gauche avec $\Omega_M = 0.3$ et $\Omega_X = 0.74$), on obtient une zone dégénérée extrêmement importante. La dégénérescence géométrique est donc particulièrement problématique et les mesures du CMB ne peuvent pas distinguer ces divers modèles.

- Pour les modèles fermés avec $\Omega_T > 1.06$ (plot en bas à droite avec $\Omega_M = 0.3$ et $\Omega_X = 0.8$), R est bien en-dessous de la valeur 1.70 pour toutes valeurs de (w_0,w_a). Par conséquent, la dégénérescence géométrique n'est pas un problème pour les modèles fermés avec $\Omega_T > 1.06$, sauf si les contraintes du CMB sur R réduisent fortement la valeur centrale obtenue (par exemple à cause de nouvelles hypothèses d'analyse).

Ces résultats permettent de comprendre indirectement les résultats expérimentaux actuels, en particulier ceux contraignant simultanément la courbure et une équation d'état dynamique pour l'énergie noire présentés en section 3 de ce chapitre, qui indiquent une préférence pour les modèles légèrement fermés mais absolument compatible avec les modèles plats. C'est pour cet ensemble de paramètres que l'espace de phase est le plus grand, et de très loin. Les modèles fermés avec $\Omega_T > 1.06$ sont exclus car incapables de fournir $R = 1.70 \pm 0.03$ quelque soit (w_0,w_a). Pour les modèles ouverts la dégénérescence géométrique

est opérationnelle : on peut avoir $R = 1.70 \pm 0.03$ avec $\Omega_M \approx 0.3$ pour satisfaire les contraintes issus des grandes structures et avec des couples (w_0,w_a) en accord avec les mesures de SNIa. Cependant ces modèles ouverts sont exclus, ou plutôt négligés, par les méthodes statistiques habituelles, car l'espace de phase associé est extrêmement faible.

Les problèmes rencontrés précédemment se retrouvent pour toutes les autres sondes cosmologiques avec quelques nuances. Par exemple, pour les SNIa les dégénérescences entre les paramètres sont dues[88] à la forme de la distance lumineuse (éq.(2.14)) mais à présent la borne d'intégration n'est plus $z_{CMB} = 1089$ mais le redshift de la SNIa la plus lointaine qui aujourd'hui est $z_{SN} = 1.7$. Cette différence a son importance car elle va permettre de briser partiellement les dégénérescences lors de la combinaison des deux sondes. La brisure n'est que partielle car malheureusement la description des anisotropies du CMB implique tellement de paramètres qu'il y a de nombreuses dégénérescences en sus de la géométrique. On pourra consulter [82, 96] qui discutent en détails ces problèmes pour le CMB. Les travaux présentés dans la prochaine section traitent ces problèmes dans le cas des SNIa.

2.2 Supernovae : biais et prospectives

Dans cette partie nous nous concentrons sur l'étude des SNIa. Les paramètres cosmologiques concernés sont au nombre de cinq : Ω_M, Ω_X, w_0, w_a (ou ${w_1}^4$) et M_S le paramètre de normalisation des SNIa. Ce dernier paramètre est surtout contraint par les SNIa proches (*i.e.* $z < 0.1$) et nous l'étudierons très peu. Il apparaît que les SNIa seules ne peuvent pas contraindre les quatre paramètres restant. Si on essaye de le faire on obtient des erreurs très grandes, même avec les projets de mesure de plus de 2000 SNIa (*e.g.* SNAP). On est donc obligé de contraindre à la main (ou grâce à des analyses combinées, voir la prochaine section) deux de ces paramètres. Les hypothèses qui sont généralement faites sont les suivantes :

- On suppose que l'énergie noire est une constante cosmologique ($w_X = -1$). Les quantités que l'on cherche à contraindre sont alors Ω_M et Ω_X , et donc la courbure. Un article est en cours de rédaction sur ce type d'approche mais dans le cadre d'analyses combinées.

- On suppose que l'univers est plat, ce qui impose la relation $\Omega_X = 1 - \Omega_M$ et donc supprime un paramètre. La deuxième hypothèse concerne l'équation d'état qui est choisie constante $w_X(z) = w = cste$. Le premier article s'intéresse aux effets de cette dernière hypothèse qui peuvent être très important, surtout sur la détermination de Ω_M.

[4]Pour les deux premiers articles nous avons utilisé le développement de Taylor au premier ordre de l'équation d'état : $w_X(z) = w_0 + w_1 z$. Pour les SN seules, les résultats avec w_a sont très similaires et on a grossièrement la relation $w_1 \approx w_a/2$.

- On suppose que l'univers est plat et on rajoute une contrainte extérieure sur Ω_M (prior). Si l'erreur supposée pour Ω_M est petite, cela revient à éliminer du jeu les densités et les paramètres restants sont w_0 et w_a. Le deuxième article étudie les effets d'un prior erroné sur Ω_M. Nous verrons que le choix $\Omega_M = 0.27 \pm 0.04$ utilisé par plusieurs collaborations expérimentales force les données à converger vers le modèle ΛCDM quelque soit la veritable cosmologie.

Le troisième article étudie les contraintes directes sur l'accélération. En effet, il est possible de relier directement la distance lumineuse au paramètre de décélération $q(z)$. Avec cette approche on n'utilise pas les équations de Friedmann mais on a besoin d'une prescription pour décrire $q(z)$. La méthode utilisée par Riess et collaborateurs [97], était de supposer une évolution linéaire (*i.e.* $q(z) = q_0 + q_1 z$). Nous avons montré que cette hypothèse linéaire est dangereuse pour l'interprétation des résultats. Depuis, les analyses tentant de contraindre $q(z)$ directement sont plus raffinées [98].

Dans le quatrième article, nous négligeons les problèmes de biais et nous nous concentrons sur l'optimisation des projets d'observation de SNIa. Plus précisément, nous essayons de répondre à la question suivante : "Vaut-il mieux un sondage profond ou un sondage large pour extraire des informations sur la dynamique de l'énergie noire ?" En d'autres termes, nous tentons d'optimiser la profondeur en redshift ainsi que le nombre total de SNIa à découvrir caractérisant le sondage.

2.2.1 Biais dû à une équation d'état dynamique

Article publié sous la référence : Phys. Rev. **D70** (2004) 043514.

Probing Dark Energy with Supernovae : Bias from the time evolution of the equation of state

J.-M. Virey, P. Taxil

Centre de Physique Théorique, Case 907, F-13288 Marseille Cedex 9, France
and Université de Provence, Marseille, France

A. Tilquin, A. Ealet, D. Fouchez, C. Tao

Centre de Physique des Particules de Marseille, Case 907
F-13288 Marseille Cedex 9, France

Abstract

Observation of thousands of type Ia supernovae should offer the most direct approach to probe the dark energy content of the universe. This will be undertaken by future large ground-based surveys followed by a space mission (SNAP/JDEM). We address the problem of extracting the cosmological parameters from the future data in a model independent approach, with minimal assumptions on the prior knowledge of some parameters. We concentrate on the comparison between a fiducial model and the fitting function and adress in particular the effect of neglecting (or not) the time evolution of the equation of state. We present a quantitative analysis of the bias which can be introduced by the fitting procedure. Such bias cannot be ignored as soon as the statistical errors from present data are drastically improved.

PACS Numbers : 98.80.Es, 98.80.Cq
Key-Words : cosmological parameters - supernovae

Number of figures : 10

March 2004
CPT-2004/P.009
CPPM-P-2004-01

anonymous ftp or gopher : cpt.univ-mrs.fr
E-mails : virey@cpt.univ-mrs.fr, tilquin@cppm.in2p3.fr

1 Introduction

The general paradigm in cosmology is that we are living in a flat universe, which is dominated by a nearly homogeneous component with negative pressure. This component is often called Dark Energy (DE) and causes the expansion rate of the universe to accelerate.

The recent measurements of type Ia supernovae (thereafter denoted SN) are the most direct evidence of the presence of this component [1, 2, 3, 4]. It is also confirmed by the combination of results from the large-scale distribution of galaxies [6] and the most precise data on the cosmic microwave background (CMB) from the Wilkinson Microwave Anisotropie Probe (WMAP) [7]. A recent combined analysis is presented in [8].
Recently the detection of the late Integrated Sachs-Wolfe (ISW) effect has reinforced the case for DE [9]. All this is most frequently interpreted in the framework of the so-called "concordance Cosmology" [10].

A fundamental problem is the identification of the underlying nature of DE : cosmological constant, quintessence or something else (for a review see [11]). The most common way is to measure its equation of state (EoS) defined as $w = p_X/\rho_X$ where p_X is the pressure and ρ_X the energy density of the DE. The ratio of the DE density to the critical density will be denoted Ω_X in a general model and Ω_Λ in the simplest case of a Cosmological Constant ($w = -1$). Ω_M is the corresponding parameter for (baryonic+cold dark) matter.

An ambitious SN program is now on the way. Important pieces of information will be provided by large ground-based surveys such as the Supernova Legacy Survey (SNLS) [12] and these investigations will culminate with a space mission as the Supernova Acceleration Probe (SNAP) instrument, part of the Joint Dark Energy Mission (JDEM), which aims at the discovery and follow-up of some 2000 SNIa per year in the redshift range $z = 0.2 - 1.7$ with very precise magnitude measurements [13]. Of course, the validity of the obtained precision will not depend on the size of the SN sample only, but also on the ability to control the systematic uncertainties at the same level [14]. These systematic errors are coming on one side from the instrument itself (calibration, etc, ...) and also from the SN astrophysical environment (evolution, lensing effects, ...). The SNAP collaboration proposes a global strategy to control such effects at the percent level [13].

In this context, it is necessary to analyze very carefully at which precision level it will be possible to draw any conclusions from the expected rich amount of data.

Authors have used the present SN data together with simulated sets to :

- evaluate the accuracy on the Ω_Λ parameter to validate the acceleration.
- measure the DE through the equation of state with w constant in redshift.
- evidence a possible redshift dependence $w(z)$ with various parametrizations.
- look at the model dependences and degeneracies and study the possible strategies to break the latter.

There is a large consensus that the future SN data *alone* will have difficulties to constrain an evolving equation of state and to break model degeneracies. It is mandatory to have a prior knowledge of the values of some parameters. In particular, a precise

knowledge of Ω_M will be essential if one hopes to pick out the z dependence of w (see e.g. [15, 16, 17, 18, 19, 20, 21]) even in the simplest flat cosmology. However, to use some pieces of information from other sources than SN, it will be essential to combine the data in a coherent way, that is under the same hypothesis, in particular on the DE properties.

On the other hand, some potential difficulties have been pointed out by various authors. Indeed, most papers have been mainly interested in predicting, for each cosmological parameter, the errors around some fiducial value, close to the ones obtained from the present data as $\Omega_M = 0.3, \Omega_X = 0.7, w = -1, dw/dz = 0$. In this procedure, the framework is a particular fiducial model and the chosen fitting function is usually the one used to generate the data. This strategy is valuable for a first estimate but is too restrictive to pin down the underlying physics which is so far unknown.

For example, Maor et al. [16] and Gerke and Efstathiou [20] have stressed the problems which arise if the redshift dependence of the equation of state is neglected whereas this dependence is present. The multiple integral relation between the luminosity distance and w smears out information about w and its time-variation. Assuming in the fitting function that w is a constant, whereas it is not in the fiducial model, can lead to a very wrong estimate of the "constant" or even "effective" w value. At the same time, the central value of Ω_M (or Ω_X) is badly reconstructed.

It is unavoidable to get some ambiguities when trying to fit a particular fiducial cosmology with the "wrong" model ! In the following, we will call this problem the "bias problem". For present SN data, as will be shown, this question is not a concern as the statistical errors on model parameters stay large due to the limited statistics. In the perspective of much richer SN samples, this bias problem cannot be ignored. We address the problem in a more quantitative way than the authors of [22] which have only considered some specific classes of models. In this paper, we investigate the full parameter range, in a model independent way, to quantify where the 'bias' creates potential difficulties and where it can be ignored. We also evaluate the impact of priors when only SN measurements are used. We get a handle on the possible bias introduced in the analysis by looking at the different hypothesis which are done at the fitting function level. Results are presented in the parameter space of the fiducial models we have simulated.

This paper is organized as follows. In Section 2 we recall the theoretical description of the magnitude-redshift diagram for supernovae and we present the experimental situation. We identify the relevant parameters which enter as the parameters of the fiducial models and we define the bias which could be introduced by the fitting procedure.

In section 3, we focus on the extraction of the EoS parameter w_0. We illustrate the confusion created by the bias on examples. Then we analyze the impact of bias on simulated data : we consider future statistical samples corresponding to SNAP, SNLS and also a sample corresponding to present data. We try to find the safest way for extracting an effective w from the data with minimum bias and minimum priors. Our summary and conclusions are given in Section 4.

2 The experimental and theoretical framework

2.1 The experimental framework

The studies presented in this paper are performed with simulated supernovae samples with statistics equivalent to what we expect to have in the future. We concentrate on three sets of data which simulate the statistical power of the present and future data. We want to emphasize the importance of the future sample of supernovae taken on ground which are limited by the systematics inherent to this approach but are statistically one order of magnitude greater than the present sample.

- We reproduce the published data of Perlmutter et al. from [4]. We take directly the effective magnitude of the sample 3 of this paper, which corresponds to 60 SNIa, corrected from K corrections, extinction and stretch (the values are given in Table 3 of [4]). The errors on magnitude vary in the range [0.16-0.22].

- We simulate some future data coming from ground survey as the large SNLS survey at CFHT [5]. This survey has started in 2003 and the estimation after 5 years of running is to register a sample of 700 identified SNIa in the redshift range $0.3 < z < 1$. We simulate a sample as reported in Table 1 in agreement with the expected rate of [5]. We assume a magnitude dispersion of 0.15 for each supernova and constant in redshift after all corrections.

- We simulate data from a future space mission like SNAP, which plans to discover around 2000 identified SNIa, at redshift $0.2< z <1.7$ with very precise photometry and spectroscopy. The SN distribution is given in Table 1(from[14]). The magnitude dispersion is assumed to be constant and independent of the redshift at 0.15 for all SN's after correction. On some studies, we include the effect of adding a constant and uncorrelated in redshift systematic error of 0.02 on the magnitude.

A set of 300 very well calibrated SnIa at redshift < 0.1 should be measured by the incoming SN factory project [23]. This sample is needed to normalize the Hubble diagram and will be called in the following the "Nearby" sample.
A "SNAP" ("SNLS") sample means in this paper a simulation of the statistics expected from the SNAP like mission ("SNLS" survey) combined with the 300 nearby SN's. To make our point clear, we do not consider in the presented studies the experimental systematic errors, unless otherwise specified.

z	0.2	0.3	0.4	0.5	0.6	0.7	0.8	0.9	1.0	1.1	1.2	1.3	1.4	1.5	1.6	1.7
SNLS	-	44	56	80	96	100	104	108	-	-	-	-	-	-	-	-
SNAP	35	64	95	124	150	171	183	179	170	155	142	130	119	107	94	80

Table 1: *number of simulated supernovae by bin of 0.1 in redshift for SNLS and SNAP respectively.*

2.2 The theoretical framework

In the standard Friedmann-Roberston-Walker metric, the apparent magnitude of astrophysical objects can be expressed as a function of the luminosity distance :

$$m(z) \;=\; 5\,log_{10}(D_L) + M_B - 5\,log_{10}(H_0/c) + 25 \;=\; M_s + 5\,log_{10}(D_L) \tag{1}$$

where M_B is the absolute magnitude of SNIa, M_s may be considered as a normalization parameter and $D_L(z) \equiv (H_0/c)\; d_L(z)$ is the H_0-*independent* luminosity distance to an object at redshift z. It is related to the comoving distance $r(z)$ by
$D_L(z) \;=\; (1+z)r(z)$, where

$$r(z) \;=\; \begin{cases} \frac{1}{\sqrt{-\Omega_k}}\sin(\sqrt{-\Omega_k}\,J), & \Omega_k < 0 \\ J, & \Omega_k = 0 \\ \frac{1}{\sqrt{\Omega_k}}\sinh(\sqrt{\Omega_k}\,J), & \Omega_k > 0 \end{cases} \tag{2}$$

$$\text{with}\;\; \Omega_k \;=\; 1 - \Omega_m - \Omega_X \equiv 1 - \Omega_T, \tag{3}$$

$$J \;=\; \int_0^z \frac{H_0}{H(z')} dz' \tag{4}$$

and

$$\left(\frac{H(z)}{H_0}\right)^2 \;=\; (1+z)^3\,\Omega_m + \frac{\rho_X(z)}{\rho_X(0)}\,\Omega_X + (1+z)^2\,\Omega_k, \tag{5}$$

with

$$\frac{\rho_X(z)}{\rho_X(0)} \;=\; \exp\left[3\int_0^z\,(1+w(z'))\;d\,\ln(1+z')\right] \tag{6}$$

Note that we have neglected the radiation component Ω_R.

2.2.1 Choice of a fitting function

A fitting function is an expression for $H(z)$ in terms of a number of parameters. $H(z)$ is usually expressed in term of the cosmological parameters contained in Eq.(5)[15, 16, 17, 18, 19, 20, 21] but other possibilities relying on geometrical parametrizations or arbitrary ansatz have been proposed [24]. In this paper, we adopt the first approach where the cosmological parameters have a direct physical interpretation within General Relativity. With such analysis, the constraints are aimed to be model independent and can be used for investigation of a large variety of DE models. However, we have to choose a parametrization for the time (or redshift) variation of the EoS.

The current parametrizations of $w(z)$ which can be found in the literature are the linear one [17]: $w(z) = w_0 + w_1 z$; the one advocated by Linder [25] with a better asymptotic behavior : $w(z) = w_0 + w_a z/(1+z)$; and also $w(z) = w_0 - \alpha\,\ln(1+z)$ from [20] which is advocated to describe a large sample of quintessence models characterized by a weakly varying EoS. We choose the linear one which allows to compare most easily to previous works. In this case, Eq.(6) becomes:

$$\rho_X(z) \;=\; \rho_X(0)\,e^{3w_1 z}\,(1+z)^{3(1+w_0-w_1)} \tag{7}$$

Nevertheless, our results are essentially independent of the choice of this parametrization since the redshift range of the SN data is limited to $z < 2$ and the sensitivity of the data

on $w(z)$ concerns mainly the values taken by w at relatively low redshifts $z \simeq 0.2 - 0.4$ (the "sweet spot" of [18, 17, 21]) where all parametrizations reduce roughly to the linear one.

Finally, note that models with non-trivial variations of the EoS $w(z)$, like the pseudo-goldstone model of ref.[26], cannot be described by such parametrizations. Consequently, our analysis does not apply to this kind of models.

Therefore, five parameters have to be fitted in the most general procedure:
$M_s, \Omega_M, \Omega_X, w_0, w_1$.

2.2.2 Choice of a fiducial model

We define fiducial models which depend on the parameters $M_s^F, \Omega_M^F, \Omega_X^F, w_0^F, w_1^F$.

In order to keep this paper clear, we concentrate on the case where the paradigm $\Omega_T = 1$ is verified by the fiducial models. This value is in agreement with the inflationary paradigm and it is supported by the analysis of the rich amount of data from the CMB [7]. Ω_X^F is then no longer free ($\Omega_X^F = 1 - \Omega_M^F$) and, if not stated otherwise, the parameters M_s^F and Ω_M^F are fixed at: $M_s^F = -3.6$ and $\Omega_M^F = 0.3$.

It turns out that M_s being a normalisation parameter (see eq.(1)), the chosen fiducial value M_s^F has no influence on our conclusions. The variation due to different Ω_M^F values has been investigated. If $\Omega_T^F \neq 1$, it appears that our results can change significantly. Analysis of non-flat models will be presented elsewhere [27].

To focus on the dark energy measurement, we propose to scan a large variety of fiducial models as a function of the couple (w_0^F, w_1^F). We have scanned the plane (w_0^F, w_1^F) (hereafter denoted by $\mathcal{P}$) for the values $-2 < w_0^F < 0$ and $-2 < w_1^F < 2$. We pay particular attention to the reduced plane $\mathcal{P}_\mathcal{R}$ associated to the ranges $-1 < w_0^F < 0$ and $-1 < w_1^F < 1$, which represents a reasonable class of theoretical models. Indeed, in most of the models available in the literature, like the quintessence models [11], the weak energy condition $w_0^F > -1$ is satisfied (see e.g. [28]). They also possess in general a relatively weak z dependence for the EoS [20, 17]. However, we consider the full plane $\mathcal{P}$ in order to include in our analysis more exotic models which violate the weak energy condition or which are described by a modified Friedmann equation or by a modified theory of gravity (we refer to [29] for a recent list of models and references).

2.2.3 The fitting method

To analyse the (simulated) data, a minimization procedure has been used [30]. A standard Fisher matrix approach allows a fast estimate of the parameter errors. This method is however limited as it does not yield the central values of the fitted parameters. Then we adopt, unless specified, a minimization procedure based on a least square method. The least square estimators are determined by the minimum of the $\chi^2 = (\mathbf{m} - M(z, \Omega, w)^T \mathbf{V}^{-1} (\mathbf{m} - M(z, \Omega, w))$, where $\mathbf{m} = (m_1 ... m_n)$ is the vector of magnitude measurements, $M(z, \Omega, w)$ the corresponding vector of predicted values and $\mathbf{V}$ the covariance matrix of the measured magnitudes. The error on cosmological parameters is estimated at the minimum by using

the first order error propagation technique: $\mathbf{U} = \mathbf{A}.\mathbf{V}.\mathbf{A^T}$ where $\mathbf{U}$ is the error matrix on the cosmological parameters and $\mathbf{A}$ the Jacobian of the transformation.

A full 5-parameter fit (5-fit) of the real or simulated data gives the central values and errors for the five parameters. In the following, the normalization parameter M_s is left free in the fit, unless specified, as its correlation with the cosmological parameters is strong [19]. To constrain accurately this parameter, which is fixed in most of the papers, we use the very low redshift simulated "Nearby" sample of 300 SN.

2.3 Choice of a fitting procedure

There are different ways to choose a fitting procedure. If one only wants to minimize the errors on the fitting parameters, a simple Fisher approach should be sufficient and should give conclusions depending on the initial fit hypothesis. Nevertheless, as we have already emphasized, this approach is fiducial model dependent and can lead to some bias that we want to quantify. Then, after a presentation of different Fisher results, we will expose our strategy to understand and explore the bias introduced by some fitting approach.

2.3.1 The Fisher approach

To perform a Fisher matrix analysis, a fiducial model is chosen and fixed. We take the "concordance model" version of the simplest flat ΛCDM model :

$$\Omega_M^F = 0.3,\ \Omega_X^F = 0.7,\ w_0^F = -1,\ w_1^F = 0 \text{ with } M_s^F = -3.6$$

We call this model 'Λ' in the following.

Each *fitting procedure* is defined by a particular choice of the parameters to be fitted: reducing the number of parameters will improve the parameter errors in the fitting function. Priors are introduced by fixing a parameter at a predefined value or inside a given range.

Table 2 gives the errors obtained with the Fisher matrix analysis for various fitting procedures with the SNLS and SNAP simulated data. The numbers are in agreement with the analysis of various authors [15, 16, 17, 18, 19, 20, 21].
Figure 1 gives the contours obtained in the plane (Ω_M, w_0) at 68.3 % CL with the SNAP statistics, for this fiducial model within the same fitting procedures.
As can be seen from the first line of Table 2 and from the black ellipse in Fig. 1, a complete 5 parameter-fit (5-fit)$(M_s, \Omega_M, \Omega_X, w_0, w_1)$, with no assumptions on the values of the cosmological parameters - including no constraint on the flatness of the universe- yields too large errors on the cosmological parameters to set any definite conclusions even with the high statistics sample expected for the SNAP+Nearby data.
Fig. 1 shows clearly that the reduction of the number of fitted parameters or/and the strengthening of the Ω_M prior, reduces the contours.

The second line of Table 2 presents errors with the paradigm of a perfectly flat universe $(\Omega_T = 1)$ and the 5-fit reduces to a 4-fit $(M_s, \Omega_M, w_0, w_1)$. It appears that for the SNAP statistics, one gets better estimates of w_0 and Ω_M but the error on w_1 is always large. For SNLS, even the error on w_0 is large.

Table 2: Statistical errors obtained with a Fisher matrix analysis on the cosmological parameters for various fitting procedures with the SNLS and SNAP data repectively. The fiducial model is a cosmological constant with $M_s^F = -3.6$, $\Omega_M^F = 0.3$, $\Omega_X^F = 0.7$, $w_0^F = -1$, $w_1^F = 0$. The weak (strong) Ω_M prior corresponds to the constraint $\Omega_M = 0.3 \pm 0.1$ ($\Omega_M = 0.3 \pm 0.01$). The labels 5-fit, 4-fit and 3-fit corresponds to the fitting procedures 5-fit$(M_s, \Omega_M, \Omega_X, w_0, w_1)$, 4-fit$(M_s, \Omega_M, w_0, w_1)$ and 3-fit(M_s, Ω_M, w_0), respectively. $\sigma(\Omega_X)$ has been omitted from the table since $\Omega_X = 1 - \Omega_M$ is no longer a free parameter except for the 5-fit where $\sigma(\Omega_X)$ is very large. $\sigma(M_s)$ has been omitted from the table since its value, roughly 1% , changes weakly for the various fitting procedures thanks to the inclusion of the Nearby SN sample.

Fit	Ω_M prior	assumptions	$\sigma(\Omega_M)$ SNAP	$\sigma(w_0)$ SNAP	$\sigma(w_1)$ SNAP	$\sigma(\Omega_M)$ SNLS	$\sigma(w_0)$ SNLS	$\sigma(w_1)$ SNLS
5-fit	no	no	1.51	4.15	11.07	19.10	63.37	>100
4-fit	no	$\Omega_T = 1$	0.14	0.11	1.31	1.08	1.21	7.94
4-fit	weak	$\Omega_T = 1$	0.082	0.076	0.77	0.10	0.161	0.89
4-fit	strong	$\Omega_T = 1$	0.01	0.055	0.174	0.01	0.117	0.511
3-fit	no	$\Omega_T = 1$,$w_1 = 0$	0.016	0.063	/	0.069	0.19	/
3-fit	weak	$\Omega_T = 1$,$w_1 = 0$	0.016	0.063	/	0.057	0.158	/
3-fit	strong	$\Omega_T = 1$,$w_1 = 0$	0.008	0.040	/	0.01	0.047	/

Adding some prior knowledge of Ω_M improves greatly the situation: the same 4-fit $(M_s, \Omega_M, w_0, w_1)$ for SNAP and SNLS with a weak prior on Ω_M $(0.2 < \Omega_M < 0.4)$ yields a good estimation of w_0 but still a very large error for w_1 (see line 3 of Table 2). Only a strong prior on Ω_M $(\Omega_M = 0.3 \pm 0.01)$ really improves the situation for w_1 as can be seen from line 4 of Table 2. These conclusions are in agreement with other published results [15, 16, 17, 18, 19, 20, 21].

One can conclude that the determination of a possible redshift dependence of the EoS remains the most difficult task. All authors agree on the following statement: to get a good precision on the parameter governing the redshift evolution of the EoS, a fit with a strong prior on Ω_M ("strong" means at the percent level) is needed within the $\Omega_T = 1$ paradigm.

2.3.2 The bias problem

Several comments on the previous approach are in order :

- The setting of strong priors inside the fit should be taken with caution.
  First of all, the cosmological parameter Ω_M is far from being measured at the percent level [31]. So, this kind of prior cannot be applied blindly, even if there is hope that this parameter might be well measured by the time SNAP provides data.

- Even in a future context, some doubts can be raised about the relevance of very precise priors [15, 16] and their use has to be set with some cautions : all the Ω's should be obtained under the same hypothesis (astrophysical, experimental, DE

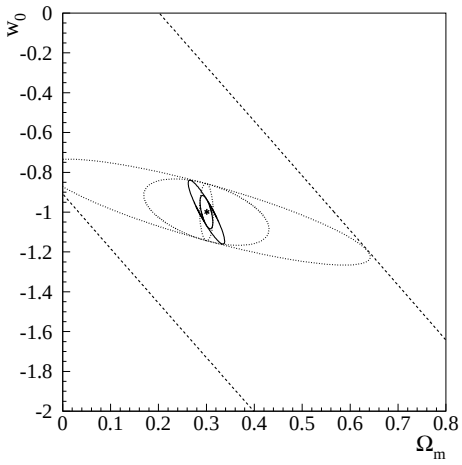

Figure 1: Fisher contours in the plane (Ω_M, w_0) at 68,3 % CL for a cosmological constant as the fiducial model. The large dashed contour corresponds to the 5-fit$(M_s, \Omega_M, \Omega_X, w_0, w_1)$. The three dotted contours correspond to the 4-fit$(M_s, \Omega_M, w_0, w_1)$ with no prior (largest), with a weak Ω_M prior (i.e. $\Omega_M = 0.3 \pm 0.1$) and with a strong Ω_M prior (i.e. $\Omega_M = 0.3 \pm 0.01$, smallest ellipse). The solid contours correspond to the 3-fit(M_s, Ω_M, w_0) with a weak Ω_M prior (largest) and with a strong Ω_M prior (smallest). For this fitting procedure, there is almost no difference between the cases "no" and "weak" prior for Ω_M.

properties) and correlations among fitted parameters have to be taken properly into account for the combined statistical analysis to be relevant.

In this paper, we attempt to extract the informations from SN data, therefore avoiding the (consistency) problems encountered when constraining Ω_M with external data.

The results from Table 2 and Fig. 1 lead us to leave aside the determination of the redshift dependence of the EoS and to consider w_0 as an "effective" constant w^{eff} EoS parameter. Then we concentrate on the best strategy to extract w_0 from present or future SN data with minimal assumptions on priors : we use the paradigm $\Omega_T = 1$ either with no priors or with weak priors on Ω_M. We focus on a 3-fit (M_s, Ω_M, w_0) or on a 4-fit $(M_s, \Omega_M, w_0, w_1)$ where we know already that the precision on w_1 will be low.

A 3-fit should always provide better constraints than a 4-fit. Table 2 shows, however, that the reduction of the errors is more important for Ω_M than for w_0 and since the w_0 error is not strongly improved, the use of the 4-fit seems the best strategy for extracting w_0 [21, 14]. We want to point out that this conclusion is only valid for the Λ fiducial model. In some other fiducial models, the 3-fit can increase considerably the constraints on w_0 with respect to the 4-fit: Figure 2 gives the expected contours in the plane (Ω_M, w_0) for the two fiducial models $(w_0^F = -2, w_1^F = 0)$ and $(w_0^F = -1, w_1^F = 0.2)$. The best constraints on Ω_M and w_0 are given by the 3-fit.

On the other hand, doing a complete minimization procedure shows that the central values given by the 3-fit can be far away from the fiducial values. This fact has been pointed out by several authors [15, 16, 20, 22]. This happens when the fitting hypothesis are not verified by the fiducial model, namely a constant EoS in the 3-fit $(w_1 = 0)$ and a

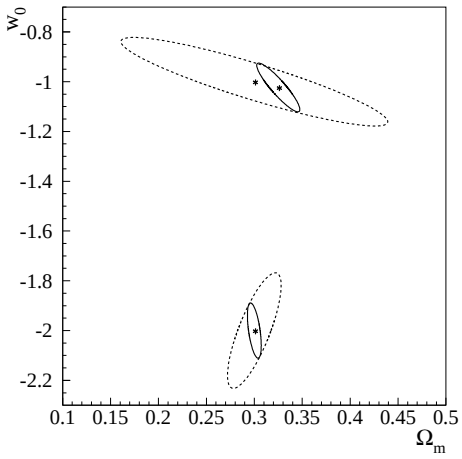

Figure 2: Contours in the plane (Ω_M, w_0) at 68,3 % CL for the fiducial models ($w_0^F = -2$, $w_1^F = 0$) and ($w_0^F = -1$, $w_1^F = 0.2$). The large dashed (small solid) contours correspond to the 4-fit (3-fit). A weak Ω_M prior has been used.

varying one in the fiducial model ($w_1^F \neq 0$). In this case *bias are introduced on the estimate of the cosmological parameters*. This bias problem is due to the degeneracy of the fitting function among the various cosmological parameters [15, 16]. A wrong hypothesis on one parameter is compensated in a non trivial way by the value of the others. We know also from the various Fisher analysis presented in the litterature [18, 19, 21, 14] that the *errors* depend on the central values of the cosmological parameters. Since these last ones are biased, their errors are also biased [21, 14].
Then the question of choosing between the 3-fit and the 4-fit is not so obvious and appears to be fiducial model dependent.

In the next section we present in detail a study of this bias by exploring the range of fiducial models which is affected, in order to conclude on the validity of a 3-fit.
Let us point out that other bias would be introduced by a departure from the $\Omega_T = 1$ paradigm in the fiducial model or if the central value of the Ω_M prior used in the fitting procedure is not the same as the fiducial one. These bias will be studied in a future paper [27].

3 How to extract w_0 : a quantitative analysis of the validity of a 3-fit

To be able to choose the best strategy for extracting w_0, we want to test the relevance of the fitting procedure. We have performed for that purpose a complete study of the bias introduced by the different fitting procedures. After a description of the problem through a short illustration, we present the results of a full scan of the (w_0^F, w_1^F) plane for SNAP, SNLS and a sample corresponding to present data. The scanning is done by fixing the fitting procedure and varying the various parameters of the fiducial model ; we perform

a 3-fit and compare it to the result of the 4-fit where w_1 is left free.

3.1 Illustration of the bias effect

Let us start with some illustrations of the bias introduced by the 3-fit procedure. We choose three different models and look at the central values of the parameters obtained from the fit:

• The one of Maor et al. [16] ($w_0^F = -0.7$, $w_1^F = 0.8$). The 3-fit applied to this model clearly provides some erroneous results : $\Omega_M = 0.62 \pm 0.013$ and $w_0 = -1.548 \pm 0.194$. Note that our central values are slightly different from the ones of [16], this is due to small differences between the chosen SN samples.

Figure 3 shows the two elliptical contours from the 3-fit and the 4-fit : the 4-fit ellipse is centered on the fiducial values as expected whereas the 3-fit ellipse is very far away. This is due to the large chosen w_1^F value and this behavior has been already pointed out by Maor et al. (see Fig. 5 of ref. [16]). As discussed by these authors, the w_0 and w_1 parameters are strongly correlated due to the functional form of $\rho_X(z)$ (Eq.(7)). Assuming a zero value for w_1 (as in the 3-fit) whereas the fiducial value is large and positive, is compensated by a fitted w_0 value which is much more negative than its fiducial value. However, the whole effect is more subtle due to the strong correlations between Ω_M and w_0 (and w_1 also) entering the integral relation Eqs.(4,5,6). This is the reason why Ω_M is also biased.

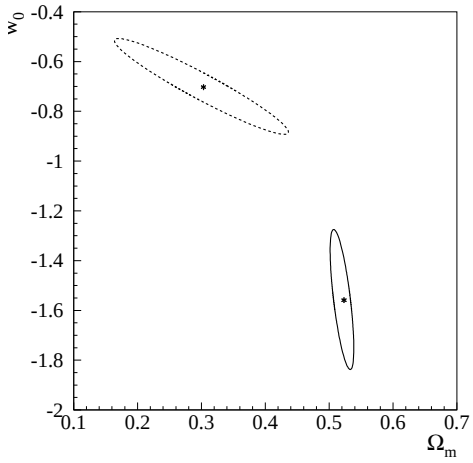

Figure 3: Contours in the plane (Ω_M, w_0) at 68,3 % CL for the fiducial models ($w_0^F = -0.7$, $w_1^F = 0.8$)(Maor et al. model[16]). The dashed (solid) contour corresponds to the 4-fit (3-fit) contour. A weak Ω_M prior has been used. We can observe the large differences in the central values coming from the two 3-fit and 4-fit fitting procedures.

• If we take the model ($w_0^F = -1$, $w_1^F = 0.2$), which has a "small" w_1^F value, it leads to a smaller bias : we get $\Omega_M = 0.324 \pm 0.016$ and $w_0 = -1.021 \pm 0.067$. We see that there is a bias of the order of 1.5σ for Ω_M, and a small bias within the statistical error for w_0.

The central values (crosses) displayed in Figure 2 of the ellipses for the 3-fit and the 4-fit are different but the 3-fit ellipse is included in the 4-fit one, indicating a small bias on one parameter (w_0) and a not too big bias on the second (Ω_M).

• Finally, with the model ($w_0^F = -2$, $w_1^F = 0$) which has no z dependence of the EoS, there is no bias and both ellipses are centered on the same point (see Figure 2).

Note that there is no significant bias for the normalization parameter M_s in the three cases.

3.2 Validity zones for the 3-fit

To quantify the bias, we scan the full plane $\mathcal{P}$ (w_0^F, w_1^F) using the procedure 3-fit, assuming a flat universe. We first define different zones in this plane where the effects of the bias can be quantitatively estimated.

The plane $\mathcal{P}$ is divided in three distinct zones :

- The Non Converging Zone (NCZ) where the fit has some detectable problems: the fit is bad either because $\chi^2 > 3n$ (n being the number of degrees of freedom), or because the error on one of the fitted parameter is above 1. We also reject fits yielding some Ω_M values far away from current expectations, namely we require $0.1 - \sigma(\Omega_M) < \Omega_M < 1. + \sigma(\Omega_M)$.
  This zone is shaded in our plots. None of the fiducial models located in this NCZ can be fitted with the procedure 3-fit. Therefore, with real data, the fit procedure will be excluded.

- The Biased Zone (BZ) is the part of $\mathcal{P}$ where the fit converges perfectly, but where we know from the simulation that we are far from the fiducial values: We quantify this bias as the difference between the central value of a fitted parameter $\mathcal{O}$ and the fiducial value $\mathcal{O}^{\mathcal{F}}$. Namely the "bias" is defined as

$$B(\mathcal{O}) \;=\; |\mathcal{O}^F - \mathcal{O}| \tag{8}$$

  In general, $B \neq 0$ and we define the biased zone as the part of $\mathcal{P}$ where $B(\mathcal{O}) > \sigma(\mathcal{O})$ where $\sigma(\mathcal{O})$ is the statistical error on $\mathcal{O}$.

  The important point is that this zone is undetectable with real data. It is the region we want to identify and to minimize through an appropriate choice of the fitting procedure.

- The Validity Zone (VZ) is the remaining part of $\mathcal{P}$ where the fit converges perfectly and where $B(\mathcal{O}) < \sigma(\mathcal{O})$. If we require this condition for the full set of fitted parameters together, we can define a "full" validity zone (full VZ).

  Consequently, the contours separating the BZ and the VZ in the plane $\mathcal{P}$ correspond to the intrinsic limitation of the fitting procedure which is considered.

We now apply this strategy of analysis to the SNAP and SNLS simulated data. The impact of the bias on the present SN statistical sample is also presented.

3.3 Fitting procedures for SNAP

3.3.1 Determination of the 3-fit validity zones

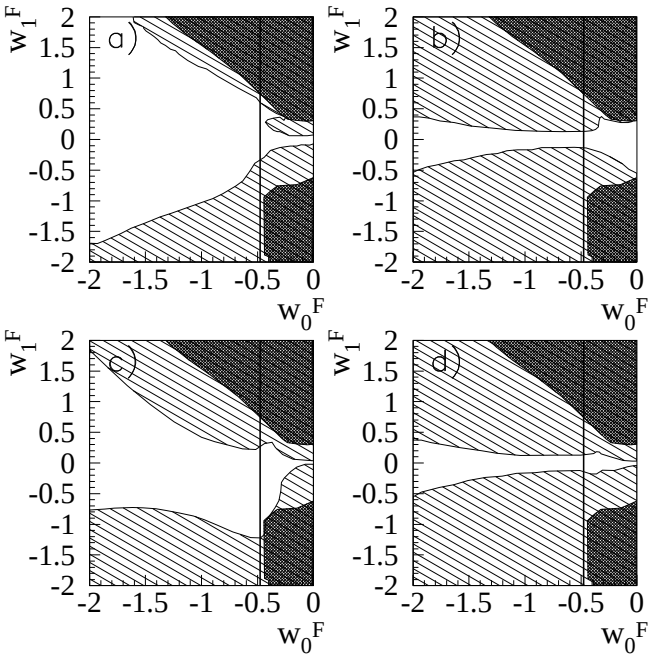

Figure 4: Validity Zones(white), Biased Zones (hatched) and Non Converging Zones (black) for a SNAP like data set for M_s only (a), Ω_M (b), w_0 (c) and all the parameters together (d). The procedure is a 3-fit with a weak Ω_M prior. The vertical line at $w_0^F = -0.48$ separates decelerating models from accelerating ones.

We apply this method to determine the validity zones using the 3-fit on the SNAP simulated data. A weak prior on Ω_M, $\Omega_M = 0.3 \pm 0.1$, has been used.
Figure 4a,b,c,d give the different validity zones for M_s (Figure 4a), Ω_M (Figure 4b), w_0 (Figure 4c) and for the three parameters taken together (Figure 4d).

In all the figures, the line $w_1^F = 0$ corresponds to the actual unbiased fiducial models. One can see that the Biased Zone is always limited by the NCZ. The line $w_0^F = -1/(3\Omega_X^F) \simeq -0.48$ separates the models which correspond to an accelerating universe today ($w_0^F < -0.48$) from the decelerating ones ($w_0^F > -0.48$).

Looking at the validity zone for each parameter individually :

- M_s (Figure 4a) is essentially unbiased for models which correspond to acceleration ($w_0^F < -0.48$) except for large negative values of w_1^F. We notice that M_s is always measured with an error better than the percent thanks to the "Nearby" sample. Therefore it is easy to get a bias greater than this error. However this bias has no real consequence on the determination of the other parameters.
- Ω_M (Figure 4b), conversely, is unbiased only for a small band around the line $w_1^F = 0$. It means that for most of DE models with varying EoS, the fitted Ω_M is strongly biased in this fitting procedure.
- w_0 (Figure 4c) is valid in a large part of the reduced plane $\mathcal{P}_\mathcal{R}$, which corresponds to the present acceleration region ($w_0^F < -0.48$). Otherwise we fall in the Biased Zone which, for instance, contains the previously quoted model of Maor et al.[16]. Outside $\mathcal{P}_\mathcal{R}$, for large $\mid w_1^F \mid$ values, we are in the Biased Zone. Consequently, one has to take some cautions when using the 3-fit for extracting w_0.

The full Validity Zone is shown in Fig. 4d ans is driven mainly by the bias on the Ω_M parameter. One can conclude that the 3-fit is valid on all parameters together for fiducial models which have a small dependence in redshift: when $w_0^F > -1$, the validity is for $|w_1^F| < 0.2$, otherwise it increases to $|w_1^F| < 0.4$.

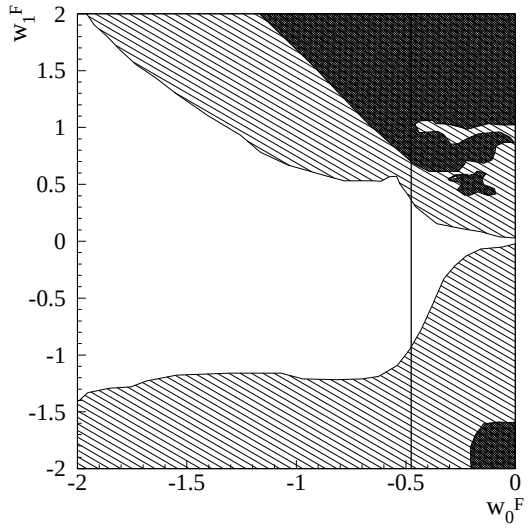

Figure 5: Same as Fig.4c for w_0 in the case where we add an uncorrelated and constant in redshift systematic error of 0.02 on the magnitudes.

One has to emphasize that the experimental error will also contain systematic errors. These latter have been estimated for SNAP [14]. We have simulated this case and the result is given on Fig. 5, where we have included a constant uncorrelated systematic error on each magnitude measurement. The consequence of increasing the error is an increase

of the Validity Zones. Compared to Fig. 4c, the VZ for w_0 is substantially enlarged. Note that the NCZ is reduced in the same time. The VZ for M_s follows the same behaviour, the one of Ω_M being much less affected.

We have also looked at the impact of the Ω_M prior on our results:

• When there is no prior, the results are very comparable (but slightly worse) to the weak prior case described above.

• When a strong prior is used (e.g., $\sigma(\Omega_M) = 0.01$), the error on the parameters are reduced but the VZ also. Fig. 6a gives the VZ for w_0 with this prior. Due to the strong prior on Ω_M, all the bias effect is reported on the w_0 parameter which is strongly biased as shown on Figure 6a. Looking more closely at the reduced $\mathcal{P}_{\mathcal{R}}$, one sees that the VZ is limited to the line $w_1^F = 0$. Therefore we lose the fact that w_0 is in general well fitted by this fitting procedure.

The conclusion is that the fitting procedure 3-fit used in the case of a high SN statistics experiment like SNAP, can be useful to constrain w_0 for a large part of the plane $\mathcal{P}$, which corresponds to accelerating models, only when no prior or a weak prior on Ω_M is used. The other cosmological parameters (Ω_M especially) are strongly biased, and strengthening the Ω_M prior worsens the situation. Concerning DE models which lead to a present deceleration, it appears clearly from the preceding figures, that the cosmological parameters are biased even if the time dependence of the EoS is weak.

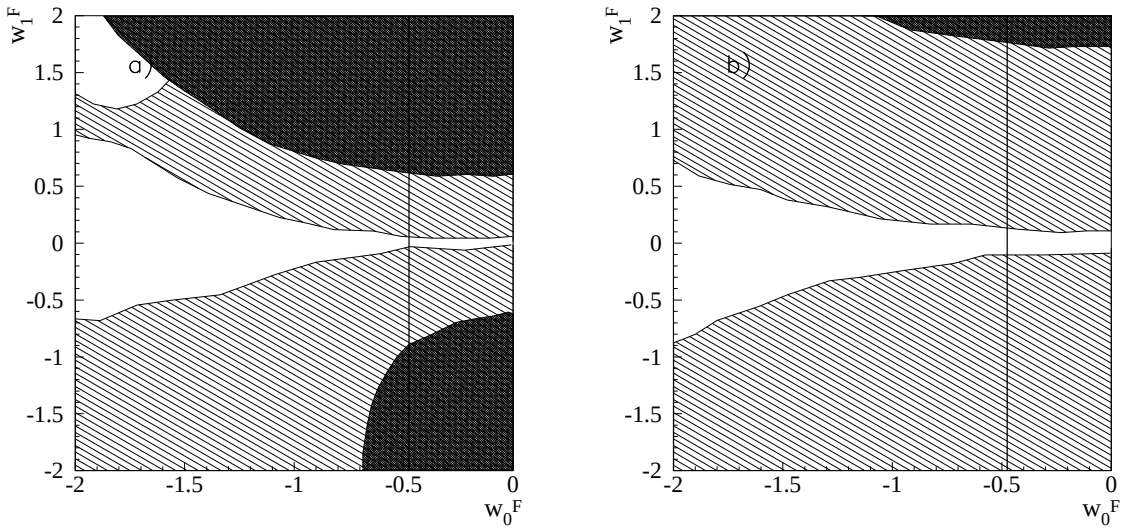

Figure 6: Same as Fig.4c for w_0 in the case of a strong Ω_M prior a) : SNAP, b) : SNLS.

3.3.2 Comparison between the 3-fit and the 4-fit

We have shown previously that the 3-fit procedure may be useful to extract w_0 even in the presence of the bias due to the hypothesis $w_1 = 0$. The simplest 4-fit procedure (with no constraint on w_1) allows the extraction of w_0 without any bias since w_1 is included in the fit, but with an increase of the statistical errors on each parameter. We adress now a

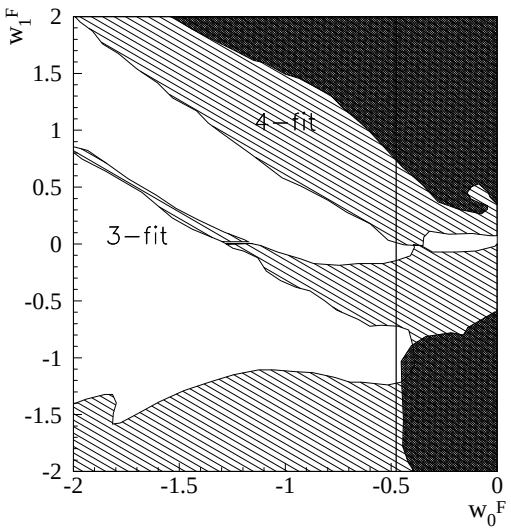

Figure 7: $E(w_0, 3-\text{fit}) - \sigma(w_0, 4-\text{fit})$ for the SNAP data and a weak Ω_M prior. The white part corresponds to a negative difference, the hatched part to a positive difference, the black region corresponds to the Non Converging zones.

comparison of the errors obtained on w_0 with these two different fitting procedures.

To combine the bias error and the statistical error, we choose a fit quality estimator of the procedure as $E(w_0) = \sqrt{\sigma^2(w_0) + B^2(w_0)}$ which reduces to $\sigma(w_0)$ for the 4-fit. Figure 7 compares the two procedures by displaying the difference of errors $E(w_0, 3-\text{fit}) - \sigma(w_0, 4-\text{fit})$ with a weak prior on Ω_M. The 3-fit is preferred, with this estimator, in a large part of the plane $\mathcal{P}$ which corresponds to models with present acceleration.

The two black areas correspond to the NCZ of both fitting procedures. Therefore, one cannot conclude for a preference for the 4-fit in this zone. The two hatched zones, corresponding to large values of $|w_1^F|$, indicate a preference for the 4-fit. This is due to the bias on w_0 inherent to the 3-fit. There is also a narrow hatched band where the 4-fit is still preferred although the bias is small. This appears to be a zone where the correlation between w_0 and w_1 is small and then, the errors from the 4-fit and the 3-fit are similar, the 4-fit being slightly better (less than 2%) except on the line $w_1^F = 0$.

In the white regions, the two parameters w_0 and w_1 are strongly correlated and then the 3-fit has clearly a smaller error.

So, we can conclude that with a weak, thus conservative, prior on Ω_M the 3-fit is in general better than the 4-fit to extract w_0 for accelerating models.

3.4 Analysis for SNLS

3.4.1 Determination of the 3-fit validity zones

A similar analysis has been performed for a simulated sample corresponding to the SNLS-like statistics.

The various Validity Zones obtained for SNLS with a weak Ω_M prior are shown in Figures 8a,b,c,d

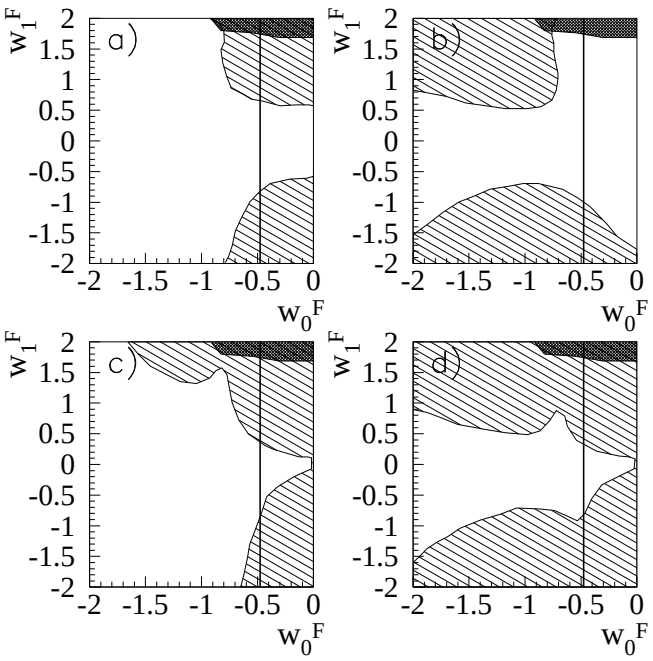

Figure 8: Validity Zones (white), Biased Zones (hatched) and Non Converging Zones (black) for a SNLS like data set for M_s only (a), Ω_M (b) and w_0 (c) and all the parameters together (d). The procedure is a 3-fit with a weak Ω_M prior.

We deduce from this figure that :

- M_s is almost unbiased for accelerating models and also for decelerating ones provided the redshift dependence is small ($|w_1^F| < 0.6$) (Fig. 8a).
- Ω_M is not biased in most of the reduded plane $\mathcal{P}_\mathcal{R}$ and it is biased outside this plane if $|w_1^F| > 0.6$ (Fig. 8b).
- w_0 is not biased for an important part of the plane corresponding to acceleration ($w_0 < -0.48$) (Fig. 8c).
- The 3-fit is a good fitting procedure for reconstructing *all* cosmological parameters simultaneously for accelerating models ($w_0 < -0.48$) when the redshift dependence is small $|w_1^F| < 0.6$ (see Fig. 8d). Otherwise the result is biased.
- The use of a strong prior on Ω_M worsens the situation : w_0 is biased for most of the plane $\mathcal{P}$ as shown on Fig. 6b.

Comparing these results with the SNAP case shows that the conclusions are quite similar but the validity zones for SNLS are much larger than for SNAP. Due to the lower statistics our criterion $B(\mathcal{O}) < \sigma(\mathcal{O})$ is less constraining. Note that the NCZ zones are strongly reduced as expected with the lower statistics.

3.4.2 Comparison between the 3-fit and the 4-fit

We perform the same comparison of the errors on w_0 obtained from the two procedures 3-fit and 4-fit, still with a weak prior on Ω_M.

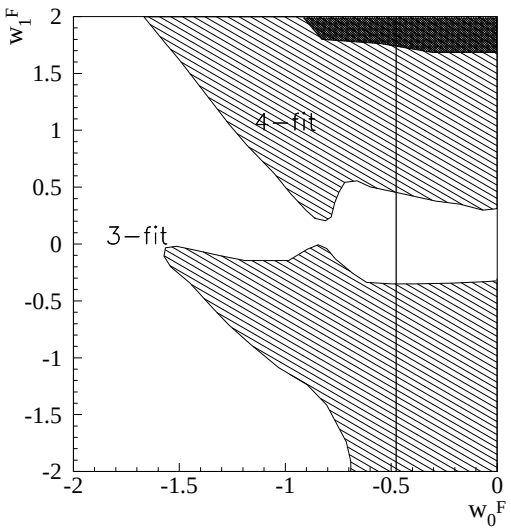

Figure 9: $E(w_0, 3-\text{fit}) - \sigma(w_0, 4-\text{fit})$ on w_0 for a SNLS like data set and a weak Ω_M prior. The white part corresponds to a negative difference, the dashed part to a positive difference, the black region corresponds to the Non Converging Zones.

Figure 9 shows the difference of errors between the 3-fit and the 4-fit. The 3-fit is preferred when the bias is small or when the two parameters w_0 and w_1 are strongly correlated. When $w_1^F < 0$ the hatched region in the accelerating zone has similar origin and properties as the narrow hatched zone of Fig. 7, namely that both fitting procedures provide in fact very comparable errors.

3.5 Analysis for a statistical sample corresponding to the SCP data

We can define the validity zones for the statistics of the present SN sample from the SCP collaboration [4] introduced in Section 2.1.

Figure 10a gives the full Validity Zone obtained without any prior on Ω_M. The large size of this zone shows that the results are not biased (at 1σ) for most of the plane $\mathcal{P}$. In

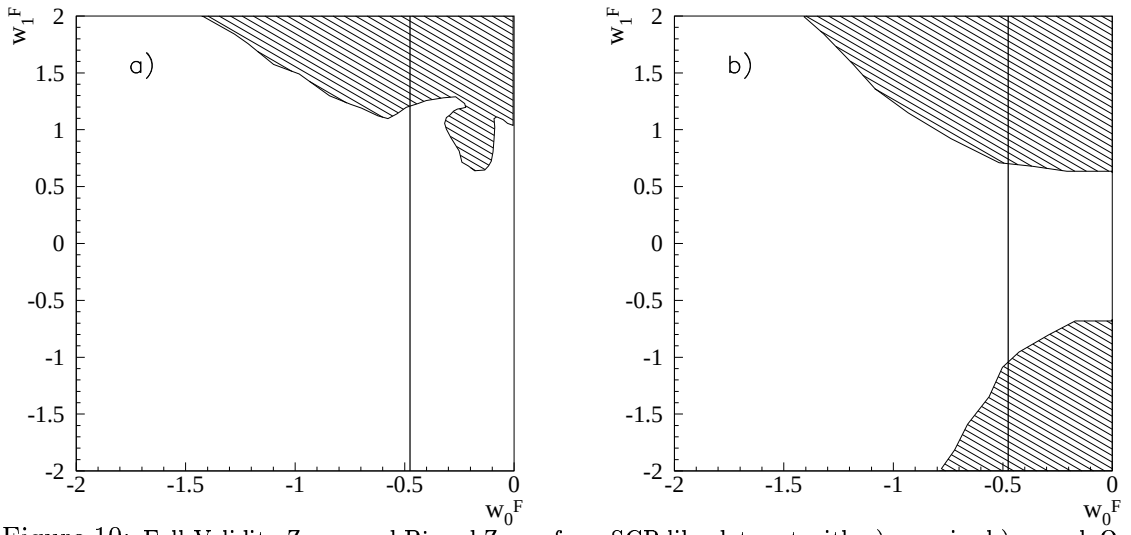

Figure 10: Full Validity Zones and Biased Zones for a SCP like data set with a) no prior b) a weak Ω_M prior. The NCZ are not plotted due to the large errors on Ω_M and w_0.

fact only Ω_M is affected by a bias.

A weak Ω_M prior of $\sigma(\Omega_M) = 0.1$ has been used to draw Fig. 10b, giving the Validity Zone for w_0 (identical to the full VZ). The VZ is slightly reduced compared to the no prior case but it remains quite important within the plane $\mathcal{P}$. More precisely, it appears that the upper part of the biased zones are comparable for both no and weak prior cases. Only the lower part of the biased zone of Fig. 10b is specific to the weak prior case. Note that changing the error value of the prior has little consequences on the shape of the VZ.

This fitting procedure is widely used to extract informations from present SN data [1, 2, 3, 4, 32]. The results published in these references are valid for models with constant EoS. From our findings, one can extend the validity of these results and conclude that models with a redshift dependent EoS which verify $\mid w_1^F \mid < 0.7$ may be fitted by this 3-fit procedure with a bias which stays below the statistical error.
So, we conclude that we can trust (at 1σ) the results based on present SN data obtained with a 3-fit where we neglect the redshift dependence of the EoS, using a Ω_M prior or not. Only (fiducial) models with a strong recent variations of the EoS may lead to biased results.

The comparison of the potentialities of the 3-fit and the 4-fit to extract w_0 does not seem very relevant. However, we have checked this point, and it appears that the 3-fit provides some constraints on w_0 which are roughly 30% better than with the 4-fit for most of $\mathcal{P}$.

Finally, we have remarked that the central values of w_0 and Ω_M are shifted as follows: if w_1^F is positive we have $w_0 > w_0^F$ and $\Omega_M > \Omega_M^F$, and the converse if $w_1^F < 0$. We do not recover this simple behaviour with the SNAP and SNLS samples.

4 Summary and conclusions

In this paper, we have studied the best strategy to extract the cosmological parameters and in particular the dark energy component from the future supernovae data within the $\Omega_T = 1$ paradigm. We have compared results from the present statistics with the ones we can expect from future large ground-based surveys and from a future space experiment like SNAP.
In order to be as model independent as possible we have looked at a large range of fiducial models by varying the parameters of the equation of state of the dark energy w_0^F and w_1^F where $w^F(z) = w_0^F + w_1^F z$ [17].

With present statistics or the one expected from a survey like SNLS, precision on w_1 is very weak and the physical question concerns the extraction of w_0 and Ω_M. For a SNAP like experiment a good precision on w_1 is only possible with a strong prior on Ω_M.

To avoid the use of strong priors on Ω_M, we have focused on the extraction of w_0 only and neglected the w_1 contribution by fixing it in the fitting procedure. We have to face in this case the problem of introducing a bias if the fiducial value of w_1^F is far away from the fixed one. We compare the bias to the statistical error which is expected for each survey.

To study the validity of such a strategy, we have presented an extensive study of fiducial models in a flat universe in which we vary w_0^F and w_1^F in a complete range $-2 < w_0^F < 0$ and $-2 < w_1^F < 2$ corresponding to a large variety of DE theoretical models. On the other hand M_s^F and Ω_M^F are fixed. In the fit we have used in general a weak prior on $\Omega_M (\sigma(\Omega_M) < 0.1)$ and we have looked at the bias introduced by fixing $w_1 = 0$. We call this procedure the 3-fit (M_s, Ω_M, w_0) procedure.

For SNAP (and SNLS) like statistics, we obtain the following conclusions :

- w_0 is not biased for an important part of the scanned plane (w_0^F, w_1^F) which corresponds to models describing a Universe which is today in acceleration.
- for M_s, we get the same conclusion but we emphasize that this parameter is so much constrained in the fitting procedure that a small bias has no visible effect.
- Ω_M is strongly biased if the redshift dependence is large $(|w_1^F| > 0.2(0.6))$.
- If a strong prior on Ω_M is used, w_0 is biased for most of the plane. Namely, the 3-fit procedure is relevant to extract w_0 if only a weak Ω_M prior is used.

We have compared the accuracy of the results on the w_0 parameter to the ones obtained if w_1 is left free as in a 4-fit $(M_s, \Omega_M, w_0, w_1)$ procedure.

We found that, in spite of the bias, the 3-fit procedure, where w_1 is fixed, can be used for SNAP and SNLS to test accelerating models and give better or equivalent results than the simplest 4-fit where w_1 is completely free. This is no longer true if $\mid w_1^F \mid$ is large. For decelerating models the 4-fit is mandatory. Note that, concerning the choice of the number of parameters to be fitted, the bayesian method presented in [33] seems promising.

These conclusions have been set using only the value $\Omega_M^F = 0.3$ for the fiducial models. If the true value is different the areas of the different Validity Zones increase if the contribution of DE is smaller, namely if Ω_M^F is larger. Conversely, if $\Omega_M^F < 0.3$, the validity of the 3-fit is reduced.

Using the presently available statistics of the SCP collaboration [4], it appears that the procedure where w_1 is fixed can be trusted for almost all the fiducial models considered here. Only fiducial models with strong recent variations of the EoS ($\mid w_1^F \mid > 0.7$) may lead to biased results.

Let us point out that other bias would be introduced, by a departure from the $\Omega_T = 1$ paradigm in the fiducial model, or if the central value of the Ω_M prior itself (used in the fitting procedure) is not the same as the fiducial value. Indeed a small bias in the prior could induce some strong bias for the other cosmological parameters. These bias will be studied in a future paper [27].

It has been advocated recently [34] that it should be easier to constrain the DE density $\rho_X(z)$ and its time derivative $\rho'_X(z)$, instead of constraining the equation of state $w(z)$.

These authors have simulated a large variety of fiducial models in the range $-1.2 \leq w_0^F \leq -0.5$ and $-1.5 \leq w_1^F \leq 0.5$, which is almost completely contained in our Validity Zone for SNAP (see Fig. 5). They interpret physically parts of this plane in term of increasing, decreasing or non-monotonic DE densities $\rho_X(z)$.

Their approach is interesting to answer if the DE energy density is a constant or not. Nevertheless, focusing on the equation of state itself remains mandatory if, for instance, one wants to validate precisely the acceleration since, in this case, a precise knowledge of w_0 (and also on Ω_M and Ω_X) is necessary. Finally, we would like to point out that trying to answer any particular question on the nature of DE requires an investigation on the choice of the most relevant fitting procedures.

Acknowledgments

We wish to thank A. Mazure and the members of the Laboratoire d'Astrophysique de Marseille, for their support, and also E. Linder, R. Miquel and F. Steiner, for helpful discussions. "Centre de Physique Théorique" is UMR 6207 - "Unité Mixte de Recherche" of CNRS and of the Universities "de Provence", "de la Méditerranée" and "du Sud Toulon-Var"- Laboratory affiliated to FRUMAM (FR 2291). "Centre de Physique des Particules de Marseille" is "Unité Mixte de Recherche" of CNRS/IN2P3 and of the University "de la Méditerranée".

References

[1] S. Perlmutter et al. Astrophys. J. **517**, 565 (1999)

[2] A.G. Riess et al., Astron. J. **116**, 1009 (1998)

[3] J. Tonry et al., Astrophys. J. **594**, 1 (2003).

[4] R.A. Knop et al. astro-ph/0309368

[5] see e.g. http://cfht.hawai.edu/Science/CFHTLS-OLD/history_2001.html

[6] G. Efstathiou et al., Mon. Not. R. Astron Soc. **330**, L39 (2002).

[7] D.N. Spergel et al. (WMAP Collaboration) Astrophys. J. Suppl. **148**, 175 (2003).

[8] M. Tegmark et al., astro-ph/0310723

[9] R. Scranton et al. astro-ph/0307335

[10] see e.g. N. Bahcall, J.P. Ostriker, S. Perlmutter and P.J. Steinhardt, Science **284**, 1481 (1999) and refs. therein.

[11] P.J.P. Peebles and B. Ratra, Rev. Mod. Phys., **75**, 559 (2003) and references therein; T. Padmanabhan, Phys. Rept. **380**, 235 (2003).

[12] see e.g. http://snls.in2p3.fr

[13] see e.g. http://snap.lbl.gov

[14] A.G. Kim et al., Mon. Not. R. Astron Soc. **347**, 909 (2004).

[15] I. Maor, R. Brustein and P.J. Steinhardt, Phys. Rev. Lett. **86**, 6 (2001).

[16] I. Maor et al., Phys. Rev. **D65**, 123003 (2002).

[17] J. Weller and A. Albrecht, Phys. Rev. Lett. **86**, 1939 (2001); Phys. Rev. **D65**, 103512 (2002), and references therein.

[18] D. Huterer and M.S. Turner, Phys. Rev. **D64**, 123527 (2001).

[19] M. Goliath et al., Astron.& Astrophys. **380**, 6 (2001).

[20] B. F. Gerke and G. Efstathiou, Mon. Not. R. Astron Soc. **335**, 33 (2002).

[21] E. V. Linder and D. Huterer, Phys. Rev.**D67**, 081303 (2003).

[22] E. Di Pietro and J.-F. Claeskens, Mon. Not. R. Astron Soc. **341**, 1299 (2003).

[23] W.M. Wood-Vasey et al., astro-ph/0401513

[24] V. Sahni et al., JETP Lett. **77**, 201 (2003); U. Alam et al., Mon. Not. R. Astron Soc. **344**, 1057 (2003); M. Tegmark, Phys. Rev. **D66**, 103507 (2002); D. Huterer and G. Starkman, Phys. Rev. Lett. **90**, 031301 (2003); P.S. Corasaniti and E.J. Copeland, Phys. Rev. **D67**, 063521 (2003).

[25] E. V. Linder, Phys. Rev. Lett. **90**, 091301 (2003).

[26] J. A. Frieman et al., Phys. Rev. Lett. **75**, 2077 (1995).

[27] J.-M. Virey et al., in preparation.

[28] P.H. Frampton, astro-ph/0302007 and references therein.

[29] S. Nesseris and L. Perivolaropoulos astro-ph/0401556 and references therein.

[30] Our simulation tool, the "Kosmoshow", has been developped by A. Tilquin and is available upon request or directly at
http://marwww.in2p3.fr/renoir/Kosmoshow.html.

[31] A. Blanchard et al., Astron.& Astrophys. **412**, 35 (2003); T. Shanks astro-ph/0401409.

[32] A. Melchiorri et al., Phys. Rev. **D68**, 043509 (2003); S. Hannestad and E. Mortsell, Phys. Rev. **D66**, 063508 (2002); R. Bean and A. Melchiorri, Phys. Rev. **D65**, 041302 (2002).

[33] T.D. Saini, J. Weller and S.L. Bridle, astro-ph/0305526.

[34] Y. Wang et al., astro-ph/0402080 and references therein.

2.2.2 Biais dû à Ω_M

Article publié sous la référence : Phys. Rev. **D70** (2004) 121301.

Probing Dark Energy with Supernovae : a concordant or a convergent model?

J.-M. Virey[1], A. Ealet[2], C. Tao[2], A. Tilquin[2], A. Bonissent[2], D. Fouchez[2] and P. Taxil[1]

[1]Centre de Physique Theorique*, CNRS-Luminy, Case 907, F-13288 Marseille Cedex 9, France and Universite de Provence

[2]Centre de Physique des Particules de Marseille+, CNRS-Luminy, Case 907, F-13288 Marseille Cedex 9, France

Abstract

We present a revised interpretation of recent analysis of supernovae data. We evaluate the effect of the priors on the extraction of the dark energy equation of state. We find that the conclusions depend strongly on the Ω_M prior value and on its uncertainty, and show that a biased fitting procedure applied on non concordant simulated data can converge to the "concordance model". Relaxing the prior on Ω_M points to other sets of solutions, which are not excluded by observational data.

PACS Numbers : 98.80.Es, 98.80.Cq
Key-Words : cosmological parameters - supernovae

Number of figures : 6

July 2004
CPT-2004/P.034
CPPM-P-2004-02

anonymous ftp or gopher : cpt.univ-mrs.fr
E-mail : virey@cpt.univ-mrs.fr

---

*"Centre de Physique Théorique" is UMR 6207 - "Unité Mixte de Recherche" of CNRS and of the Universities "de Provence", "de la Méditerranée" and "du Sud Toulon-Var"- Laboratory affiliated to FRUMAM (FR 2291).

+"Centre de Physique des Particules de Marseille" is UMR 6550 of CNRS/IN2P3 and of the University "de la Méditerranée".

Introduction

The existence and nature of dark energy is one of the most challenging issues of physics today. The publication of high redshift supernovae discovered by the Hubble Space Telescope, by the SCP collaboration [1] and recently by Riess et al. [2], has been interpreted as agreement of the data with the so named ΛCDM "concordance model" ($\Omega_M \approx 0.3$, $\Omega_\Lambda \approx 0.7$, $w = p/\rho = -1$). We have reconsidered some conclusions in the light of our previous analysis of simulated data [3].

Riess et al.[2] have selected 157 well measured SNIa, which they call the "gold" sample, a set of data we will use throughout this paper. Assuming a flat Universe ($\Omega_T = 1$) they conclude that: *i)* Using the strong prior $\Omega_M = 0.27 \pm 0.04$, a fit to a static dark energy equation of state yields -1.46< w <-0.78 ($95\% CL$); *ii)* Looking at a possible redshift dependence of $w(z)$ (using $w(z) = w_0 + w_1 z$), the data with the strong prior indicate that the region $w_1 < 0$ and especially the quadrant ($w_0 > -1$ and $w_1 < 0$) are the least favoured. They reject large time variation and are compatible with the concordance model.

We have shown in [3] that it is unavoidable to get some ambiguities when trying to fit a particular fiducial cosmology with a "wrong" model. This "bias problem" has been mentioned several times in the literature, see *e.g.*[4, 5, 6, 7]. In this letter, we explore the effect of the Ω_M prior on the determination of $w(z)$.

Following [3], we assume a flat universe and keep the same parametrisation of $w(z)$ as in [2], for the sake of comparison. We call 3-fit (4-fit) the fitting procedure which involves the 3 (4) parameters M_S, Ω_M and w_0 (M_S, Ω_M, w_0 and w_1), M_S being a normalisation parameter (see [3] for definitions and formulae). We have performed 3-fits and 4-fits and compared the results in different cases, varying the central value and the uncertainty on the Ω_M prior.

Fit	Ω_M prior	Ω_M	w_0	w_1
3-fit	no	0.48 ± 0.06	-2.2 ± 0.95	/
3-fit	0.27 ± 0.2	0.45 ± 0.07	-1.9 ± 0.73	/
3-fit	0.50 ± 0.2	0.48 ± 0.06	-2.3 ± 0.94	/
3-fit	0.27 ± 0.04	0.28 ± 0.04	-1.0 ± 0.15	/
3-fit	0.50 ± 0.04	0.49 ± 0.03	-2.5 ± 0.77	/
4-fit	no	0.48 ± 0.20	-2.2 ± 1.34	0.12 ± 23
4-fit	0.27 ± 0.2	0.35 ± 0.18	-1.6 ± 0.80	1.74 ± 1.3
4-fit	0.50 ± 0.2	0.49 ± 0.20	-2.6 ± 1.20	1.60 ± 18
4-fit	0.27 ± 0.04	0.28 ± 0.04	-1.3 ± 0.26	1.50 ± 0.84
4-fit	0.5 ± 0.04	0.49 ± 0.04	-2.6 ± 1.40	0.95 ± 10

Table 1: Fit results obtained using the gold data from [2] for various fitting procedures. The χ^2 is very stable, it is around 173 (for 157 SNIa) for all procedures except for the 3-fit with the strong prior $\Omega_M = 0.27 \pm 0.04$ where $\chi^2 \approx 176$.

Applying no prior or the strong prior on Ω_M (lines 1, 4 and 9 of the Table), we recover the results obtained by Riess et al.[2]. Nevertheless, some interesting points can be underlined:

- With no prior or a weak prior on Ω_M, the preferred Ω_M values are always greater than 0.3.
- Without any assumption on Ω_M nor w_1, the error on Ω_M is close to 0.2 (line 6 of Table I).
- Changing the central value of the Ω_M prior leads to a change in the w_0 values of more than 1σ. The w_0 values are strongly correlated to Ω_M and are thus always smaller than the ΛCDM value, when the strong prior on Ω_M is relaxed. χ^2 is very stable but the correlation matrix can vary a lot for the 4-fits and the (w_0,w_1) solution.
- If the Ω_M prior is strong, the conclusion on w_0 depends on the prior value : for Ω_M=0.27, w_0 is forced to values compatible with -1, in particular for the 3-fit and the errors are strongly reduced. For Ω_M=0.5, w_0 is more negative and the errors are significantly larger.
- The only cases where "reasonable" errors can be found on w_1 occur for Ω_M around 0.3.

To illustrate these points, Figure 1 shows the results in the (Ω_M,w_0) plane for the 3-fits(left) and the 4-fits(right), using no prior on Ω_M or two strong priors with the two central values: 0.27 and 0.5. As expected the contours strongly depend on the procedure used to analyse the data. For instance, the $95\%CL$ contours for the two strong prior cases are disconnected. However, we note that $\Omega_M < 0.6$ is valid for all procedures, hence it is one of the strong conclusions from present SN data.

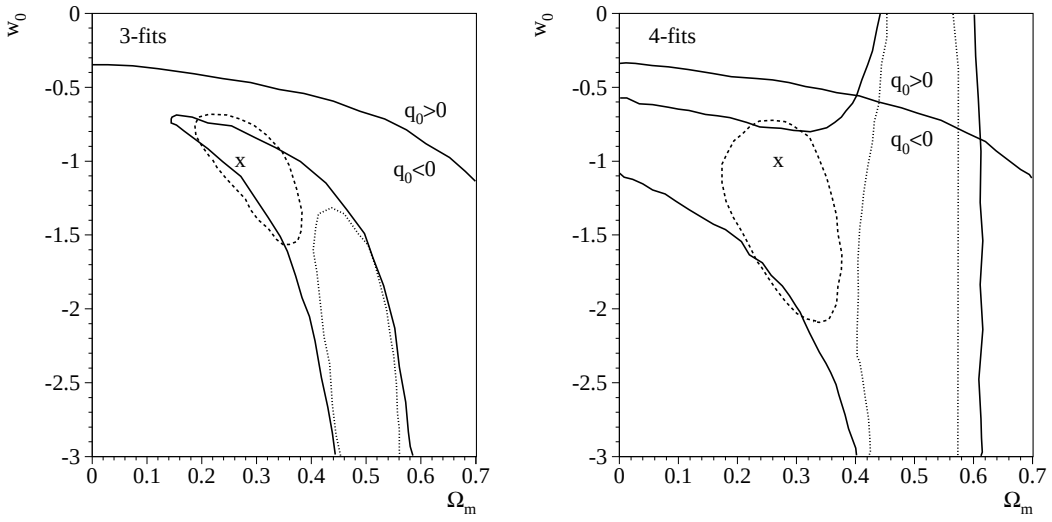

Figure 1: $95\%CL$ contours for 3-fits(left) and 4-fits(right) with no prior on Ω_M (plain) and two strong priors $\Omega_M = 0.27(0.5) \pm 0.04$ (dashed (dotted)). The (x) indicates the ΛCDM point ($\Omega_M = 0.27, w_0 = -1, w_1 = 0$). The plain line separates accelerating ($q_0 < 0$) from decelerating ($q_0 > 0$) models.

Simulation and interpretation :

We have simulated, as in our previous paper[3], SNIa data corresponding to the same statistical power as the data sample, where we vary the fiducial values to study the effects of the priors (on Ω_M or/and w_1).

We start with some illustrations of the bias introduced by the Ω_M prior when it is different from the fiducial value. We consider two fiducial models which are compatible with the data, when no prior is applied: one in acceleration with Ω_M^F =0.5, w_0^F=-2.2, w_1^F=1.6 and one in deceleration with Ω_M^F =0.5, w_0^F=-0.6, w_1^F=-10. We apply the 4-fit to the two models with the two strong priors: $\Omega_M = 0.27 \pm 0.04$ and $\Omega_M = 0.5 \pm 0.04$. Figure 2 shows how the prior affects the conclusions:

• When the correct prior on Ω_M is applied, the central values are not biased but the errors are very large.

• When the wrong prior $\Omega_M = 0.27 \pm 0.04$ is applied, the fitted values are wrong but in agreement with the concordance model. The statistical errors are very small. In all cases, χ^2 is good and does not indicate that something is wrong.

• With the data, it is not possible to distinguish between these two models, but the prior value can lead to wrong conclusions both on values and errors of the fitted parameters.

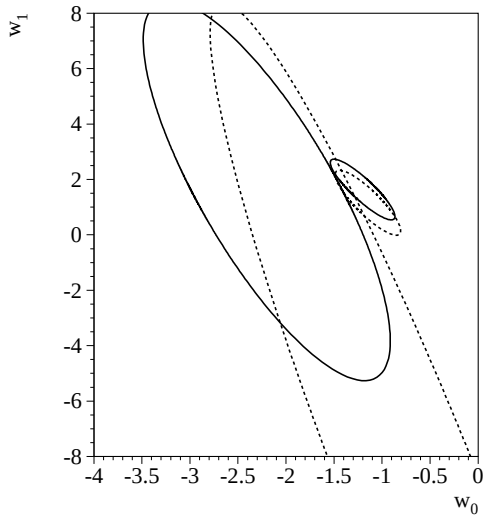

Figure 2: Fisher contours in the (w_0, w_1) plane at 68.3%CL for the two fiducial models: (in acceleration) Ω_M^F =0.5, w_0^F=-2.2, w_1^F=1.6 and (in deceleration) Ω_M^F =0.5, w_0^F =-0.6, w_1^F=-10. The upper indice F is added to avoid confusion between Fiducial values and fitted values. The plain big and small ellipses correspond to the first model analysed with the strong prior $\Omega_M = 0.5 \pm 0.04$ (big ellipse) or with $\Omega_M = 0.27 \pm 0.04$ as in [2](small ellipse). The dashed big and small ellipses correspond to the second model.

We have then performed a complete fit analysis on the simulated data and scanned a large plane of fiducial values (w_0^F, w_1^F) with 3-fits and 4-fits, assuming a flat universe and using two fiducial values for Ω_M^F : 0.27 or 0.5. We always use in the fitting procedures, the strong prior $\Omega_M = 0.27 \pm 0.04$. The case $\Omega_M = \Omega_M^F$ is equivalent to a Fisher analysis and only the errors are studied. In the case $\Omega_M \neq \Omega_M^F$, biases are introduced in the fitted values.

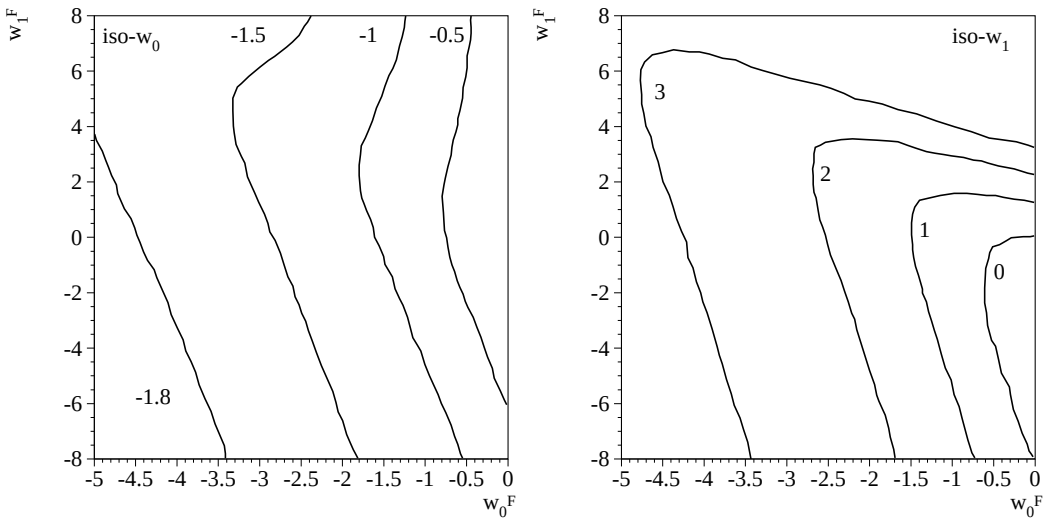

Figure 3: Fitted w_0 (left) and w_1 (right) iso-lines with 4-fits for a fiducial with Ω_M^F =0.5 and a prior $\Omega_M = 0.27 \pm 0.04$, in the plane (w_0^F, w_1^F).

Figure 3 shows the fitted w_0 and w_1 iso-lines for the 4-fits in the biased case. The iso-lines are straight lines (not shown on the figure) when $\Omega_M^F = 0.27$ (unbiased correct prior), but are biased when $\Omega_M^F = 0.5$. This is due to the strong correlations between w_0 and Ω_M, and between w_0 and w_1.

In this configuration, we observe that, for the 4-fit, when $-5 < w_0^F < 0$ (a relatively wide range), the fitted values for w_0 are in a narrow range centred on -1 : $-1.8 < w_0 < 0$. For w_1, the situation is even worse since with fiducial values $-8 < w_1^F < 8$, we get essentially positive values for the fitted w_1. The actual shapes of the distortions between the fiducial and the fitted values are readable on Fig. 3.

A similar analysis performed with the 3-fit shows that the situation is even worse : one gets $-1.5 < w_0 < 0$ whatever the value of w_0^F. As w_1 is forced to 0 and Ω_M to 0.27, w_0 is closer to -1 which corresponds to the preferred solution for the fit.

One can illustrate further this very problematic point, by defining "confusion contours", namely some contours which identify the models in the fiducial parameter space (*e.g.* (w_0^F, w_1^F)) that could be confused with another model. For instance, the contours of Figure 4 give the models in the plane (w_0^F, w_1^F) with $\Omega_M^F = 0.5$ that can be confused (at 1 and 2σ) with the concordance model if the (wrong) strong prior is applied. The two models used for the illustrative Fig. 2 are taken from extreme positions in this confusion contour of Fig. 4.

For the 3-fit, the confusion contours with the concordance model are very large and include all models having roughly $w_1^F < (-5w_0^F - 10)$. The situation here is particularly bad since the fitting procedure is making two strong assumptions ($w_1 = 0$ and $\Omega_M = 0.27 \pm 0.04$) which are not verified by the fiducial cosmology (two biases).

The next step is to study the parameter errors. We look at the correlation of the errors using fiducial models where Ω_M^F =0.27 or 0.5. We determine the w_0 and w_1 errors, scanning the full plane (w_0^F, w_1^F) using 4-fits.

Some regions of the parameter space (see Figure 5) are favoured and always produce

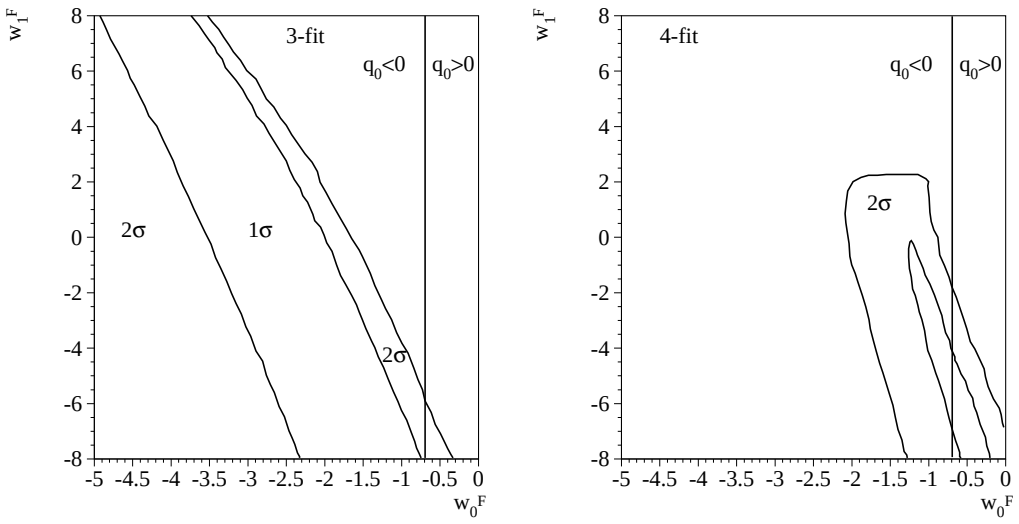

Figure 4: Confusion contours in the fiducial plane (w_0^F, w_1^F) which identify the models that would be confused with the concordance model at 1 and 2σ for the 3-fit(left) and the 4-fit(right) procedures. The strong prior is $\Omega_M = 0.27 \pm 0.04$ whereas the fiducial model is $\Omega_M^F = 0.5$. The vertical line separates accelerating from decelerating models.

small errors. This is due to the correlation between w_0 and w_1. The error depends strongly on the fitted w_0 and w_1 values but not strongly on the Ω_M value: a different value of Ω_M affects the scale of the errors but not the shape of the plots. We find a linear scaling of the error when we change Ω_M from 0.27 to 0.5 (*i.e.* a factor 2).

Combining this with the previous paragraph leads to an interesting point, *i.e.* the favoured fitted values of the fit ($w_0 > -1.8$ and $w_1 > 0$), which were shown to be mainly driven by the prior value, correspond also to the region of the plane where the parameters errors are always small.

We conclude that the applied fitting procedure with this strong prior can bias the conclusions by constraining the (w_0, w_1) solution near the (-1,0) solution, where the statistical error is always very small. In particular, Riess et al.[2] found a gain factor of order 8 on the accuracy of the neasurement compared to previous analysis. This is mainly due to the Ω_M prior and not to the inclusion of the high z HST events. The present observational constraints on Ω_M are thus an important issue.

Revisited conclusions on existing data :

Most reviewers of cosmological parameters favour a value close to the strong prior choice made by [2]. This result is based on WMAP[8] data combined with 2dF data[9] or more recently with SDSS data[10], and corresponds to [8]([10]) $\Omega_M = 0.27(0.3) \pm 0.04$ with $h = 0.71(0.70)^{+0.04}_{-0.03}$. However, these results are based on several prior assumptions in order to lift the degeneracies among the various cosmological parameters (*e.g.* Ω_M, h, σ_8, w ...). For instance, Spergel et al.[8] mention that a solution with $\Omega_M = 0.47$, $w = -0.5$ and $h = 0.57$ in the CMB is degenerate with the ΛCDM model. This kind of solution is excluded for three reasons: the Hubble Constant value is 2σ lower than the HST Key Project value and the model is a poor fit to the 2dF and SN data.

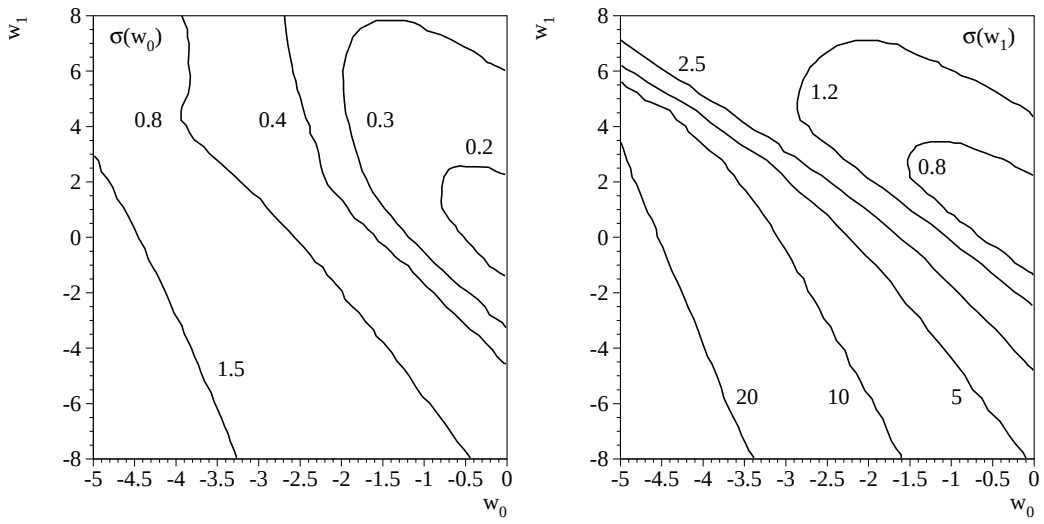

Figure 5: w_0 and w_1 errors for a 4-fit with the correct strong prior, for a fiducial with Ω_M^F =0.27.

However, *i)* in spite of the precise HST result, the Hubble constant value is still controversial[11, 12]. *ii)* We have shown in the previous section that the SN data analysis can only conclude that $\Omega_M < 0.6$ (see Fig. 1). *iii)* The 2dF and the SDSS Collaborations [9, 13] have extracted $\Omega_M h$ from an analysis of the power spectrum of galaxy redshift surveys. The degeneracy between $\Omega_M h$ and the baryon fraction is lifted thanks mainly to the precise determination of the baryon fraction by CMB data (see Fig.38 of [13]). Should that prior change, the preferred values from SDSS would indicate a higher value of $\Omega_M h$.

In addition, a large variety of observations give constraints on Ω_M, which is found to vary from 0.16 ± 0.05 [14] up to a value above 0.85 [15].

Conversi et al.[12] provide an interesting critical analysis on the present constraints on cosmological parameters, especially on Ω_M, h, and w. Through the study of the degeneracies, they show that the result $\Omega_M = 0.27 \pm 0.04$ is obtained under the assumption of the ΛCDM model, and provide specific examples with smaller h ($h < 0.65$) and higher Ω_M ($\Omega_M > 0.35$) which are in perfect agreement with the most recent CMB and galaxy redshift surveys.

In conclusion, we follow the point of view of Bridle et al.[16], who argue that it may be "that the real uncertainty is much greater" than the 0.04 error obtained from the combination of CMB and large scale structure data.

Returning to SN data analysis, we suggest, for the time being, to reevaluate the conclusions by relaxing the Ω_M central value. Figure 6 shows the $95\% CL$ constraints in the (w_0,w_1) plane obtained from the gold sample [2] with no prior assumption on Ω_M. Taking an uncertainty of 0.2, which is the intrinsic sensitivity of SN results (see Table I, line 6), does not change the conclusions:

• Large positive variations in time of the equation of state are excluded (at $95\% CL$) since the dark energy density blows up as $e^{3w_1 z}$ [17].

• The quintessence models which have in general ($w_0 > -1$, $1 > w_1 > 0$) [5] are seriously constrained. For instance, the SUGRA model [18] characterized by $w_0 \approx -0.8$ and $w_1 \approx 0.3$[5] is close to the border of the $95\% CL$ contour (precisely, one gets $\Delta\chi^2$=3.5

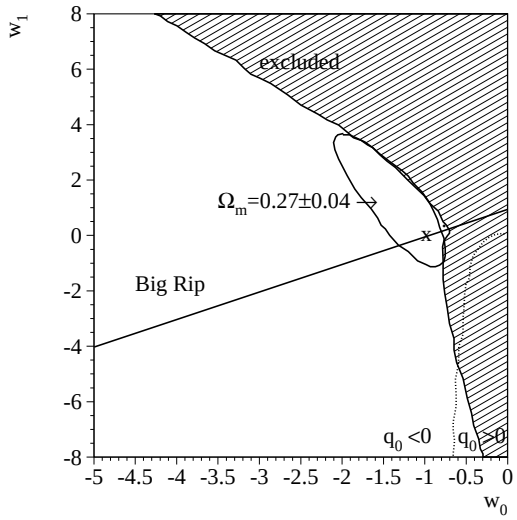

Figure 6: The shaded region is excluded at $95\%CL$ when no prior on Ω_M is applied. The ellipse corresponds to the strong prior constraints as in [2]. The (x) is ΛCDM. The dotted line separates accelerating from decelerating models.

corresponding to an exclusion at $80\%CL$).

• The quadrant ($w_0 > -1$, $w_1 < 0$) corresponding to k-essence models [19] or some Big Crunch models [20, 2], is not the "least favoured", contrary to the conclusions drawn with the strong prior [2]. We find that if w_0 goes towards 0, then w_1 should be more and more negative.

• If $w_0 < -1$, the constraints on w_1 are weak (except for large positive values). This region of the plane corresponds to phantom models [21] which have unusual properties and may have very different consequences for the fate of the Universe (*e.g.* models with $w_1 > w_0 + 1$ will end in a Big Rip [17]). Models with very exotic $w(z)$ may come from modified gravity[22]. The class of models with $w_1 < 0$ is roughly excluded at $95\%CL$, if the strong prior $\Omega_M = 0.27 \pm 0.04$ is used [2], but is perfectly allowed for higher Ω_M values (or larger prior errors).

• As can be seen on Fig. 6 (and also on Figures 1, 4 and the decelerating model used to draw Fig.2), our analysis without assumptions on Ω_M and w_1, allows decelerating models with specific properties : low w_0, $\Omega_M \approx 0.5$ and $w_1 << 0$. One can wonder if this result is not in tension with the geometrical test performed in [2] where the only assumption is to use a linear functional form for $q(z)$ (*i.e.* $q_0 + q_1 z$). It can be shown that a varying equation of state implies a non-linear $q(z)$, in particular, the linear approximation breaks down if $w_1^F < -1.5$. More details on this more subtle analysis will be presented in a forthcoming paper [23].

To go further, a coherent combined analysis of all data is mandatory, with a proper treatment of correlations and no prior assumptions. Some recent papers go in that direction [17, 24, 25, 26].

In addition, as soon as the statistical errors will become smaller, systematic questions cannot be neglected and should be controlled at the same level of precision. This is the challenge for the next generation of experiments. A promising approach is to combine SNIa with weak lensing, as proposed by the future dedicated SNAP/JDEM mission [27].

Acknowledgments :

We thank the members of the cosmology group of the Laboratoire d'Astrophysique de Marseille (LAM), and in particular C. Marinoni for helpful discussions. *"Centre de Physique Théorique" is UMR 6207 - "Unité Mixte de Recherche" of CNRS and of the Universities "de Provence", "de la Méditerranée" and "du Sud Toulon-Var"- Laboratory affiliated to FRUMAM (FR 2291). +"Centre de Physique des Particules de Marseille" is UMR 6550 of CNRS/IN2P3 and of the University "de la Méditerranée".

References

[1] R.A. Knop et al. Astrophys.J. **598**, 102 (2003)

[2] A.G. Riess et al., Astrophys.J. **607**, 665 (2004)

[3] J.-M. Virey et al., Phys.Rev. **D70**, 063414 (2004)

[4] I. Maor et al., Phys.Rev.Lett. **86**, 6 (2001) ; I. Maor et al., Phys.Rev. **D65**, 123003 (2002)

[5] J. Weller and A. Albrecht, Phys.Rev. **D65**, 103512 (2002)

[6] B. F. Gerke and G. Efstathiou, MNRAS **335**, 33 (2002)

[7] E. Linder, astro-ph/0406189

[8] D.N. Spergel et al. Astrophys. J. Suppl. **148**, 175 (2003)

[9] E. Hawkins et al., MNRAS **347**, 78 (2003)

[10] M. Tegmark et al., Phys.Rev. **D69**, 103501 (2004)

[11] A. Blanchard et al., Astron.Astrophys. **412**, 35(2003)

[12] L. Conversi et al., Astropart.Phys. **21** 443 (2004)

[13] M. Tegmark et al., Astrophys.J. **606**, 702 (2004)

[14] N. Bahcall et al., Astrophys.J. **541**, 1 (2000)

[15] S. Vauclair et al., Astron.Astrophys. **412** (2003) L37

[16] S. Bridle et al., Science **299**, 1532 (2003)

[17] Y. Wang and M. Tegmark, Phys.Rev.Lett. **92**, 241302 (2004)

[18] P. Brax and J. Martin, Phys.Lett.**B468**, 40 (1999)

[19] C. Armendariz-Picon et al., Phys.Rev.Lett.**85**, 4438 (2000); Phys.Rev.**D63**, (2001) 103510

[20] R. Kallosh and A. Linde, JCAP **302**, 2 (2003)

[21] R. Caldwell, Phys.Lett.**B545**, 23 (2002)

[22] E. Linder, astro-ph/0402503

[23] J.-M. Virey et al., in preparation

[24] A. Melchiorri et al., Phys. Rev. **D68**, 043509 (2003)

[25] S. Hannestad and E. Mörstell, astro-ph/0407259

[26] P. Corasaniti et al., astro-ph/0406608

[27] E. Linder, astro-ph/0406186

2.2.3 Biais dû à une évolution non-linéaire de $q(z)$

Article publié sous la référence : Phys. Rev. **D72** (2005) 061302.

On the determination of the deceleration parameter from Supernovae data

J.-M. Virey[1], P. Taxil[1], A. Tilquin[2], A. Ealet[2], C. Tao[2] and D. Fouchez[2]

[1]Centre de Physique Theorique*, CNRS-Luminy, Case 907, F-13288 Marseille Cedex 9, France and Universite de Provence

[2]Centre de Physique des Particules de Marseille+, CNRS-Luminy, Case 907, F-13288 Marseille Cedex 9, France

Abstract

Supernovae searches have shown that a simple matter-dominated and decelerating universe should be ruled out. However a determination of the present deceleration parameter q_0 through a simple kinematical description is not exempt of possible drawbacks. We show that, with a time dependent equation of state for the dark energy, a bias is present for q_0 : models which are very far from the so-called Concordance Model can be accommodated by the data and a simple kinematical analysis can lead to wrong conclusions. We present a quantitative treatment of this bias and we present our conclusions when a possible dynamical dark energy is taken into account.

PACS Numbers : 98.80.Es, 98.80.Cq
Key-Words : cosmological parameters - supernovae

Number of figures : 3

February 2005
CPT-2005/P.007

anonymous ftp or gopher : cpt.univ-mrs.fr
E-mail : virey@cpt.univ-mrs.fr

---

*"Centre de Physique Théorique" is UMR 6207 - "Unité Mixte de Recherche" of CNRS and of the Universities "de Provence", "de la Méditerranée" and "du Sud Toulon-Var"- Laboratory affiliated to FRUMAM (FR 2291).

+"Centre de Physique des Particules de Marseille" is UMR 6550 of CNRS/IN2P3 and of the University "de la Méditerranée".

Observations [1, 2] of Type Ia Supernovae (SNe) allow to probe the expansion history of the universe. The measurements of the apparent magnitudes $m(z)$ of SNe determine the luminosity distance versus redshift $d_L(z)$ which reads for a flat ($\Omega_T = 1$) universe :

$$\begin{aligned} d_L(z) &= c(1+z)\int_0^z \frac{du}{H(u)} \\ &= \frac{c(1+z)}{H_0}\int_0^z du\, e^{\left[-\int_0^u [1+q(x)]d\ln(1+x)\right]} \end{aligned} \tag{1}$$

where $d_L(z)$ is written here in terms of the epoch-dependent deceleration parameter $q(z) \equiv (-\ddot{a}/a)/H^2(z)$ with $H(z) = \dot{a}/a$. $d_L(z)$ is related to the measured magnitude by $m(z) = M_S + 5log_{10}(H_0/c\, d_L(z))$, M_S being a normalisation parameter which combines the absolute SNe magnitude and the Hubble constant.

The present behavior of the expansion is attributed to a new "Dark Energy" (DE) component with negative pressure : $p_X = w\,\rho_X$, with a possibly time dependent equation of state (EoS) $w(z)$ (for a recent review see Ref. [3]). Ω_X (Ω_M) will denote the ratio of the present DE (Matter) density to the critical density. In this framework, with $\Omega_T = 1$ and neglecting the radiation component :

$$\begin{aligned} d_L(z) &= \frac{c(1+z)}{H_0}\int_0^z du \\ &\left[(1+u)^3\Omega_M + \Omega_X e^{3\int_0^u [1+w(x)]d\ln(1+x)}\right]^{-1/2} \end{aligned} \tag{2}$$

The connection with Eq.(1) is given by :

$$q(z) = \frac{1}{2} + \frac{3}{2}w(z)\Omega_X(z)\ ;\ \Omega_X(z) = \Omega_X\frac{\rho_X(z)H_0^2}{\rho_X(0)H^2(z)} \tag{3}$$

In Ref.[2] Riess et al. have recently presented an analysis of 156 SNe including a few at $z > 1.3$ from the Hubble Space Telescope (HST) GOODS ACS Treasury survey. They use a kinematical description (no dynamical hypothesis) with a simple parametrization of $q(z)$ in Eq.(1), $q(z) = q_0 + q_1\, z$, and conclude to the evidence for present acceleration $q_0 < 0$ at 99% C.L. ($q_0 \approx -0.7$) and for past deceleration $q(z) > 0$ beyond $z_t = 0.46 \pm 0.13$. Concerning the dynamics in a flat universe, they conclude on the validity of the Cosmic Concordance version of the ΛCDM Model that is $\Omega_M \approx 0.3$, $w(z = 0) \approx -1$ and no rapid evolution of the EoS.

Performing the same kind of analysis, we confirm the numbers and errors obtained with the Gold Sample (see Ref. [2]) of SNe for the "kinematical fit" : $q_0 = -0.74 \pm 0.18$ and $q_1 = 1.59 \pm 0.63$. In spite of the goodness of the fit and of the relatively small errors it yields, this simple strategy leads to some bias which we quantify in the following.

As noticed several times, [4, 5, 6, 7, 8] the physical parameters Ω's and $w(z)$ are related to the measured quantity $d_L(z)$ through a multiple integral relation which results in a somewhat uncertain determination of these parameters, even at their present values Ω_M and $w(0)$. In Ref.[8] we have analysed quantitatively the bias which occurs when one tries to extract $w(0)$ neglecting a possible redshift dependence of $w(z)$. In the same time, other fitted quantities (essentially Ω_M) are affected, due to strong correlations between Ω_M, $w(0)$ and $dw(z)/dz$. Another pitfall originates from the assumed value (and uncertainty)

of the prior on Ω_M which is used for the fit [9] : an artificial convergence towards the Concordance Model seems to occur whereas the simulated fiducial model is very different.

Concerning the determination of the deceleration parameter, one encounters a similar problem : the extraction of q_0 is not independent of the assumed form of the function $q(z)$, a form which is related (dynamical approach) or not (kinematical approach of Riess et al.) to the evolution of the DE EoS and to the value of Ω_M. Indeed, when choosing the kinematical approach, Riess et al. are in some sense model independent but they must use a particular *description* of the kinematics : e.g. the linear form $q(z) = q_0 + q_1\, z$. It is valuable to question this description, for instance in the light of some dynamical models which include an evolution of the DE EoS.

To modelize the evolution of the EoS, in the absence of deep physical insight, the choice of a parametrization is arbitrary. Simplicity imposes a two-parameter parametrization for $w(z)$, then consistency with the data from the Cosmic Microwave background (CMB) imposes $w(z) \leq 0$ at high redshift. Therefore, the simple linear parametrization :

$$w(z) = w_0 + w_1\, z \tag{4}$$

we have used previously [8, 9] (with many other authors) is too badly behaved at high z. We prefer to switch to the parametrization advocated in [10, 11] and which is now widely used in the literature [12, 14, 15, 13, 16].

$$w(z) = w_0 + w_a z/(1+z) \tag{5}$$

Then from Eq.(5), one gets :

$$\Omega_X(z) = \Omega_X\, \frac{H_0^2}{H^2(z)}\, (1+z)^{3(1+w_0+w_a)} e^{-3w_a z/(1+z)} \tag{6}$$

and $q(z)$ reads :

$$\begin{aligned} q(z) &= \frac{1}{2} + \frac{3}{2}(w_0 + w_a \frac{z}{1+z}) \\ &\quad \times \left[1 + \frac{\Omega_M}{\Omega_X}(1+z)^{-3(w_0+w_a)} e^{3w_a z/(1+z)}\right]^{-1} \end{aligned} \tag{7}$$

The behavior of $q(z)$ is plotted in Fig.1 for various models listed in Table I : it is obvious that $q(z)$ is in general far from a linear shape. Even in the ΛCDM model, $q(z)$ is not exaclty linear in z as can be seen from Eq.(7) and Fig.1.

To illustrate the consequence of the non-linear form of $q(z)$ on the kinematical fit, we simulate SNe data samples corresponding to the same statistical power as the true data sample by fixing the fiducial(^{F}) values for the parameters M_S^F, Ω_M^F, w_0^F and w_a^F. In the following, we consider a flat cosmology and we fix $M_S^F = -3.6$. Then we perform a three-parameter (M_S, q_0, q_1) kinematical fit of the simulated data. The results for the models we use are presented in Table I.

First, the ΛCDM Concordance model ($w_0^F = -1$, $w_a^F = 0$) with the Ω_M value (0.27) of [2], yields a fitted value: $q_0 = -0.57 \pm 0.17$ which reproduces well the fiducial value in the limit of the errors. Note however that the value $q_0^{data} = -0.74 \pm 0.18$ obtained from the real data is 1σ away from the actual ΛCDM value.

With Model A, where a time variation of the EoS is allowed ($w_a^F \neq 0$), we illustrate the fact that even if q_0^F from Eq. (7) is independent of w_a^F, its fitted value is not.

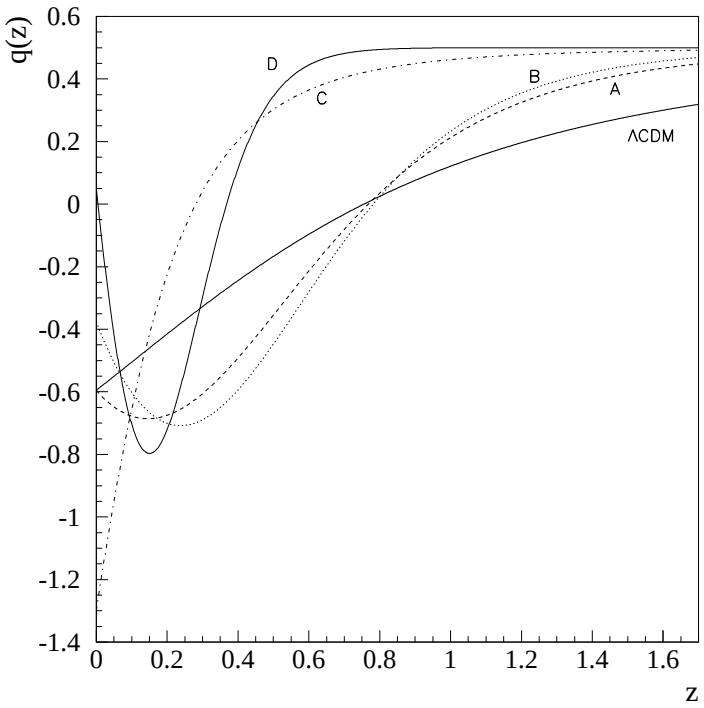

Figure 1: $q(z)$ from Eq.(7) with $\Omega_T = 1$ and some particular values of the parameters (Ω_M, w_0, w_a) given in Table I.

model	Ω_M	w_0	w_a	$q_0(\Omega_M, w_0)$	fitted q_0
ΛCDM	0.27	-1	0	-0.6	-0.57 ± 0.17
A	0.27	-1	-2	-0.6	-0.79 ± 0.17
B	0.27	-0.8	-3.2	-0.38	-0.74 ± 0.17
C	0.50	-2.4	1.4	-1.3	-0.75 ± 0.18
D	0.50	-0.6	-15	0.05	-0.75 ± 0.18

Table 1: Model examples with fiducial values (Ω_M, w_0, w_a). The fiducial $q_0(\Omega_M, w_0)$ is calculated from Eq.(7). The fitted q_0 are obtained with a linear 3-fit (M_S, q_0, q_1) of the simulated data. These values are well in agreement with the one extracted from the Gold Sample ($q_0^d = -0.74 \pm 0.18$). For consistency, Models A,B,C,D have been chosen to give a good dynamical 4-fit $(M_S, \Omega_M, w_0, w_a)$ of the Gold Sample.

Ω_M prior	Ω_M	w_0	w_a	q_0
0.27 ± 0.04	$0.27^{+0.04}_{-0.04}$	$-1.49^{+0.31}_{-0.34}$	$3.20^{+1.60}_{-1.60}$	$-1.12^{+0.33}_{-0.36}$
0.27 ± 0.20	$0.33^{+0.15}_{-0.21}$	$-1.70^{+0.60}_{-0.60}$	$3.50^{+2.20}_{-4.30}$	$-1.21^{+0.49}_{-0.45}$

Table 2: Results of a "dynamical" 4-fit with $w(z) = w_0 + w_a z/(1+z)$ using the Gold data from [2].

With model B (this model could correspond to one of the k-essence models [17]), the fitted q_0 value is now 2σ away from the fiducial ($q_0^F = -0.38$) .

In model C, we have changed the fiducial Ω_M^F value to 0.5. We have $w_0^F < -1$ (as in phantom models [18], see e.g. [19] for a list of references) and a positive w_a^F. The bias is then very large since the fitted q_0 is more than 3σ away from the fiducial value.

One can even get a truly slowly decelerating model with model D : $q_0^F = 0.05$, still with $\Omega_M^F = 0.5$, $w_0^F = -0.6$ and a very rapid and recent evolution of $w(z)$: $w_a^F = -15$. Of course the behavior of Model D seems somewhat artificial and the result of the fit can be seen from the non-monotonicity of $q(z)$ in this model (see Fig.1), which leads to compensations in the integral of Eq.(1). However, let us stress again that Model D as well as Models A,B,C fit perfectly the present SNe data, yielding in particular $q_0 \approx q_0^{data}$.

More quantitatively, it is interesting to pin down some regions in the parameter space where the kinematical fit gets in trouble. Following Ref.[8], we fix Ω_M^F and M_S^F and we consider the plane of the fiducial (w_0^F, w_a^F). In this plane, we define the Biased Zone (BZ) for q_0 as the zone where the kinematical fit converges perfectly but where the difference between the fitted value and the fiducial value q_0^F is larger than the statistical error $\sigma(q_0)$. The validity zone (VZ) is the complementary region. It must be stressed that the BZ is undetectable with real data. We give the two zones in Fig. 2 for $\Omega_M^F = 0.27$. The ΛCDM falls in the VZ as expected, and the models A,B,C,D belong to the BZ. Within the VZ, the zone where the linear approximation $q(z) = q_0 + q_1 z$ of Eq.(7) is acceptable is quite small. In fact the rest of the VZ is due to accidental cancellations when Eq.(7) is injected in Eq.(1). The lower-right corner of the BZ corresponds to models such that $w_a \leq -3w_0^2\Omega_M$; they display a non-monotonic behavior for $q(z)$ which explains the bias. In addition, even with $\Omega_M^F = 0.27$, there exists a region in this zone where the conclusion on the sign of q_0 could be misleading, i.e. a zone where $q_0 + \sigma(q_0) \leq 0$ whereas $q_0^F \geq 0$. This zone corresponds to $-0.5 < w_0^F < 0$ with large and negative w_a^F.

Therefore, it appears that the linear expression of $q(z)$ at first order : $q(z) = q_0 + q_1 z$, cannot be satisfactorily used over a large range of EoS parameters. Going to a second order parametrization will not improve the issue, as it will only enlarge the number of parameters, will degrade the errors, and will not solve the bias problem.

Alternatively, one can deduce a q_0 value from real data using Eq.(7) (with $z = 0$) where we consider the dynamical description Eqs.(2)and (5), by performing a 4-parameter fit $(M_S, \Omega_M, w_0, w_a)$ of the Gold Sample of [2]. We have calculated asymetric standard deviations (deviation $\delta\chi^2 = 1$ for a given parameter), marginalizing over the other parameters by minimisation. For q_0, which is a derived parameter, we use a Monte-Carlo technique : generating 1000 simulated experiments around the data best fit, we estimate the width of the q_0 distribution.

The extracted values are displayed in Table II. In this Table, we have used a strong

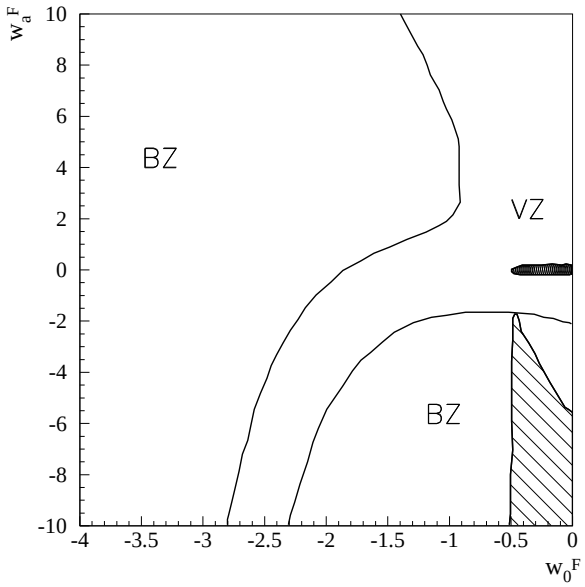

Figure 2: Biaised Zone (BZ) and Validity Zone (VZ) for the deceleration parameter q_0, for the kinematical fit (M_S, q_0, q_1) of the simulated data in the fiducial plane (w_0^F, w_a^F) with $\Omega_M^F = 0.27, M_S^F = -3.6$. Small dark zone : where the linear approximation $q(z) = q_0 + q_1 z$ is acceptable ; hatched zone : where the conclusion on the sign of q_0 could be misleading.

prior on Ω_M (0.27 ± 0.04) and also a more reasonable weaker uncertainty of ± 0.2, since adopting strong priors is recognized to be dangerous (see [9, 16]). Comparing with our previous fits, we see that changing the $w(z)$ parametrization from Eq.(4) to Eq.(5) has not changed the behaviors discussed in [9]. In particular choosing a strong prior around $\Omega_M = 0.3$ pushes w_0 towards -1 whereas, with a weaker prior the central value of w_0 is clearly lower than -1, a fact which has been noticed by many authors (see e.g. [14, 16, 20, 21, 22]).

The estimated q_0 values confirm that the Universe is presently in an acceleration phase, at 95% $C.L.$ We note that the extracted value for a weak prior is 2σ away from the ΛCDM value $q_0 = -0.6$. This is a direct consequence of the extracted value of the point (w_0, w_a), which is 2σ away from $(-1, 0)$. With the strong prior, the errors on q_0, as on other parameters, are systematically smaller when Ω_M is close to the Concordant Model value (≈ 0.3). This conclusion would be different if we use a larger central value for Ω_M : in this case, the q_0 value would be even more negative, but with such a large error that it is not possible to conclude.

Finally, if no prior is applied on Ω_M, one can conclude with some caution that $q_0 < 0$ at 80% C.L.

We can also address the problem of the determination of the value of the transition redshift z_t between deceleration and acceleration. Since the kinematical fit yielding the q_0 and q_1 values found in Ref.[2] is biased, one cannot be too confident with the advocated value $z_t = 0.46 \pm 0.13$.

Fig. 3 displays the function $q(z) = q_{bf}(z)$ computed from the best fit (bf) values of the parameters entering Eq.(7). The 1σ and 2σ intervals are computed by taking the probability density of simulated experiments around the $q_{bf}(z)$ value in each redshift bin.

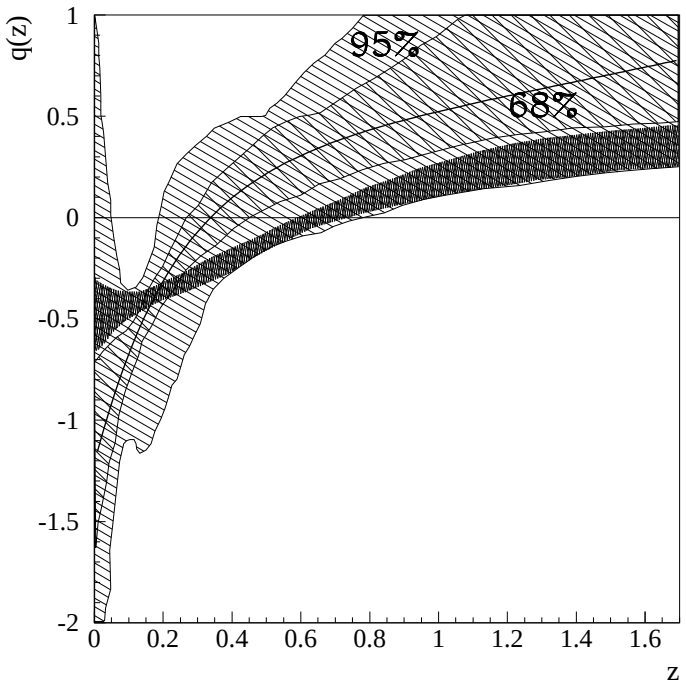

Figure 3: best fit $q_{bf}(z)$ function computed with Eq.(7) using the best fit values of the cosmological parameters from the current data (heavy plain curve). The uncertainty contours are constructed from the probability density function around the best fit at a given redshift from one thousand simulated experiments. The dark stripe corresponds to the 1σ error on the fitted function from a simulation around the ΛCDM concordant model fiducial values, with the SNAP statistics.

We still use a weak prior $\Omega_M = 0.27 \pm 0.2$. The extracted z_t value corresponds to the point where $q_{bf}(z_t) = 0$ and $\frac{dq_{bf}}{dz}(z = z_t) > 0$. We find $z_t = 0.34^{+0.12}_{-0.06}$, where the errors are evaluated from the z_t probability density. With the dynamical $q(z)$, our errors are small because the transition is steeper than in the linear kinematical case ($q(z) = q_0 + q_1 z$), as can be seen from Fig. 3.

Our central value is far from the "theoretical" z_t of the Concordance Model : $z_t = [\frac{2\Omega^0_\Lambda}{\Omega^0_M}]^{1/3} - 1 = 0.76\,(\text{for}\,\Omega_M = 0.27)$. Moreover, we have observed that, contrary to the extraction of q_0, the extraction of z_t is very much dependent upon the chosen parametrization for $w(z)$, a fact mentioned by various authors [23, 20]. Then, one can stay prudent and state that, with present data, the extracted z_t value is certainly much less robust than the extracted q_0 value, even in a dynamical approach. We should also point out that no systematical effects are taken into account in these evaluations, in particular a normalisation effect between low and high redshift supernovae would affect directly the determination of z_t.

It is interesting to evaluate what should be the best strategy to extract q_0 and z_t in the future. Using a biased method, as the linear kinematical one, will be worse when the statistical errors will decrease. A dynamical, although model-dependent approach, remains a good way to estimate the behavior of the acceleration. In Fig. 3, we show the

results for a statistical sample expected from the space-based SNAP mission [24] where the systematical uncertainties should be controlled at the same level of precision. Thanks to the rich sample of 2000 SNe and also to the large range of redshift ($0.2 \leq z \leq 1.7$) a very precise determination of the transition region should be allowed. For instance, with the ΛCDM fiducial values ($w_0 = -1, w_a = 0, \Omega_M = 0.27$), keeping a weak prior on Ω_M, one gets $z_t = 0.67^{+0.08}_{-0.06}$ and $q_0 = -0.55^{+0.26}_{-0.13}$.

We estimate that the correct procedure for the future is to avoid using priors on Ω_M. We prefer instead the combination of supernovae data with other probes such as the CMB, the Weak Gravitational Lensing and the galaxy power spectrum. This kind of method will not introduce external biases and some recent papers go in that direction (see e.g. [16, 21, 22, 25]).

Acknowledgments :

We thank the members of the Laboratoire d'Astrophysique de Marseille and Alain Mazure in particular for fruitful discussions.

References

[1] R.A. Knop et al. Astrophys.J. **598**, 102 (2003)

[2] A.G. Riess et al., Astrophys.J. **607**, 665 (2004)

[3] T. Padmanabhan, Current Science, in press, astro-ph/0411044

[4] I. Maor, R. Brustein and P.J. Steinhardt, Phys.Rev.Lett. **86**, 6 (2001) ; I. Maor et al., Phys.Rev. **D65**, 123003 (2002)

[5] J. Weller and A. Albrecht, Phys.Rev. **D65**, 103512 (2002)

[6] B. F. Gerke and G. Efstathiou, MNRAS **335**, 33 (2002)

[7] E. Linder, astro-ph/0406189

[8] J.-M. Virey et al., Phys.Rev. **D70**, 043514 (2004)

[9] J.-M. Virey et al., Phys.Rev. **D70**, 121301(R) (2004)

[10] M. Chevallier and D. Polarski, Int.J.Mod.Phys. **D10**, 213 (2001)

[11] E. V. Linder, Phys. Rev. Lett. **90**, 091301 (2003)

[12] Y. Wang and M. Tegmark, Phys.Rev.Lett. **92**, 241302 (2004)

[13] U. Seljak et al., astro-ph/0407372

[14] T.R. Choudurhy and T. Padmanabhan, Astron.Astrophys. **429** 807 (2005)

[15] D. Rapetti, S.W. Allen and J. Weller, astro-ph/0409574

[16] A. Upadhye, M. Ishak, P.J. Steinhardt, astro-ph/0411803

[17] C. Armendariz-Picon et al., Phys.Rev.Lett.**85**, 4438 (2000); Phys.Rev.**D63**, (2001) 103510

[18] R. Caldwell, Phys.Lett.**B545**, 23 (2002)

[19] S.M. Carrol, A. De Felice and M. Trodden, astro-ph/0408081

[20] D.A. Dicus and W. W Repko, Phys. Rev. **D70**, 083527 (2004)

[21] S. Hannestad and E. Mörstell, J. Cosmol. Astropart.Phys 09, (2004) 001.

[22] P.S. Corasaniti et al., Phys. Rev. **D70**, 0830006 (2004)

[23] B.A. Basset, P.S. Corasaniti and M. Kunz, Astrophys.J. **617** L1-L4 (2004)

[24] see http://snap.lbl.gov or E. V. Linder, astro-ph/0406186

[25] M. Ishak, astro-ph/0501594

2.2.4 Prospective SNIa : champ large ou profond ?

Article publié sous la référence : Astronomy and Astrophysics **464** (2007) 837.

Sensitivity and figures of merit for dark energy supernovae surveys

J.-M. Virey[1], **A. Ealet**[2]

[1]Centre de Physique Theorique*, CNRS-Luminy, Case 907, F-13288 Marseille Cedex 9, France and Universite de Provence

[2]Centre de Physique des Particules de Marseille+, CNRS-Luminy, Case 907, F-13288 Marseille Cedex 9, France

Abstract

Tracking the origin of the accelerating expansion of the Universe remains one of the most challenging research activities today. The final answer will depend on the precision and on the consistency of future data. The sensitivity of future surveys and the control of the errors are crucial. We focus on futur supernovae surveys in the light of the figure of merit defined by the Dark Energy Task Force. We compare different optimisation and emphasize the importance of the understanding of the systematic error level in this approach and their impact on the conclusions. We discuss different representations of the results to distinguish ΛCDM from other theoretical models. We conclude that all representations should be controlled through combined analyses and consistency checks to avoid some bias.

PACS Numbers : 98.80.Es, 98.80.Cq
Key-Words : cosmological parameters - supernovae - observations
Number of figures : 6
July 2006
anonymous ftp or gopher : cpt.univ-mrs.fr
E-mail : virey@cpt.univ-mrs.fr

---

*"Centre de Physique Théorique" is UMR 6207 - "Unité Mixte de Recherche" of CNRS and of the Universities "de Provence", "de la Méditerranée" and "du Sud Toulon-Var"- Laboratory affiliated to FRUMAM (FR 2291).

+"Centre de Physique des Particules de Marseille" is UMR 6550 of CNRS/IN2P3 and of the University "de la Méditerranée".

1 Introduction

The discovery of the acceleration of the Universe is one of the most intriging question today and has been the driver of many theoretical developments trying to find an explanation for this acceleration. These models introduced in general a new component called dark energy with an unknown nature ("the DE models") (see e.g., [21, 20, 5]). The individual test and comparison to observationnal data of these different theoretical models is complicated and need to develop as possible a 'model independent approach' to provide an interpretation of experimental observations. The strategy is not unique today and is linked to the definition of the cosmological parameters, in particular those which describes the properties of the dark energy component.

Many studies concentrate on the equation of state (w = pressure/density ratio) of this new component. w is equal to -1 for a classical cosmological constant but can be different and/or can vary with time depending on the various DE models. In this approach, a common way to introduce this redshift dependence inside a DE model is to use a parameterization as the following one [13, 3] :

$$w(z) = w_0 + w_a z/(1+z) = w_0 + (1-a)w_a \tag{1}$$

which exhibits useful properties [14, 16], a being the scale factor. $w(z)$ can be related to the observational data in one side and to DE models in another way.

On the theoretical side, one question is to determine if this parameterization is sufficient to describe different models whatever the source of the acceleration is. This has been investigated by [17, 1, 15] and seems adequate for a large class of models, even those which have no real dynamical component. Nevertheless, there are still some potential biases when estimating the effective w_0 and w_a parameters from the actual theoretical phase space [17, 23].

On the experimental side, many new probes have shown their capabilities to constrain $w(z)$. To test the sensitivity of various DE surveys, "the data models", one need to define figures of merit, related to the statistical error of the $w(z)$ parameters, to compare and, then, to test the different strategies.

The aim of this article is to compare the informations provided by the various figures of merit calculated for Supernovae (SN) DE surveys. In particular, we distinguish the figures of merit needed to compare the sensitivities of various data models, from the figures of merit needed to compare and separate the various DE models. In section 2, we define the SN data models used in this article. In section 3, we recall the definition of the figure of merit used by the Dark Energy Task Force [8] and compare the sensitivities of the data models. Then, we try to optimize the total number of SN, N, and the redshift depth, z_{max}, of the survey in light of the systematic errors. In section 4, we compare the impact of different figures of merit to distinguish among the DE models the source of the cosmic acceleration.

2 Generic supernova data models

Future observationnal surveys are under studies [8] to estimate the capabilities of various combinations and estimate their uncertainties. We concentrate on Supernovae Dark Energy surveys. To this end, we define generic SN data models which are well representative

of future data:

a) $N = 2000$ and $z_{max} = 1$: such a survey is close to what can be reach on ground in a near future. Using the DETF terminology, this will be our definition of a stage 2 data model.

b) N=15000 and $z_{max} = 1$: this is achievable from ground or space with very large surveys, limitated by an optical coverage. We will named it a stage 3 data model.

c) N=2000 and $z_{max} = 1.7$: this need an infrared coverage which implies a space mission. This will be a later stage and we will define it as our stage 4.

d) N=15000 and $z_{max} = 1.7$: this is certainly expensive and later, we will define it as a stage 5.

Comparison of the potentialities of theses data models is interesting to give some insight on the improvement of the constraints of the DE equation of state following the chronology of future SN surveys. It allows also to compare the relative importance of increasing the total number of SN (N) collected or/and the redshift depth (z_{max}). We will give a particular attention to the question of "doing a deep or a wide survey ?" : this means comparing stage 3 and stage 4 (large N and small z_{max} compared to small N and large z_{max}). In order to answer these questions, we will fix the other parameters identical for all the data models. Namely, the analysis will be done with the following hypothesis for the cosmology:

- a ΛCDM model
- a flat universe
- a strong Ω_m prior, as expected from Planck : $\Omega_m = 0.27 \pm 0.01$. The central value has been chosen to be in agreement with the WMAP-3 year data analysis

We add the following assumptions:

- we add a sample of nearby supernovae as expected from the SN Factory survey [25] (150 SN at z=0.03 and 150 at 0.08), that we call "nearby sample" in the following
- the magnitude dispersion is defined as 0.15 per redshift bin of width $\Delta z = 0.1$, corresponding to a "statistical error" of $\delta m_{stat} = 0.15/\sqrt{N_{bin}}$ per redshift bin

The level of systematic errors will be shown to be a fundamental ingredient in the data model comparison (it is true for any analysis as it has been emphasized by [8, 11]). We define a systematic case where we add an extra term $\delta m_{syst} = 0.02$ in the magnitude, uncorrelated in redshift bins, for all data models. We study the two cases with and without this systematic term. The total error on the magnitude $m(z)$ is then $\delta m^2 = \delta m^2_{stat} + \delta m^2_{syst}$.

In our simulations, we have studied the effects of different type of systematic errors, constant (i.e., uncorrelated in redshift bins) or redshift dependent (i.e., correlated in redshift bins), and with different amplitudes. We point out that adding a redshift dependence does not change our conclusions. The amplitude of the systematic errors has a strong impact on the physical results.

The choice $\delta m_{syst} = 0.02$ is already for us an optimistic estimation of the experimental systematic errors. With 2000 SN, it is of the same size than the statistical error δm_{stat} in a redshift bin and the systematic error will then be the limiting factor since increasing N will only decrease δm_{stat}. Lower systematic effects ($\delta m_{syst} < 1\%$) are not realistic experimentally but provide some results which are comparable to the pure statistical case. Since many papers still provide some analysis with statistical errors only, we keep this case in our study.

To perform the simulations we adopt a standard Fisher matrix approach which allows a fast estimate of the parameter errors following the procedure described in [24]. We use the public tool "Kosmoshow" developped by A. Tilquin[1].

3 Supernovae Data models sensitivity

We have studied the 4 generic data models in details to understand their potential sensitivity in term of coverage and statistic, with and without systematic errors. We have examined the interpretation of the pivot redshift and of the figure of merit defined by the DETF. The impact of a systematic error on the sensitivity of these surveys is emphasized. Finally, we give some insight on the optimization of z_{max} and N.

3.1 The DETF figure of merit

Recently, the DETF[8] has proposed a figure of merit derived from the definition of the pivot point.The pivot parameterization is defined as :

$$w(z) = w_p + (a_p - a)w_a = w_p + \frac{w_a}{1+z_p} - \frac{w_a}{1+z} \tag{2}$$

and is equivalent to the parameterization given in eq.1. The pivot redshift z_p is defined by [9]:

$$z_p = -C_{w_0 w_a}\sigma(w_0)/(\sigma(w_a) + C_{w_0 w_a}\sigma(w_0)) \tag{3}$$

where $C_{w_0 w_a}$ is the correlation between w_0 and w_a and is data and analysis dependent [18, 19]. $\sigma(w_i)$ is the expected error on the parameter w_i.

It has been shown [19] that the (w_0,w_a) and (w_p,w_a) contours are mathematically equivalent. In fact, w_p is directly related to w_0 and w_a through a linear transformation : $w_p = w(z_p) = w_0 + w_a z_p/(1+z_p)$. Consequently, any volume in phase space is conserved. This change of definition is convenient to determine the mathematical redshift z_p where w_0 and w_a are decorrelated which is also the redshift for which $w(z)$ has the smallest error (the so-called "sweet-spot", see e.g., [10]). Note also that the error on w_p is equivalent to the one obtained on w when we fix a constant w (as often done in previous work in the literature) since w_p and w_a are decorrelated.

The DETF figure of merit is defined as $[\sigma(w_p) \times \sigma(w_a)]^{-1}$ [8] and is proportional to the inverse of the area of the error ellipse enclosing the 95%CL in the w_0-w_a plane. In

[1]Our simulation tool, the "Kosmoshow", has been developped by A. Tilquin and is available upon request or directly at http://marwww.in2p3.fr/renoir/Kosmoshow.html

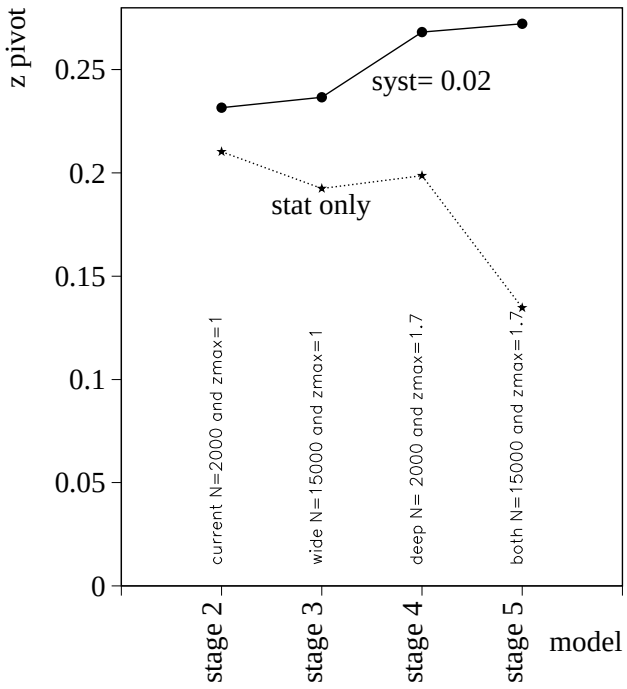

Figure 1: Evolution of z_p for the data models with (plain curve) and without (dotted curve) systematic errors.

the following, to compare surveys we prefer to quote some ratio of the DETF figure of merit, where the normalization changes from case to case. We will study and show how this number is useful to compare data models, but we will show as mentioned recently in [18] that it is not sufficent to compare DE models and that the interpretation needs more valuable information (see section 4).

3.2 Evolution of z_p

Figure 1 gives the evolution of z_p for the four data models under consideration, with and without systematic errors. One can see that z_p ranges from 0.14 to 0.27 and is sensitive to the systematic errors and the data model. We have studied also the impact on the z_p values due to the variations of the nearby sample, the Ω_m prior and the fiducial cosmology. We find, for instance, that the statistic of the nearby sample or the precision of the Ω_m prior have a stronger impact on the z_p values than the variations of z_{max}. In conclusion, z_p varies in the range 0 to 0.5 and the variations are not intuitive. This study has confirmed the feeling that this parameter is not representative of any physical characteristic of a survey (or of the DE dynamics) and should not be used for any comparison.

Comparing constraints on w_p for different data models is then ambiguous as this corresponds to different regions, since the z_p values are different ! The contours in a plane where w_p is one of the two variables (e.g., the (w_p, w_a) or (Ω_m, w_p) planes) will be more difficult to interpret and should be taken with caution when comparing surveys with different characteristics. Note, however, that w_p is useful in certain circumstances. For instance, for the DETF figure of merit, using the property that the area of the error

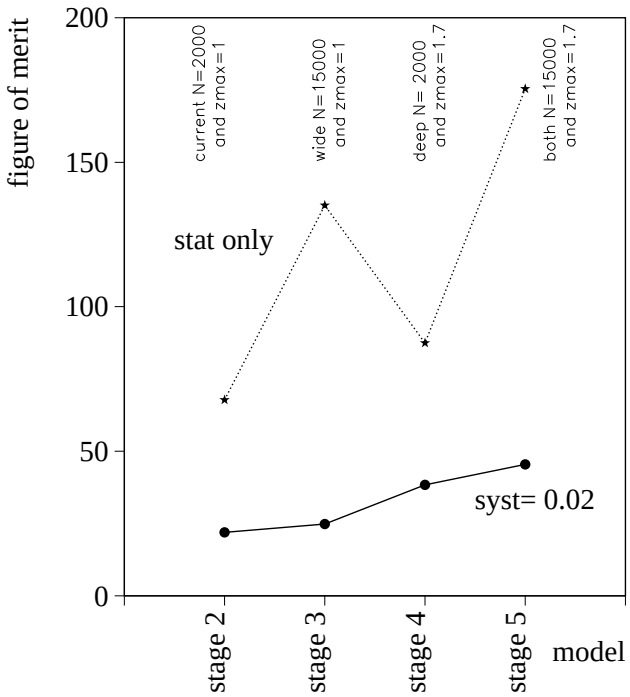

Figure 2: DETF figure of merit, normalized to the stage 2 data model, with (plain curve) and without (dotted curve) systematic errors.

ellipses in the planes (w_p, w_a) and (w_0, w_a) are identical [8], the ambiguity is reduced. Similarly, comparing w_p to -1, to exclude a cosmological constant, has no ambiguity (but other observables are maybe more efficient, see section 4).

3.3 The DETF figure of merit for the SN data models

The comparison of the (normalized) DETF figure of merit for our data models is shown on figure 2. The plot shows the quantity $(\sigma(w_p) \times \sigma(w_a))^{stage2}/(\sigma(w_p) \times \sigma(w_a))^{stageX}$ where the normalization to the stage 2 data model is given explicitly.

The strong impact of the systematic errors appears very clearly on the figure of merit. With statistical errors only, we see that a large statistical sample yields a better figure of merit compared to a deep survey. This is evident with the comparison of the stages 3 and 4. The figure of merit ratio for stage 3 relative to stage 2 is of the order of 2.0 whereas it is only 1.3 for stage 4 relative to stage 2. This indicates a preference for increasing N rather than z_{max} after stage 2. Similarly, if we compare directly the stages 3 and 4, we find that the stage 3 data model provide some constraints on the DE equation of state parameters which are 55% better than the ones reachable by a stage 4 (space based) data model (figure of merit ratio stage 3 relative to stage 4 : 1.55).

With systematic errors, the conclusion is reversed and stage 4 has a far better potential than stage 3 : the figure of merit ratio of stage 4 relative to stage 3 is 1.56. The figure of merit ratio compared to stage 2 is only 1.15 for stage 3 but 1.75 for stage 4, showing it is preferable to increase z_{max} rather than N after stage 2. Concerning stage 5, the constraints increase by 18% only relative to stage 4 (figure of merit ratio : 1.18) which is moderate compared to the increase in complexity for the realization of such surveys.

For other choices of sytematics, these results are confirmed :

- With systematic errors higher than $\delta m_{syst} = 0.02$, the slope between stages 3 and 4 steepens (i.e., the figure of merit ratio increases) which reinforces the need for a deep survey.
- Stages 3 and 4 are equivalent (i.e., the slope is zero), if both have some systematic errors of the order of 0.006! Below this value a wide survey (stage 3) is better, and above it a deep survey (stage 4) is preferable.
- If we keep $\delta m_{syst} = 0.02$ for stage 4, then the systematic errors of stage 3 should be controlled at a better level than 0.012 to be more efficient than stage 4.
- Using a redshift dependence gives similar conclusions, only the various quoted values will slightly change.
- The relative merit of stage 5 compared to stage 4, is very dependent on the systematic errors assumed for the analysis.

Consequently, the control of the level of systematic errors is the key discriminant between wide or deep SN surveys. This is perfectly understandable since the number of SN is now limited by these systematic errors. Let us point out anyway that a large sample helps for understanding systematic errors. Then our conclusions are only valid to estimate the impact of systematic errors. The methods to derive such a level have still to be explored. Our knowledge of the SN systematic effects, hopefuly, will change at the time of realization of the data models considered in this analysis. Then, in the next section, we perform a more detailed analysis of the interplay of N, z_{max} and the systematic errors.

3.4 z_{max} optimization

[12] have emphasized that "the required survey depth depends on the rigor of our scientific investigation". They show that SN at $z > 1.5$ are necessary to reduce cosmological and DE models degeneracies, and also to obtain realistic predictions, taking into account systematic errors, in order to avoid a false precision on a biased result.

In figure 3, we give the DETF figure of merit ratio assuming either $N = 2000$ or $N = 15000$ SN and for the two cases with and without systematic errors (black/plain (blue/dash-dotted) curve : systematic with 15000 (2000) SN, green/dashed (red/dotted) curve : statistic with 15000 (2000) SN). The figure of merit ratio is defined for adjacent redshift bin : the data model is labelled by its z_{max} whereas the reference model corresponds to the data model with $z_{max} - 0.1$ i.e., data model with one less redshift bin. With this particular definition of the figure of merit ratio we are able to see the direct improvement of the DETF figure of merit by adding one redshift bin in the survey (while keeping the total number of SN fixed). If adding a new redshift bin, i.e., increasing z_{max} by 0.1, doesn't increase the constraints then the figure of merit ratio is close to one.

For the 4 curves of fig.3, we see that at "low" z_{max} there is a net improvement of the DETF figure of merit by adding a z-bin, but the gain saturates rapidly with the increase of z_{max}. The horizontal line fixes this gain to 5%. If we take these 5% as the minimal

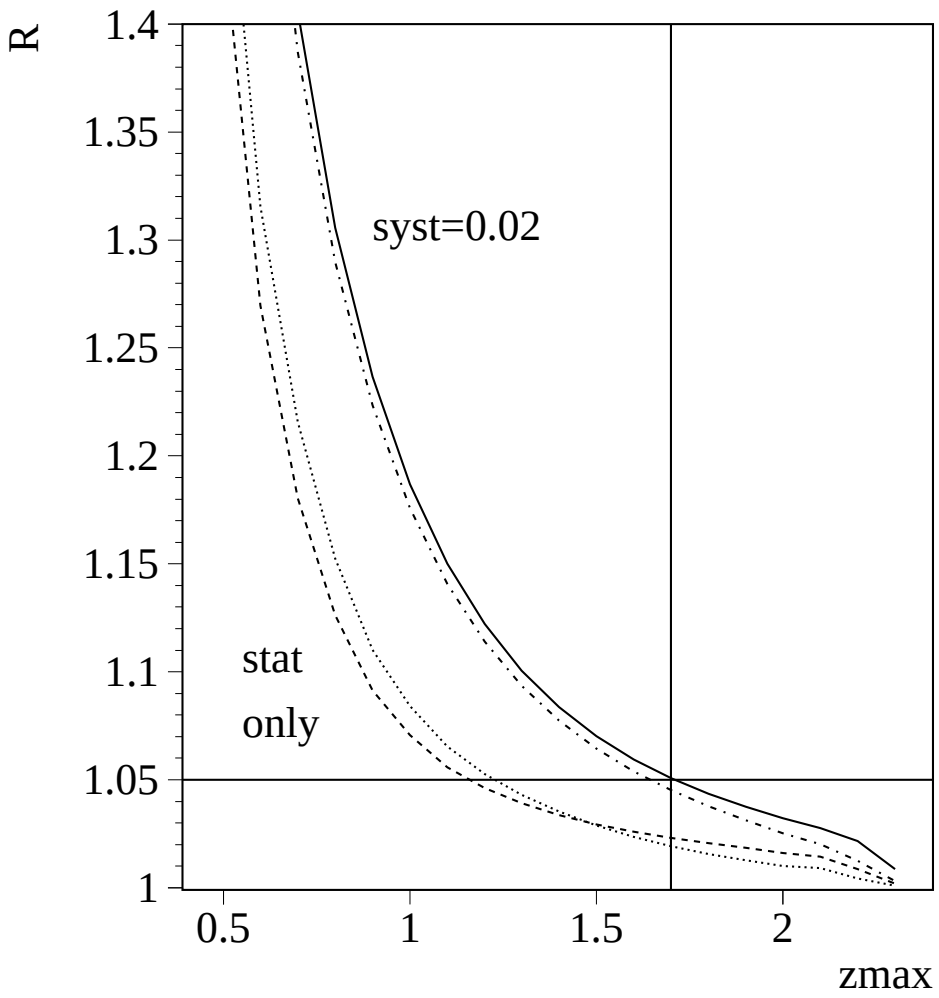

Figure 3: Evolution with z_{max} of the DETF figure of merit ratio assuming either $N = 2000$ or $N = 15000$ SN and for the two cases with and without systematic errors (plain (dash-dotted) curve : systematic case with 15000 (2000) SN, dashed (dotted) curve : statistical case with 15000 (2000) SN). The figure of merit ratio is defined for adjacent z-bin (see text).

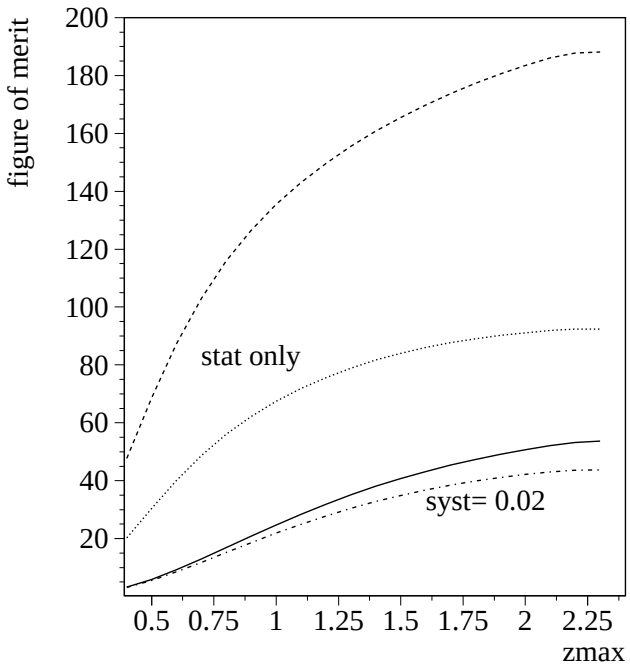

Figure 4: The DETF figure of merit (unnormalized) is given in function of z_{max} with the same labels as fig.3.

gain on constraints when increasing the redshift depth by $\Delta z = 0.1$, we are now able to give an optimum z_{max}. With this criteria, for the case with systematic and $N = 15000$ (black/plain curve) we find $z_{max} = 1.7$ (the vertical line corresponds to $z_{max} = 1.7$). For $N = 2000$ (blue/dash-dotted curve) the change is small and $z_{max} \approx 1.65$. With statistical errors only the z_{max} is strongly reduced and, surprisingly, it has also a relative small dependence on N. For $N = 2000$ one gets $z_{max} \approx 1.25$, but it is 1.15 only with $N = 15000$. The weak dependence on N comes from cancellations in the z_{max} evolution of the w_a and w_p constraints, which exhibits strong variations with N but in opposite directions.

To study better the N dependence, we have looked at the figure of merit directly and not at the ratio. In figure 4, we give directly the DETF figure of merit for the four cases of study. We find clearly that the figure of merit increases with z_{max} and with N. With systematic errors the figure of merit has small variations due to N. We get the contrary with statistical errors only. We even find that the variations due to N are stronger than the ones due to z_{max}. For example, one has the same figure of merit (90) for N=2000 with $z_{max} = 1.7$ and for N=15000 with $z_{max} = 0.7$!

Consequently, we deduce from these figures :

- If systematic errors are of the order of $\delta m_{syst} = 0.02$, a SN sample at $z > 1$ is mandatory to increase the constraints. Beyond $z > 1.7$, the improvement is marginal (less than 5% by redshift bin of size 0.1). This result is weakly dependent on N but dependent on δm_{syst}. A survey with a higher level of systematic errors prefers a higher z_{max} and has a reduced dependancy on N.

- When the systematic errors are negligeable, N is the fundamental parameter and z_{max} around 1 is sufficient.

4 Comparing Dark Energy models

The question we want to address is not only the sensitivity of the SN surveys but also their capability to separate Dark Energy models. More precisely, we would like to know if a particular DE model is in agreement with the standard ΛCDM model. Then we need to test the compatibility of the two models. The figure of merit is only one number and does not allow to answer this question. For example, Linder has shown recently [18] that the key discriminant for thawing (freezing) models (see [2] for model definitions) is the long (short) axis of the (w_0,w_a) ellipse .

Consequently, contour plots should provide more information than the DETF figure of merit and/or the pivot point to interpret data. We have looked in more details at the different informations to estimate the most useful figures of merit when we compare DE models.
All informations are contained in the following figures of merit: $\sigma(w_0)$, $\sigma(w_a)$, $\sigma(w_p)$, $\sigma(w_0) \times \sigma(w_a)$, $\sigma(w_p) \times \sigma(w_a)$, the two-dimensional ($w_0$,$w_a$) contours and the redshift function $w(z)$ with its error shape $\sigma(w(z))$. We do not consider contours with w_p since they are mathematically equivalent to the contours with w_0 instead [19], and that multiple w_p contours are difficult to interpret (see section 3.2).

The study of the variations of the different errors, as we have done in the previous section for the DETF figure of merit, are particularly interesting for comparing data models. The individual variations of w_0, w_a and w_p do not provide any supplementary pieces of information than given by the DETF figure of merit. The behaviours of $\sigma(w_0)$, $\sigma(w_a)$ and the DETF figure of merit are very similar. Only $\sigma(w_p)$ behaves very differently as it has a very weak dependence on data models, in particular it has almost no dependence on z_{max} (see fig.3 of [12]).

To compare DE models, in addition to the errors we need also the central values of the cosmological parameters. We focus now on two different figures of merit : contour plots in the (w_0,w_a) plane and some representation of $w(z)$ with error shape variations with the redshift.

Figure 5 gives the 95% CL contours in the (w_0,w_a) plane for the four data models with systematic errors. We see immediatly two sets of contours, the larger ones with the data models with $z_{max} < 1$ and the smaller ones with $z_{max} > 1$, a result already obtained from the DETF figure of merit. (Adding in this figure the curves corresponding to the pure statistical cases for the four data models allows to recover the results of section 3.3, however the resulting figure is not easily readable.)

The net advantage of the (w_0,w_a) contour representation is the possibility to define "directly" some classes of DE models in this plane. Several recent works have been devoted to this subject (Barger et al., 2006; Linder, 2006a; see also Caldwell & Linder, 2005; Scherrer, 2006; Chiba, 2006, for DE model trajectories/locations in the (w,$w' = dw/dlna$) plane). Consequently, on fig.5 we can represent the different classes of models and study their compatibility with ΛCDM in each data models. In this way, Linder has shown [18] as mentionned previously, that to increase the constraints on "thawing" ("freezing") models we need to reduce the long (short) axis of the ellipse. However, to optimize such constraints we need to know which parameters control the long and short axis (and their

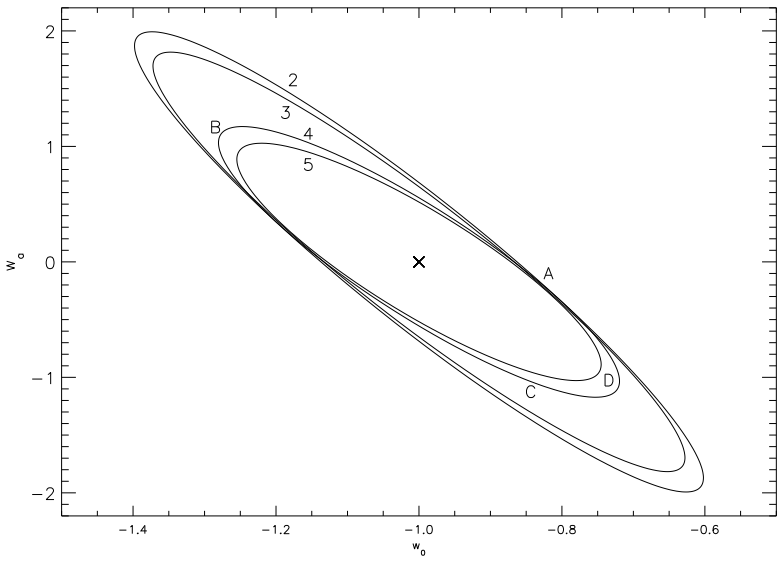

Figure 5: 95% CL contours in the (w_0,w_a) plane for the four data models with systematic errors. The labels of the DE models are given on the plot at the right place (except a small shift of model D for clarity). Stage number for the data models are given on each contour.

directions) of the contour. To understand what is important in any surveys to improve the discrimination among DE models, we introduce 4 phenomenological models defined by their (w_0,w_a) couple of values (see table 1) and which are at the boundary of the 95% CL of the stage 4 data model. We study the variation of the constraints for these DE models for the four data models.

DE model	w_0	w_a	parameters	z-region
A	-0.82	-0.2	w_p	z_p
B	-1.27	1.15	w_0,w_a	low-z & high-z
C	-0.85	-1	w_a	high-z
D	-0.75	-0.95	w_0	low-z

Table 1: *Definition and properties of the DE models taken for illustration. The "parameters" ("z-region") column gives the cosmological parameters (the redshift region) which are the most efficient to distinguish the DE model from a cosmological constant.*

Model A is close to the border of the thawing region and, from fig.5, we see it will be difficult to exclude this model even with stage 5! Conversely, better is the survey, better is the exclusion of the models B, C and D. It appears that the sensitivity to the data models is more sizeable along the larger axis. Consequently, the optimization of future SN surveys are able to reduce the degeneracy among w_0 and w_a which is represented by a reduction of the long axis, whereas it has almost no impact on the short axis. This

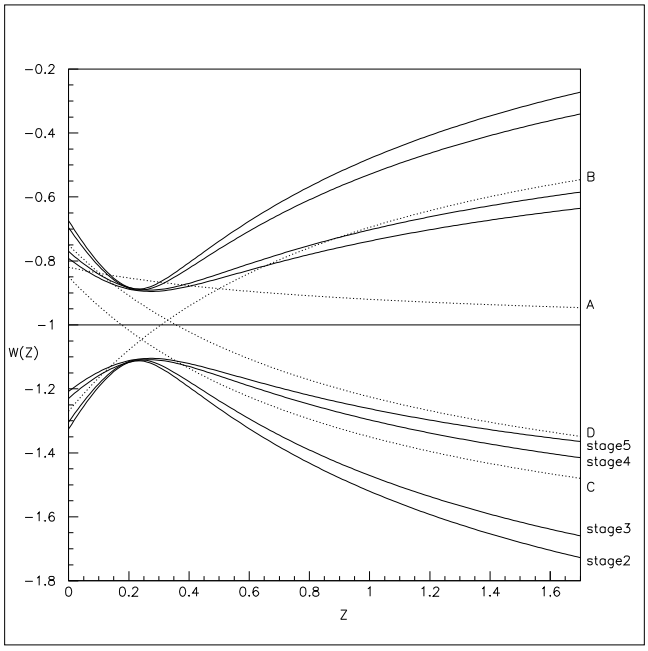

Figure 6: Reconstructed $w(z)$ and the associated errors for the four data models with systematic errors. The errors correspond by increasing order to stage 5, 4, 3 and 2, respectively. The dotted curves give the equation of state for the models A-D and are labelled on the plot.

conclusion should be tempered. Indeed, if all the ellipses for the data models meet in two points (model A being one of them) this is mainly due to two assumptions : we have taken the same SN distributions (including the same nearby sample) and the same systematic errors ($\delta m_{syst} = 0.02$). An important effect of these assumptions concerns the orientation of the ellipse but realistic survey characteristics allow only small rotations of the contours. The strongest effect, as mentionned in the previous section, comes from the assumed level of systematic errors which is the fundamental limitation of the size of the constraints. Then to go beyond, a better understanding of the systematic errors is mandatory.

It is possible to represent the result in a different way which can be easier for theoreticians. The error on $w(z)$, within the Fisher matrix approximation, is given by :

$$\begin{aligned} \sigma^2(w(z)) = \sigma^2(w_0) &+ \sigma^2(w_a)\frac{z^2}{(1+z)^2} \\ &+ 2C_{w_0 w_a}\sigma(w_0)\sigma(w_a)\frac{z}{(1+z)} \end{aligned} \quad (4)$$

Figure 6 represents the equation of state $w(z)$ for the different DE models with the error shapes obtained for the various data models.

In this figure, we represent the expected error at 2 σ of each surveys for a ΛCDM fiducial model compared with the true $w(z)$ of each DE models (A-D). This representation has the merit to be complete and to give explicitely the z dependence of the constraints. The four DE models are described with the same parameterization and show behaviours outside the 2 σ limit of the error shape of the ΛCDM model for stages 4 and 5. They are

excluded for different reasons:

- model A is excluded thanks to the best constraints at the pivot redshift, i.e., the best observable to exclude A is w_p.
- model B is excluded thanks to the low z and high z constraints.
- model C is excluded thanks to the high z (i.e., w_a) behaviour.
- model D is excluded thanks to the low z (i.e., w_0) behaviour.

The $w(z)\,vs\,z$ representation has the advantage to visualize the existence of the sweet-spot at the pivot point and its impact on the result. Anyway, it shows also that it is not possible to use w_p only. For example, model A is excluded thanks to the w_p constraints at $z = z_p$ and not thanks to the SN discovered at this redshift. This is an example of the difficulty to use this information as a physical one. Then, even if this representation is quite convenient for the understanding, its interpretation should be taken with some caution. The error shapes given by eq.4 are strongly parameterization dependent. Consequently, some bias may be present if the chosen parameterization ($w(z) = w_0 + w_a z/(1+z)$ in this study) is far from reality. In addition, there are strong correlations among the cosmological parameters and among the redshift bins, then, the error shapes of $w(z)$ may have some artefacts if not used in a realistic redshift range (i.e., the range probed by data).

Nevertheless, beside the above difficulties this representation may be useful for consistency checks. This representation is also sensitive to the systematic errors and whatever the parameterization is, one can express the constraints and make some data model comparisons. We want to emphasize that it is also possible to provide some results in this plane which are independent of any choice of parameterization to describe the DE dynamics like the so-called "kinematical" approach (see e.g., [6, 7]), that we have not followed in this article. This kind of analysis has also some problems of interpretation: firstly, errors are in general difficult to estimate and more noisy, and secondly, it doesn't avoid the correlation in redshift bins of the results. However, these various approaches are complementary and may be confronted in this plane.

In conclusion to this part, excluding particular DE models from a cosmological constant, need the use of the (w_0,w_a) plane and/or of the $w(z)\,vs\,z$ representation. This is far better than to simply comparing w_p with -1. In order to obtain more subtle details, like the connection to a particular class of DE models or the z dependence of the constraints, both representations are useful. For instance, the expression of the redshift dependence has some advantages to break the degeneracy line present in the (w_0,w_a) plane. Models along this line may be discriminated from a cosmological constant by the measurement of the low and high redshift behaviour of the equation of state, as encoded in the w_0 and w_a parameters. But DE models which are orthogonal to the degeneracy line, may be excluded thanks to the constraints at the pivot redshift, whose expected precision depend weakly on the SN survey configuration but more on the control of systematic errors.
The expected interpretation is then very dependent on all the details of the design of the SN surveys, and in particular very dependent on the level of systematic errors. This strategy is also dependent on the chosen parameterization whose effect should also be carrefully estimated.

5 Conclusions

We have studied in light of the DETF figure of merit the optimisation and interpretation of future supernovae surveys compared to the forthcoming ground precision.

We find that the DETF figure of merit is a good approach for testing the optimisation of a survey.

We test this approach by looking at the sensitivity of the surveys in term of the number of SN and on the depth of the survey. We emphasize that conclusions are driven by the control of systematic errors which fix the amount of information inside data. Ignoring them can provide strong biases on the fitting value and increasing statistic will only reduce the statistical error on a wrong cosmology. This conclusion is not depending on the distribution of the systematic errors.

Then, for an optimistic case of 2% of uncorrelated systematic errors, we show that there will be no extra information for the cosmology with a statistic larger than 2000 SN and that the gain will mainly come from an increase of the depth of the survey up to a redshift of 1.7. This optimisation is very strong and only change for a statistical error only scenario.

The drawback of the DETF method is the lack of information to estimate the discrimination power among DE models, as the central values of the parameters are not used.

Contour plots in the (w_0, w_a) plane give a better understanding and a good discrimination since classes of DE models can be placed in this plane. Comparing data model we find that some degeneracies among cosmological models remain even for the most ambitious project. Complementary information is contained in a representation of $w(z)$ with its error shape. This allows to understand the compatibility of the model with the differents observables, and in particular, to know the redshift dependence of the constraints. However, the results remain in general parameterization dependent and the interpretation challenging. This redshift plane may be useful for consistency checks and data model compatibility and comparison.

A solution to improve the sensitivity of the SN analysis is to combine SN data with other probes informations. This is certainly powerful as emphasized by the DETF but this should be manipulated wih some caution as systematic errors will dominate the future analyses and will introduce even stronger bias in a combination. The best test will be to check the compatibility between probes when dominated by systematic errors, in a coherent way (same theoritical assumptions, same framework, same treatment of systematic errors). Combinaison of probes two by two will then help to control systematic effects. This will be also a good cross check of internal hypothesis and of the control of results.

Acknowledgments

Special thanks to A. Tilquin, P. Taxil, C. Marinoni, C. Tao, D. Fouchez and A. Bonissent for helpful comments and suggestions. We thank also the members of the "Laboratoire d'Astrophysique de Marseille" for interesting discussions and in particular A. Mazure, J.-P. Kneib and R. Malina.

References

[1] Barger, V., Guarnaccia, E. & Martafia, D., 2006, Phys. Lett.**B635**, 61

[2] Caldwell, R.R. & Linder, E.V., 2005, Phys. Rev. Lett. **95**, 141301

[3] Chevallier, M. & Polarski, D., 2001, Int. J. Mod. Phys. **D10**, 213

[4] Chiba, T., 2006, Phys. Rev.**D73**, 043501

[5] Copeland, E.J., Sami, M. & Tsujikawa, S., 2006, hep-th/0603057

[6] Daly, R.A. & Djorgovski, S.G., 2003, ApJ, **597**, 9

[7] Daly, R.A. & Djorgovski, S.G., 2004, ApJ, **612**, 652

[8] Dark Energy Task Force report to the Astronomy and Astrophysics Advisory Committee, http://www.nsf.gov/mps/ast/detf.jsp

[9] Hu, W., 2005, ASP Conf. Ser., **399**, 215 and references therein

[10] Huterer, D. & Turner, M.S., 2001, Phys. Rev. **D64**, 123527

[11] Kim, A.G., et al., 2004, MNRAS, **347**, 909

[12] Linder, E.V. & Huterer, D., 2003, Phys. Rev. **D67**, 081303

[13] Linder, E.V., 2003, Phys. Rev. Lett. **90**, 091301

[14] Linder, E.V., 2004a, Phys. Rev. **D70**, 061302

[15] Linder, E.V., 2004b, Phys. Rev. **D70**, 023511

[16] Linder, E.V. & Huterer, D., 2005, Phys. Rev. **D72**, 043509

[17] Linder, E.V., 2006a, Phys. Rev. **D73**, 063010

[18] Linder, E.V., 2006b, astro-ph/0604280

[19] Martin, D. & Albrecht, A., 2006, astro-ph/0604280

[20] Padmanabhan, T., 2003, Phys. Rep. **380**, 235

[21] Peebles, P.J.E. & Ratra, B., 2003, Rev. Mod. Phys. **75**, 559

[22] Scherrer, R., 2006, Phys. Rev.**D73**, 043502

[23] Simpson, F. & Bridle, S., 2006, Phys. Rev. **D73**, 083001

[24] Virey, J.-M., et al., 2004, Phys. Rev. **D70**, 043514

[25] Wood-Vasey, W.M., et al., 2004, New Astronomical Review **48**, 637

2.3 Analyses combinées

Afin d'éviter le problème des biais, et dans le but de fournir les meilleures contraintes possibles, il apparaît indispensable de réaliser des analyses de données combinant plusieurs sondes cosmologiques. Cependant, les sondes faisant appel aux modèles de fluctuations primordiales de densité soit directement (*e.g.* CMB) soit indirectement à travers la seule utilisation du spectre de puissance aujourd'hui (*e.g.* grandes structures), font intervenir beaucoup plus de paramètres cosmologiques (et astrophysiques) que les seules études de distances comme les SNIa. Cette multitude de paramètres nous force tout de même à effectuer un certain nombre d'hypothèses. Par ailleurs, chaque sonde à ses propres sources d'erreurs systématiques qui trouvent leurs origines dans les incertitudes de mesure ou de calibration de nature purement astrophysique mais aussi dans les aspects purement expérimentaux des appareillages fournissant les mesures.

Dans les articles qui vont suivre nous avons négligé ces problèmes de biais potentiels et d'erreurs systématiques. Nous avons surtout cherché à obtenir des contraintes directement à partir des données. Nous présentons également quelques travaux de prospectives réalisés afin d'estimer la puissance des analyses combinées.

Le premier travail a été réalisé en 2005 en collaboration avec des équipes du CPPM et de Saclay. Nous avons combiné les données les plus récentes (à cette époque) venant de l'étude des SNIa et du rayonnement de fond cosmologique pour contraindre l'équation d'état (dynamique) de l'énergie noire. Nous avons également réalisé un travail de prospective sur les contraintes que l'on pourrait placer sur cette équation d'état en combinant les SNIa et le CMB avec les mesures de cisaillement gravitationnel.

Un second travail a été réalisé, fin 2006, en collaboration avec une équipe chinoise de l'institut des hautes énergies de Pékin. Nous avons combiné les données les plus récentes des SNIa, du CMB, mais aussi des grands sondages de galaxies (spectre de puissance des galaxies mesuré par SDSS). Pour la première fois cette analyse tentait de contraindre simultanément l'équation d'état dynamique de l'énergie noire ainsi que la courbure de l'Univers.

Le programme d'étude futur sera justement d'estimer l'impact des biais et des erreurs systématiques quelle que soit leur nature, sur la détermination des paramètres cosmologiques. Comme mentionné précédemment un travail est en cours sur les effets de l'hypothèse $w_X = -1$ sur la reconstruction de la courbure dans le cadre d'une nalyse combinant les SNIa, le CMB et les BAO.

2.3.1 Combinaison SN+CMB et prospective avec WL sur les propriétés de l'énergie noire

Article publié sous la référence : Astronomy and Astrophysics **448** (2006) 831.

Prospects for Dark Energy Evolution: a Frequentist Multi-Probe Approach

Ch. Yèche[1], A. Ealet[2], A. Réfrégier[1], C. Tao[2], A. Tilquin[2], J.-M. Virey[3], and D. Yvon[1]

[1] DSM/DAPNIA, CEA/Saclay, F-91191, Gif-sur-Yvette, France,
[2] Centre de Physique des Particules de Marseille, CNRS/IN2P3-Luminy and Universit´e de la M´editerran´ee, Case 907, F-13288 Marseille Cedex 9, France,
[3] Centre de Physique Th´eorique⋆, CNRS-Luminy and Universit´e de Provence, Case 907, F-13288 Marseille Cedex 9, France.

September 9, 2007

Abstract. A major quest in cosmology is the understanding of the nature of dark energy. It is now well known that a combination of cosmological probes is required to break the underlying degeneracies on cosmological parameters. In this paper, we present a method, based on a frequentist approach, to combine probes without any prior constraints, taking full account of the correlations in the parameters. As an application, a combination of current SNIa and CMB data with an evolving dark energy component is first compared to other analyses. We emphasise the consequences of the implementation of the dark energy perturbations on the result for a time varying equation of state. The impact of future weak lensing surveys on the measurement of dark energy evolution is then studied in combination with future measurements of the cosmic microwave background and type Ia supernovae. We present the combined results for future mid-term and long-term surveys and confirm that the combination with weak lensing is very powerful in breaking parameter degeneracies. A second generation of experiment is however required to achieve a 0.1 error on the parameters describing the evolution of dark energy.

Key words. cosmology: cosmological parameters – supernovae – CMB – gravitational lensing – large-scale structure in the universe – dark energy – equation of state – evolution

1. Introduction

Supernovae type Ia (SNIa) observations (Knop et al. 2003, Riess et al. 2004) provide strong evidence that the universe is accelerating, in very good agreement with the WMAP Cosmic Microwave Background (CMB) results (Bennett et al. 2003, Spergel et al. 2003) combined with measurements of large scale structures (Hawkins et al. 2003, Tegmark et al. 2004). The simplest way to explain the present acceleration is to introduce a cosmological constant in Einstein's equations. Combined with the presence of Cold Dark Matter, it forms the so-called ΛCDM model. Even if this solution agrees well with current data, the measured value of the cosmological constant is very small compared to particle physics expectations of vacuum energy, requiring a difficult fine tuning. A favourite solution to this problem involves the introduction of a new component, called "dark energy" (DE), which can be a scalar field as in quintessence models (Wetterich 1988, Peebles & Ratra 1988).

The most common way to study this component is to measure its "equation of state" (EOS) parameter, defined as $w = p/\rho$, where p is the pressure and ρ the energy density of the dark energy. Most models predict an evolving equation $w(z)$. It has been shown (e.g., Maor et al. 2001, Maor et al. 2002, Virey et al. 2004a, Gerke & Efstathiou 2002) that neglecting such evolution biases the discrimination between ΛCDM and other models. The analysis of dark energy properties needs to take time evolution (or redshift z dependence) into account.

Other attractive solutions to the cosmological constant problem imply a modification of gravity (for a review, cf., e.g., Lue et al. 2004, or Carroll et al. 2005 and references therein). In this case, there is no dark energy as such and thus no dark energy equation of state. In this paper, we consider only the dark energy solution, keeping in mind that Lue et al. (2004), among others, have shown that the induced changes in the Friedmann equations could be parameterised in ways very similar to a dark energy evolving solution.

⋆ "Centre de Physique Th´eorique" is UMR 6207 - "Unit´e Mixte de Recherche" of CNRS and of the Universities "de Provence", "de la M´editerran´ee" and "du Sud Toulon-Var"- Laboratory affiliated to FRUMAM (FR 2291).

As various authors have noted (e.g., Huterer & Turner 2001, Weller & Albrecht 2002), SNIa observations alone will not be able to distinguish between an evolving equation of state and ΛCDM. This technique indeed requires prior knowledge of the values of some parameters. In particular, the precision on the prior matter density Ω_m has an impact on the constraints on the time evolution of the equation of state w, even in the simplest flat Universe cosmology (e.g., Virey et al. 2004b).

Extracting dark energy properties thus requires a combined analysis of complementary data sets. This can be done by combining SNIa data with other probes such as the CMB, the large scale distributions of galaxies, Lyman α forest data, and, in the near future, the observation of large scale structure with the Sunyaev-Zeldovich effect (SZ) (Sunyaev & Zeldovich 1980) or with weak gravitational lensing surveys (WL), which provide an unique method to directly map the distribution of dark matter in the universe (for reviews, cf., e.g., Bartelmann & Schneider 2001, Mellier et al. 2002; Hoekstra et al. 2002, Refregier 2003, Heymans et al. 2005 and references therein).

Many combinations have already been performed with different types of data and procedures, (e.g., Bridle et al. 2003, Wang & Tegmark 2004, Tegmark et al. 2004, Upadhye et al. 2004, Ishak 2005, Seljak et al. 2004, Corasaniti et al. 2004, Xia et al. 2004). All studies have shown the consistency of existing data sets with the ΛCDM model and the complementarity of the different data sets in breaking degeneracies and constraining dark energy for future experiments. But the results differ by as much as 2σ on the central values of the parameters describing an evolving equation of state.

In this paper, we have chosen three probes, which seem to best constrain the parameters of an evolving equation of state when combined, namely, SNIa, CMB and weak lensing. Considering a flat Universe, we combine the data in a coherent way, that is to say, under identical assumptions for the dark energy properties for the three probes, and we completely avoid the use of priors. This had not always been done systematically in all previous combinations. We also adopt a frequentist approach for the data combination, where the full correlations between the cosmological parameters are taken into account. This method allows us to provide, simultaneously, confi dence intervals on a large number of distinct cosmological parameters. Moreover, this approach is very flexible as it is easy to add or remove parameters in contrast with other methods.

The paper is organised as follows: In Sec. 2, we describe our framework and statistical procedure, based on a frequentist approach, which can accommodate all parameters without marginalisation. For our simulation and analysis, we use the CMBEASY package for CMB (Doran 2003), the Kosmoshow program for SNIa (Tilquin 2003) and an extension of the calculations from Refregier et al. (2003) for weak lensing. In each case, the programs take into account the time evolution of the equation of state (cf Sec. 2.2 for details).

In Sec. 3, we apply this method to current data sets of SNIa and WMAP data. We fi rst verify that the constraints on the cosmological parameters estimated with a Fisher matrix technique (Fisher 1935), are consistent with those obtained with a complete error analysis. We then compare these errors with other works and discuss the differences. In particular, we discuss how the treatment of the dark energy perturbations can explain some of the differences found in the literature.

In Sec. 4, we study the statistical sensitivities of different combinations of future surveys. We simulate expectations for the ground surveys from the Canadian French Hawaii Telescope Legacy Surveys (CFHTLS) and new CMB data from Olimpo as well as the longer term Planck and SNAP space missions. For these future experiments, the results are combined with a Fisher matrix technique, compared and discussed.

Finally, our conclusions are summarised in Sec. 5.

2. Combination method

In this section, we fi rst summarise the framework used in this paper, and describe our approach based on frequentist statistics.

2.1. Dark Energy Parametrization

The evolution of the expansion parameter is given by the Hubble parameter H through the Friedmann equation

$$\left(\frac{H(z)}{H_0}\right)^2 = (1+z)^3\,\Omega_m + \frac{\rho_X(z)}{\rho_X(0)}\,\Omega_X + (1+z)^2\,\Omega_k, \tag{1}$$

with

$$\frac{\rho_X(z)}{\rho_X(0)} = \exp\left[3\int_0^z (1+w(z'))\;d\,\ln(1+z')\right] \tag{2}$$

where the ratio of the dark energy density to the critical density is denoted Ω_X in a general model and Ω_Λ in the simplest case of a Cosmological Constant ($w=-1$). Ω_M is the corresponding parameter for (baryonic+cold dark) matter. Note that we have neglected the radiation component Ω_R. The present total and curvature density parameters are Ω and $\Omega_\kappa = 1-\Omega$, respectively. The present value of the Hubble constant is parameterised as $H_0 = 100h$ km s^{-1} Mpc^{-1}.

As it is not possible to constrain a completely unknown functional form $w(z)$ of the time evolution of the equation of state, we adopt a parametric representation of the z dependence of the equation of state. We need this parametric form to fit all the data sets over a large range of z: from $z \simeq 0-1$ for the SNIa and weak lensing, up to $z \simeq 1100$ for the CMB. For this purpose, we choose the parametrization proposed by Chevallier & Polarski (2001) and Linder (2003) :

$$w(z) = w_0 + w_a z/(1+z), \tag{3}$$

which has an adequate asymptotic behaviour. In this paper, we thus use two parameters, w_0 and w_a, to describe the time evolution of the equation of state (see justifications in Linder & Huterer 2005). For this parametrization of $w(z)$, Eq. 2 reduces to:

$$\rho_X(z) \;=\; \rho_X(0)\, e^{-3w_a z/(1+z)}\, (1+z)^{3(1+w_0+w_a)}. \tag{4}$$

For a constant $w \equiv w_0$ ($w_a = 0$), the usual form $\rho_X(z) \;=\; \rho_X(0)\,(1+z)^{3(1+w_0)}$ is recovered.

The comoving distance χ is defined as

$$\chi(z) = \int_0^z \frac{c}{H(z')} dz', \tag{5}$$

and the comoving angular-diameter distance $r(\chi)$ is equal, respectively, to χ, $R_0 sin(\chi/R_0)$, $R_0 \sinh(\chi/R_0)$, for a flat, closed and open Universe where the present curvature radius of the universe is defined as $R_0 = c/(\kappa H_0)$ with respectively $\kappa^2 \equiv 1$, $-\Omega_\kappa$, and Ω_κ.

2.2. Statistical approach

Most recent CMB analysis use Markov Chains Monte Carlo simulations (Gilks et al. 1996, Christensen & Meyer 1998) with bayesian inference. The philosophical debate between the bayesian and the frequentist statistical approaches is beyond the scope of this paper (for a comparison of the two approaches see, for instance, Feldman & Cousins 1998 and Zech 2002). Here, we briefly review the principles of each approach.

For a given data set, the bayesian approach computes the probability distribution function (PDF) of the parameters describing the cosmological model. The bayesian probability is a measure of the plausibility of an event, given incomplete knowledge. In a second step, the bayesian constructs a 'credible' interval, centered near the sample mean, tempered by 'prior' assumptions concerning the mean. On the other hand, the frequentist determines the probability distribution of the data as a function of the cosmological parameters and gives a confidence level that the given interval contains the parameter. In this way, the frequentist completely avoids the concept of a PDF defined for each parameter. As the questions asked by the two approaches are different, we might expect different confidence intervals. However, the philosophical difference between the two methods should not generally lead, in the end, to major differences in the determination of physical parameters and their confidence intervals when the parameters stay in a physical region.

Our work is based on the 'frequentist' (or 'classical') confidence level method originally defined by Neyman (1937). This choice avoids any potential bias due to the choice of priors. In addition, we have also found ways to improve the calculation speed, which gives our program some advantages over other bayesian programs. Among earlier combination studies (e.g., Bridle et al. 2003, Wang & Tegmark 2004, Tegmark et al. 2004, Upadhye et al. 2004, Ishak 2005, Seljak et al. 2004, Corasaniti et al. 2004, Xia et al. 2004) only that of Upadhye et al. (2004) uses also a frequentist approach.

2.2.1. Confidence levels with a frequentist approach

For a given cosmological model defined by the n cosmological parameters $\theta = (\theta_1, \ldots, \theta_n)$, and for a data set of N quantities $x = (x_1, \ldots, x_N)$ measured with gaussian experimental errors $\sigma_x = (\sigma_1, \ldots, \sigma_N)$, the likelihood function can be written as:

$$\mathcal{L}(x, \sigma_x; \theta) = \frac{1}{\sqrt{2\pi}\sigma_i} exp\left(-\frac{(x_i - x_{i,model})^2}{2\sigma_i^2}\right). \tag{6}$$

where $x_{model} = (x_{1,model}, \ldots, x_{N,model})$ is a set of corresponding model dependent values.

In the rest of this paper, we adopt a χ^2 notation, which means that the following quantity is minimised:

$$\chi^2(x, \sigma_x; \theta) = -2 \ln(\mathcal{L}(x, \sigma_x; \theta)) \tag{7}$$

We first determine the minimum χ_0^2 of $\chi^2(x, \sigma_x; \theta)$ letting free all the cosmological parameters. Then, to set a confidence level (CL) on any individual cosmological parameter θ_i, we scan the variable θ_i: for each fixed value of θ_i, we minimise again $\chi^2(x, \sigma_x; \theta)$ but with $n-1$ free parameters. The χ^2 difference, $\Delta\chi^2(\theta_i)$, between the new minimum and χ_0^2, allows us to compute the CL on the variable, assuming that the experimental errors are gaussian,

$$1 - \mathrm{CL}(\theta_i) = \frac{1}{\sqrt{2^{N_{dof}}}\Gamma(N_{dof}/2)} \int_{\Delta\chi^2(\theta_i)}^{\infty} e^{-t/2} t^{N_{dof}/2-1} dt \tag{8}$$

where Γ is the gamma function and the number of degrees of freedom N_{dof} is equal to 1. This method can be easily extended to two variables. In this case, the minimisations are performed for $n-2$ free parameters and the confidence level $\mathrm{CL}(\theta, \theta_j)$ is derived from Eq. 8 with $N_{dof} = 2$.

By definition, this frequentist approach does not require any marginalisation to determine the sensitivity on a single individual cosmological parameter. Moreover, in contrast with bayesian treatment, no prior on the cosmological parameters is needed. With this approach, the correlations between the variables are naturally taken into account and the minimisation fit can explore the whole phase space of the cosmological parameters.

In this study, the minimisations of $\chi^2(x, \sigma_x; \theta)$ are performed with the MINUIT package (James 1978). For the 9 parameter study proposed in this paper, each fit requires around 200 calculations of χ^2. The consumed CPU-time is dominated by the computation of the angular power spectrum (C_ℓ) of the CMB in CMBEASY (Doran 2003). In practice, to get the CL for one variable, as shown, for instance, in Fig. 1, the computation of the C_ℓ is done around 10000 times. The total number of calls to perform the study presented in Tab. 1, is typically 3 or 4 times smaller than the number of calls in the MCMC technique used by Tegmark et al. (2004). This method is very powerful for studying the impacts of the parameters: it is not costly to add or remove parameters because the number of C_ℓ computations scales with the number of parameters, in contrast with the MCMC method, which requires the generation of a new chain.

2.2.2. Combination of cosmological probes with Fisher matrices

In parallel with this frequentist approach, to study the statistical sensitivities of different combinations of future surveys, we perform a prospective analysis based on the Fisher matrix technique (Fisher 1935). We validate this approach by comparing its estimates of the statistical errors for the current data set with those obtained with the frequentist method described above.

The statistical errors on the n cosmological parameters $\theta = (\theta_1, \ldots, \theta_n)$ are determined by using the inverse of the covariance matrix V called the Fisher matrix F defined as:

$$(V^{-1})_{ij} = F_{ij} = -\frac{\partial^2 \ln \mathcal{L}(x;\theta)}{\partial\theta_i \partial\theta_j}, \tag{9}$$

where $\mathcal{L}(x;\theta)$ is the likelihood function depending on the n cosmological parameters and a data set of N measured quantities $x = (x_1, \ldots, x_N)$. A lower bound, and often a good estimate, for the statistical error on the cosmological parameter θ_i is given by $(V_{ii})^{1/2}$.

When the measurements of several cosmological probes are combined, the total Fisher matrix F_{tot} is the sum of the three Fisher matrices F_{SN}, F_{WL} and F_{CMB} corresponding respectively to the SNIa, weak lensing and CMB observations. The total covariance matrix F_{tot}^{-1} allows us to estimate both, the expected sensitivity on the cosmological parameters, with the diagonal terms, and the correlations between the parameters, with the off-diagonal terms. The Fisher matrices for each probe are computed as follows.

CMB: In the case of CMB experiments, the data set vector x corresponds to the measurements of C_ℓ, the angular power spectrum of the CMB from $\ell = 2$ to some cutoff ℓ_{max}. Using Eq. 9, the Fisher matrix is written as

$$(F_{CMB})_{ij} = \sum_{l=2}^{\ell_{max}} \frac{1}{\sigma_{C_\ell}^2} \cdot \frac{\partial C_\ell}{\partial\theta_i} \cdot \frac{\partial C_\ell}{\partial\theta_j} \tag{10}$$

where σ_{C_ℓ} is the statistical error on C_ℓ obtained directly from published results or estimated as (see Knox 1995):

$$\sigma_{C_\ell} = \sqrt{\frac{2}{(2\ell+1) f_{sky}}} \left[C_\ell + (\theta_{fwhm} s)^2 \cdot e^{\frac{\ell^2 \theta_{fwhm}^2}{8\ln(2)}} \right] \tag{11}$$

where the second term incorporates the effects of instrumental noise and beam smearing. In Eq. 11, θ_{fwhm}, f_{sky}, and s are respectively the angular resolution, the fraction of the sky observed and the expected sensitivity per pixel.

The C_ℓ and their derivatives with respect to the various cosmological parameters are computed with CMBEASY (Doran 2003), an object oriented C++ package derived from CMBFAST (Seljak & Zaldarriaga 1996).

SNIa: The SNIa apparent magnitudes m can be expressed as a function of the luminosity distance as

$$m(z) = M_{s_0} + 5 log_{10}(D_L) \tag{12}$$

where $D_L(z) \equiv (H_0/c)\, d_L(z)$ is the H_0-*independent* luminosity distance to an object at redshift z. The usual luminosity distance $d_L(z)$ is related to the comoving angular-diameter distance $r(\chi)$ by $d_L(z) = (1+z)\cdot r(\chi)$, with the definition of $r(\chi)$ and $\chi(z)$ given in Sec. 2.1. The normalisation parameter M_{s_0} thus depends on H_0 and on the absolute magnitude of SNIa.

The Fisher matrix, in this case, is related to the measured apparent magnitude m_k of each object and its statistical error σ_{m_k} by

$$(F_{SN})_{ij} = \sum_k \frac{1}{\sigma^2_{m_k}} \cdot \frac{\partial m_k}{\partial \theta_i} \cdot \frac{\partial m_k}{\partial \theta_j}. \tag{13}$$

Weak lensing: The weak lensing power spectrum is given by (e.g., Hu & Tegmark 1999, cf, Refregier 2003 for conventions)

$$C_\ell = \frac{9}{16}\left(\frac{H_0}{c}\right)^4 \Omega_m^2 \int_0^{\chi_h} d\chi \left[\frac{g(\chi)}{a r(\chi)}\right]^2 P\left(\frac{\ell}{r}, \chi\right), \tag{14}$$

where $r(\chi)$ is the comoving angular-diameter distance, and χ_h corresponds to the comoving distance to horizon. The radial weight function g is given by

$$g(\chi) = 2\int_\chi^{\chi_h} d\chi'\; n(\chi') \frac{r(\chi) r(\chi'-\chi)}{r(\chi')}, \tag{15}$$

where $n(\chi)$ is the probability of finding a galaxy at comoving distance χ and is normalised as $\int d\chi\, n(\chi) = 1$.

The linear matter power spectrum $P(k,z)$ is computed using the transfer function from Bardeen et al. (1986) with the conventions of Peacock (1997), thus ignoring the corrections on large scales for quintessence models (Ma et al. 1999). The linear growth factor of the matter overdensities δ is given by the well known equation:

$$\ddot{\delta} + 2H\dot{\delta} - \frac{3}{2}H^2 \Omega_m(a)\delta = 0, \tag{16}$$

where dots correspond to time derivatives, and $\Omega_m(a)$ is the matter density parameter at the epoch corresponding to the dimensionless scale factor a. This equation is integrated numerically with boundary conditions given by the matter-dominated solution, $G = \delta/a = 1$ and $\dot{G} = 0$, as $a \to 0$ (see eg. Linder & Jenkins 2003). We enforce the CMB normalisation of the power spectrum $P(k,0)$ at $z = 0$ using the relationship between the WMAP normalisation parameter A and σ_8 given by Hu (2004). Considerable uncertainties remain for the non-linear corrections in quintessence models (cf. discussion in Hu (2002)). Here, we use the fitting formula from Peacock & Dodds (1996).

For a measurement of the power spectrum, the Fisher matrix element is defined as:

$$(F_{WL})_{ij} = \sum_\ell \frac{1}{\sigma^2_{C_\ell}} \frac{\partial C_\ell}{\partial \theta_i} \frac{\partial C_\ell}{\partial \theta_j}, \tag{17}$$

where the summation is over modes ℓ which can be reliably measured. This expression assumes that the errors σ_{C_ℓ} on the lensing power spectrum are gaussian and that the different modes are uncorrelated. Mode-to-mode correlations have been shown to increase the errors on cosmological parameters (Cooray & Hu 2001) but are neglected in this paper.

Neglecting non-gaussian corrections, the statistical error σ_{C_ℓ} in measuring the lensing power spectrum C_ℓ (cf., e.g., Kaiser 1998, Hu & Tegmark 1999, Hu 2002) is given by:

$$\sigma_{C_\ell} = \sqrt{\frac{2}{(2l+1) f_{\rm sky}}}\left(C_l + \frac{\sigma_\gamma^2}{2 n_g}\right), \tag{18}$$

where $f_{\rm sky}$ is the fraction of the sky covered by the survey, n_g is the surface density of usable galaxies, and $\sigma_\gamma^2 = \langle|\gamma|^2\rangle$ is the shear variance per galaxy arising from intrinsic shapes and measurement errors.

2.3. Cosmological parameters and models

For the studies presented in this paper, we limit ourselves to the 9 cosmological parameters: $\theta = \Omega_b, \Omega_m, h, n_s, \tau, w_0, w_a, A$ and M_{s_0}, with the following standard definitions:
- (Ω_i , i=b,m) are densities for baryon and matter respectively (Ω_m includes both dark matter and baryons),
- h is the Hubble constant in units of 100 km/s/Mpc,
- n_s is the spectral index of the primordial power spectrum,
- τ is the reionisation optical depth,
- A is the normalisation parameter of the power spectrum for CMB and weak lensing (cf Hu & Tegmark (1999) for definitions).

The matter power spectrum is normalised according to the COBE normalisation (Bunn & White 1997), which corresponds

to $\sigma_8 = 0.88$. This is consistent with the WMAP results (Spergel et al. 2003) and with the average of recent cosmic shear measurements (see compilation tables in Mellier et al. 2002, Hoekstra et al. 2002, Refregier 2003).
- M_{s_0} is the normalisation parameter from SNIa (cf Sec. 2.2.2),
- Dark energy is described by the w_0 parameter corresponding to the value of the equation of state at z=0. When the z dependence of the equation of state is studied, an additional parameter w_a is defined (cf Sec. 2.1).

The reference fiducial model of our simulation is a ΛCDM model with parameters $\Omega_m = 0.27$, $\Omega_b = 0.0463$, $n_s = 0.99$, $h = 0.72$, $\tau = 0.066$, $A = 0.86$, consistent with the WMAP experiment (see tables 1-2 in Spergel et al. 2003). In agreement with this experiment, we assume throughout this paper that the universe is flat, i.e., $\Omega = \Omega_m + \Omega_X = 1$. We also neglect the effect of neutrinos, using 3 degenerate families of neutrinos with masses fixed to 0.

In the following, we will consider deviations from this reference model. For the equation of state, we use as a reference $w_0 = -0.95$ and $w_a = 0$ as central values (we have not used exactly $w_0 = -1$ to avoid transition problems in the CMB calculations). To estimate the sensitivity on the parameters describing the equation of state, we also consider two other fiducial models: a SUGRA model, with ($w_0 = -0.8, w_a = 0.3$) as proposed by, e.g., Weller & Albrecht (2002) to represent quintessence models, and a phantom model (Caldwell 2002) with ($w_0 = -1.2, w_a = -0.3$).

In this analysis, the full covariance matrix on all parameters is used with no prior constraints on the parameters, avoiding biases from internal degeneracies. We have implemented the time evolving parametrization of the equation of state in simulations and analysis of the three probes we consider in this paper, i.e. CMB, SNIa and weak lensing.

3. Combination of current surveys

We first apply our statistical approach to the combination of recent SNIa and CMB data, without any external constraints or priors. The comparison of the statistical errors obtained with a global fit using this frequentist treatment, with those predicted with the Fisher matrix technique, also allows us to validate the procedure described in Sec. 2. Finally, we compare our results with other published results.

3.1. Current surveys

We use the 'Gold sample' data compiled by Riess et al. (2004), with 157 SNIa including a few at $z > 1.3$ from the Hubble Space Telescope (HST GOODS ACS Treasury survey), and the published data from WMAP taken from Spergel et al. (2003).

We perform two distinct analyses: in the first case, the equation of state is held constant with a single parameter w_0 and we fit 8 parameters, as described in Sec. 2.2; in the second case, the z dependence of the equation of state is modelled by two variables w_0 and w_a as defined in Sec. 2.1, and we fit 9 parameters.

3.2. Results

The results of this frequentist combination of CMB and SNIa data are summarised in Tab. 1. When the equation of state is considered constant, we obtain $w_0 = -0.92^{+0.10}_{-0.13}$ (1-σ) and the shape of the CL is relatively symmetrical around the value of w_0 obtained at the χ^2 minimum. When a z dependence is added to the equation of state, the CL is still symmetrical with $w_0 = -1.09^{+0.13}_{-0.15}$ but w_a becomes asymmetrical with a long tail for smaller values of w_a, as can be seen in Fig. 1. The 1-D CL for w_a gives the resulting CL at 68%(1σ) and 95%(2σ): $w_a = 0.82^{+0.21\ +0.42}_{-0.26\ -0.80}$.

Tab. 1 compares the 1σ errors obtained with the frequentist method and the errors predicted with the Fisher matrix techniques. The agreement is good, and in the remaining part of this paper, for the combination of expectations from future surveys, we will use the Fisher matrix approach.

However Upadhye et al. (2004) noticed that the high redshift limit of the parametrization of the EOS plays an important role when we consider CMB data which impose $w(z \to \infty) < 0$. With our choice of parametrization (see definition in Eq. 3), we get the condition $w_0 + w_a < 0$. When a fit solution is found close to this boundary condition, as is the case with the current data, the CL distributions are asymmetric, giving asymmetrical errors. The Fisher matrix method is not able to represent complicated 2-D CL shapes, as those shown in Fig. 2. For example, the error on w_a increases when the (w_0, w_a) solution moves away from the 'unphysical' region $w_0 + w_a > 0$. To avoid this limitation, we will thus use fiducial values of w_a closer to zero for the prospective studies with future surveys.

It is worth noting that the solution found by the fit corresponds to a value of w slightly smaller than -1 for $z = 0$, and a value of w slightly larger than -1 for high z. The errors are such that the value of w is compatible with -1. However, this technically means that the Universe crosses the phantom line in its evolution. This region ($w < -1$) cannot be reached by the fit, if dark energy perturbations are computed in the CMBEASY version we use. To obtain a solution and compare with other published results, we therefore probed two different conditions, both illustrated in Fig. 2.

Table 1. Results of the frequentist fit to WMAP and Riess et al. (2004) SNIa data. For the 8 parameter fit with a constant EOS, the first column gives the value of the variable at the χ^2 minimum, with the confidence interval at 68% (1 σ), the second column shows the 1σ error computed with the Fisher matrix techniques. The third and fourth columns present the same information for the 9 parameter fit with a z dependent EOS. The 1σ errors are symmetrical for all the variables except for w_a. Its error goes from $^{+0.21}_{-0.26}$ for CL at 68% to $^{+0.42}_{-0.80}$ for CL at 95% (see text).

	constant EOS		z **dependent EOS**	
	fit	σ_{Fisher}	fit	σ_{Fisher}
$\mathbf{\Omega}_b$	$0.049^{+0.005}_{-0.003}$	± 0.003	$0.055^{+0.003}_{-0.003}$	± 0.003
$\mathbf{\Omega}_m$	$0.29^{+0.05}_{-0.04}$	± 0.04	$0.33^{+0.04}_{-0.04}$	± 0.04
$\mathbf{h}$	$0.69^{+0.03}_{-0.02}$	± 0.03	$0.69^{+0.03}_{-0.02}$	± 0.03
$\mathbf{n}_S$	$0.97^{+0.03}_{-0.03}$	± 0.03	$0.97^{+0.03}_{-0.03}$	± 0.03
τ	$0.13^{+0.04}_{-0.04}$	± 0.04	$0.14^{+0.04}_{-0.04}$	± 0.04
$\mathbf{w}_0$	$-0.92^{+0.10}_{-0.13}$	± 0.11	$-1.09^{+0.13}_{-0.15}$	± 0.14
$\mathbf{w}_a$	-	-	$0.82^{+0.21}_{-0.26}$	± 0.25
$\mathbf{A}$	$0.79^{+0.08}_{-0.07}$	± 0.10	$0.80^{+0.08}_{-0.07}$	± 0.10
$\mathbf{M}_{s0}$	$15.94^{+0.03}_{-0.03}$	± 0.03	$15.95^{+0.03}_{-0.03}$	± 0.03

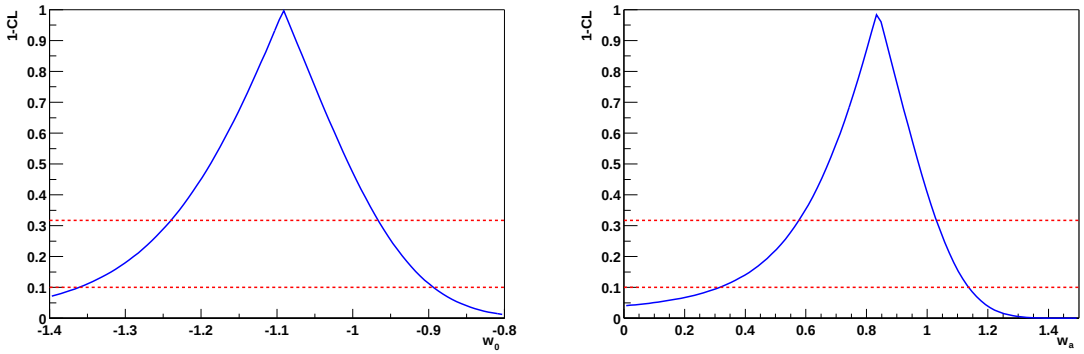

Fig. 1. Confidence level (CL) plots on parameters w_0 (left) and w_a (right), using WMAP and Riess et al. 2004 SNIa data for a 9 parameter fit with evolving EOS. The dashed lines correspond to the 68%(1σ) and 90%(1.64σ) confidence intervals.

First, we removed altogether the perturbations for the dark energy, which gives the results presented above. This allows a comparison with Seljak et al. (2004), who have likely removed dark energy perturbations. Their central value corresponds to $w_0 = -0.98^{+0.38}_{-0.37}$ and $w_a = -0.05^{+1.92}_{-1.13}$ at 95%(2σ). It is closer to $w = -1$ than our result and gives errors for w_a larger than the ones we get. The comparison is however not exact, since Seljak et al. use a bayesian approach for the fits, and give results for an evolving equation of state, only for the total combination of the WMAP and SNIa data with other SDSS probes (galaxies clustering, bias, and Lyman α forest).

We also performed the fits, including dark energy perturbations, only when $w > -1$ (which is the default implementation in CMBFAST). Caldwell & Doran (2005) have argued convincingly that crossing the cosmological constant boundary leaves no distinct imprint, i.e., the contributions of $w < -1$ are negligible, because $w < -1$ dominates only at late times and dark energy does not generally give strong gravitational clustering. Our analysis, including dark energy perturbations only when $w > -1$, gives a minimum (cf. right hand side plot in Fig. 2) for $w_0 = -1.32^{+0.15}_{-0.19}$ and $w_a = 1.2^{+0.5}_{-0.8}$ at 1σ. This is some 2σ away from the no perturbation case. We remark that these values are very close to those obtained by Upadhye et al.(2004), who use a procedure similar to ours, without any marginalisation on parameters, a weak constraint $w_0 + w_a \leq 0$ inside their fit. Their result, $w_0 = -1.3^{+0.34}_{-0.39}$ and $w_a = 1.25^{+0.40}_{-2.17}$ at 95%(2σ), has almost the same central value as our fit, when we switch on the dark energy perturbation for $w > -1$. The errors we get are also compatible, and are much larger than in the no perturbation case.

The importance and impact of introducing dark energy perturbations has been discussed by Weller & Lewis (2003). Their combined WMAP and SNIa analysis with a constant sound speed also gives a more negative value of w, when a redshift dependence is taken into account. Although Rapetti et al. (2004) observe a reduced effect when they add cluster data, they still indicate a similar trend. Finally, when dark energy perturbations are included, we observe that the minimisation is more difficult and correlations between parameters increase.

We conclude that our results are compatible with other published papers using various combinations of cosmological probes. There is a good agreement of all analysis when w_0 is constant, showing that data agree well with the ΛCDM model. However,

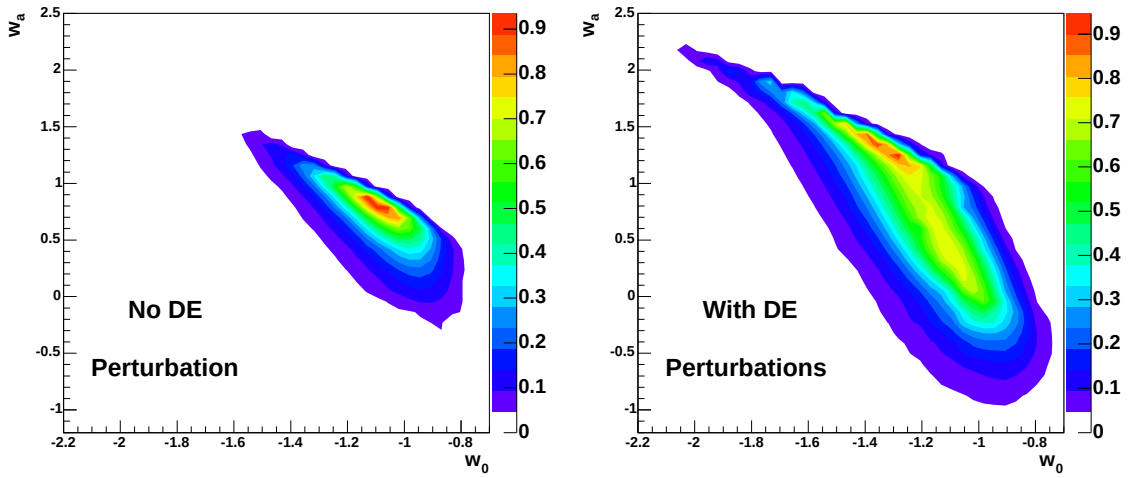

Fig. 2. Confidence level contour plots with WMAP and Riess et al. 2004 SNIa data, for the 9 parameter fit with a z dependent EOS in the plane (w_0, w_a). The plot on the left hand side corresponds to the case when we introduce no dark energy perturbation. For the plot on the right hand side, we introduce dark energy perturbations only when $w > -1$.

large uncertainties remain for the location of the minimum in the (w_0, w_a) plane, when a redshift variation is allowed. We emphasise that this is not due to the statistical method but to internal assumptions. Upadhye et al.(2004) mention the sensitivity to the choice of parametrization. We show that the introduction of dark energy perturbations for $w > -1$, can change the minimum by nearly 2σ and that the minimum is not well established as correlations between parameters increase, and errors, in this zone of parameter space are very large.

For the sake of simplicity, we decided to present, in the rest of this paper, a prospective study without dark energy perturbations, using a Fisher matrix technique.

4. Combination of future surveys

In this section, we study the sensitivity of the combination of future CMB, SNIa and weak lensing surveys for dark energy evolution. We expect new measurements from the CHTLS surveys in SNIa and weak lensing in the next few years, which can be combined with the first-year WMAP together with the expected CMB data from the Olimpo CMB balloon experiment. These are what we call 'mid term' surveys.

The combined mid term results will be compared to the 'long term' expectations from the next generation of observations in space which are under preparation, i.e., the Planck Surveyor mission for CMB, expected in 2007, and the SNAP/JDEM mission, a large imaging survey, expected for 2014, which includes both SNIa and weak lensing surveys.

4.1. Mid term surveys

The different assumptions we use for the mid term simulations are as follows, and are summarised in Tab. 3.

CMB: We add to the WMAP data, some simulated CMB expectations from the Olimpo balloon experiment (Masi et al. 2003), equipped with a 2.6 m telescope and 4 bolometers arrays for frequency bands centered at 143, 220, 410 and 540 GHz. This experiment will also allow us to observe the first "large" survey of galaxies cluster through the SZ effect. For this paper, we will limit our study to CMB anisotropy aspects.

For a nominal 10 days flight with an angular resolution $\theta_{fwhm} = 4'$ and with $f_{sky} \simeq 1\%$, the expected sensitivity per pixel is $s = 3.4 \times 10^{-6}$. We use Eq. 11 to estimate the statistical error σ_{C_ℓ} on the angular power spectrum.

SNIa: We simulate future SNIa measurements derived from the large SNLS (2001) ground based survey within the CFHTLS (2001). This survey has started in 2003 and expects to collect a sample of 700 identified SNIa in the redshift range $0.3 < z < 1$, after 5 years of observations. We simulate the sample, as explained in Virey et al. (2004a) with the number of SNIa shown in Tab. 2, in agreement with the expected SNIa rates from SNLS. We assume a magnitude dispersion of 0.15 for each supernova, constant

in redshift after all corrections. This uncertainty corresponds to the most favourable case in which experimental systematic errors are not considered.

A set of 200 very well calibrated SNIa at redshift < 0.1 should be measured by the SN factory (Wood-Vasey et al. 2004) project. This sample is needed to normalise the Hubble diagram and will be called the 'nearby' sample.

Table 2. Number of simulated SNIa by bins of 0.1 in redshift for SNLS+HST and SNAP respectively.

z	0.2	0.3	0.4	0.5	0.6	0.7	0.8	0.9	1.0	1.1	1.2	1.3	1.4	1.5	1.6	1.7
SNLS + HST	-	44	56	80	96	100	104	108	10	14	7	12	5	2	3	1
SNAP	35	64	95	124	150	171	183	179	170	155	142	130	119	107	94	80

Finally, to be as complete as possible, we simulate a set of 54 SNIa, expected from HST programs, with a magnitude dispersion of 0.17 for each supernova, at redshifts between 1 and 1.7. Tab. 3 summarises the simulation parameters.

Weak lensing: The coherent distortions that lensing induces on the shape of background galaxies have now been fi rmly measured from the ground and from space. The amplitude and angular dependence of this 'cosmic shear' signal can be used to set strong constraints on cosmological parameters.

Earlier studies of the constraints on dark energy from generic weak lensing surveys can be found in Hu & Tegmark (1999), Huterer (2001), Hu (2002). More recently, predictions for the constraints on an evolving $w(a)$ were studied by several authors (e.g., Benabed & van Waerbeke 2004, Lewis & Bridle 2002). We expect, in the near future, new cosmic shear results from the CFHTLS wide survey (CFHTLS 2001).

In this paper, we will consider measurements of the lensing power spectrum C_ℓ with galaxies in two redshift bins. We will only consider modes between $\ell = 10$ and 20000, thus avoiding small scales where instrumental systematics and theoretical uncertainties are more important.

For the CFHTLS survey, we assume a sky coverage of $170^{\circ 2}$. The rms shear error per galaxy is taken as $\sigma_\gamma = 0.35$ and the surface density of usable galaxies as $20\,\mathrm{amin}^{-2}$ which is divided evenly into to redshift bins with median redshifts $z_m = 0.72$ and 1.08. The redshift distribution of the galaxies in each redshift bin is taken to be as in Bacon et al. (2000) with the above median redshifts (cf Tab. 3 for a summary of the survey parameters). We use Eq. 18 to estimate the statistical error σ_{C_ℓ}.

4.2. Long term survey

The future will see larger surveys both from the ground and space. To estimate the gain for large ground surveys compared to space, critical studies taking into account the intrinsic ground limitation (both in distance and in systematics) should be done, and systematic effects, not included here, will be the dominant limitation. In this paper, we limit ourselves to the future space missions.

We simulate the Planck Surveyor mission using Eq. 11 with the performances described in Tauber et al. (2004). Assuming that the other frequency bands will be used to identify the astrophysical foregrounds, for the CMB study over the whole sky, we consider only the three frequency bands (100, 143 and 217 GHz) with respectively ($\theta_{fwhm} = 9.2'$, $7.1'$ and $5.0'$) resolution and ($s = 2.0\,10^{-6}$, $2.2\,10^{-6}$ and $4.8\,10^{-6}$) sensitivity per pixel.

We also simulate observations from the future SNAP satellite, a 2 m telescope which plans to discover around 2000 identifi ed SNIa, at redshift $0.2 < z < 1.7$ with very precise photometry and spectroscopy. The SNIa distribution, given in Tab. 2, is taken from Kim et al. (2004). The magnitude dispersion $\sigma(m)_{disp}$ is assumed to be 0.15, constant and independent of the redshift, for all SNIa after correction. Moreover, we introduce an irreducible systematic error $\sigma(m)_{irr}$ following the prescription of Kim et al. (2004). In consequence, the total error on the magnitude $\sigma(m)_{tot}$ per redshift bin i, is defi ned as: $\sigma(m)^2_{tot,i} = \sigma(m)^2_{disp}/N_i + \sigma(m)^2_{irr}$ where N_i is the number of SNIa in the ith 0.1 redshift bin. In the case of SNAP, $\sigma(m)_{irr}$ is equal to 0.02.

The SNAP mission also plans a large cosmic shear survey. The possibilities for the measurement of a constant equation of state parameter w with lensing data were studied by Rhodes et al. (2004), Massey et al. (2004), Refregier et al. (2004). We extend here the study in the case of an evolving equation of state. We use in the simulation the same assumptions as in Refregier et al. (2004) with a measurement of the lensing power spectrum in 2 redshift bins, except for the survey size, which has increased from $300^{\circ 2}$ to $1000^{\circ 2}$ (Aldering et al. 2004) and for the more conservative range of multipoles ℓ considered (see §4.1).

The long term survey parameters are summarised in Tab. 3.

4.3. Results

The combination of the three data sets is performed with, and without, a redshift variation for the equation of state, for both mid term and long term data sets.

Table 3. Simulation inputs for CMB, SNIa and Weak Lensing observations

CMB surveys					
		$\mathbf{f_{sky}}$	**f(GHz)**	$\theta_{\mathbf{fwhm}}(')$	**s(10^{-6})**
Current Data	WMAP (Spergel et al.(2003))	full sky	23/33/41/61/94	13	-
Mid term Data	Olimpo + WMAP	0.01	143/220/410/540	4	3.4
Long term data	Planck	full Sky	100	9.2	2.0
			143	7.1	2.2
			217	5.0	4.8
SN surveys					
		SN #	**Redshift range**	**Statistical error**	**Systematic error**
Current Data	Riess et al. (2004) + HST	157	$z < 1.7$	~ 0.25	-
Mid term Data	SNfactory	200	$z < 0.1$	0.15	-
	SNLS	700	$0.3 < z < 1$	0.15	-
	HST	54	$1 < z$	0.17	
Long term Data	SNfactory	300	$z < 0.1$	0.15	
	SNAP	2000	$0.1 < z < 1.7$	0.15	0.02
WL surveys					
		$\mathbf{z_m}$ **(2 bins)**	**A**(deg^2)	**total** $\mathbf{n_g}$**(amin**$^{-2}$**)**	σ_γ
Mid term Data	CFHTLS	0.72, 1.08	170	20	0.35
Long term Data	SNAP	0.95, 1.74	1000	100	0.31

The different plots in Fig. 3 show the results for individual mid term probes and for their combination. The results are for a constant w_0, plotted as a function of the matter density Ω_m. The combined contours are drawn using the full correlation matrix on the 8 parameters for the different sets of data.

The SNLS survey combined with the nearby sample will improve the present precision on w by a factor 2. The expected contours from cosmic shear have the same behaviour as the CMB but provide a slightly better constraint on Ω_m and a different correlation with w: CMB and weak lensing data have a positive (w, Ω_m) correlation compared to SNIa data, which have a negative correlation. This explains the impressive gain when the three data sets are combined, as shown in Tab. 4. Combining WMAP with Olimpo data, helps to constrain w through the correlation matrix as Olimpo expects to have more information for the large ℓ of the power spectrum.

Fig. 4 gives the expected accuracy of the mid term surveys on the parameters of an evolving equation of state. The CL contours plots of w_a versus w_0, are obtained with a 9 cosmological parameter fit. Here also, we observe a good complementarity: there is little information on the time evolution from SNIa with no prior, while the large redshift range from CMB data is adding a strong anti-correlated constraint on w_a.

A combined analysis proves far superior to analysis with only SNIa. In the favourable case, where we add more SNIa from HST survey, we expect a gain of a factor 2 on the errors, but it is not enough to lift degeneracies and the expected precision on w_a with these data will not be sufficient to answer questions on the nature of the dark energy.

The simulated future space missions show an improved sensitivity to the time evolution of the equation of state. The accuracy on w_a for the different combinations are summarised in Tab. 4. There is again a large improvement from the combination of the three data sets. The precision, for the long term surveys, will be sufficient to discriminate between the different models we have chosen, as shown in the left hand side plot of Fig. 5 and in Tab. 5, while it is not the case for the mid term surveys. This figure illustrates, moreover, that the errors on w_a and w_0, and the correlation between these two variables are strongly dependent on the choice of the fiducial model.

More generally, the combination of the probes with the full correlation matrix allows the extraction of the entire information available. For instance, the large correlation between n_S and w_a observed for the weak lensing probe combined with the precise measurement of n_s given by the CMB, gives a better sensitivity on w_a than the simple combination of the two w_a values, obtained separately for the CMB and weak lensing. Such an effect occurs for several other pairs of cosmological parameters considered

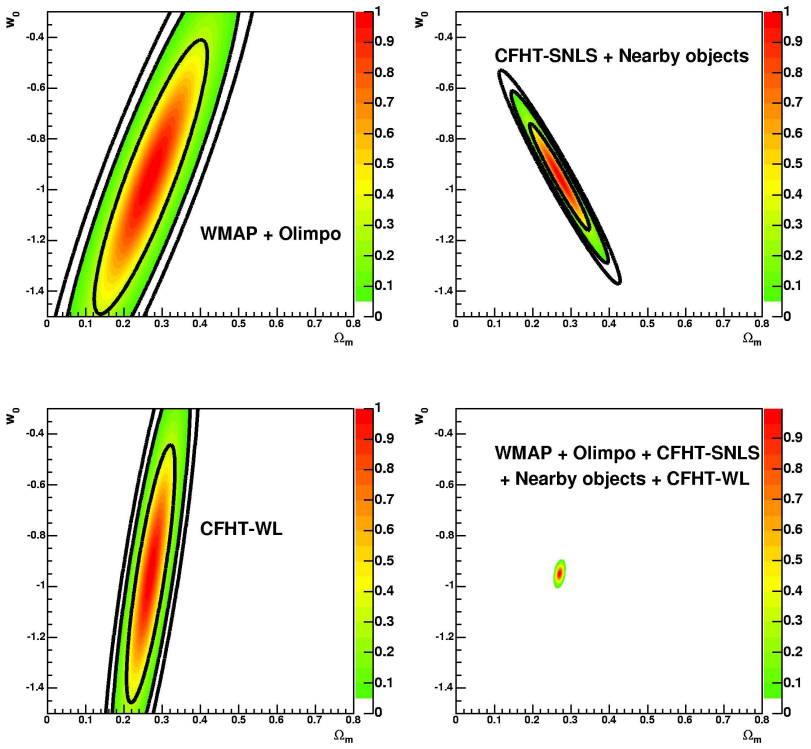

Fig. 3. CL contours for mid term CMB (WMAP +Olimpo), SNIa and weak lensing data from CFHTLS and the combination of the three probes for the 8 parameter fit in the plane (Ω_m, w_0) (see also Tab. 4). The solid lines represent 68% (1 σ), 95% (2σ), and 99% CL contours.

Table 4. Expected sensitivity on cosmological parameters for three scenarii: Current supernova and CMB experiments (WMAP and Riess et al.2004), mid term experiments (CFHT-SNLS (supernova surveys), CFHTLS-WL (weak lensing) and CMB (WMAP+Olimpo)), long term experiments (CMB (Planck) and SNAP (supernovae and weak lensing)). For each scenario, the first column gives the 1σ error computed with the Fisher matrix techniques for the 8 free parameter configuration and the second columns gives the 1σ error for the 9 free parameter configuration.

Scenario	**Today**		**Mid term**		**Long Term**	
$\mathbf{\Omega}_b$	0.003	0.004	0.001	0.002	0.0008	0.0008
$\mathbf{\Omega}_m$	0.04	0.04	0.01	0.01	0.004	0.004
h	0.03	0.03	0.01	0.01	0.006	0.006
$\mathbf{n}_s$	0.03	0.03	0.006	0.009	0.003	0.003
τ	0.05	0.04	0.01	0.01	0.01	0.01
$\mathbf{w}_0$	0.11	0.22	0.02	0.10	0.02	0.04
$\mathbf{w}_a$	–	0.99	–	0.43	–	0.07
A	0.10	0.10	0.02	0.02	0.02	0.02
$\mathbf{M}_{s0}$	0.03	0.03	0.01	0.01	0.01	0.01

in this study. The plot, in the right hand side of Fig 5, is an illustration of this effect. It shows the combination of the 3 probes in the (w_0, w_a) plane. The 1σ contour for the combined three probes, is more constraining than the 2-D combination in the (w_0, w_a) plane of the three probes.

Finally, in the long term scenario, the weak lensing probe provides a sensitivity on the measurement of (w_0, w_a) comparable with those of the combined SN and CMB probes, whereas in the mid term scenario the information brought by weak lensing was marginal. This large improvement observed in the information provided by the weak lensing, can be explained by the larger survey size and the deeper volume probed by SNAP/JDEM, compared to the ground CFHTLS WL survey. We thus conclude that adding weak lensing information will be an efficient way to help distinguishing between dark energy models. If systematic effects are well controlled, the future dedicated space missions may achieve a sensitivity of order 0.1 on w_a.

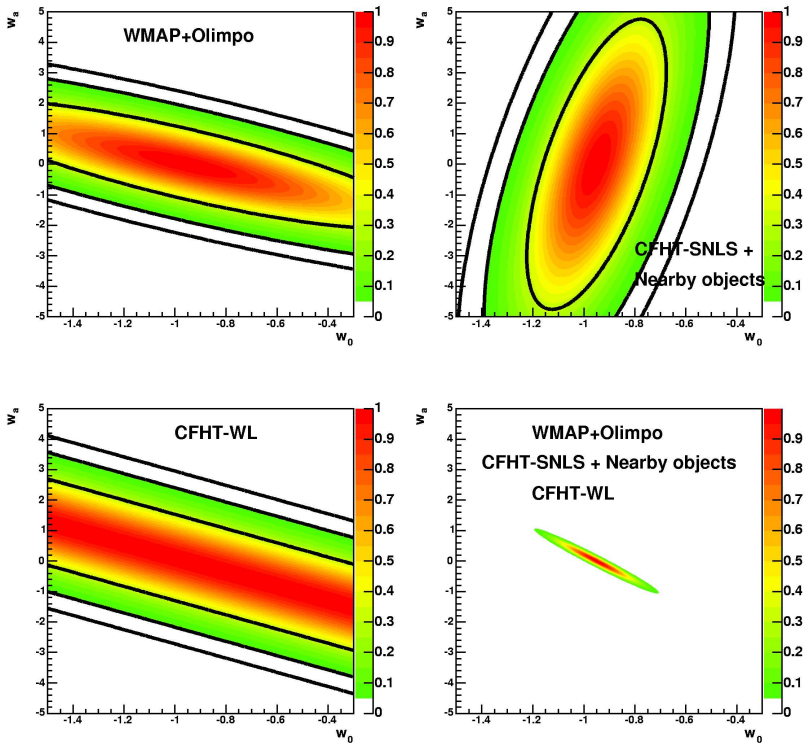

Fig. 4. CL contours for mid term CMB (WMAP +Olimpo), SNIa and weak lensing data from CFHTLS and the combination of the three probes for the 9 parameter fit in the plane (w_0, w_a) (see also Tab. 4). The solid lines represent 68% (1 σ), 95% (2σ), and 99% CL contours.

Table 5. Expected sensitivity on cosmological parameters for the long term missions with CMB (Planck) and SNAP (supernova surveys and weak lensing) for the 9 free parameter configuration.

Model	**ΛCDM**	**SUGRA**	**Phantom**
$\mathbf{\Omega}_b$	0.0008	0.0008	0.0007
$\mathbf{\Omega}_m$	0.004	0.004	0.003
h	0.006	0.006	0.005
$\mathbf{n}_S$	0.003	0.003	0.003
τ	0.01	0.01	0.01
$\mathbf{w}_0$	0.04	0.04	0.03
$\mathbf{w}_a$	0.07	0.06	0.14
A	0.02	0.02	0.02
$\mathbf{M}_{s0}$	0.015	0.014	0.013

The SNAP/JDEM space mission is designed, in principle, to control its observational systematic effects for SNIa to the % level, which is probably impossible to reach for future ground experiments. In this study, we assign an irreducible systematic error on SNIa magnitudes of 0.02 and systematic effects have been neglected for CMB and weak lensing. This can have serious impacts on the fi nal sensitivity, in particular, on the relative importance of each probe.

Other probes, whose combined effects we have not presented in this paper, but intend to do in forthcoming studies, remain therefore most useful. For example, the recent evidence for baryonic oscillations (Eisenstein et al. 2005) is a proof that new probes can be found. The present constraints that these results provide, do not improve the combined analysis we present here. However, getting similar results from different probes greatly contributes to the credibility of a result, in particular, when the systematical effects can be quite different, as is the case for the different probes we consider. Finally, the joint analysis of cluster data observed simultaneously with WL, SZ effect and X-rays, will allow the reduction of the intrinsic systematics of the WL probe.

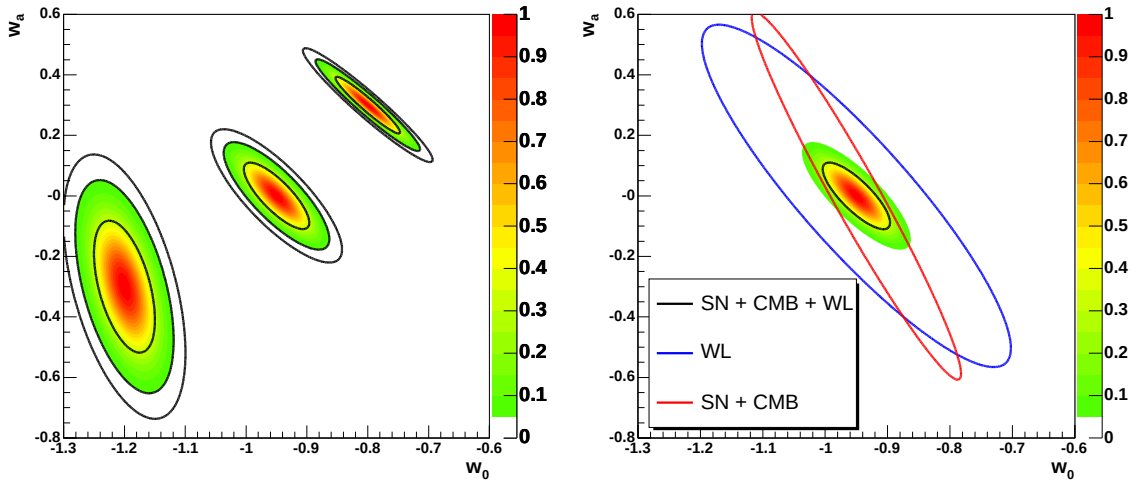

Fig. 5. CL contours for future space data from SNAP (SNIa and WL) and Planck (CMB) for a 9 parameter fit in the plane (w_0, w_a). The left hand side figure shows the combination of SNAP (SNIa+WL) and CMB for three different models (ΛCDM, SUGRA and Phantom). The solid lines represent 68% (1 σ), 95% (2σ), and 99% CL contours. The right hand side figure shows the CL for the combined three "long term" probes. The solid lines are the 1σ contours for different combinations: WL alone, combined SNIa and CMB, and the three combined probes.

5. Conclusions

In this paper, we have presented a statistical method based on a frequentist approach to combine different cosmological probes. We have taken into account the full correlations of parameters without any priors, and without the use of Markov chains.

Using current SNIa and WMAP data, we fit a parametrization of an evolving equation of state and find results in good agreement with other studies in the literature. We confirm that data prefer a value of w less than -1 but are still in good agreement with the ΛCDM model. We emphasise the impact of the implementation of the dark energy perturbations. This can explain the discrepancies in the central values found by various authors. We have performed a complete statistical treatment, evaluated the errors for existing data and validated that the Fisher matrix technique is a reliable approach as long as the parameters (w_0, w_a) are in the 'physical' region imposed by CMB boundary condition: $w(z \to \infty) < 0$.

We have then used the Fisher approximation to calculate the expected errors for current surveys on the ground (e.g., CFHTLS) combined with CMB data, and compared them with the expected improvements from future space experiments. We confirm that the complete combination of the three probes, including weak lensing data, is very powerful for the extraction of a constant w. However, a second generation of experiments like the Planck and SNAP/JDEM space missions is required, to access the variation of the equation of state with redshift, at the 0.1 precision level. This level of precision needs to be confirmed by further studies of systematical effects, especially for weak lensing.

Acknowledgements. The authors are most grateful to M. Doran for the CMBEASY package, the only code that was not developed by this collaboration, and for his readiness to answer all questions. They wish to thank A. Amara, J. Berg´e, A. Bonissent, D. Fouchez, F. Henry-Couannier, S. Basa, J.-M. Deharveng, J.-P. Kneib, R. Malina, C. Marinoni, A. Mazure, J. Rich, and P. Taxil for their contributions to stimulating discussions.

References

Aldering G. *et al.*, SNAP Collaboration, 2004, astro-ph/0405232
Bacon, D.J., Refregier, A., & Ellis, R., 2000, MNRAS **318**, 625
Bacon, D.J., Refregier, A., Clowe, D., Ellis, R. , 2001, MNRAS **325**, 1065
Bardeen, J.M., Bond, J.R., Kaiser, N., Szalay, A.S., 1986, Astrophys.J. **304**, 15
Bartelmann, M., & Schneider, P., 2001, Phys. Rep. **340**, 291
Benabed K. & Van Waerbeke L., 2004, Phys. Rev. **D70**, 123515
Bennett C.*et al.*, (WMAP Collaboration), 2003, Astrophys. J. Suppl. **148**, 1
Bunn E. & White S., 1997, Astrop. J. **480**, 6
Bridle S.L.*et al.*, 2003, Science **299**, 1532
Caldwell, R.R., 2002, Phys. Lett. B. **545**, 23
CFHTLS: see e.g. http://cfht.hawaii.edu, http://cfht.hawai.edu/Science/CFHTLS-OLD/history_2001.html

Caldwell R.R. and Doran M., 2005, astro-ph/0501104
Carlin B.P. and Louis T.A., *Bayes and Empirical Bayes Methods for Data Analysis*, 1996, (Chapman and Hall, London)
Carroll S.M. et al., 2005, Phys.Rev. **D71**, 063513
Chevallier M.& Polarski D., 2001, Int.J.Mod.Phys. **D10**, 213
Christensen N. and Meyer R., 1998, Phys. Rev. **D58**, 082001
Cooray, A., & Hu, W., 2001, Astrophys. J. **554**, 56
Corasaniti P. *et al.*, 2004, Phys.Rev. **D70**, 083006
Doran M., 2003, astro-ph/0302138
Eisenstein et al., 2005, astro-ph/0501171
Fisher, R.A. 1935, J. Roy. Stat. Soc. **98**, 39
Feldman G.J., Cousins R.D., 1998, Phys. Rev. **D57**, 3873
Gerke B. F. & Efstathiou G., 2002, MNRAS **335**, 33
Gilks W.R., Richardson S., Spiegelhalter D. J., 1996, *Markov Chain Monte Carlo in Practice* (Chapman and Hall, London)
Hawkins E. *et al.*, 2003, MNRAS **347**, 78
Heymans C. *et al.*, 2005, astro-ph/0506112
Hoekstra, H., Yee, H., & Gladders, M., 2002, New Astron. Rev.**46**, 767
Hu, W., & Tegmark, M., 1999, Astrophys.J. **514**, L65
Hu, W., 1999, Astrophys. J. **522**, L21
Hu, W., 2002, Phys. Rev. **D65** 023003
Hu, W., 2004, preprint astro-ph/0407158
Huterer, D., 2001, Phys. Rev. **D65**, 063001
Huterer, D. and Turner, M.S., 2001, Phys. Rev. **D64** 123527
Ishak M., 2005, astro-ph/0501594.
James F., 1978, CERN Program Library Long Writeup, D506.
Kaiser, N., 1998, Astrophys.J. **498**, 26.
Kim A.G.*et al.*, 2004, Mon. Not. R. Astron Soc. **347**, 909
Knop R.A.*et al.*, 2003, Astrophys. J. **598**, 102
Knox L., 1995, Phys. Rev. **D52**, 4307
Lewis A. & Bridle S., 2002, Phys. Rev **D66**, 103511
Linder E.V., 2003, Phys. Rev. Lett. **90**, 091301
Linder E.V. & Jenkins A., 2003, MNRAS **346**, 573
Linder E.V. and Huterer D., 2005, astro-ph/0505330
Lue A., Scoccimaro R. and Starkman G., 2004, Phys. Rev. **D69**, 044005
Ma, C.-P., Caldwell, R.R., Bode, P., & Wang, L., 1999, Astrophys.J. **521**, L1
Maor I.*et al.*, 2001, Phys. Rev. Lett. **86**, 6
Maor I. *et al.*, 2002, Phys. Rev. **D65**, 123003
Masi S. *et al.*, Olimpo Collaboration, 2003, Mem. S.A.It. Vol **74**, 96
Massey R. *et al.*, 2004, Astron. J. **127** 3089
Mellier, Y. et al., 2002, SPIE Conference 4847 Astronomical Telescopes and Instrumentation, Kona, August 2002, preprint astro-ph/0210091
Neyman J., Phil. Trans. Royal Soc. London, Series A, **236**, 333-80.
Peacock, J.A., & Dodds, 1996, MNRAS **280** L19
Peacock, J.A., 1997, MNRAS **284** 885
Peebles P.J.E. & Ratra R., 1988, Astrophys. J. Lett. **325** L17
Rapetti D., Allen S., Weller J., 2004, astro-ph/0409574, accepted, MNRAS
Refregier A., 2003, ARAA **41**, 645
Refregier A. *et al.*, 2004, Astron.J. **127**, 3102
Rhodes J.*et al.*, 2004, Astrophys.J. **605** 29
Riess A.G. *et al.*, 2004, Astrophys. J. **607**, 665
Seljak U. & Zaldarriaga M., 1996, Astrophys. J. **469**, 437
Seljak U.*et al.*, astro-ph/0407372
Spergel D.N., 2003, Astrophys.J.Suppl. **148**, 175
SNLS http://cfht.hawaii.edu/Science/CFHTLS-OLD/history_2001.html, cf e.g. http://cfht.hawaii.edu_SNLS
Sugiyama N., 1995, Astrophys.J.Suppl. **100**, 281
Sunyaev R.A. and Zeldovich Ya.B., 1980, Ann. Rev. Astron. Astrophys. **18**, 537
Tauber J.A. *et al.*, Planck Collaboration, 2004, Advances in Space Research, **34**, 491
Tilquin A.,2003, *http* : *//marwww.in2p3.fr/renoir/Kosmoshow.html*
Tegmark M. *et al.*, 2004, Phys. Rev. **D69**, 103501
Upadhye A.*et al.*, astro-ph/0411803
Virey J.-M. *et al.*, 2004a, Phys. Rev. **D70**, 043514
Virey J.-M. *et al.*, 2004b, Phys. Rev. **D70**, 121301
Wang Y. & Tegmark M., 2004, Phys. Rev. Lett. **92**, 241302
Weller J. & Albrecht A., 2002, Phys. Rev. **D65**, 103512
Weller J. & Lewis A.M , 2003, MNRAS **346**, 987
Wetterich C., 1988, Nucl. Phys. **B302**, 668
Wood-Vasey W.M.*et al.*, Nearby Supernova Factory, 2004, New Astron.Rev. **48**, 637
Xia J.-Q., Feng B. & Zhang X.-M., 2004, astro-ph/0411501
Zech, G., 2002, Eur.Phys.J.direct **C4**, 12

2.3.2 Contraintes sur la courbure et une énergie noire dynamique simultanément

Article publié sous la référence : Phys. Lett. **B648** (2007) 8 .

Probing for dynamics of dark energy and curvature of universe with latest cosmological observations

Gong-Bo Zhao[a], Jun-Qing Xia[a], Hong Li[b], Charling Tao[c], Jean-Marc Virey[d], Zong-Hong Zhu[e], and Xinmin Zhang[a]
[a] *Institute of High Energy Physics, Chinese Academy of Science, P.O. Box 918-4, Beijing 100049, P. R. China*
[b] *Department of Astronomy, School of Physics, Peking University, Beijing, 100871, P. R. China*
[c] *Centre de Physique des Particules de Marseille, CNRS/IN2P3-Luminy and Université de la Méditerranée, Case 907, F-13288 Marseille Cedex 9, France*
[d] *Centre de Physique Théorique, CNRS-Luminy and Université de Provence, Case 907, F-13288 Marseille Cedex 9, France. and*
[e] *Department of Astronomy, Beijing Normal University, Beijing 100875, P. R. China*

We use the newly released 182 Type Ia supernova data combined with the third-year Wilkinson Microwave Anisotropic Probe data (WMAP3) and large scale structure (LSS) information including SDSS and 2dFGRS to constrain the dark energy equation of state (EoS) as well as the curvature of universe Ω_K. Using the full dataset of Cosmic Microwave Background (CMB) and LSS rather than the shift parameter and linear growth factor, we make a Markov Chain Monte Carlo (MCMC) global fit, while paying particular attention to the dark energy perturbation. Parameterizing the EoS as $w_{DE}(a) = w_0 + w_1(1-a)$, we find the best fit of (w_0, w_1) is $(-1.053, 0.944)$ and for $w_{DE}(a) = w_0 + w_1 \sin(\frac{3}{2}\pi \ln(a))$, the best fit for (w_0, w_1) is $(-1.614, -1.046)$. We find that a flat universe is a good approximation, namely, $|\Omega_K| > 0.06$ has been excluded by 2σ yet the inclusion of Ω_K can affect the measurement of DE parameters owing to their correlation and the present systematic effects of SNIa measurements.

I. INTRODUCTION

Dark energy (DE), the very power to drive universe's acceleration, is one of the most important issues in modern cosmology. Its existence was firstly revealed by the measurement of the relationship between redshift z and luminosity distance d_L of Type Ia supernova (SN Ia)[1]. Dark Energy encodes its mystery in its equation of state (EoS) defined as the ratio of pressure over energy density thus DE models can be classified in terms of EoS[2].

The simplest candidate of dark energy is the cosmological constant (CC) whose EoS remains -1. Favored by current astronomical observations as it is, CC suffers from severe theoretical drawbacks such as the fine-tunning and coincidence problem[3]. Alternative DE models with rolling scalar field, such as quintessence[4], phantom[5], k-essence[6], etc have been studied. The EoS of these models varies with cosmic time either above -1 or below -1 during evolution but the statement of "No-Go" theorem forbids it to cross the -1 boundary[7]. Models where gravity is modified can also give these observed effects.

Given our ignorance of the nature of dark energy, constraining the evolution of DE the EoS by cosmological observations is of great significance. Various methods have been used to constrain DE including parametric fitting[8–10], non-parametric reconstruction[11], *etc.* Interestingly, there exists some hint that the EoS of DE has crossed over -1 at least once from current observations[9, 11–13], which greatly challenges the above mentioned dark energy models, albeit the evidence is still marred by systematic effects. Quintom, whose EoS can smoothly cross -1[14], has attracted a lot of attention in the literature since its invention[15]. There have been many efforts in quintom model building, for example, double-scalar-field realization[14, 16], a single scalar field with high derivative[17], vector fields[18] and so forth.

A special and interesting example of quintom is Oscillating Quintom, whose EoS oscillates with time and crosses -1 many times. The oscillating behavior in the EoS leads to oscillations in the Hubble constant and a recurrent universe. Oscillating Quintom is physically well motivated, since this scenario, to some extent, unifies early inflation and the current acceleration of the universe[19]. In Ref.[20], we have presented some preliminary studies on oscillating quintom.

The nature of dark energy is a dominant factor of the fate of our universe. Another critical point is the curvature, Ω_K. neutrino masses, which probably exists, albeit small, and the curvature, Ω_K. We concentrate, in this paper, on the correlation between Ω_K and the dark energy parameters.[1]

We use the newly released 182 SN Ia "Gold sample" (SN182)[24] combined with WMAP3[25][2] and LSS information to constrain the evolution of the DE EoS and the curvature of universe. For DE EoS, we choose two parameterizations

---

[1] Other cosmological parameters also affect the probing of dark energy, such as neutrino mass[21] and inflationary parameters[22].
[2] Available at http://lambda.gsfc.nasa.gov/product/map/current/

as in (1) and (2) and we will address our motivation for such a choice in the next section. In our study, we treat the curvature of the universe Ω_K as a free parameter rather than simply assuming a flat universe and make a Markov Chain Monte Carlo (MCMC) global fit based on Bayesian statistics. Paying particular attention to the dark energy perturbation especially when EoS crosses -1[8], we find the latest observations mildly favor quintom model however ΛCDM remains a good fit. We have also found that the inclusion of Ω_K can affect the determination of DE parameters significantly due to their correlation.

We structure this paper as follows: after this introductory part, we propose our method and define the data set used in section II. The in section III we present our results and end up with discussion and comments.

II. METHOD AND DATA

To study the dynamical behavior of dark energy, we choose two kinds of parametrization of dark energy equation of state:
I)

$$w_{DE}(a) = w_0 + w_1(1-a) \tag{1}$$

II)

$$w_{DE}(a) = w_0 + w_1 \sin(w_2 \ln(a)) \tag{2}$$

where a is the scale factor, w_0 denotes the EoS at present epoch and w_1 and w_2 characterize the time evolution of DE. Parametrization I) is the most popular in literature since w_1 simply equals to $-dw_{DE}(a)/da$, which is the time derivative of $w_{DE}(a)$[26]. Thus it is straightforward to study the dynamical behavior of DE. The physical motivation of parametrization II) is oscillating quintom. From (2) we can see at low redshift, II) takes a form similar to I). At medium and high redshift, the EoS keeps oscillating.

From the latest SN Ia paper[24], one can find some hint of oscillating behavior of the EoS in their FIG.10 where they use a quartic polynomial fit. Our sine function has the advantage of preserving the oscillating feature of the EoS at high redshift measured by the CMB data. For simplicity and focus on the study at lower redshift, we set w_2 to be $\frac{3}{2}\pi$ in order to allow the EoS to evolve more than one period within the redshift range of 0 to 2 where SN data are most robust.

When using the MCMC global fitting strategy to constrain cosmological parameters, it is crucial to include dark energy perturbation. This issue has been realized by many researchers including the WMAP group[7, 8, 25, 27]. However one cannot handle the dark energy perturbation when the parameterized EoS crosses -1 based on quintessence, phantom,k-essence and other non-crossing models. By virtue of quintom, the perturbation at the crossing points is continuous, thus we have proposed a sophisticated technique to treat dark energy perturbation in the whole parameter space, say, EoS> -1, < -1 and at the crossing pivots. For details of this method, we refer the readers to our previous companion paper [7, 8].

In this study, we have modified the publicly available Markov Chain Monte Carlo package CAMB/CosmoMC[28] to include the dark energy perturbation when the equation of state crosses -1.

The dark energy EoS and curvature of the universe Ω_K can affect the determination of the geometry of our universe thus DE parameters are correlated with Ω_K. Therefore, in our study, we relax the curvature of universe Ω_K as a free parameter rather than simply assuming a flat universe. We assume purely adiabatic initial conditions and set our most general parameter space as:

$$\mathbf{P} \equiv (\omega_b, \omega_c, \Theta_s, \tau, \Omega_K, w_0, w_1, n_s, \ln(10^{10} A_s)) \tag{3}$$

where $\omega_b \equiv \Omega_b h^2$ and $\omega_c \equiv \Omega_c h^2$ are the physical baryon and Cold Dark Matter densities relative to the critical density, Θ_s is the ratio (multiplied by 100) of the sound horizon to the angular diameter distance at decoupling, τ is the optical depth to re-ionization, $\Omega_K \equiv 1 - \Omega_m - \Omega_{DE}$ is the spatial curvature, w_0, w_1 portray the dynamical feature of dark energy as illustrated in (1) and (2). A_s and n_s characterize the primordial scalar power spectrum. For the pivot of the primordial spectrum we set $k_{s0} = 0.05\mathrm{Mpc}^{-1}$. Furthermore, we make use of the Hubble Space Telescope (HST) measurement of the Hubble parameter $H_0 \equiv 100\mathrm{h\ km\ s^{-1}\ Mpc^{-1}}$[29] by multiplying the likelihood by a Gaussian likelihood function centered around $h = 0.72$ and with a standard deviation $\sigma = 0.08$. We also impose a weak Gaussian prior on the baryon density $\Omega_b h^2 = 0.022 \pm 0.002$ ($1\ \sigma$) from Big Bang Nucleosynthesis[30]. The weak priors we take are as follows: $\tau < 0.8$, $0.5 < n_s < 1.5$, $-0.3 < \Omega_K < 0.3$, $-3 < w_0 < 3$, $-5 < w_1 < 5$ [3] and a

[3] We set the prior of w_0 and w_1 broad enough to ensure the EoS can evolve in the whole parameter space.

TABLE 1. Constraints of dark energy equation of state and some background parameters when relaxing Ω_K as a free parameter (Left panel) and assuming a flat universe (Right). For each case, we consider two forms of parametrization of dark energy EoS: Linear ($w(a) = w_0 + w_1(1-a)$) and Oscillating ($w(a) = w_0 + w_1 \sin(w_2 \ln(a))$, set $w_2 = \frac{3}{2}\pi$, see text for explanation). Best fit models, which give the minimum χ^2, and the marginalized 2σ errors are shown. All these constraints are from data combination of WMAP3 + SN182 + SDSS + 2dFGRS.

	$w(a) = w_0 + w_1(1-a)$			
	Ω_K free		Ω_K=0	
	Best fit	2σ	Best fit	2σ
Ω_K	-0.015	$[-0.058, 0.028]$	set to 0	set to 0
w_0	-1.053	$[-1.441, -0.615]$	-1.149	$[-1.269, -0.606]$
w_1	0.944	$[-1.983, 1.223]$	1.017	$[-1.078, 1.163]$
Ω_m	0.282	$[0.238, 0.423]$	0.291	$[0.246, 0.332]$

	$w(a) = w_0 + w_1 \sin(w_2 \ln(a))$			
	Ω_K free		Ω_K=0	
	Best fit	2σ	Best fit	2σ
Ω_K	-0.012	$[-0.051, 0.015]$	set to 0	set to 0
w_0	-1.614	$[-2.720, -0.660]$	-1.149	$[-2.454, -0.593]$
w_1	-1.046	$[-2.591, 0.557]$	-0.525	$[-2.508, 0.518]$
Ω_m	0.280	$[0.240, 0.393]$	0.276	$[0.230, 0.318]$

cosmic age tophat prior 10 Gyr $< t_0 <$ 20 Gyr.

In our calculations, we have taken the total likelihood to be the products of the separate likelihoods $\mathcal{L}$ of CMB, LSS and SNIa. In other words, defining $\chi^2 \equiv -2\log\mathcal{L}$, we get

$$\chi^2_{total} = \chi^2_{CMB} + \chi^2_{LSS} + \chi^2_{SNIa} \ . \tag{4}$$

If the likelihood function is exactly Gaussian, χ^2 coincides with the usual definition of χ^2 up to an additive constant corresponding to the logarithm of the normalization factor of $\mathcal{L}$. In the calculation of the likelihood from SNIa we have marginalized over the nuisance parameter [31]. The supernova data we use are the "gold" set of 182 SNIa recently published by Riess *et al* in Ref.[24]. In the computation of CMB we have used the full dataset of the WMAP3 data with the routine for computing the likelihood supplied by the WMAP team [25]. For LSS information, we have used the 3D power spectrum of galaxies from the SDSS [32] and 2dFGRS[33]. To be conservative but more robust, in the fittings to the 3D power spectrum of galaxies from the SDSS, we have used the first 14 bins only, which are supposed to be well within the linear regime [34].

For each regular calculation, we run six independent chains comprising $150,000 - 300,000$ chain elements and spend thousands of CPU hours to calculate on a cluster. The average acceptance rate is about 40%. We discard the first 30% chain elements to be the "burn-in" process, test the convergence of the chains by Gelman and Rubin criteria[35] and find $R-1$ of order 0.01, which is more conservative than the recommended value $R-1 < 0.1$.

III. RESULTS

We summarize our main results in Table I. For all the combined data (SN182+WMAP3+SDSS+2dFGRS), we find that the flat universe is a good fit since the best fit value of Ω_K is -0.015 and -0.012 for DE parametrization I) and II) respectively and $|\Omega_K| > 0.06$ has been excluded for more than 2σ for both DE parameterizations. This can be seen graphically in FIG.1. From these 2-D contour plots of energy density of dark energy and matter from different data combination and different DE parameterizations, we find that the data of supernova-only favor a non-flat universe, however when CMB and LSS data are combined, a flat universe is preferred.

For parametrization I), we find the best fit value of (w_0, w_1) to be $(-1.149, 1.107)$ for a flat universe. When Ω_K is freely relaxed, the best fit value of (w_0, w_1) is changed to $(-1.053, 0.944)$ and the error bars of nearly all the cosmological parameters have been enlarged. We find dark energy models whose EoS can cross -1 are mildly favored.

The 1-D posterior distribution of w_0, w_1, Ω_K and their 2-D correlation are shown in FIG.2. In the $w_0 - \Omega_K$ and $w_1 - \Omega_K$ panel, we find interesting correlation among curvature and DE parameters. This is expected since Ω_K can contribute to luminosity distance d_L via:

$$d_{\rm L}(z) = \frac{1+z}{H_0\sqrt{|\Omega_k|}}{\rm sinn}\left[\sqrt{|\Omega_k|}\int_0^z \frac{dz'}{E(z')}\right], \tag{5}$$

$$E(z) \equiv \frac{H(z)}{H_0} = [\Omega_m(1+z)^3 + \Omega_{DE}\ \exp\left(3\int_0^z \frac{1+w(z')}{1+z'}dz'\right) + \Omega_K(1+z)^2]^{1/2}\ . \tag{6}$$

where ${\rm sinn}(\sqrt{|k|}x)/\sqrt{|k|} = \sin(x)$, x, $\sinh(x)$ if $k = 1,\ 0,\ -1$. Furthermore, Ω_K can modify the angular diameter distance to last scattering surface and the transfer function, which leaves imprints on the CMB and matter power spectrum.

In the $w_0 - w_1$ panel of FIG.2, the parameter space has been divided into four parts. The upper right and lower left parts denote for $w > -1$ and $w < -1$, the regions for quintessence and phantom models respectively. The other two parts dubbed "Quintom A(B)" represent models whose EoS can cross -1 during evolution. Quintom A crosses -1 from upside down while Quintom B transits -1 from the opposite direction. We also plot the results when assuming a flat universe for comparison. We see the best fit model is in the region of Quintom A and the ΛCDM(the intersect of two dot dashed lines) is still a good fit. Moreover, relaxing Ω_K enlarges the $w_0 - w_1$ contour as expected.

For parametrization II), again we find a small absolute value of Ω_K. The best fit models can cross -1 twice in the evolution. In FIG.3, we show the correlation between Ω_K and dark energy parameters, and we find the Quintom model whose EoS crosses -1 during evolution is preferred.

We can see the dynamics of dark energy more clearly from FIG.4. We show the best fit model and 2σ errors of $w(z)$ for the case of flat universe and relaxing Ω_K as a free parameter for the two DE parameterizations. The best fit model of each case is quintom-like.

IV. SUMMARY AND DISCUSSIONS

In this paper we investigate the dynamics of dark energy and curvature of universe from the data of newly released 182 supernova data combined with CMB and LSS information. Rather than assuming a flat universe, we relax Ω_K as a free parameter and make a MCMC global fit to measure the dark energy parameters as well as the curvature of universe. We find the model whose EoS can cross over -1 is favored for two dark energy parameterizations we considered in this work, albeit the ΛCDM model remains a good fit. A flat universe is preferred, namely, the best fit value of $|\Omega_K|$ is smaller than 0.015 for the two DE parameterizations and $|\Omega_K| > 0.06$ has been excluded by more than 2σ. However, the correlation among dark energy parameters and Ω_K might not be neglected. Freeing Ω_K enlarges the contours and even modifies the best fit value of dark energy parameters. For example, for parametrization II), relaxing Ω_K has changed the best fit value of (w_0, w_1) from $(-1.149, -0.525)$ to $(-1.614, -1.046)$. This is because adding Ω_K can reduce the total χ^2 by 1.2 thus the global minimum moves to a deeper point.

For CMB information, we use the full dataset of WMAP3, rather than the shift parameter. The shift parameter has the advantage of easy implementaton and much shorter calculation time, but it is not really "model independent". It is derived from a fiducial ΛCDM model, thus it might lead to biased results, if one fits to models departing significantly from the fiducial model. Another drawback is that the shift parameter can merely offer part of the CMB information related to background parameters, thus it cannot constrain the perturbated dark energy.

We will have a deeper and deeper understanding of dark energy with the accumulation of high quality cosmological observation especially for supernova data, such as future SNAP, ESSENCE, etc. To be bias-free as much as possible, it is better to add Ω_K into the global analysis, use full datasets of CMB and carefully treat dark energy perturbation.

Acknowledgement. — We acknowledge the use of the Legacy Archive for Microwave Background Data Analysis (LAMBDA). Support for LAMBDA is provided by the NASA Office of Space Science. We have performed our numerical analysis on the Shanghai Supercomputer Center(SSC). We thank Bo Feng, Mingzhe Li, Weidong Li, Pei-Hong Gu, Xiao-Jun Bi, David Polarski and André Tilquin for helpful discussions. This work is supported in part by National Natural Science Foundation of China under Grant Nos. 90303004, 10533010 and 19925523.

[1] A. G. Riess *et al.*, Astron. J. **116**, 1009 (1998); S. Perlmutter *et al.*, Astrophys. J. **517**, 565 (1999).

[2] R. R. Caldwell and E. V. Linder, Phys. Rev. Lett. **95**, 141301 (2005); Z. K. Guo, Y. S. Piao, X. Zhang and Y. Z. Zhang, arXiv:astro-ph/0608165.
[3] S. Weinberg, Rev. Mod. Phys. **61**, 1 (1989); I. Zlatev, L. M. Wang, and P. J. Steinhardt, Phys. Rev. Lett. **82**, 896 (1999).
[4] B. Ratra and P. J. E. Peebles, Phys. Rev. D **37**, 3406 (1988); P. J. E. Peebles and B. Ratra, Astrophys. J. **325**, L17 (1988); C. Wetterich, Nucl. Phys. B **302**, 668 (1988); C. Wetterich, Astron. Astrophys. **301**, 321 (1995).
[5] R. R. Caldwell, Phys. Lett. B **545**, 23 (2002).
[6] C. Armendariz-Picon, V. Mukhanov and P. J. Steinhardt, Phys. Rev. Lett. **85**, 4438 (2000); Phys. Rev. D **63**, 103510 (2001).
[7] G. B. Zhao, J. Q. Xia, M. Li, B. Feng and X. Zhang, Phys. Rev. D **72**, 123515 (2005)
[8] J. Q. Xia, G. B. Zhao, B. Feng, H. Li and X. Zhang, Phys. Rev. D **73**, 063521 (2006);
[9] J. Q. Xia, G. B. Zhao, B. Feng and X. Zhang, JCAP **0609**, 015 (2006);
G. B. Zhao, J. Q. Xia, B. Feng and X. Zhang, arXiv:astro-ph/0603621.
[10] M. Tegmark *et al.*, arXiv:astro-ph/0608632;
U. Seljak, A. Slosar and P. McDonald, JCAP **0610**, 014 (2006);
U. Seljak *et al.* [SDSS Collaboration], Phys. Rev. D **71**, 103515 (2005);
M. Tegmark *et al.* [SDSS Collaboration], Phys. Rev. D **69**, 103501 (2004).
[11] D. Huterer and A. Cooray, Phys. Rev. D **71**, 023506 (2005);
U. Alam, V. Sahni and A. A. Starobinsky, arXiv:astro-ph/0612381.
[12] V. Barger, Y. Gao and D. Marfatia, arXiv:astro-ph/0611775.
[13] H. Li, M. Su, Z. Fan, Z. Dai and X. Zhang, arXiv:astro-ph/0612060.
[14] B. Feng, X. L. Wang and X. M. Zhang, Phys. Lett. B **607**, 35 (2005).
[15] H. Wei and R. G. Cai, hep-th/0501160; R. G. Cai, H. S. Zhang and A. Wang, hep-th/0505186; A. A. Andrianov, F. Cannata and A. Y. Kamenshchik, gr-qc/0505087; X. Zhang, astro-ph/0504586; Q. Guo and R. G. Cai, gr-qc/0504033; B. McInnes, Nucl. Phys. B **718**, 55 (2005); E. Elizalde, S. Nojiri, S. D. Odintsov and P. Wang, Phys. Rev. D **71**, 103504 (2005); I. Y. Aref'eva, A. S. Koshelev, and S. Yu. Vernov, astro-ph/0507067; A. Anisimov, E. Babichev and A. Vikman, J. Cosmol. Astropart. Phys. **0506**, 006 (2005); H. Stefancic, astro-ph/0504518; J. Zhang, X. Zhang and H. Liu, arXiv:astro-ph/0612642.
[16] X. F. Zhang, H. Li, Y. S. Piao and X. M. Zhang, Mod. Phys. Lett. A **21**, 231 (2006);
Z. K. Guo, Y. S. Piao, X. M. Zhang and Y. Z. Zhang, Phys. Lett. B **608**, 177 (2005).
[17] M. Li, B. Feng and X. m. Zhang, JCAP **0512**, 002 (2005);
X. F. Zhang and T. T. Qiu, Phys. Lett. B **642** (2006) 187.
[18] H. Wei and R. G. Cai, Phys. Rev. D **73**, 083002 (2006).
[19] B. Feng, M. Li, Y. S. Piao and X. Zhang, Phys. Lett. B **634**, 101 (2006).
[20] J. Q. Xia, G. B. Zhao, H. Li, B. Feng and X. Zhang, Phys. Rev. D **74**, 083521 (2006);
J. Q. Xia, B. Feng and X. M. Zhang, Mod. Phys. Lett. A **20**, 2409 (2005).
[21] J. Lesgourgues and S. Pastor, Phys. Rept. **429**, 307 (2006);
S. Hannestad, Phys. Rev. Lett. **95**, 221301 (2005);
J. Q. Xia, G. B. Zhao and X. Zhang, arXiv:astro-ph/0609463.
[22] J. Q. Xia, G. B. Zhao, B. Feng and X. Zhang, JCAP **0609**, 015 (2006)
[23] R. R. Caldwell and M. Kamionkowski, JCAP **0409**, 009 (2004);
K. Ichikawa and T. Takahashi, Phys. Rev. D **73**, 083526 (2006);
K. Ichikawa, M. Kawasaki, T. Sekiguchi and T. Takahashi, arXiv:astro-ph/0605481;
Z. Y. Huang, B. Wang and R. K. Su, arXiv:astro-ph/0605392.
[24] A. G. Riess *et al.*, arXiv:astro-ph/0611572.
[25] D. N. Spergel *et al.*, arXiv:astro-ph/0603449.
[26] M. Chevallier and D. Polarski, Int. J. Mod. Phys. D **10**, 213 (2001); E. V. Linder, Phys. Rev. Lett. **90**, 091301 (2003).
[27] J. Weller and A. M. Lewis, Mon. Not. Roy. Astron. Soc. **346**, 987 (2003).
[28] A. Lewis and S. Bridle, Phys. Rev. D **66**, 103511 (2002); See also the CosmoMC website at: http://cosmologist.info.
[29] W. L. Freedman *et al.*, Astrophys. J. **553**, 47 (2001).
[30] S. Burles, K. M. Nollett and M. S. Turner, Astrophys. J. **552**, L1 (2001).
[31] For details see e.g. E. Di Pietro and J. F. Claeskens, Mon. Not. Roy. Astron. Soc. **341**, 1299 (2003).
[32] M. Tegmark *et al.* [SDSS Collaboration], Astrophys. J. **606**, 702 (2004).
[33] S. Cole *et al.* [The 2dFGRS Collaboration], Mon. Not. Roy. Astron. Soc. **362** (2005) 505.
[34] M. Tegmark *et al.* [SDSS Collaboration], Phys. Rev. D **69**, 103501 (2004).
[35] A. Gelman and D. Rubin, Statistical Science **7**, 457 (1992).

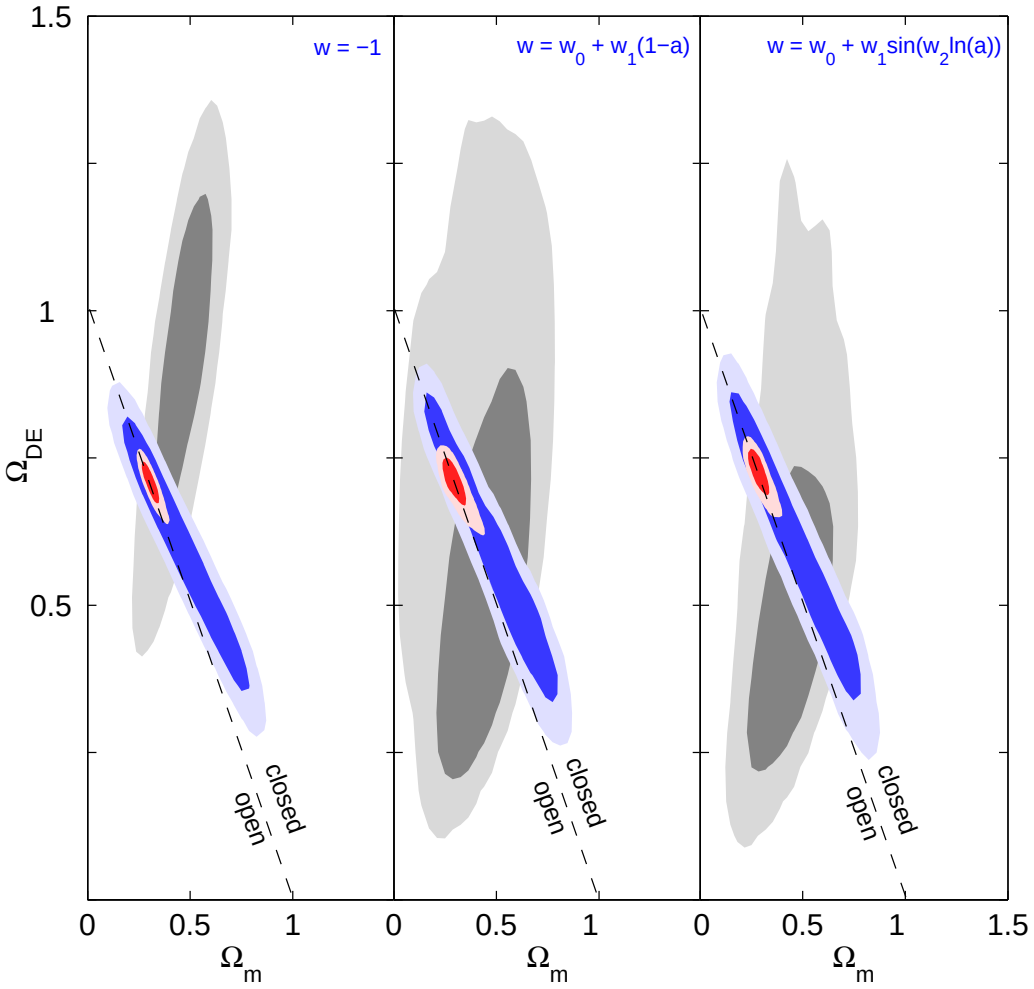

FIG. 1: 2-D contour plots of energy density of matter and dark energy using latest astronomical observations. Grey: SN182; Blue: WMAP3; Red: WMAP3 + SN182 + SDSS + 2dFGRS. The dark and light shaded regions stand for 68% and 95% C.L. respectively. Different dynamical behaviors of dark energy have been considered. Left: vacuum energy ($w = -1$ forever); Middle: linearly growing ($w(a) = w_0 + w_1(1-a)$); Right: Oscillating ($w(a) = w_0 + w_1 \sin(w_2 \ln(a))$), with $w_2 = \frac{3}{2}\pi$.

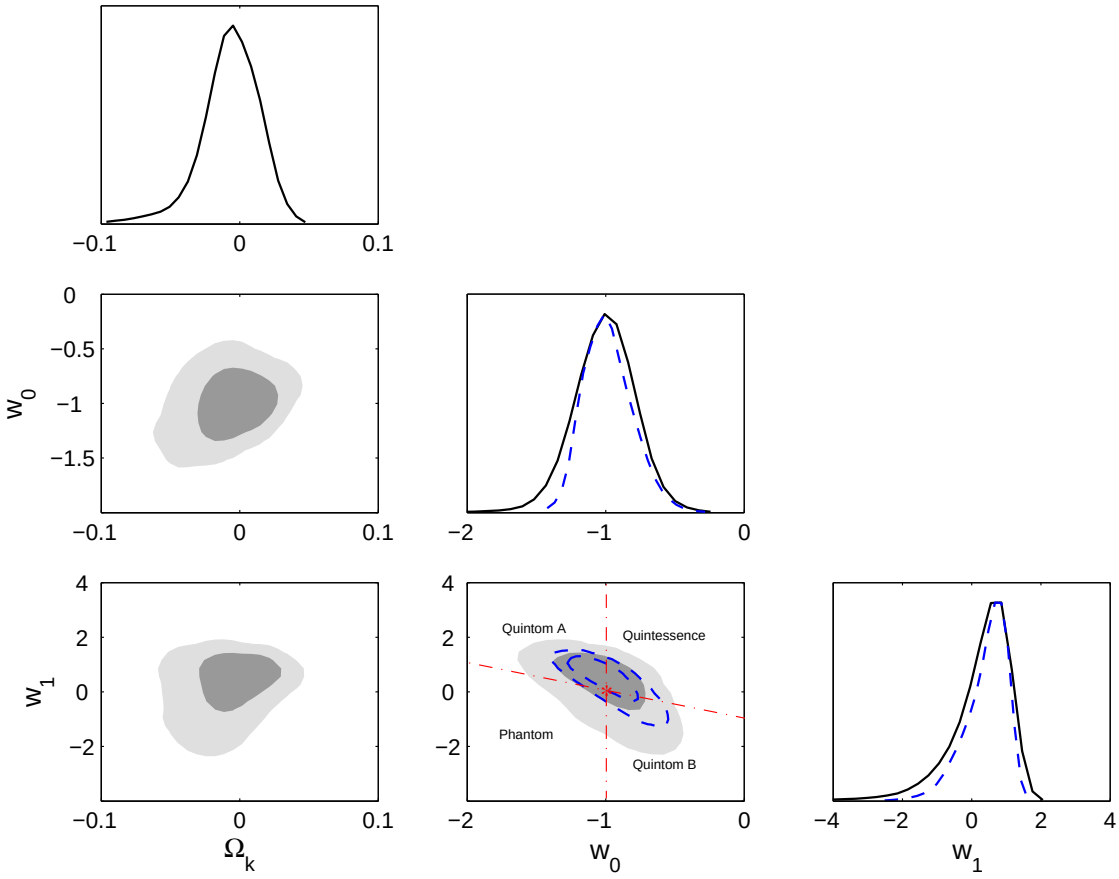

FIG. 2: Constraints on the curvature Ω_K and dark energy parameters w_0 and w_1 when parameterizing DE EoS as $w(a) = w_0 + w_1(1-a)$. 1-D plots show the posterior distribution of Ω_K,w_0 and w_1 while the 2-D contour plots illustrate their correlation. The dark and light shaded area stand for 68% and 95% C.L. respectively. Blue dashed curves denote the case of flat universe for comparison. Different dark energy models can be distinguished from the $w_0 - w_1$ panel (See text). All these constraints are from data of WMAP3 + SN182 + SDSS + 2dFGRS.

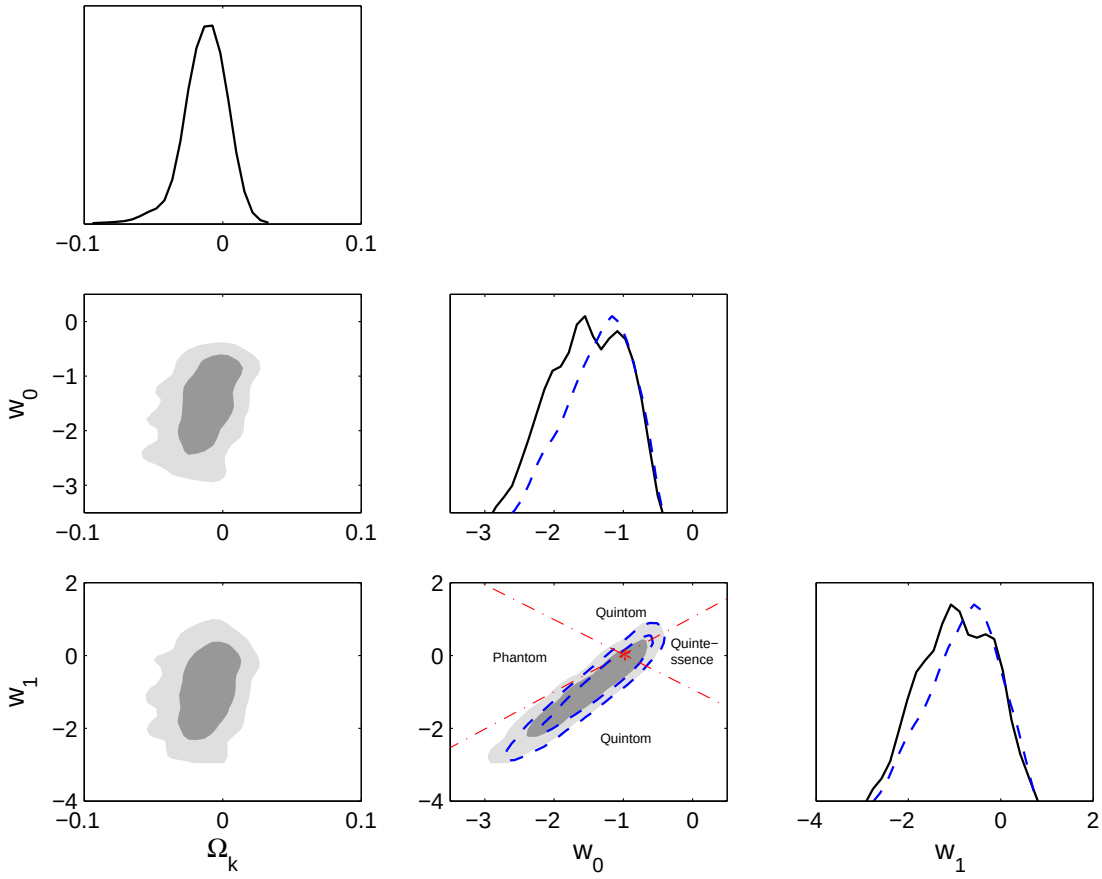

FIG. 3: The same graphic convention as in FIG.2 except for the parametrization of the EoS of DE: $w(a) = w_0 + w_1 \sin(w_2 \ln(a))$. For simplicity, we have chosen w_2 to be $\frac{3}{2}\pi$. Note the variations of the error on Ω_k for negative Ω_k, as a function of w_1, which reflect the oscillating feature of this parametrization of the EoS.

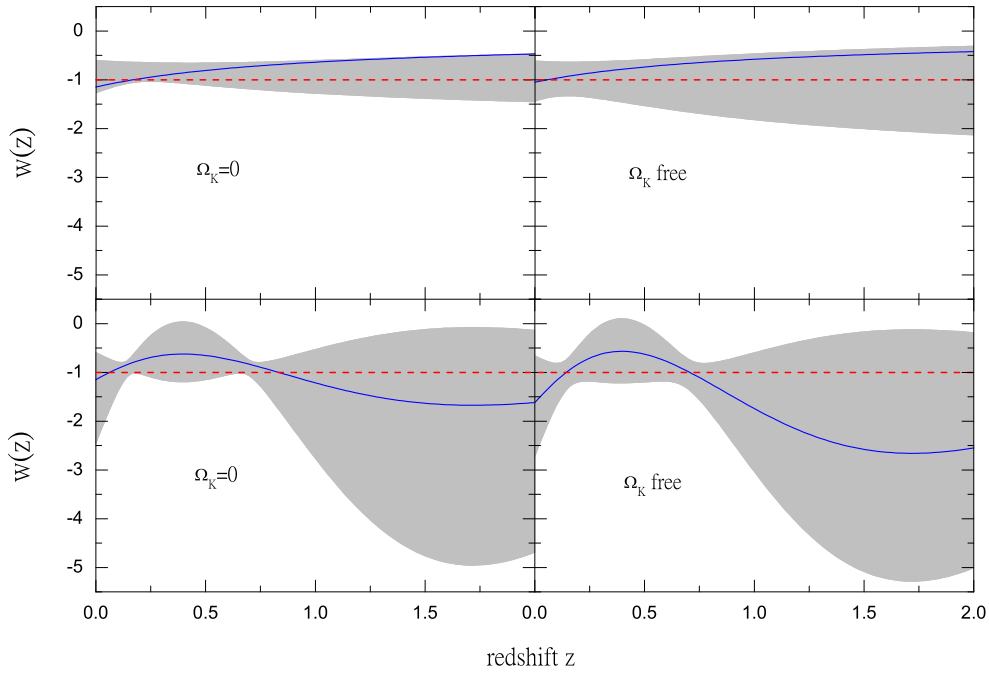

FIG. 4: Constraints of the time evolving of equation of state of DE using WMAP3 + SN182 + SDSS + 2dFGRS. Upper panel: $w(a) = w_0 + w_1(1-a)$; Lower panel: $w(a) = w_0 + w_1 \sin(w_2 \ln(a))$. The cases of flat universe and treating Ω_K as a free parameter are both considered as illustrated in the plot. The solid blue lines denote the best fit models while the shaded areas illustrate the 2σ errors. Red dashed lines show the cosmological constant boundary.

2.4 Test cosmologique à partir de la cinématique des galaxies

Dans cette partie nous proposons un nouveau test cosmologique à partir des propriétés cinématiques des galaxies. L'idée originale, essentiellement due à Christian Marinoni, est d'utiliser les vitesses particulières des galaxies afin de construire des "règles" standard ainsi que des chandelles standard.

Il est connu depuis longtemps (Tully & Fisher 1977 [99, 100]) qu'il existe une relation, basée sur les observations, entre la vitesse de rotation d'une galaxie spirale et son diamètre, ainsi qu'avec sa luminosité. Du point de vue théorique, on s'attend à l'existence d'une telle relation dans le cadre des modèles de formation des structures avec matière noire froide [101]. La relation de Tully-Fisher est utilisée localement pour déterminer les distances des galaxies et la constante de Hubble H_0.

Dans les articles qui suivent il est proposé d'utiliser cette relation dans un contexte cosmologique afin de définir des "règles" standard et des "chandelles" standard à haut redshift. Plus précisemment, la relation de Tully-Fisher nous indique que des galaxies spirales possédant la même vitesse de rotation ont statistiquement la même taille et la même luminosité. L'expansion de l'univers a un effet direct sur l'évolution dans le temps (*i.e.* en redshift) de ces propriétés physiques. On peut alors utiliser les catalogues de galaxies à haut redshift, tel que ceux fournis par les collaborations VVDS [102](disponible) ou zCOSMOS [103] (en cours de mesure), pour tenter de mettre en application ce test cosmologique et contraindre les paramètres du fond (Ω_M, Ω_X et w_X).

Malheureusement, la situation se complique lorsque l'on prend en compte les évolutions dans le temps des diamètres et des luminosités dues à la physique interne des galaxies. On obtient alors une correspondance entre les effets cosmologiques et les effets d'évolution intrinsèque. On s'est aussi intéressé aux biais sur les paramètres cosmologiques que peuvent entrainer les effets d'évolution intrinsèque et aux moyens de reconnaitre sans ambiguités ses effets.

Le premier article, relativement théorique, présente l'idée de base. Le second applique cette idée aux mesures réalisées par la collaboration VVDS qui a réalisé un sondage profond de galaxies avec une spectroscopie très précise. Ces deux articles seront publiés prochainement dans Astronomy & Astrophysics.

Astronomy & Astrophysics manuscript no. aa7116-07
September 7, 2007

Geometrical tests of cosmological models

I. Probing dark Energy using the kinematics of high redshift galaxies

C. Marinoni[1], A. Saintonge[2], R. Giovanelli[2], M. P. Haynes[2], K. L. Masters[3], O. Le Fèvre[4], A. Mazure[4], P. Taxil[1], and J.-M. Virey[1]

[1] Centre de Physique Théorique*, CNRS-Université de Provence, Case 907, 13288 Marseille, France
e-mail: marinoni@cpt.univ-mrs.fr
[2] Department of Astronomy, Cornell University, Ithaca, NY 14853, USA
[3] Harvard-Smithsonian Center for Astrophysics, Cambridge, MA 02143, USA
[4] Laboratoire d'Astrophysique de Marseille, UMR 6110, CNRS Université de Provence, 13376 Marseille, France

Received 17 January 2007 / Accepted 2 August 2007

ABSTRACT

We suggest to use the observationally measured and theoretically justified correlation between size and rotational velocity of galactic discs as a viable method to select a set of high redshift standard rods which may be used to explore the dark energy content of the universe via the classical angular-diameter test. Here we explore a new strategy for an optimal implementation of this test. We propose to use the rotation speed of high redshift galaxies as a standard size indicator and show how high resolution multi-object spectroscopy and ACS/HST high quality spatial images, may be combined to measure the amplitude of the dark energy density parameter Ω_Q, or to constrain the cosmic equation of state parameter for a smooth dark energy component ($w = p/\rho$, $-1 \leq w < -1/3$). Nearly 1300 standard rods with high velocity rotation in the bin $V = 200 \pm 20$ km s^{-1} are expected in a field of 1 sq. degree and over the redshift baseline $0 < z < 1.4$. This sample is sufficient to constrain the cosmic equation of state parameter w at a level of 20% (without priors in the $[\Omega_{\rm m}, \Omega_Q]$ plane) even when the [OII]λ3727 Å linewidth-diameter relationship is calibrated with a scatter of ∼40%. We evaluate how systematics may affect the proposed tests, and find that a linear standard rod evolution, causing galaxy dimensions to be up to 30% smaller at $z = 1.5$, can be uniquely diagnosed, and will minimally bias the confidence level contours in the [Ω_Q, w] plane. Finally, we show how to derive, without a priori knowing the specific functional form of disc evolution, a cosmology-evolution diagram with which it is possible to establish a mapping between different cosmological models and the amount of galaxy disc/luminosity evolution expected at a given redshift.

Key words. cosmological parameters – cosmology: observations – cosmology: theory – cosmology: cosmological parameters – galaxies: high-redshift – galaxies: fundamental parameters – galaxies: evolution

1. Introduction

Several and remarkable progresses in the understanding of the dynamical status of the universe, encourage us to believe that, after roaming from paradigm to paradigm, we are finally converging towards a well-founded, internally consistent standard model of the universe.

The picture emerging from independent observations and analysis is sufficiently coherent to be referred to as the *concordance* model (e.g. Tegmark 2006). Within this framework, the universe is flat ($\Omega_K = -0.003^{+0.0095}_{-0.0102}$) composed of ∼1/5 cold dark matter ($\Omega_{\rm cdm} \sim 0.197^{+0.016}_{-0.015}$) and ∼3/4 dark energy ($\Omega_\Lambda = 0.761^{+0.017}_{-0.018}$), with large negative pressure ($w = -0.941^{+0.017}_{-0.018}$), and with a very low baryon content ($\Omega_{\rm b} = 0.0416^{+0.0019}_{-0.0018}$). Mounting and compelling evidence for accelerated expansion of the universe, driven by a dark energy component, presently relies on our comprehension of the mechanisms with which Supernovae Ia (SNIa) emit radiation (see Perlmutter et al. 1999; Riess et al. 2001) and of the physical processes that produced temperature fluctuations in the primeval plasma (see Lee et al. 2001; de Bernardis et al. 2002; Halverson et al. 2002; Spergel et al. 2006.)

Even if the ambitious task of determining geometry and evolution of the universe as a whole, which commenced in the 1930s, now-day shows that the relativistic Friedman-Lemaître model passes impressively demanding checks, we are faced with the challenge of developing and adding new lines of evidence supporting (or falsifying) the *concordance* model. Moreover, even if we parameterize our ignorance about dark energy describing its nature only via a simple equation of state $w = p/\rho$, we only have loose constraints on the precise value of the w parameter or on its functional behavior.

In this spirit we focus this analysis on possible complementary approaches to determining fundamental cosmological parameters, specifically on geometrical tests.

A whole arsenal of classical geometrical methods has been developed to measure global properties of the universe. The central feature of all these tests is the attempt to directly probe the various operative definitions of relativistic distances by means of scaling relationships in which an observable is expressed as a function of redshift (z) and of the fraction of critical density contributed by all forms of matter and energy (Ω).

The most remarkable among these classical methods are the *Hubble diagram* (or magnitude-redshift relation $m = m(M, z, \Omega)$), the *Angular diameter test* (or angle-redshift rela-

* Centre de Physique Théorique is UMR 6207 - "Unité Mixte de Recherche" of CNRS and of the Universities "de Provence", "de la Méditerranée" and "du Sud Toulon-Var"- Laboratory affiliated to FRUMAM (FR 2291).

tion $\theta = \theta(L, z, \Omega)$), the *Hubble test* (or count-redshift relation $N = N(n, z, \Omega)$) or the *Alcock-Paczinsky test* (or deformation-redshift relation $\Delta z/z\Delta\theta \equiv k = k(z, \Omega)$). The common key idea is to constrain cosmological parameters by measuring, at various cosmic epochs, the scaling of the apparent values m, θ, N, k of some reference standard in luminosity (M), size (L), density (n) or sphericity and compare them to corresponding model predictions.

The observational viability of these theoretical strategies has been remarkably proved by the Supernova Cosmology Project (Perlmutter et al. 1999) and the High-z Supernova Team (Riess et al. 2001) in the case of the Hubble diagram. With a parallel strategy, Newman et al. (2002) recently showed that a variant of the Hubble test ($N(z)$ test) can be in principle applied to distant optical clusters selected in deep redshift survey such as VVDS (Le Fèvre et al. 2005) and DEEP2 (Davis et al. 2000), in order to measure the cosmic equation-of-state parameter w.

Unfortunately, the conceptually simple pure geometrical tests of world models, devised to anchor relativistic cosmology to an observational basis, have so far proved to be difficult to implement. This is because the most effective way to constrain the evolution of the cosmological metric consists in probing deep regions of the universe with a primordial class of cosmological objects. Besides the complex instrumental technology this kind of experiments requires, it becomes difficult at high redshift to disentangle the effects of object evolution from the signature of geometric evolution.

Since geometrical tests are by definition independent from predictions of theoretical models or simulations, as well as from assumptions about content, quality and distribution of matter in the universe (mass fluctuations statistics, e.g. Haiman et al. 2001; Newman et al. 2001, galactic biasing, e.g. Marinoni et al. 1998; Lahav et al. 2001; Marinoni et al. 2006, Halo occupation models, e.g. Berlind et al. 2001; Marinoni & Hudson 2002; van den Bosch et al. 2006) it is of paramount importance to try to devise an observational way to implement them. The technical maturity of the new generation of large telescopes, multi object spectrographs, large imaging detectors and space based astronomical observatories will allow these tests to be more effectively applied in the near future (Huterer & Turner 2000). In this paper, we describe a method to select a class of homologous galaxies that are at the same time standard in luminosity and size, that can be in principle applied to data coming from the zCOSMOS spectro-photometric survey (Lilly et al. 2006); of the deep universe.

An observable relationship exists between the speed of rotation V of a spiral galaxy and its metric radial dimension D as well as its total luminosity L (Tully & Fisher 1977; Bottinelli et al. 1980). From a theoretical perspective, this set of scaling relations are expected and explicitly predicted in the context of CDM models of galaxy formation (Mo et al. 1998). The Tully-Fisher relations for diameter and luminosity have been extensively used in the local universe to determine the distances to galaxies and the value of the Hubble constant. We here suggest that they may be used in a cosmological context to select in a physically justified way, high redshift standard rods since galaxies having the same rotational speed will statistically have the same narrow distribution in physical sizes.

The picture gets complicated by the fact that the standard model of the universe implies some sort of evolution in its constituents. In a non static, expanding universe, where the scale factor changes with time, we expect various galaxy properties, such as galaxy metric dimensions, to be an explicit function of redshift. In principle, one may break this circular argument between model and evolution with two strategies: either by understanding the effects of different standard rod evolutionary patterns on cosmological parameters, or by looking for cosmological predictions that are independent from the specific form of the disc evolution function.

In this paper, following the first approach, we study how different disc evolution functions may bias the angular-diameter test. We simulate the diameter-redshift experiment using the amount of data and the realistic errors expected in the context of the zCOSMOS survey. We then evaluate how different disc evolution functions may be unambiguously recognized from the data and to what extent they affect the estimated values of the various cosmological parameters. We also explore the second approach and show how cosmological information may be extracted, without any knowledge about the particular functional form of the standard rod evolution, only by requiring as a prior an estimate of the upper limit value for the relative disc evolution at some reference redshift.

This paper is set out as follow: in Sect. 2 we review the theoretical basis of the angular diameter test. In Sect. 3 we describe the proposed strategy to select high redshift standard rods. In Sect. 4 we digress on how implement in practice the "$\theta - z$" test with zCOSMOS data, and in Sect. 5 we present the zCOSMOS expected statistical constraints on cosmological parameters. In Sect. 6 we discuss different possible approaches with which to address the problem of standard rod evolution. Conclusions are drawn in Sect. 7.

2. The angular diameter test

We investigate the possibility of probing the cosmological metric using the redshift dependence of the apparent angular diameter of a cosmic standard rod. What gives this test special appeal is the possibility of detecting the "*cosmological lensing*" effect, which causes incremental magnification of the apparent diameter of a fixed reference length.

Let's consider the transverse comoving distance (see Hogg 1999)

$$r(z, \Omega_{\rm m}, \Omega_Q, w) = \frac{c}{H_0\sqrt{|\Omega_k|}} S_k\Big(\sqrt{|\Omega_k|}\int_0^z E(x)^{-1}{\rm d}x\Big) \qquad (1)$$

where

$$E(x) = \Big[\Omega_{\rm m}(1+x)^3 + \Omega_Q(1+x)^{3+3w} + \Omega_k(1+x)^2\Big]^{1/2} \qquad (2)$$

and where $S_{-1}(y) = \sinh(y)$, $S_1(y) = \sin(y)$, $S_0(y) = y$ while $\Omega_k = 1 - \Omega_{\rm m} - \Omega_Q$.

An object with linear dimension D at a redshift z has thus an observed angular diameter θ

$$\theta(z, \boldsymbol{p}) = \frac{D}{r(z, \boldsymbol{p})}(1+z) \qquad (3)$$

which depends on the general set of cosmological parameters $\boldsymbol{p} = [\Omega_{\rm m}, \Omega_Q, w]$ via the relativistic definition of angular distance, $d_{\rm A} = r(z, \boldsymbol{p})/(1+z)$.

This test may be implemented without requiring the knowledge of the present expansion rate of the universe (the dependence from the Hubble constant cancels out in Eq. (3)). At variance, although characterized by a smooth and diffuse nature, dark energy significantly affect the dynamic of the universe. From Eq. (1) it is clear that the angular-diameter test depends on the dark energy component via the expansion rate evolution $E(z)$.

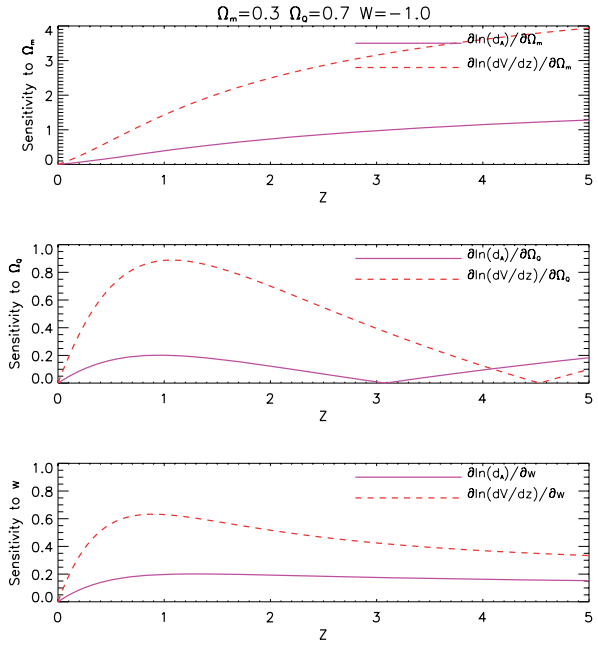

Fig. 1. The relative sensitivity of the angular diameter distance ($d_{\rm A}$) and volume element (dV/dz) to a change in the values of $\Omega_{\rm m}$, Ω_Q and w. The partial derivatives are computed with respect to the position ($\Omega_{\rm m} = 0.3, \Omega_Q = 0.7, w = -1$) in the parameter space.

The more negative w, the more accelerated the expansion is and the smaller a fixed standard rod will appear to an observer.

The efficiency of different cosmological observables in probing the nature of space-time ultimately depends upon their sensitivity to the cosmological parameters $\Omega_{\rm m}, \Omega_Q, w$. The relative sensitivity of empirical cosmological tests based on the scaling of the angular diameter distance ($d_{\rm A}$) and of the volume element (dV/dz = $(c/H_0)(r^2/E(z))$ is derived in Fig. 1, where we assume that Poissonian errors are constant in time and no redshift-dependent systematics perturb the measurements (e.g. Huterer & Turner 2000). Since the luminosity distance (i.e. the distance inferred from measurements of the apparent magnitude of an object of known absolute luminosity) is defined as $d_{\rm L} = (1+z)^2 d_{\rm A}$, we note that the angular diameter test has the same cosmological discriminatory power as the Hubble diagram. The upper panel of Fig. 1 shows that the sensitivity of both $d_{\rm A}$ and dV/dz to the mean mass density parameter, $\Omega_{\rm m}$, increases monotonically as a function of redshift. This means that the deeper the region of the universe surveyed, the more constrained the inferred value of $\Omega_{\rm m}$ is.

Conversely, the sensitivity of both empirical tests to a change in the constant value of w peaks at redshift around unity, and levels off at redshifts greater than ∼5. The reason for this is that the dark energy density ρ_Q, which substantially contributes to the present-day value of the expansion rate was negligible in the early universe ($\rho_Q/\rho_M \propto (1+z)^{3w}$, see Eq. (2)).

The fact that we are living in a special epoch, when two or more terms in the expansion rate equation make comparable contributions to the present value of $E(z)$, can be appreciated in the central panel of Fig. 1. Because each of the terms in Eq. (2) varies with cosmic time in a different way, there is a redshift window where the search for Ω_Q is less efficient (i.e. $2 < z < 4$). Therefore one can maximize the cosmological information which can be extracted from the classical tests of cosmology, and specifically from the angular diameter test, by devising observational programs probing a large field of view in the redshift range $0 \leq z \leq 2$.

3. The standard rod

A variety of standard rod candidates have been explored in previous attempts of implementing the angular diameter-redshift test: galaxies (Sandage 1972; Djorgovski & Spinrad 1981), clusters (Hickson 1977; Bruzual & Spinrad 1978; Pen 1997), halo clustering (Cooray et al. 2001). Those methods failed to yield conclusive evidence because the available redshifts were few and local, and the quality of the imaging data used in the estimate of sizes was poor.

Good quality size measurements for high redshift objects have become available for radio sources (e.g. Miley 1971; Kapahi 1975; and recently several authors Kellermann 1993; Wilkinson et al. 1998, have reported a redshift dependence of radio source angular sizes at $0.5 < z < 3$, which is not easily reconciled with other recent measurements of the cosmological parameters (but see Daly & Djorgovski 2004, for results more consistent with the concordance model.)

The radio source results may be affected by a variety of selection and evolutionary effects, the lack of a robust definition of size, and by difficulties in assembling a large, homogeneous sample of radio observations (Buchalter et al. 1998; Gurvits et al. 1999).

A common thread of weakness in all these studies is that there are no clear criteria by which galaxies, clusters, extended radio lobes or compact radio jets associated with quasars and AGNs should be considered universal standard rods. Moreover, lacking any local calibration for the metric size of the standard rod, the standard rod dimension (parameter D in Eq. (3)) is often considered as a free fitting parameter. Since the inferred cosmological parameters heavily depend on the assumed value for the object size (Lima & Alcaniz 2002), an a priori independent statistical study of the standard rod distribution properties is an imperative prerequisite.

We thus propose to use information on the kinematics of galaxies, as encoded in their optical spectrum, a) to identify in an objective and empirically justified way a class of objects behaving as standard rods, and b) to measure the absolute value of the standard rod length. The basic idea consists in using the velocity-diameter relationship for disc galaxies (e.g. Tully & Fisher 1977; Saintonge et al. 2007) as a cosmological metric probe. In Fig. 2 we plot the local relationship we have derived in Paper II of this series (Saintonge et al. 2007) between half-light diameters and rotational velocities inferred using the $H_\alpha \lambda 6563$ Å line. The sample used to calibrate the diameter-velocity relationship is the SFI++ sample described by Springob et al. (2007). Also shown is the the amplitude of the scatter in the zero-point calibration of the standard rods.

In the local universe, rotation velocities can be estimated from either 21 cm HI spectra or from the $H_\alpha \lambda 6563$ Å optical emission lines. However, the H_α line is quickly redshifted into the near-infrared and cannot be used in ground-based optical galaxy redshift surveys at $z > 0.4$, while HI is not detectable much past $z = 0.15$. Only [OII]$\lambda 3727$ Å line widths can be successfully used in optical surveys to infer the length of a standard rod dimension D at $z \sim 1$. Clearly one could obtain rotational velocity information for high redshift objets by observing the H_α line with near-IR spectrographs. However it is much easier to get large samples of kinematic measurements using OII and

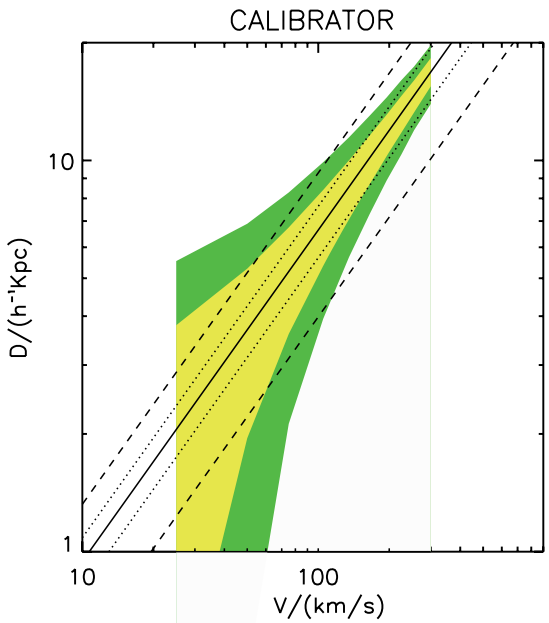

Fig. 2. The diameter vs. velocity relationship calibrated in Paper II is plotted using a black line. Shadowed regions represent the 1 and 2σ uncertainties in the calibrated relationship. D represents the corrected (face on) half light diameter while the velocity has been measured using the H_α line. Dotted lines represent the upper and lower relative uncertainty $[\sigma_D/D]_{\rm int} = 0.15$ in diameters. The *conservative* relative dispersion in the relationship assumed in this study ($[\sigma_D/D]_{\rm int} = 0.4$) is also presented using dashed lines. With this conservative choice we take into account that sizes and velocity are measured in the high redshift universe with greater uncertainties. Within the interval centered at $V = 200 \pm 20$ km s^{-1} (mean physical galaxy dimension $\sim 10 \pm 1.5\ h^{-1}$ kpc which roughly corresponds to an isophotal diameter $D_{25} \sim 20 \pm 3\ h^{-1}$ kpc), we will select galaxies with total absolute I magnitude $M_I - 5\log h = -22.4$ (see Paper II). The velocity selected standard rods at $z \sim 1$ are thus well within the visibility window of deep galaxy redshift surveys such as the VVDS (Le Fèvre et al. 2005) or zCOSMOS (Lilly et al. 2006). For exemple the VVDS is flux limited at $I < 24$ and selects objects brighter then $M_I \sim -20 + 5\log h$ at $z = 1$.

multi-slit devices, rather than get sparser samples using a single-object, near-IR spectrograph.

A detailed study of the kinematical information encoded in the [OII] line are presented in Paper II. In that paper we have explored the degree of correlation of optical H_α and [OII] rotational velocity indicators, i.e. how well the rotation velocities extracted from these different lines compare. Moreover, we have derived a local diameter-velocity relationship, and we have investigated the amplitude of the scatter in the zero-point calibration of the standard rods.

We finally note that the present-day expansion rate sets the overall size and time scales for most other observables in cosmology. Thus, if we hope to seriously constrain other cosmological parameters it is of vital importance either to pin down its value or to devise H_0-independent cosmological tests. Note that, given the calibration of the diameter–linewidth relation in the form $H_0 = f(V)$, the θ-expression in Eq. (3) is effectively independent of the value of the Hubble constant.

4. Optimal test strategies

In this section we outline the optimal observational strategy required in order to perform the proposed test. With the proposed selection technique, the photometric standard rod D is spectroscopically selected and the sample is therefore free from luminosity-size selection effects, that is from the well known tendency to select brighter and bigger objects at higher redshifts (Malmquist bias) in flux-limited samples. However it is crucial that a large sample of spectra be collected, in order to obtain $\sqrt{N}$ gain over the intrinsic scatter in the calibrated V(OII)-diameter relationship.

4.1. Galaxy sizes measurement

Since galaxies do not have sharp edges, their angular diameter is usually defined in terms of isophotal magnitudes. However since surface brightness is not constant with distance, the success in performing the experiment revolves around the use of metric rather than isophotal galaxy diameters (Sandage 1995).

A suitable way to measure the photometric parameter θ, without making any a-priori assumption about cosmological models, consists in adopting as the standard scale length estimator either the half-light radius of the galaxy or the η-function of Petrosian (1976). The Petrosian radius is implicitly defined as

$$\eta(\theta) = \frac{\langle \mu(\theta) \rangle}{\mu(\theta)}, \tag{4}$$

i.e. as the radius θ at which the surface brightness averaged inside θ is a predefined factor η larger than the local surface brightness at θ itself.

Both these size indicators are independent of K-correction, dust absorption, luminosity evolution (provided the evolutionary change of surface brightness is independent of radius), waveband used (if there is no color gradient) and source light profile (Djorgovski & Spinrad 1981).

4.2. Standard rods optimal selection

The choice of the objects for which the velocity parameter V and the metric size is to be measured is a compromise between the observational need of detecting high signal-to-noise spectral and photometric features (i.e. selecting high luminosity and large objects) and the requirement of sampling the velocity distribution function ($n(V)\mathrm{d}V \sim V^{-4}$ for galaxy-scale halos) within an interval where the rotator density is substantial.

Given the estimated source of errors (see next section), and the requirement of determining both Ω_Q and w with a precision of 20%, we find, guided by semi analytical models predicting the redshift distribution of rotators (i.e. Narayan & White 1988; Newman & Davis 2000), that an optimal choice are $V = 200$ km s^{-1} rotators.

In particular, as shown in Paper II, the I band characteristic absolute magnitude of the $V = 200$ km s^{-1} objects is $M_I \sim -22.4 + 5\log h_{70}$ i.e. well above the visibility threshold of flux-limited surveys such as zCOSMOS or VVDS (as an example, for $I_{\rm ab} = 24$ the limiting magnitude of the VVDS, one obtains that $M_I \lesssim -21 + 5\log h_{70}$ at $z = 1.5$). Therefore, with this velocity choice, the selected standards do not suffer from any Malmquist bias (i.e. any effect which favors the systematic selection of the brighter tails of a luminosity distribution at progressively higher redshifts).

4.3. The zCOSMOS potential

In Sect. 2 we have emphasized that an optimal strategy to study the expansion history of the universe consists in probing, with the angular diameter test, the $0 \leq z \leq 2$ interval. However, in order to collect a large and minimally biased sample of standard rods over such a wide redshift baseline, we need the joint availability of high quality images and high resolution multi-object spectra.

Space images allow a better determination of galaxy structural parameters (sizes, luminosity, surface brightness, inclination etc) at high redshift. In particular, the ACS camera of the Hubble Space Telescope can survey large sky regions with the key advantages of a space-based experiment: diffraction limited images no seeing blurring, and very deep photometry. Ground multi-object spectrographs operating in high resolution mode allow a better characterisation of the gravitational potential-well of galaxies, facilitating the fast acquisition of large samples of standard rods. For example, in the spectroscopic resolution mode $R = 2500$ ($1''$ slits), the VIMOS spectrograph (Le Fèvre et al. 2003) allows to resolve the internal kinematics of galaxies via their rotation curve or line-width. Note that the VIMOS slitlets can be tilted and aligned along the major axis of the galaxies in order to remove a source of potentially significant error in the estimate of the rotation velocities.

These observational requirements are mandatory for a succesfull implementation of the proposed cosmological probe. The practical feasibility of the strategy is graphically illustrated in Fig. 3. In this figure we show a high resolution spectra of a galaxy at $z = 0.5016$ obtained with a total exposure of 90 min with VIMOS. The ground and space (ACS) images of the galaxy are also shown for comparison.

Interestingly, a large sample of rotators can be quickly assembled by the currently underway zCOSMOS deep redshift survey, which uses the VIMOS multi-object spectrograph at the VLT to target galaxies with ACS photometry in the 2 sq. degree COSMOS field Scoville et al. 2003). In principle, one can measure in high resolution modality $R = 2500$ the line-widths of [OII]λ3727 Å up to $z \sim 1.4$ by re-targeting objects for which the redshift has already been measured in the low-resolution ($R = 600$) zCOSMOS survey. Since the spectral interval covered in high resolution mode is limited to ~2000 Å, this allows us to determine the optimal telescope and slitlets position angles in order to maximize the number of spectra whose OII emission lines fall onto the CCDs. With this fast follow-up strategy one could be able to target about 200 rotators per pointing with an exposure time of 4 h down to $I_{\rm ab} = 24$.

In the following we will use the zCOSMOS sample as a test case to assess the performances of the proposed cosmological test.

5. Constraints on cosmological parameters

In this section we present in detail some merits and advantages of the proposed approach for constraining the value of the fundamental set of cosmological parameters. We evaluate the potential of the test, within the zCOSMOS operational specifications, in placing constraints not only on the simplest models of the universe, which include only matter and a cosmological constant, but also on so-called "quintessence" models (Turner & White 1997; Newman et al. 2002), For the purposes of this study, we assume in this section w to be constant in time up to the redshift investigated $z \sim 1.4$.

We assume that a V(OII)-diameter relation can be locally calibrated, and that the diameter of $V = 200$ km s^{-1} rotators may be inferred with a worst(/optimal) case relative error $[\sigma_D/D]_{\rm int} = 40\%(/15\%)$ (see Sect. 3 and Fig. 2). The main contributions to this error figure are uncertainties in measuring linewidths, galaxy inclinations and the intrinsic scatter of the empirical relation itself. We then linearly combine this intrinsic scatter with the uncertainties with which the Petrosian or half-light radius may be determined from the ACS photometry. The error on the half light radii is about $\sigma_\theta = \pm 0.04''$ almost independent of galaxy sizes in the range 0.1–$1''$ (S. Gwyn, private communication).

We consider as the observable of the experiment the logarithm of the angle subtended by a standard rod. We use the logarithms of the angles rather than angles themselves because we assume that the object magnitudes, rather than diameters, are normally distributed around some mean value. Moreover, in this way the galactic diameter becomes an additive parameter, whose fitted value (when a $z = 0$ calibration is not available) does not distort the cosmological shape of the $\theta(z)$ function.

The observed values $\log\theta$ are randomly simulated around the theoretical value $\log\theta^r$ (cf. Eq. (3)) using the standard deviation given by

$$\sigma = \left[\left(\frac{\sigma_D}{D}\right)^2_{\rm int} + \left(\frac{\sigma_\theta}{\theta}\right)^2_{\rm obs}\right]^{1/2}. \quad (5)$$

For the purposes of this section, θ^r is computed assuming a flat, vacumm dominated cosmology with parameters $\Omega_{\rm m} = 0.3, \Omega_Q = 0.7$, and $w = -1$ as reference model. The confidence with which these parameters are constrained by noisy data is evaluated using the χ^2 statistic

$$\chi^2 = \sum_i \frac{[\log\theta_i - \log\theta^{\rm th}_i(z, \boldsymbol{p})]^2}{\sigma^2}, \quad (6)$$

where $\theta^{\rm th}$ is given by Eq. (3).

We also derive the expected redshift distribution of galaxies having circular velocity in the $180 \leq V \leq 220$ km s^{-1} range, in various cosmological scenarios within the framework of the Press & Schechter formalism (Narayan & White 1988; Newman & Davis 2000). We note that due to the correlation between circular velocity and luminosity, these galaxies could be observed to the maximum depth ($z \sim 1.4$) out to which the OII is within the visibility window of VIMOS. We take into account the uncertainties in the semi-analytic predictions and our ignorance about the fraction of discs to be observed that will have a spectroscopically resolved [OII]λ3727 Å line, by multiplying the calculated halo density by a "conservative" factor $f = 0.2$. Using the VIMOS $R = 2500$ resolution mode data, we thus expect to be able to implement our angular-diameter research program using nearly 1300 standard rods per square degree, which is what has been simulated (see Fig. 4).

Since we do not make a-priori assumptions about any parameter, and in particular we do not assume a flat cosmology, results should be distributed as a χ^2_ν with $\nu = 3$ degrees of freedom, which can be directly translated into statistical confidence contours, as presented in Fig. 5. This figure shows that even without assuming a flat cosmology as a prior and considering a diameter-linewidth relationship with a 40% scatter, by targetting ~1300 rotators we can directly infer the presence of a dark energy component with a confidence level better than 3σ. At the same time, its equation of state can be constrained to better than 20% (~10% if the the diameter-linewidth relationship is calibrated with a ~15% relative precision).

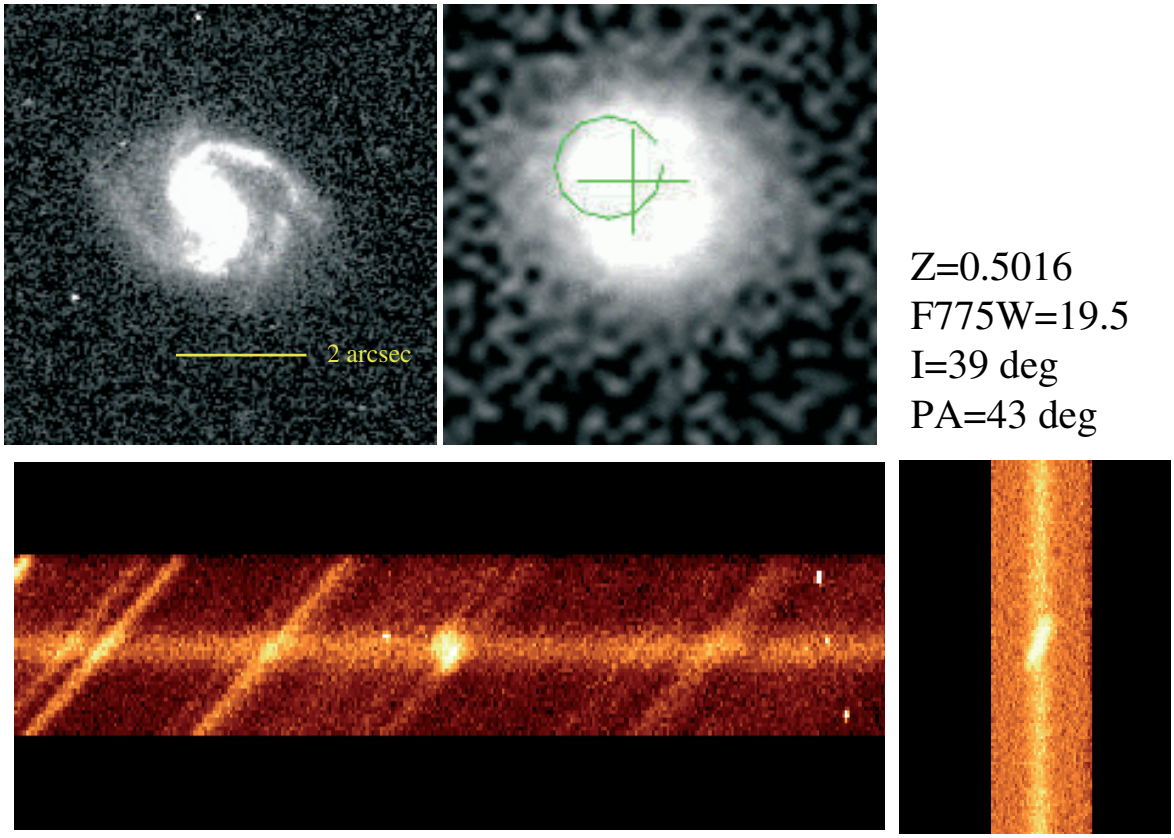

Fig. 3. *Upper*: public release image of the galaxy $\alpha = 53.1874858$, $\delta = -27.910975$ at redshift 0.5016, taken with the filter $F775W$ (nearly I band) of the ACS camera by the GOODs program. For comparison the same galaxy as imaged in the EIS survey with the WFI camera at the ESO 2.2mt telescope at La Silla. *Botton left:* raw spectrum of the galaxy taken by VIMOS at the VLT-UT3 telescope with a total exposure time of 90 min and a spectral resolution $R = 2000$. Slitlets have been tilted according to the major axis orientation (Position Angle = 43°). *Botton right:* final processed spectrum showing the rotation curve as traced by the Hb (λ4859 Å) line.

6. Standard rod evolution

The previous analysis shows that the angular diameter test, when performed using fast high resolution follow-up of zCOSMOS spectroscopic targets may be used as a promising additional tool to explore the cosmological parameter space and directly measure a dark energy component. However, the impact of any standard rod evolution on these results needs to be carefully examined.

First of all, we may note that the expected variation with cosmic time of the total galaxy luminosity due to evolution in its stellar component does not affect the metric definition of angular diameters unless this luminosity change depends on radius (see Paper III of this series, marinoni et al. 2007, for a detailed analysis of this issue). Moreover, we can check each galaxy spectrum or image for peculiarities indicating possible evolution or instability of the standard rod which may be induced by environmental effects, interactions or excess of star formation.

Any possible size evolution of the standard rod needs to be taken into account next. Interestingly, it has been shown by different authors that large discs in high redshift samples evolve much less in size than in luminosity in the redshift range $0 < z < 1$. Recent studies show that the amount of evolution to $z \sim 1$ appears to be somewhat smaller than expected: disc sizes at $z \sim 1$ are typically only slightly smaller than sizes measured locally (Takamiya 1999; Faber et al. 2001; Nelson et al. 2002; Totani et al. 2002). This is also theoretically predicted by simulations; Boissier & Prantzos (2001), for example, show that large discs (i.e. fast rotators) should have basically completed their evolution already by $z \sim 1$ and undergo very little increase in size afterwards. Infall models (e.g., Chiappini et al. 1997; Ferguson & Clarke 2001; Bouwens & Silk 2002) also predict a mild disk size evolution. Disk sizes at $z \sim 1$ in these models are typically only 20% smaller than at $z = 0$.

6.1. Analysis of the biases introduced by evolution

Even if literature evidences are encouraging, we have to be aware that even a small amount of evolution may introduce artificial features and bias the reliability of the cosmological inferences.

In this section we directly address this issue by considering different evolutionary patterns for the standard rods, and by analyzing to what level the simulated true cosmological model may still be correctly inferred using evolved data. In other words, we investigate how different disc evolutionary histories affect the determination of cosmological parameters by answering to the following three questions:

a) is there a feature that may be used to discriminate the presence of evolution in the data?

b) which cosmological parameter is more sensitive to the eventual presence of disc evolution?, and in particular what are the

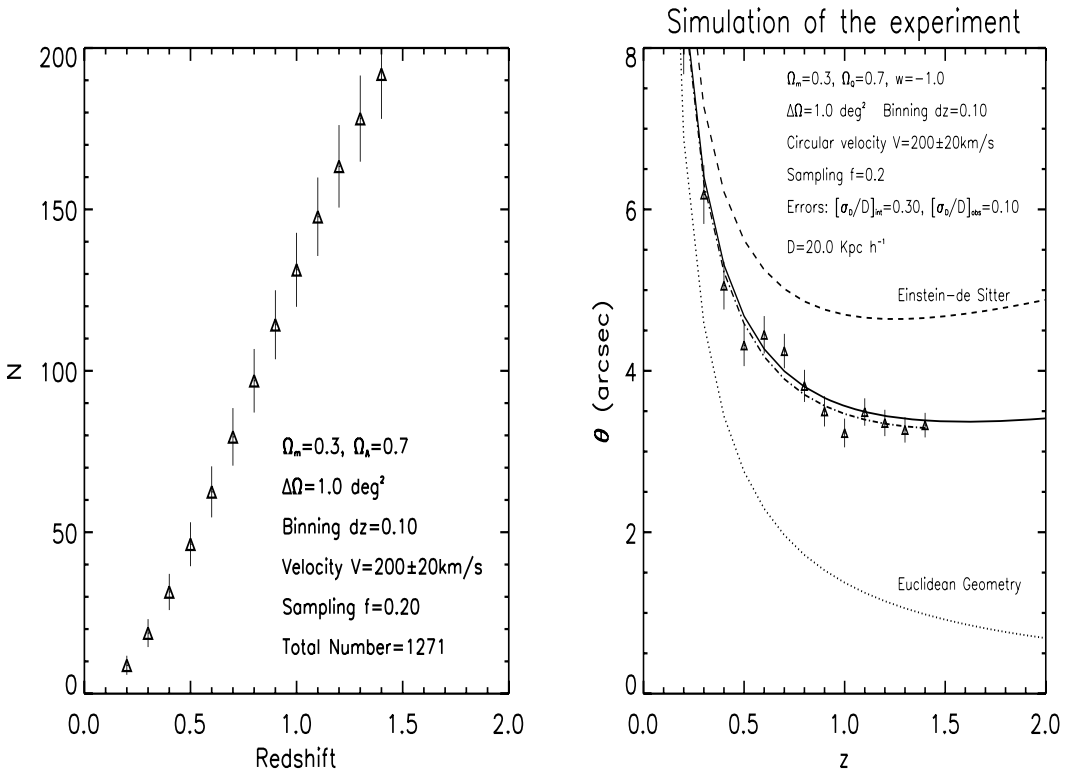

Fig. 4. *Left*: redshift evolution of the differential comoving number density of halos with a circular velocity of 200 km s^{-1} computed according to the prescriptions of Newman & Davis (2000) in the case of a flat cosmological model having $\Omega_{\rm m} = 0.3$ today and a cosmological constant. Only a fraction $f = 0.2$ of the total predicted abundance of halos (i.e. ∼1300 objects per square degree) is conservatively supposed to give line-width information useful for the angular-diameter test. *Right*: simulation of the predicted scatter expected to affect the angular diameter-redshift diagram should in principle achieve with the angular diameter test. The simulation is performed assuming the sample is composed by ∼1300 rotators with $V = 200$ km s^{-1} and that a flat model with parameters $[\Omega_{\rm m} = 0.3, \Omega_Q = 0.7, w = -1]$ is the true underlying cosmological framework. The circular velocity has been converted into an estimate of the galaxy diameter ($D_v = 20$ kpc) by using the velocity-diameter template calibrated by Bottinelli et al. (1980). The *worst-case* scenario ($[\sigma_D/D]_{\rm int} = 40\%$) is presented. The solid line visualizes the underlying input cosmological model $\theta^{\Lambda{\rm CDM}}(z)$, while triangles are drawn from the expected Poissonian fluctuations. The dot-dashed line represents the expected scaling of the angular diameter in our best recovered cosmological solution. The dashed and the dotted lines represent the angular scaling in a Einstein-de Sitter and Euclidean (non-expanding type cosmology with zero curvature) geometry respectively.

effects of evolution on the value of the inferred dark energy density parameter Ω_Q?

c) is there a particular evolutionary scenario for which the inferred values of Ω_Q and w are minimally biased?

For the purposes of this analysis, we consider for the angular diameter-redshift test the baseline ($0.1 \leq z \leq 1.4$) divided in bins of width d$z = 0.1$ and assume a relative scatter in the mean size per bin of 5%. This scatter nearly corresponds to that expected for a sample of 1300 rotators (with $0 < z < 1.4$ and d$z = 0.1$) whose diameters are individually (and locally) calibrated with a 40% precision. We then select a given fiducial cosmology (input cosmology), apply an arbitrary evolution to the standard rods, and then fit the evolved data with the unevolved theoretical prediction given in Eq. (3) in order to obtain the best fitting (biased) output cosmology and the associated confidence levels contours. We decide that the best fitting cosmological model offers a good fit to the evolved data if the probability of a worse χ^2 is smaller that 5% (i.e. $P(\chi^2 > \chi^2_{\rm obs}) < 0.05$).

We adopt three different parameterizations to describe an eventual redshift evolution of the velocity selected sample of galaxy discs D_v: a *late-epoch* evolutionary scenario ($\Delta D/D \equiv (D_v(z) - D_v(0))/D_v(0) = -|\delta_1|\sqrt{z}$) where most of the evolution is expected to happen at low redshifts and levels off at greater distances (δ_1 is the relative disc evolution at $z = 1$), a *linear* evolutionary scenario ($\Delta D/D = -|\delta_1|z$) without any preferred scale where major evolutionary phenomena take place (i.e. the gradient of the evolution is nearly constant), and an *early-epoch* evolution scenario ($\Delta D/D = -|\delta_1|z^2$) where most of the evolution is expected to happen at high redshift.

We note that for modest disc evolution, the linear parameterization satisfactorily describes the whole class of evolutionary models whose series expansion may be linearly represented (for example, the hyperbolic model ($D_v(z) = D_v(0)/(1 + |\delta_1|z)$)). For $z \ll 1$ it also represents fairly well the exponential model ($D_v(z) = D_v(0)(1-z)^\delta$). Moreover, the linear model is the favored scenario for disc size evolution at least at low redshift ($\lesssim$1.5) as predicted by simulations (e.g. Mo et al. 1998; Bouwens & Silk 2002).

First, let's assume that $w = -1$ and that the dark energy behaves like Einstein's cosmological constant. In Fig. 6 we consider three different input fiducial cosmological models (a flat Λ-dominated universe ($\Omega_\Lambda = 0.7$), an open model ($\Omega_{\rm m} = 0.3$) and an Einstein-de Sitter universe ($\Omega_{\rm m} = 1$)) and show the characteristic pattern traced by the best fitting output values ($\Omega_{\rm m}$,

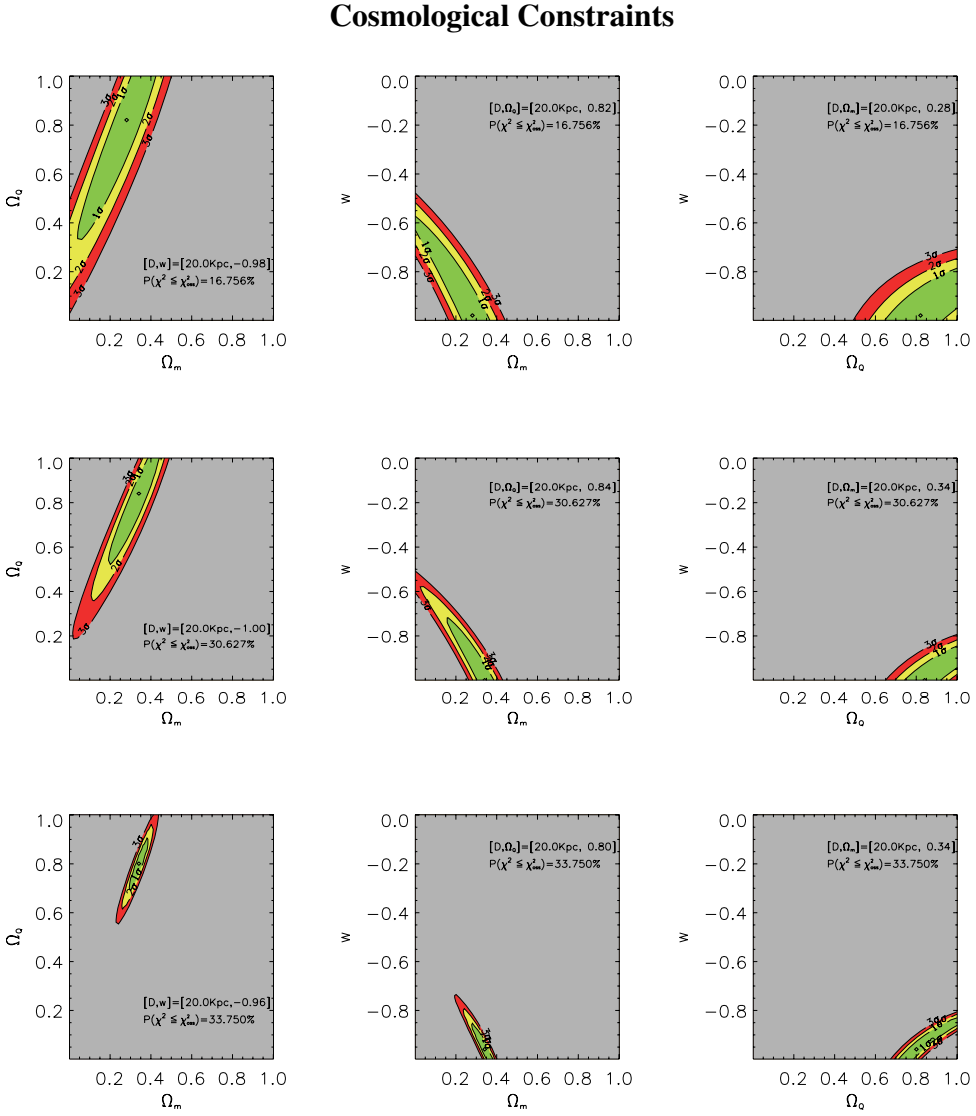

Fig. 5. Predicted 1, 2, and 3σ confidence level contours for application of the angular-diameter test. The likelihood contours have been derived by adopting a Λ-cosmology $[\Omega_{\rm m}, \Omega_Q, w] = [0.3, 0.7, -1]$ as the fiducial model we want to recover, and by conservatively assuming one can obtain useful line-widths information for a sample of galaxies having the redshift distribution and the Poissonian diameter fluctuations simulated in Fig. 4. Confidence contours are projected onto various 2D-planes of the $[\Omega_{\rm m}, \Omega_Q, w]$ parameter space, and the jointly best fitted value along the projection axis, together with the statistical significance of the fit, are reported in the insets. Note the strong complementarity of the confidence region orientation which is orthogonal to the degeneration axis of the CMB measurements. *Top*: constraints derived assuming that one might survey only 1 square degree of sky and that the V(OII)-diameter relation is locally calibrated with a 40% of relative scatter in diameter. *Center*: as before but assuming a scatter of 15% in diameters. *Bottom*: confidence contours for a survey of 16 deg^2 (which corresponds to the full area surveyed by VIMOS-VLT Deep Survey) assuming a template V(OII)-diameter relationship with a scatter of 30% in diameters.

Ω_Λ) inferred by applying the angular diameter test to data affected by evolution. A common feature of all the various evolutionary schemes considered is that the value of $\Omega_{\rm m}$ is systematically underestimated with respect to its true input value: the stronger the evolution in diameter and the smaller $\Omega_{\rm m}$ will be, irrespectively of the particular disc evolutionary model considered. Since many independent observations consistently indicate the existence of a lower bound for the value of the normalized matter density ($\Omega_{\rm m} \gtrsim 0.2$), we can thus use this parameter as a sensitive indicator of evolution.

Once the presence of evolution is recognized, the remaining problem is to determine the level of bias introduced in the dark energy determination. If the gradient of the disk evolution function increases with redshift (*quadratic* evolution), then the estimates of Ω_Λ are systematically biased low. The contrary happens if the evolutionary gradient decreases as a function of look-back time (*square root* model). If the disc evolution rate is constant (*linear* model), then even if discs are smaller by a factor as large as 40% at $z = 1.5$ the estimate of the dark energy parameter is only minimally biased. The net effect of a linear evolution is to approximately shift the best fitting Ω_Λ value in a direction parallel to the $\Omega_{\rm m}$ axis in the $[\Omega_{\rm m}, \Omega_\Lambda]$ plane.

More generally, by linearly evolving disc sizes so that they are up to 40% smaller at $z = 1.5$, and by simulating the apparent

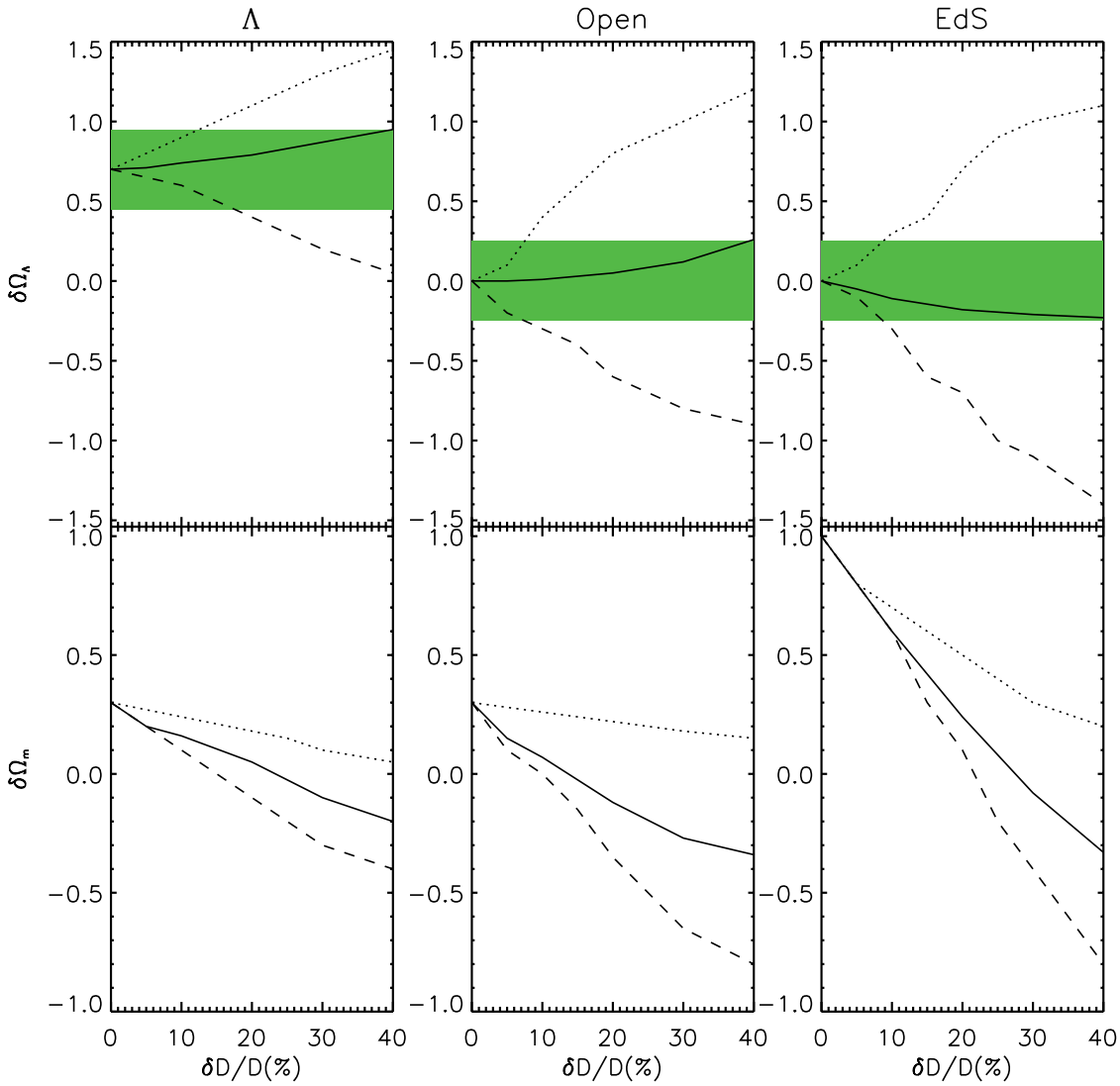

Fig. 6. Best fitting cosmological parameters inferred by applying the angular diameter test to data affected by evolution. The output (biased) estimates of $\Omega_{\rm m}$ and Ω_Λ are plotted as a function of the relative diameter evolution for the following evolutionary models: linear (solid line), square-root (dotted line) and quadratic evolution (dashed line). The biasing pattern is evaluated for three different fiducial cosmologies: a flat, Λ-dominated cosmology ($\Omega_\Lambda = 0.7$, *left*), a low-density open cosmology ($\Omega_{\rm m} = 0.3$, *center*) and a flat, matter-dominated model ($\Omega_{\rm m} = 1$, *right*).

angle observed in any arbitrary cosmological model with matter and energy density parameters in the range $0 < \Omega_{\rm m} < 1$ and $0 \leq \Omega_\Lambda \leq 1$ ($w = -1$) we conclude that the maximum deviation of the inferred biased value of Ω_Λ from its true input value, is limited to be $|\max(\delta\Omega_\Lambda)| \lesssim 0.2$, whatever the true input value of the energy density parameter is. In other terms, in the particular case of a linear and substantial (<40% at $z = 1.5$) evolution of galaxy discs, the central value of the dark energy parameter is minimally biased for any fiducial input model with $0 \leq \Omega_{\rm m} < 1$ and $0 \leq \Omega_\Lambda \leq 1$).

We have shown that the presence of evolution is unambiguously indicated by the "unphysical" best fitting value of the parameter $\Omega_{\rm m}$. We now investigate the amplitude of the biases induced by disc evolution in the $[\Omega_Q, w]$ plane. We assume for this purpose that w is free to vary in the range $-1 \leq w \leq -1/3$, which means assuming that the late epoch acceleration of the universe might be explained in terms of a slow rolling scalar field.

We first consider a situation where the disc size evolution is modest, and could be represented by any of the three models considered. Whatever the mild evolution model considered (less then 15% evolution from $z = 1.5$) and assuming a scatter in the angular diameter-redshift diagram of 5% in each redshift bin, we find that the input values of Ω_Q and w are contained within the 1σ biased confidence contour derived from the evolved data.

Figure 7 shows the 1, 2 and 3σ "biased" confidence contours obtained by fitting with Eq. (3) a simulated angular-diameter redshift diagram in which discs have been linearly evolved. We show that, *if disc evolution depends linearly on redshift and causes galaxy dimensions to be up to* 30% *smaller at* $z = 1.5$, the true fiducial input values of Ω_Q and w are still within 1σ of the biased confidence contours inferred in presence of a standard rod evolution (and a scatter in the angular diameter-redshift relation as low as 5% in each redshift bin). We have tested that these conclusions hold true for every fiducial input cosmology

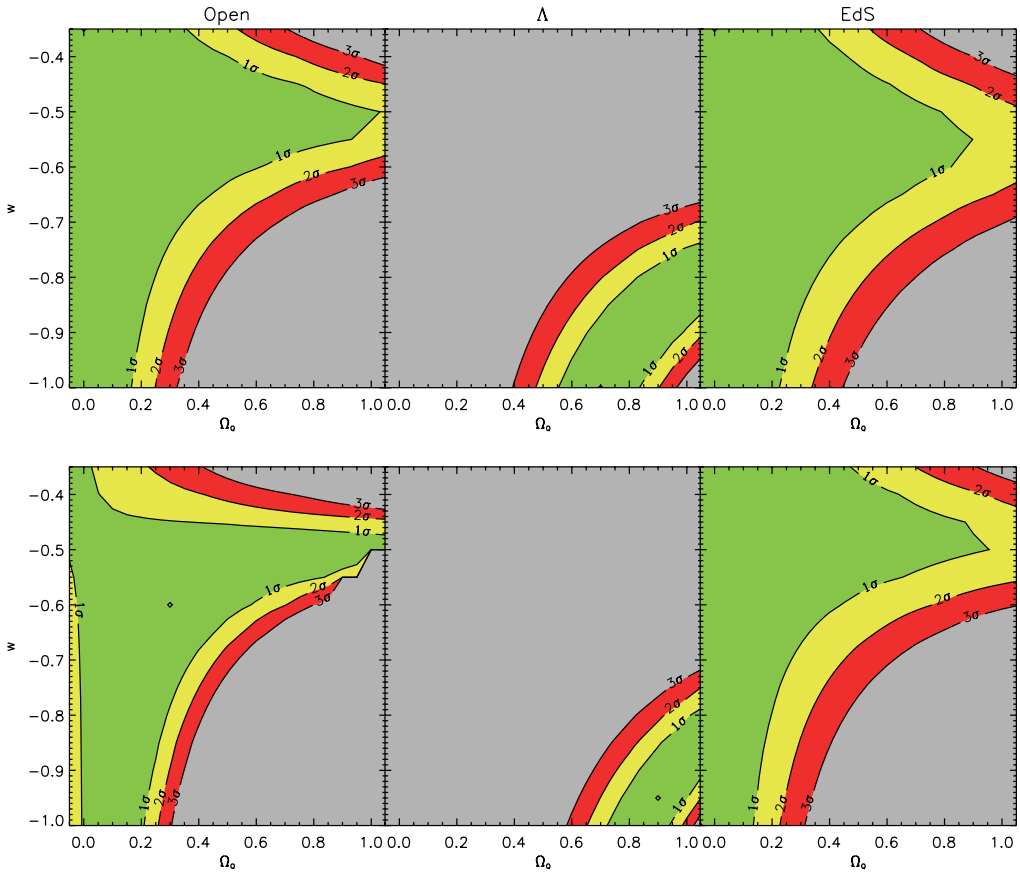

Fig. 7. 1, 2, and 3σ confidence level contours in the $[\Omega_Q, w]$ plane computed by applying the angular-diameter test to data unaffected (*upper panel*) and affected by diameter evolution (*lower panel*). We consider a linear model for disc evolution normalized by assuming that discs were smaller by 30% at $z = 1.5$, and a nominal relative error in the standard rod measures of 5% per redshift bin (see discussion in Sect. 6.1). The effects of disc evolution onto cosmological parameter estimation are compared to the evolution-free case for three different fiducial cosmologies: a low matter density open cosmology ($\Omega_m = 0.3$, *left*) a flat, Λ-dominated cosmology ($\Omega_\Lambda = 0.7$, *center*), and an Einstein-de Sitter model ($\Omega_m = 1$, *right*).

with parameters in the range $0 \leq \Omega_m \leq 1$, $0 \leq \Omega_Q \leq 1$ and $-1 \leq w \leq -1/3$.

Thus, if, disc evolution is linear (as predicted by theoretical models) and substantial (up to ∼30% at $z = 1.5$), or arbitrary and mild (up to ∼15% at $z = 1.5$), then in both cases the angular diameter test reduces from a test of the whole set of cosmological parameters, to a direct and fully geometrical test of the parameters subset (Ω_Q, w). For example, in a minimal approach, the angular diameter test could be used to test in a purely geometrical way the null hypothesis that "*a dark energy component with a constant equation of state parameter w is dominating the present day dynamics of the universe*". Moreover, as Fig. 7 shows, an universe dominated by dark energy may be satisfactorily discriminated from a matter dominated universe ($\Omega_Q = 0$).

In the evolutionary pictures considered, galaxy discs are supposed to decrease monotonically in size in the past. Since the sensitivity of the test to changes in the linear diameter D is described by a growing monotonic function in the redshift interval [0, 1.4], one may hope to test cosmology in a way which is less dependent on systematic biases by limiting the sample at $z \leq 1$. However, by doing this we would halve the number of standard rods available for the analysis (∼600 with respect to the original ∼1300). The test efficiency in constraining cosmological parameters would consequently be significantly degraded.

6.2. The Hubble-diagram using galaxies

The same velocity criterion that allows the selection of standard rods also allows the selection of a sample of standard candles. Using the same set of tracers, the Tully & Fisher relationships connecting galactic rotation velocities to luminosities and sizes offer the interesting possibility of implementing two different cosmological tests, the angular-diameter test and the Hubble diagram.

Thus, we have analyzed how the effects of luminosity evolution may bias the estimation of cosmological parameters in the case of the Hubble diagram. Assuming that the absolute luminosity L of the standard candle increases as a function of redshift according to the square root, linear and quadratic scenarios, then the value of Ω_m is systematically overestimated. The value of Ω_m is biased in an opposite sense with respect to the angular diameter test (see Fig. 6). Therefore, it is less straightforward to discriminate the eventual presence of evolution in the standard candle on the basis of the simple requirement that any "physical" matter density parameter is characterized by a positive lower bound. The different Ω_m shifts (with respect to the fiducial value) observed when the evolved data are fitted using the Hubble diagram or the angualr diameter test are due to the fact that, given the observed magnitudes and apparent angles, an increase with redshift in the standard candle absolute luminos-

ity causes the best fitting distances to be biased towards higher values, while a decrement in the physical size implies that real cosmological distances are underestimated.

Moreover, even considering a linear evolutionary picture for the absolute luminosity as well as a modest change in the standard candle luminosity, i.e. $\Delta_M = M(z) - M(0) = -0.5$ at $z = 1.5$, the input fiducial cosmology falls outside the 3σ confidence contour obtained by applying the magnitude-redshift test to the sample of evolved standard candles. Note that error contours are derived by assuming a scatter of $\sigma_M = 0.05$ per redshift bin in the Hubble diagram. Since, at variance with the size of large discs, galactic luminosity is expected to evolve substantially with redshift (within the VVDS survey, $\Delta_M \sim -1$ in the I band for M* galaxies Ilbert et al. 2005) we conclude that the direct implementation of the Hubble diagram test as a minimial test for the parameter subset $[\Omega_Q, w]$ using galaxy rotation as the standard candle indicator is more problematic. As an additional problem, we note that galaxy luminosity is seriously affected by uncertainties in internal absorption corrections, and that due to K-correction, the implementation of the Hubble diagram requires multi band images to properly describe the rest frame emission properties of galaxies.

6.3. The cosmology-evolution diagram

In this section we want to address the more general question of whether it is possible to infer cosmological information knowing a-priori only the upper limit value for disc evolution at some reference redshift (for example, the maximum redshift surveyed by a given sample of rotators). In other terms, we explore the possibility of probing geometrically the cosmological parameter space in a way which is independent of the specific evolution function with which disc sizes change as a function of time. The only external prior is the knowledge of an upper limit for the amplitude of disc evolution at some past epoch.

Given an arbitrary model specified by a set of cosmological parameters $\boldsymbol{p}$, and given the observable $\theta^{\rm obs}(z)$, i.e. the apparent angle subtended by a sample of velocity selected galaxies (with locally calibrated diameters $D_v(0)$), then

$$\epsilon_\theta(z, \boldsymbol{p}) = \theta^{\rm obs}(z) - \theta^{\rm th}(D_v(0), z, \boldsymbol{p}) \quad (7)$$

is the function which describes the redshift evolution of the standard rod, i.e $\epsilon_\theta = (D_v(z) - D_v(0))/d_\theta$ in the selected cosmology.

Let's suppose that we know the lower and upper limits of the relative (adimensional) standard rod evolution ($\delta(\bar{z}) = \frac{|\Delta D_v(\bar{z})|}{D_v(0)}$) at some specific redshift $\bar{z}$.

Assuming this prior, we can solve for the set of cosmological parameters (i.e. points $\boldsymbol{p}$ of the cosmological parameter space) which satisfy the condition

$$\delta_l(\bar{z}) \leq \frac{|\epsilon_\theta(\boldsymbol{p}, \bar{z})|}{\theta^{\rm th}(D(0), \bar{z}, \boldsymbol{p})} \leq \delta_u(\bar{z}). \quad (8)$$

This inequality establishes a mapping between cosmology and the amount of disc evolution at a given redshift which is compatible with the observed data. By solving it, one can construct a self-consistent cosmology-evolution plane where to any given range of disc size evolution at $\bar{z}$ corresponds in a unique way a specific region of the cosmological parameter space. Vice versa, for any given cosmology one can extract information about disc evolution. Clearly, the scatter in the angular-diameter diagram directly translates in the uncertainties associated to the evolution boundaries in the cosmological space.

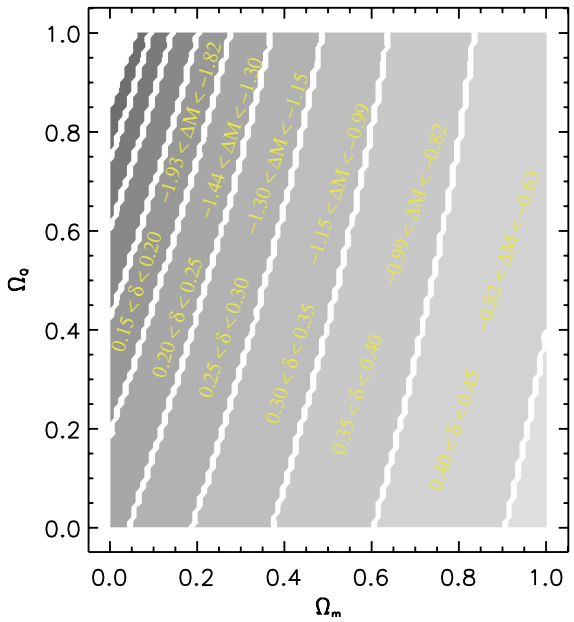

Fig. 8. Cosmology-evolution diagram for simulated data which are affected by evolution. Apparent angles and luminosities of the velocity selected sample of rotators are simulated in a ΛCDM cosmology. Standard rods and candles have been artificially evolved so that at $\bar{z} = 1.5$ discs are 26% smaller and luminosities 1.4 mag brigther. The cosmological plane is partitioned with different boundaries obtained by solving equation 8 for different values of $\delta(\bar{z} = 1.5)$, i.e. of the external prior representing the guessed upper limit of the relative disc evolution at the maximum redshift covered by data. The external prior is also expressed in term of absolute luminosity evolution (see discussion in Appendix A).

We note that the boundaries of the region of the cosmological parameter space which is compatible with the assumed prior on the evolution of diameters at $\bar{z}$ can be equivalently expressed in term of the maximum absolute evolution in luminosity (see Appendix A). This because, as stated in the previous section, velocity selected objects have the unique property of being at the same time standards of reference both in size and luminosity.

With this approach, one may by-pass the lack of knowledge about of the particular evolutionary track of disc scalelengths and luminosities and try to extract information about cosmology/evolution by giving as a prior only the fractional evolution in diameters or the absolute evolution in magnitude expected at a given redshift. The essence of the method is as follows: instead of directly putting constraints in the cosmological parameters space by mean of cosmological probes, we study how bounded regions in the evolutionary plane ($\frac{\Delta D}{D}, \Delta M$) map onto the cosmological parameter space.

In Fig. 8 we show the cosmology-evolution diagram derived by solving Eq. (8) for different ranges of $\delta(\bar{z})$. The reference model is the concordanace model ($\Omega_{\rm m} = 0.3$, $\Omega_Q = 0.7$, $w = -1$) and the reference evolution at $\bar{z} = 1.5$ is assumed to be $\delta(\bar{z}) = 0.25$ for discs, and $M_v(\bar{z}) - M_v(0) = -1.5$ for luminosities. The cosmology-evolution diagram represents the unique correspondance between all the possible cosmological models and the amount of evolution in size and luminosity which is compatible with the observed data at the given reference redshift. Using independent informations about the range of evolution expected in the structural parameters of galaxies, for exemple from simulations or theoretical models, one may constrain the value of

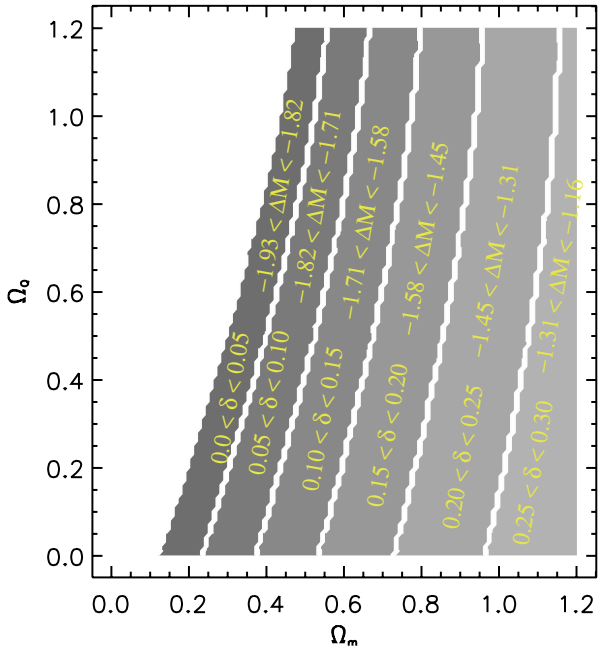

Fig. 9. As in Fig. 8 but for a different cosmology (an Einstein-de Sitter universe).

cosmological parameters Vice versa, if the cosmological model is known, then one may directly determine the evolution in magnitude and size of the velocity selected sample of rotators.

With this approach, the possibility of discriminating between different cosmologies depends on the amount of evolution affecting the standard rods at redshift $\bar{z}$. Two different sets ($\boldsymbol{p_1}$ and $\boldsymbol{p_2}$) of cosmological parameters may be discriminated at $z = \bar{z}$ if the relative disc evolution at $\bar{z}$ is known to a precision better than

$$\delta(\bar{z}) < \frac{|r(\bar{z}, \boldsymbol{p_2}) - r(\bar{z}, \boldsymbol{p_1})|}{r(\bar{z}, \boldsymbol{p_1})}. \quad (9)$$

For example, this kind of analysis shows that an Einstein-de Sitter universe may be unambigously discriminated from a critical universe with parameter $\Omega_{\rm m} = 0.3, \Omega_Q = 0.7, w = -1$. if the relative disc evolution at $\bar{z} = 1.5$ is known with a precision better than 28%. In a similar way, an open ($\Omega_{\rm m} = 0.3, \Omega_Q = 0$) universe may be discriminated from an Einstein de-Sitter universe if $\delta(\bar{z}) < 17\%$.

7. Conclusions

The scaling of the apparent angular diameter of galaxies with redshift $\theta(z)$ is a powerful discriminator of cosmological models. The goal of this paper is to explore the potentiality of a new observational implementation of the classical angular-diameter test and to study its performances and limitations.

We propose to use the velocity-diameter relationship, calibrated using the [OII]λ3727 Å line-widths, as a tool to select standard rods and probe world models. As for other purely geometrical test of cosmology, a fair sampling of the galaxy population is not required. It is however imperative to have high quality measurements of the structural parameters of high redshift galaxies (disc sizes and rotational velocity). Surveys with HST imaging and high enough spectral resolution will thus provide the fundamental ingredients for the practical realization of the recipe we have presented.

In order to avoid any luminosity dependent selection effect (such as for exemple Malmquist bias) it is necessary to apply the proposed test to high velocity rotators. We show that nearly 1300 standard rods with rotational velocity in the bin $V \sim 200 \pm 20$ km s^{-1}) are expected in a field of size 1 deg^2 over the redshift range $0 < z < 1.4$. Interestingly this large sample can be quickly assembled by the currently underway zCOSMOS deep redshift survey, which uses the VIMOS multi-object spectrograph at the VLT to target galaxies photometrically selected using high-resolution ACS images.

Even allowing a scatter of 40% for the [OII]λ3727Å linewidth-diameter relationship for disc galaxies, we show that the angular-diameter diagram constructed using this sample is affected by a scatter of only ∼5% per redshift bin of amplitude d$z = 0.1$. This scatter translates into a 20% precision in the "geometric" measurement of the dark energy constant equation of state parameter w, through a test performed without *priors* in the $[\Omega_{\rm m}, \Omega_Q]$ space.

Current theoretical models suggest that large discs (i.e. fast rotators) evolve weakly with cosmic time from $z = 1.5$ down to the present epoch. Anyway, we have explored how an eventual evolution of the velocity-selected standard rods might affect the implementation of the test. We have shown that any possible evolution in the standard rods may be unanbiguously revealed by the fact that even a small decrement with redshift of the disc sizes shifts the inferred value of the matter density parameter into "a-priori excluded" regions ($\Omega_{\rm m} < 0.2$).

We have shown that a linear (as expected on the basis of various theoretical models) and substantial (up to 40% over the range $0 < z < 1.5$) disc evolution minimally biases the inferred value of a dark energy component that behaves like Einstein's cosmological constant Λ. Moreover we have shown that assuming that discs evolve in a linear-like way as a function of redshift, and that their sizes were not more than 30% smaller at $z = 1.5$ with respect to their present epoch dimension, then the angular diameter test can be used to place interesting constraints in the $[\Omega_Q, w]$ plane. In particular, assuming a scatter of 5% per redshift bin in the angular diameter-redshift diagram (nearly corresponding to the scatter expected for a sample of 1300 rotators with $0 < z < 1.4$, d$z = 0.1$, whose diameter is locally calibrated with a 40% precision), we have shown that the input fiducial $[\Omega_Q, w]$ point is still within the 1σ error contours obtained by applying the angular diameter test to the evolved data.

Finally, we have outlined the strategy to derive a cosmology-evolution diagram with which it is possible to establish an interesting mapping between different cosmological models and the amount of galaxy disc/luminosity evolution expected at a given redshift. The construction of this diagram does not require an a-priori knowledge of the particular functional form of the galaxy size/luminosity evolution. By reading this diagram, one can infer cosmological information once a theoretical prior on disc or luminosity evolution at a given redshift is assumed. In particular if the amplitude of the relative disc evolution at $\bar{z} = 1.5$ is known to better than ∼30%, then an Einstein-de Sitter universe ($\Omega_{\rm m} = 1$) may be geometrically discriminated from a flat, vacuum dominated one ($\Omega_{\rm m} = 0.3$, $\Omega_Q = 0.7$). Viceversa, one can use the cosmology-evolution diagram to place constraints on the amplitude of the galaxy disc/luminosity evolution, once a preferred cosmology is chosen.

In conclusion, given the simple ingredients entering the proposed implementation strategy, nothing, besides evolution of discs, could in principle bias the test. Even so, evolution can be easily diagnosed and, under some general conditions, it can be shown that it does not compromise the possibility of detect-

ing the presence of dark energy and constraining the value of its equation of state.

In the following papers of this series (Saintonge et al. 2007; Marinoni et al. 2007), we implement the proposed strategy to a preliminary sample of velocity-selected high redshift rotators.

Acknowledgements. We would like to acknowledge useful discussions with R. Scaramella and G. Zamorani. This work has been partially supported by NSF grants AST-0307661 and AST-0307396 and was done while A.S. was receiving a fellowship from the *Fonds de recherche sur la Nature et les Technologies du Québec*. K.L.M. is supported by the NSF grant AST-0406906.

Appendix A

Given a spectroscopically selected sample of objects with constant rotational velocity we can derive the observed magnitude $m^{\rm o}$ of a standard candle of absolute magnitude $M_v(0)$ located at redshift z, by using the standard relation Sandage (1972)

$$m^{\rm o} = m^{\rm th}(M_v(0), z, \boldsymbol{p}) + \epsilon_M(z) + K(z) \quad (10)$$

where

$$m^{\rm th} = M_v(0) + 5\log d_{\rm L}(z, \boldsymbol{p}) + 25$$

and were d_L is the luminosity distance, $K(z)$ is the K correction term and $\epsilon_M(z)$ is the a-priori unknown evolution in luminosity of our standard candle, i.e. $\epsilon_M(z) = \Delta M_v(z) = M_v(z) - M_v(0)$ is the difference between the absolute magnitude of an object of rotational velocity V measured at redshift z and the un-evolved local standard value $M_v(0)$.

From the definition of wavelength-specific surface brightness μ we deduce that the variation as a function of redshift in the average intrinsic surface brightness (within a radius R) for our set of homologous galaxies is

$$\Delta\langle\mu^{\rm th}(z)\rangle_R = \Delta M_v(< R) - 5\log\frac{R(z)}{R(0)}.$$

By opportunely choosing the half light radius D_v as a metric definition for the size of a galaxy we immediately obtain

$$\Delta\langle\mu^{\rm th}(z)\rangle_D = \epsilon_M(z, \boldsymbol{p}) - 5\log\left(\frac{\epsilon_\theta(z, \boldsymbol{p})}{\theta^{\rm th}(D(0), z, \boldsymbol{p})} + 1\right). \quad (11)$$

The intrinsic surface brightness evolution is not an observable, but in a FRW metric this quantity is related to the surface brightness change observed in a waveband $\Delta\lambda$ by the relation

$$\Delta\langle\mu^{\rm o}(z)\rangle_D = \Delta\langle\mu^{\rm th}(z)\rangle_D + 2.5\log(1+z)^4 + K(z). \quad (12)$$

Thus, once we measure the redshift evolution of $\Delta\langle\mu^{\rm o}(z)\rangle_D$ for the sample of rotators, the absolute evolution in luminosity corresponding to a given relative evolution in diameters can be directly inferred using Eq. (11).

References

Aldering, G., et al. 2002, in SPIE Proc., 4835 [arXiv:astro-ph/0209550]
Berlind, A. A., & Weinberg, D. H. 2002, ApJ, 575, 587
Boissier, S., & Prantzos, N. 2001, MNRAS, 325, 321
Bottinelli, L., Gouguenheim, L., Paturel, G., & de Vaucouleurs, G. 1980, ApJ, 242, L153
Bouwens, R., & Silk, J. 2000, ApJ, 568, 522
Bruzual, A. G., & Spinrad, H. 1978, ApJ, 220, 1
Buchalte, A., Helfand, D. J., Becker, R. H., & White, R. L. 1998, ApJ, 494, 503
Carroll, S. M., Press, W. H., & Turner, E. L. 1992, ARA&A, 30, 499
Chiappini, C., Matteucci, F., & Gratton, R. 1997, ApJ, 477, 765
Colless, M., Glazebrook, K., Mallen-Ornelas, G., & Broadhurst, T. 1998, ApJ, 500, L75
Cooray, A., Hu, W., Huterer, D., & Joffre, M. 2001, ApJ, 557L, 7
Daly, R. A. 2004, ApJ, 612, 652
Daly, R. A., & Djorgovski, S. G. 2004, ApJ, 612, 652
Davis, M., Newman, J. A., Faber, S. M., & Phillips, A. C. 2000 in Deep Fields, Proceedings of the ESO/ECF/STScI Workshop, ed. S. Cristiani, A. Renzini, & R. E. Williams (Springer), 241
de Bernardis, P., et al. 2002, ApJ, 564, 559
de Vaucouleurs, G., de Vaucouleurs, G., & Corwin, H. G. 1976, Second Reference Cataloguwe of Bright Galaxies (Austin: University of Texas) RC2
Djorgovski, S., & Spinrad, H. 1981, ApJ, 251, 417
Faber, S. M., Phillips, A. C., Simard, L., Vogt, N. P., & Somerville, R. S. 2001, in Galaxy Disks and Disk Galaxies, ASP Conf. Ser., 230, 517
Ferguson, A. M. N., & Clarke, C. J. 2001, MNRAS, 325, 781
Gonzalez, A. H. 2002, ApJ, 567, 144
Gurvits, L. I., Kellermann, K. I., & Frey, S. 1999, A&A, 342, 378
Haiman, Z., Mohr, J. J., & Holder, G. P. 2001, ApJ, 553, 545
Halverson, N. W., et al. 2001, ApJ, 568, 38
Hickson, P., 1977a, ApJ, 217, 16
Hogg, D. W. 1999 [arXiv:astro-ph/9905116]
Hoyle, F., 1959 in Proc. IAU Symp. 9 and URSI Symp. 1, Paris Symp on Radio Astronomy, ed. R. N. Brachewell (Stanford: Stanford Univ. Press), 529
Hubble, E., & Tolman, R. C., & Astrophys, J. 1935, 82, 302
Huterer, D., & Turner, M. S. 2001, Phys. Rev. D64
Ilbert, O., et al. 2005, A&A, 439, 863
Kapahi, V. K. 1975, MNRAS, 172, 513
Kellermann, K. I. 1993, Nature, 361, 134
Kobulnicky, H. A., & Gebhardt, K. 1999, ApJ, 119, 1608
Lahav, O. 2002, MNRAS, 333, 961
Lee, A. T., et al. 2001, ApJ, 561, L1
Le Fèvre, 0., et al. 2005, A&A, 439, 845
Lilly, S. J., Schade, D., Ellis, R., et al. 1998, ApJ, 500, L75
Lilly, S. J., et al. 2006, ApJ, in press [arXiv:astro-ph/0612291]
Lima, J. A. S., & Alcaniz, J. S. 2002, A&A, 566, 15L
Marinoni, C., Monaco, P., Giuricin, G., & Costantini, B. 1998, ApJ, 505, 484
Marinoni, C., & Hudson, M. 2002, ApJ, 569, 101
Marinoni, C., et al. 2006, A&A, 442, 801
Marinoni, C., et al. 2007, A&A, submitted
Miley, G. K. 1971, MNRAS, 152, 477
Mo, H. J., Mao, S., & White, S. D. M. 1998, MNRAS, 295 319
Narayan, R., & White, S. D. M. 1988, MNRAS, 231, 97
Newman, J. A., Marinoni, C., Coil, A. L., & Davis, M. 2002, PASP, 114, 29
Newman, J. A., & Davis, M. 2000, ApJ, 534, L11
Nelson, A. E., Simard, L., Zaritsky, D., Dalcanton, J. J., & Gonzalez, A. H. 2002, ApJ, 567, 144
Pen, U.-L. 1997, New A., 2, 309
Perlmutter, S., et al. 1999, ApJ, 517, 565
Petrosian, V. 1976, ApJ, 209, L1
Riess, A. G., et al. 1999, ApJ, 560, 49
Saintonge, A., Masters, K. L., Marinoni, C., Giovanelli, R., & Haynes, M. P. 2007, A&A submitted
Sandage, A. 1972, ApJ, 173, 485
Sandage, A. 1998, ARA&A, 26, 561
Sandage, A. 1995, in Saas-Fee Advanced Course 23, The Deep Universe: Practical Cosmology, ed. B. Binggeli, & R. Buser (New York: Springer)
Spergel, D. N., et al. 2006 [arXiv:astro-ph/0603449]
Springob, C. M., Masters, K. L., Haynes, M. P., Giovanelli, R., & Marinoni, C. 2007, ApJS, in press [arXiv:astro-ph/07050647]
Takamiya, M. 1999, ApJS, 122, 109
Tegmark, M. 2006, Phys. Rev. D 74, 123507
Tolman, R. C. 1930, Proc. Natl. Acad. Sci. USA: 16, 511
Totani, T., Yoshii, Y., Maihara, T., Iwamuro, F., & Motohara, K. 2001, ApJ, 559, 592
Tully, R. B., & Fisher, J. R. 1977, A&A, 54, 661
Turner, M. S., & White, M. 1997, Phys. Rev. D, 56, 4439
van den Bosch, F. C., et al. 2006, MNRAS submitted [arXiv:astro-ph 0610686]
Wilkinson, P.N., Browne, I. W. A., Alcock, D., et al. 1998, in Observational Cosmology with new radio surveys (Dordrecht: Kluwer, Acad. Publishers), 221

Astronomy & Astrophysics manuscript no. msIII September 13, 2007
(DOI: will be inserted by hand later)

Geometrical Tests of Cosmological Models

III. The Cosmology-Evolution Diagram at $z = 1$

C. Marinoni[1], A. Saintonge[2], T. Contini[3], C.J. Walcher[4], R. Giovanelli[2], M.P. Haynes[2], K.L. Masters[5], O. Ilbert[4], A. Iovino[6], V. Le Brun[4], O. Le Fevre[4], A. Mazure[4], L. Tresse[4], J.-M. Virey[1], S. Bardelli[7], D. Bottini[8], B. Garilli[8], D. Maccagni[8], J.P. Picat[3], R. Scaramella[9], M. Scodeggio[8], P. Taxil[1], G. Vettolani[9], A. Zanichelli[9], E. Zucca[7]

[1] Centre de Physique Théorique*, CNRS-Université de Provence, Case 907, F-13288 Marseille, France.
[2] Department of Astronomy, Cornell University, Ithaca, NY 14853, USA
[3] Laboratoire d'Astrophysique de l'Observatoire Midi-Pyrénées, UMR 5572, 31400 Toulouse, France
[4] Laboratoire d'Astrophysique de Marseille, UMR 6110, CNRS Université de Provence, 13376 Marseille, France
[5] Harvard-Smithsonian Center for Astrophysics, Cambridge, MA 02143, USA
[6] INAF-Osservatorio Astronomico di Brera - Via Brera 28, Milano, Italy
[7] INAF-Osservatorio Astronomico di Bologna - Via Ranzani 1, Bologna, Italy
[8] IASF-INAF - via Bassini 15, I-20133, Milano, Italy
[9] IRA-INAF - Via Gobetti,101, I-40129, Bologna, Italy

Received ... / Accepted ...

Abstract. The rotational velocity of distant galaxies, when interpreted as a size (luminosity) indicator, may be used as a tool to select high redshift standard rods (candles) and probe world models and galaxy evolution via the classical angular diameter-redshift or Hubble diagram tests. We implement the proposed testing strategy using a sample of 30 rotators spanning the redshift range $0.2 < z < 1$ with high resolution spectra and images obtained by the VIMOS/VLT Deep Redshift Survey (VVDS) and the Great Observatories Origins Deep Survey (GOODs). We show that by applying at the same time the angular diameter-redshift and Hubble diagrams to the same sample of objects (i.e. velocity selected galactic discs) one can derive a characteristic chart, the cosmology-evolution diagram, mapping the relation between global cosmological parameters and local structural parameters of discs such as size and luminosity. This chart allows to put constraints on cosmological parameters when general prior information about discs evolution is available. In particular, by assuming that equally rotating large discs cannot be less luminous at $z = 1$ than at present ($M(z = 1) \lesssim M(0)$), we find that a flat matter dominated cosmology ($\Omega_m = 1$) is excluded at a confidence level of 2σ and an open cosmology with low mass density ($\Omega_m \sim 0.3$) and no dark energy contribution (Ω_Λ) is excluded at a confidence level greater than 1σ. Inversely, by assuming prior knowledge about the cosmological model, the cosmology-evolution diagram can be used to gain useful insights about the redshift evolution of baryonic discs hosted in dark matter halos of nearly *equal masses*. In particular, in a ΛCDM cosmology, we find evidence for a bimodal evolution where the low-mass discs have undergone significant surface brightness evolution over the last 8.5 Gyr, while more massive systems have not. We suggest that this dichotomy can be explained by the epochs at which these two different populations last assembled.

Key words. cosmology: observations—cosmology:theory—cosmology:cosmological parameters—galaxies: distances and redshifts—galaxies: fundamental parameters—galaxies: evolution

1. Introduction

Deep redshift surveys of the Universe, such as the VIMOS/VLT deep redshift survey (VVDS, Le Fèvre et al. (2005)) and the ACS/zCOSMOS survey (Lilly et al., 2006) are currently underway to study the physical properties of high redshift galaxies. Motivated by these major observational efforts, we are currently exploring whether

Send offprint requests to: C. Marinoni, e-mail: marinoni@cpt.univ-mrs.fr

* Centre de Physique Théorique is UMR 6207 - "Unité Mixte de Recherche" of CNRS and of the Universities "de Provence", "de la Méditerranée" and "du Sud Toulon-Var"- Laboratory affiliated to FRUMAM (FR 2291).

high redshift galaxies can also be used as cosmological tracers. Specifically, we are trying to figure out if these new and large sets of spectroscopic data can be meaningfully used to probe, in a geometric way, the value of the constitutive parameters of the Friedmann-Robertson-Walker cosmological model.

A whole arsenal of classical geometrical methods has been developed to measure global properties of the universe. The central feature of all these tests is the attempt to probe the various operative definitions of relativistic distances by means of scaling relationships in which a distant dependent observable, (e.g. an angle or a flux), is expressed as a function of a distance independent fixed quantity (e.g. metric size or absolute luminosity).

A common thread of weakness in all these approaches to measure cosmological parameters using distant galaxies or AGNs selected in deep redshift surveys is that there are no clear criteria by which such cosmological objects should be considered universal standard rods or standard candles.

Motivated by this, in previous papers (Marinoni et al. (2004) and Marinoni et al. (2007), hereafter Paper I) we have investigated the possibility of using the observationally measured and theoretically justified correlation between size/luminosity and disc rotation velocity as a viable method to select a set of high redshift galaxies, with statistically homologous dimensions/luminosities. This set of tracers may be used to test the evolution of the cosmological metric via the implementation of the standard angular diameter-redshift and Hubble diagram tests.

Finding valid standard rods, however, does not solve the whole problem; the implementation of the angular diameter-redshift test using distant galaxies is hampered by the difficulty of disentangling the effects of galaxy evolution from the signature of geometric expansion of the universe.

In Paper I we have determined some general conditions under which galaxy kinematics may be used to test the evolution of the cosmological metric. We have shown that in the particular case in which disc evolution is linear and modest (<30% at $z = 1.5$), the inferred values of the dark energy density parameter Ω_Q and of the cosmic equation of state parameter w are minimally biased ($\delta\Omega_Q = \pm 0.15$ for any Ω_Q in the range $0 < \Omega_Q < 1$).

In Paper I, we also looked for cosmological predictions that rely on less stringent assumptions, i.e. which do not require specific knowledge about the particular functional form of the standard rod/candle evolution. In particular, we showed how velocity-selected rotators may be used to construct a *cosmology-evolution diagram* for disc galaxies. This is a chart mapping the local physical parameter space of rotators (absolute luminosity and disc linear size) onto the space of global, cosmological parameters (Ω_m, Ω_Q). Using this diagram it is possible to extract information about cosmological parameters once the amount of size/luminosity evolution at some reference epoch is known. *Vice-versa*, once a cosmological model is assumed, the cosmology-evolution mapping may be used to directly infer the specific time evolution in magnitude and size of disc galaxies that are hosted *in dark matter halos of similar mass*.

We stress that this last way of reading the cosmology-evolution diagram offers a way to explore galaxy evolution which is orthogonal to more traditional methods. In particular, insights into the mechanisms of galaxy evolution are traditionally accessible through the study of disc galaxy scaling relations, such as the investigation of the time-dependent change in the magnitude-velocity (Tully-Fisher) relation (e.g., Vogt et al (1996); Böhm et al. (2004); Bamford et al. (2006)), of the magnitude-size relations (e.g., Lilly et al. (1998); Simard et al. (1999); Bouwens & Silk (2002); Barden et al. (2005)), or of the disc "thickness" (Reshetnikov et al., 2003; Elmegreen et al., 2005). By applying the angular size-redshift test and the Hubble diagram to velocity-selected rotators, we aim at tracing the evolution in linear size, absolute magnitude and intrinsic surface brightness of disc galaxies that are hosted halos of the same given mass at every cosmic epoch explored.

In this paper, we present a pilot observational program that allowed us to test whether galaxy rotational velocity can be used to select standard rods, and to derive the cosmology-evolution diagram for disc galaxies at redshift $z = 1$. Our observing strategy was to follow-up in medium resolution spectroscopic mode with VIMOS a set of emission-line objects selected from a sample of galaxies in the Chandra Deep Field South (CDFS) region for which high resolution photometric parameters were available (Giavalisco et al., 2004).

The outline of the paper is as follow: in §2 we describe the VVDS spectroscopic data taken in the CDFS region. In §3 we outline a strategy to test the consistency of the standard rod/candle selection. In §4 we derive the cosmology-evolution diagram for our sample of rotators, and in §5 we present our results about disc size, luminosity and surface brightness evolutions. Discussions and conclusions are presented in §6 and §7, respectively. Throughout, the Hubble constant is parameterized via $h_{70} = H_0/(70 kms^{-}1 Mpc^{-}1)$. All magnitudes in this paper are in the AB system (Oke & Gunn, 1983), and from now the AB suffix will be omitted.

2. Sample: observations and data reduction

Our strategy to obtain kinematic information for the largest possible sample of rotators at high redshift was to re-target in medium resolution mode (R=2500) galaxies in the CDFS region for which a previous pass in low-resolution mode (Le Fèvre et al., 2004) already provided spectral information such as redshifts, emission-line types, and equivalent widths, for galaxies down to I=24. Galaxies were selected as rotators if their spectra was blue and characterized by emission line features (OII, Hβ, OIII, Hα). CDFS photometry was then used to confirm the disc-like nature of their light distribution (i.e. the absence of any strong bulge component), and also to avoid including in

the sample objects with peculiar morphology or undergoing merging or interaction events.

The final sample of candidates for medium resolution re-targeting was defined by further requiring that the inclination of the galaxy be greater than 60° to minimize biases in velocity estimation, and that its identified emission line fall on the CCD under the tighter constraints imposed by the medium resolution grism. Once the telescope pointing and slit positioning were optimized using the low-resolution spectral information, the remaining space on the focal plane mask was blindly assigned to galaxies in the field.

Spectroscopic observations have been obtained with the VIMOS spectrograph on the VLT Melipal telescope in October 2002. The slit width was 1 arcsecond giving a spectral resolution R=2500 as measured on the FWHM of arc lines. Using the VIMOS mask design software and capabilities of the slit-cutting laser machine (Bottini et al., 2005), slits have been placed on each galaxy at a position angle aligned with the major axis. The seeing at the time of observations was 0.8 arcseconds FWHM with an integration time of 1 hour split in three exposures of 20 minutes each.

Most of the galaxies in the CDFS area surveyed by the VVDS have high resolution images taken with the ACS camera of the HST by GOODs. Images are available in four different filters (F435W, F606W, F775W, F850LP) noted hereafter B,V,I and Z, respectively. A small fraction of the targeted galaxies has only I band images provided by the ESO Imaging Survey (Arnouts et al., 2001).

The galaxy rotational velocity has been estimated using the linewidths of the emission lines. A detailed analysis of the velocity extraction algorithm and of the potential systematic errors implicit in this technique are presented in Paper II of this serie (Saintonge et al., 2007). This technique to measure rotation velocities imposed itself since many galaxies at high redshift were too small to measure rotation curves reliably, and since summing all the light to form velocity histograms increased the signal-to-noise ratio (S/N) of the detected lines.

Magnitudes have been computed in the I band and a K-correction was applied (see Ilbert et al. (2005) for a detailed discussion). They were also corrected for galactic absorption using the maps of Schlegel et al. (1998) in the CDFS region (i.e. on average a correction of ~ 0.0016), and for galaxy inclination by adopting a standard empirical description of internal extinction A_λ in the pass-band λ, $\gamma \log(\sec i)$, where i is the galaxy inclination angle as calculated from the galaxy axis ratio and $\gamma_I = 0.92 + 1.63(\log 2v - 2.5)$ (Tully et al., 1998) where v is the maximum rotational velocity of a galaxy.

Galaxy sizes have been specified in terms of the half-light diameter (HLD) inferred in the I band. Typical errors in the measurements are $\sigma_\theta \sim 0.04$". In Paper I we stressed the importance of using a metric rather than an isophotal definition of galaxy diameters for cosmological purposes (e.g. Sandage, 1995). We also verified that the HLDs for our sample of galaxies do not depend on wavelength; there is no systematic difference in the inferred metric diameters when the HLD is computed in the B, V, I or z filters (see also Sandage & Perelmuter (1990), de Jong (1996)). The scatter in the HLDs inferred in different bands is of order 0.02" and therefore small in comparison to the observational uncertainties σ_θ.

[OII] linewidths have been translated into an estimate of the galaxy rotational velocity, v, as detailed in §3.2 of Paper II. Rotational velocity was derived using [OII](3727Å) lines (24 objects), [OIII](5007Å) lines (10 objects) and Hα(6563Å) (5 objects). 23 galaxies have velocities in the range $0 < v(\text{ km s}^{-1}) \leq 100$ (with mean velocity of the sample ~ 60 km s^{-1}) and 16 galaxies have velocities in the range $100 < v(\text{km s}^{-1}) \leq 200$ (with mean velocity of the sample ~ 143 km s^{-1}) .

After data reduction, we were left with a sample of 39 objects, 27 of which have high resolution imaging. As for the remaining objects with ground photometry, we only consider in the following those with $z < 0.2$, in order to exclude faint and small galaxies for which the size measurements are severely compromised by seeing distortions. Therefore, our final "science" sample contains 30 objects.

Data are organized and presented in Table 1 as follows: *col*.1 : galaxy ID in the EIS catalog, *col*.2 : redshift, *col*.3 rotation velocity, *col*.4 : half-light angular radius, *col*.5 : magnitude, *col*.6 : surface brightness within the half-light radius.

3. Selection of Standard rods/candles

An observable relationship exists between the metric radial dimension D of a disc and its speed of rotation v. An analogous empirical relationship connects rotation with luminosity (Tully & Fisher, 1977). In Paper I we have proposed to use information on the kinematics of galaxies, as encoded in their OII emission-line width, to *objectively* identify standard rods/candles at high redshifts. A discussion of the requirements and of the optimal strategies to fulfill this observational program is detailed in Paper I.

A variety of standard rod candidates have been explored in previous attempts of providing a direct geometrical proof of the curvature of the universe. A common thread of weakness in all these attempts is that there are no clear physical nor statistical criteria by which the proposed objects (clusters, extended radio lobes or compact radio jets associated with quasars and AGNs) should be considered universal standard rods/candle.

Even assuming that a particular class of standards is identified, the length of the rod remains unknown. Since the inferred cosmological parameters heavily depend on the assumed value for the object size (Lima & Alcaniz, 2000), an *a-priori* independent statistical study of the standard rod absolute calibration is an imperative prerequisite. In Paper II, we used a large sample of galaxies from the SFI++ catalog (Springob et al., 2007) to fix the

EIS ID	z	v(km s^{-1})	$\theta^o(arcsec)$	m^o	μ^o (mag/arcsec^2)
30445	0.9332	97	0.180	23.744	22.03
32177	0.8934	68	0.149	23.681	21.54
31328	0.4164	79	0.606	22.297	23.20
32998	0.1464	28	0.857	20.794	22.45
34826	0.4559	204	0.715	22.684	23.95
34244	0.5321	55	0.298	22.324	21.69
29895	0.6807	44	0.220	23.571	22.23
37157	0.8677	129	0.751	23.399	24.77
33200	0.1267	96	0.806	20.519	22.04
33763	1.0220	130	0.755	23.404	24.79
31501	1.0360	140	0.747	23.513	24.87
31194	0.3320	80	0.818	21.950	23.51
29342	0.4680	55	0.481	23.565	23.97
29232	0.8610	155	0.370	22.320	22.15
34325	0.3334	26	0.221	23.570	22.20
34560	0.8618	28	0.204	23.549	22.00
36484	0.7539	25	0.202	23.781	22.30
16401	1.1000	306	0.913	21.628	23.42
17811	0.8143	170	0.726	23.573	24.87
17362	0.6814	178	0.683	22.379	23.54
22685	0.8411	115	0.891	22.147	23.88
17255	0.1787	99	1.203	21.758	24.16
15152	0.7931	169	0.895	21.702	23.46
15099	0.3661	70	0.509	21.171	21.70
19702	0.6770	62	0.295	22.812	22.16
16377	0.5621	36	0.490	22.944	23.37
17421	0.7834	99	0.361	23.280	23.06
20202	0.5763	26	0.190	23.318	21.70
18416	0.8859	99	0.205	23.637	22.18
17534	0.3493	35	0.271	23.837	22.99
15486	0.6613	146	0.551	22.495	23.20
19684	0.8588	104	0.424	22.790	22.92
18743	0.6800	81	0.447	22.950	22.70
15553	0.4584	183	0.991	19.292	21.26
18417	0.5350	36	0.342	22.877	22.54
18779	0.5623	59	0.351	22.445	22.15
21252	0.5795	102	0.414	22.854	22.93
20708	0.1228	166	1.540	18.427	21.40
18853	0.6509	116	0.556	21.350	22.10

Table 1. Properties of the Galaxy Sample

local calibration values for absolute magnitudes and linear diameters of galaxies with a given rotational velocity.

3.1. Velocity selection of rotators: test of consistency

We have seen that, in order to implement the proposed test, we need two sample of rotators: the "data sample" (galaxies with the same rotational velocity selected over the widest possible redshift range; the sample presented in §2), and the "calibration sample" (rotators at redshift $z \sim 0$ for which the physical size of the linear diameter is known; the SFI++ sample analyzed in Paper II). This last sample allows us to calibrate the zero-point of the Hubble and angular size-redshit diagrams (i.e. $M_v(0)$ and $D_v(0)$ in eqs. 2 an 4).

We stress that the disc rotational velocity of galaxies in the two samples is measured using two different velocity indicators (spectroscopic lines) and two different velocity extraction methods. Specifically we use OII linewidths to measure the rotational velocity of the distant "data" sample and H_α rotation curves to measure the velocities of the local "calibration" galaxies. Therefore, it is imperative to check that possible biases or errors introduced by combining velocities inferred using systematically different measuring techniques do not prevent a meaningful comparison between different samples at different redshifts.

To this purpose we have implemented the following testing strategy. Given a spectroscopically-selected sample of standard candles $M_v(0)$ with rotational velocity v, one can derive the observed apparent magnitude m^o of a standard candle located at redshift z, by using the relation (Sandage, 1988):

$$m^o = m^{th}(M_v(0), z, \boldsymbol{p}) + \epsilon_M(z, \boldsymbol{p}) + K(z) \quad (1)$$

where

$$m^{th} = M_v(0) + 5\log d_L(z, \boldsymbol{p}) + 25 \quad (2)$$

and where $d_L(z, \boldsymbol{p})$ is the luminosity distance (depending on the set of cosmological parameters $\boldsymbol{p}$), $K(z)$ is the K-correction term and $\epsilon_M(z, \boldsymbol{p})$ is the *a-priori* unknown cosmology-dependent evolution in luminosity of our standard candle, i.e. $\epsilon_M(z, \boldsymbol{p}) = M_v(z, \boldsymbol{p}) - M_v(0)$ is the difference between the absolute magnitude of an object of rotational velocity v measured at redshift z with respect to the un-evolved local standard value $M_v(0)$.

Similarly, one can parameterize any possible evolution affecting the standard rod $D_v(0)$ by writing its observed apparent subtended angle at redshift z as

$$\theta^0 = \theta^{th}(D_v(0), z, \boldsymbol{p})[1 + \delta(z, \boldsymbol{p})] \quad (3)$$

where the theoretically expected angular scaling (θ^{th}) is given by

$$\theta^{th} = \frac{D_v(0)}{d_A(z, \boldsymbol{p})}, \qquad d_A = d_L(1+z)^{-2} \quad (4)$$

and where $\delta(z, \boldsymbol{p})$ is a cosmology-dependent function which describes the relative redshift evolution of the standard rod, i.e $\delta \equiv (D_v(z, \boldsymbol{p}) - D_v(0))/D_v(0) \equiv \epsilon_D/D_v(0)$. We note that any possible evolution in the standard rod angular size is related to the evolution in its linear dimension as follows: $\epsilon_\theta = \epsilon_D/d_A$. Here and in the following, we assume that the angular size of fixed-velocity rotators is estimated using the galaxy half-light diameter D_v.

From the definition of wavelength-specific surface brightness, μ, we deduce that the variation as a function of redshift in the average intrinsic surface brightness within a radius R for our set of velocity selected galaxies (i.e. $\Delta\langle\mu^{in}(z)\rangle_R \equiv \langle\mu^{in}(z) - \mu^{in}(0)\rangle_R$) is

$$\Delta\langle\mu^{in}(z)\rangle_R = \Delta M_v(< R) + 5\log\frac{R(z)}{R(0)} \quad (5)$$

By choosing the half-light diameter D_v as a metric definition for the size of a standard rod, we immediately obtain the intrinsic surface brightness evolution within D_v as

$$\Delta\langle\mu^{in}(z)\rangle_{D_v} = \epsilon_M(z, \boldsymbol{p}) + 5\log(1 + \delta(z, \boldsymbol{p})). \quad (6)$$

While the specific amount of evolution in luminosity and size do in principle depend on the specific background cosmological model adopted, the corresponding evolution in intrinsic surface brightness is a cosmology-independent quantity.

The evolution in intrinsic surface brightness is not a directly measurable quantity, but, in a FRW metric, this quantity can be easily related to the apparent surface brightness change observed in a waveband $\Delta\lambda$ by the relation

$$\Delta\langle\mu^{o}(z)\rangle_{D_v} = \Delta\langle\mu^{in}(z)\rangle_{D_v} + 2.5\log(1+z)^4 + K(z) \quad (7)$$

We note that the left-hand side of Eq. 7 is directly measurable using photometric images. Moreover, it can be measured without assuming any specific galaxy light profile and it will be, in general, a non linear function of redshift. By combining eqs. 1, 3, 6 and 7 we define the η function:

$$\eta = m^o(z) - \Delta\langle\mu^o(z)\rangle_{D_v} + 5\log\theta^o(z). \quad (8)$$

The specific combination in Eq. 8 of observed magnitudes, half-light diameters, and evolution in the observed surface brightness within the HLD ($\Delta\langle\mu^o(z)\rangle_{D_v} = \langle\mu^o(z)\rangle_{D_v} - \langle\mu^o(0)\rangle_{D_v}$) is, by construction, a redshift-invariant quantity which is equal to

$$\eta = M_v(0) + 5\log D_v(0) + 25. \quad (9)$$

From a theoretical point of view, we emphasize that the η-estimator given in Eq. 8 does not explicitly depend on i) K correction, ii) evolution in luminosity or size of our standard sources and iii) on the specific gravitational model assumed to derive the exact functional form of the angular and luminosity distances.

From an observational point of view, we stress that Eq. 8 can be directly estimated using photometric images of the "data" sample, while Eq. 9 may be expressed in terms of the locally measured absolute magnitudes and linear diameters of our "calibration" sample. Therefore, by simply comparing the values of the η function inferred using the "data" sample (Eq. 8) with the constant value predicted using the "calibration" sample (Eq. 9), we can test for the presence of eventual biases in our data. The goal is to reveal possible systematics that could be introduced, for example, by the different techniques with which rotation properties are inferred locally (mainly using H_α rotation curves) and at higher redshift (mainly using OII line-widths). Clearly, a mismatch would indicate that our spectroscopic selection technique fails in selecting homologous classes of objects embedded in halos of nearly the same mass at different redshifts.

Since our total sample is still limited, at present it is practical to implement the proposed test of consistency by defining only two broad classes of velocity-selected galaxies: a low-velocity sample of standard rods/candles with $0 < v \leq 100$km s^{-1} containing 22 galaxies with mean rotational velocity of ~ 60 km s^{-1} (S_{60} sample) and a high-velocity set of objects with $100 < v < 200$km s^{-1} containing 8 rotators with mean velocity of ~ 143 km s^{-1} (S_{143} sample). The size (HLD), absolute luminosity and mean surface brightness $\mu(0)$ within the HLD of local galaxies are derived using the calibration relationships of Paper II and are quoted in Table 2. Clearly, with more high resolution data becoming available, it will be possible to split the sample in finer velocity bins and thus select standard rods/candles having smaller size/luminosity dispersions.

In Figure 1 we plot the η-estimator (see Eq. 8) for the S_{60} sample of rotators. The first and third terms on the RHS of Eq. 8 were estimated as explained in §2, while the second term was evaluated by fitting the observed SB with a linear model and subtracting from the observation the zero point of the model (i.e. the value $\langle\mu^0(0)\rangle$ inferred using the linear model).

$\langle v \rangle / (\mathrm{km\ s^{-1}})$	$D(0)/(h_{70}^{-1}\ \mathrm{kpc})$	$M(0) - 5 \log h_{70}$	$\mu(0)\ (\mathrm{mag/arcsec^2})$
60	4.30 ± 2.8	-18.80 ± 0.75	21.50 ± 0.74
143	9.00 ± 2.5	-21.40 ± 0.44	20.45 ± 0.70

Table 2. Local calibration for diameters, absolute magnitudes and surface brightness within the half light radius as derived in Paper II

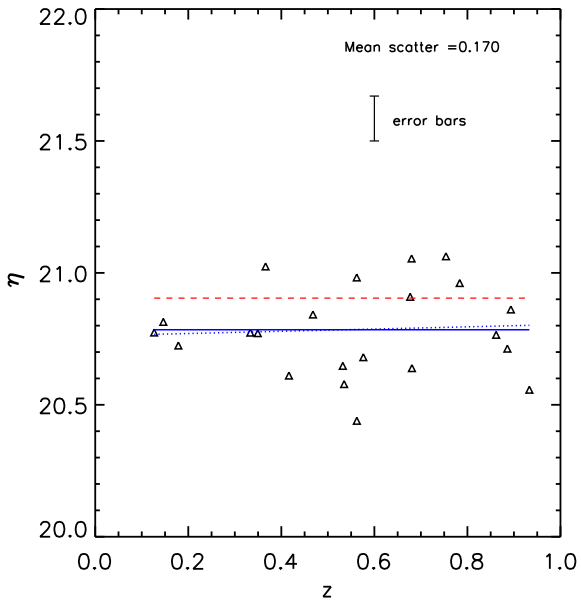

Fig. 1. The η estimator scatter plot computed using Eq. 8 and the S_{60} sample. The dotted line is the best fitted linear regression to the data, while the solid line represents the best fitted constant model. The dashed line represents the estimated values for the η function obtained by using locally calibrated values for the standard rods and candles, i.e. using Eq. 9 with the values specified in Table 2. The best fitting linear regression is consistent with being a constant function of redshift.

A series of conclusions can be immediately drawn. First, the best fitting linear regression is very well approximated by a constant function of redshift. This *shape* is not only theoretically expected, but it is consistent with the hypothesis that none of the relevant photometric parameters (angular sizes, magnitudes, surface brightnesses) measured for our sample of rotators suffer from any redshift-dependent systematics.

Secondly, the consistency of the measurements can be assessed by comparing the *scatters* in η estimated by using Eq. 8 and Eq. 9. The average scatter in Eq. 8 measures the quality with which angular diameters, magnitudes and surface brightnesses have been measured in the "data" sample. This is an extremely useful indicator since measuring structural parameters for distant, faint and small galaxies is not an error-free task. σ_η is thus a quality parameter which describes the overall consistency of our measurements of the three observables m^o, μ^o and D^o. The average scatter in Eq. 9 indicates the robustness with which local velocity data can be used to select standard candles/rods. In other terms it reflects the intrinsic scatter in the calibration of the Tully-Fisher relation for local diameters and magnitudes. Clearly, if scatter in Eq. 8 is comparable or bigger than scatter in eq 9, then our high redshift data would be of low quality and definitely useless. The scatter in Eq. 8 ($\sigma_\eta = 0.035$) is nearly one order of magnitude smaller than that inferred using Eq. 9 (~ 0.3), and, together with the absence of any trend in the distribution of the residuals, shows that the photometric parameters of the "data" sample have been consistently determined over all the redshift baseline.

Finally, the *normalization* of this constant function tells us about the effectiveness of our kinematic measurements (i.e. about the homogeneity of the sample of velocity-selected rotators). The fact that the η-value inferred using the "data" sample of rotators with $v = 60\ \mathrm{km}/s$ (Eq. 8) is well within the errors of the η value estimated using Eq. 9 and our local "calibration" sample (~ 0.3) allows us to conclude that both the high redshift sample and the local one are homogeneously selected in velocity space. The low redshift counterparts of our rotators have a mean luminosity and a mean diameter which combines in Eq. 9 to give the value which was independently inferred using available local data: the high redshift galaxies in the S_{60} sample are compatible with the hypothesis of being the progenitors of local galaxies having a standard physical size of $D_{60} = 4.30 h_{70}^{-1}$ kpc and an absolute luminosity $M_{60} = -18.80 + 5 \log h_{70}$, as derived using the SFI++ sample in Paper II.

The consistency test performed using the η indicator assures us that velocities measured using different methods both locally and at high redshift are free of systematics. Galaxies with velocity v at high redshift may actually have intrinsic luminosities and diameters different from those determined for the local sample of galaxies with similar velocity. But there is no evidence against the hypothesis that they are embedded in dark matter halos of similar masses. Moreover, if the halo mass does not change across cosmic time (for example by merging or accretion phenomena), galaxies with velocity v estimated using OII linewidths at high redshift will eventually evolve into local galaxies having linear size and absolute luminosity compatibles with the values predicted by the Tully-Fisher relations ($D(v)$ and $M(v)$) locally calibrated using H_α rotation curves.

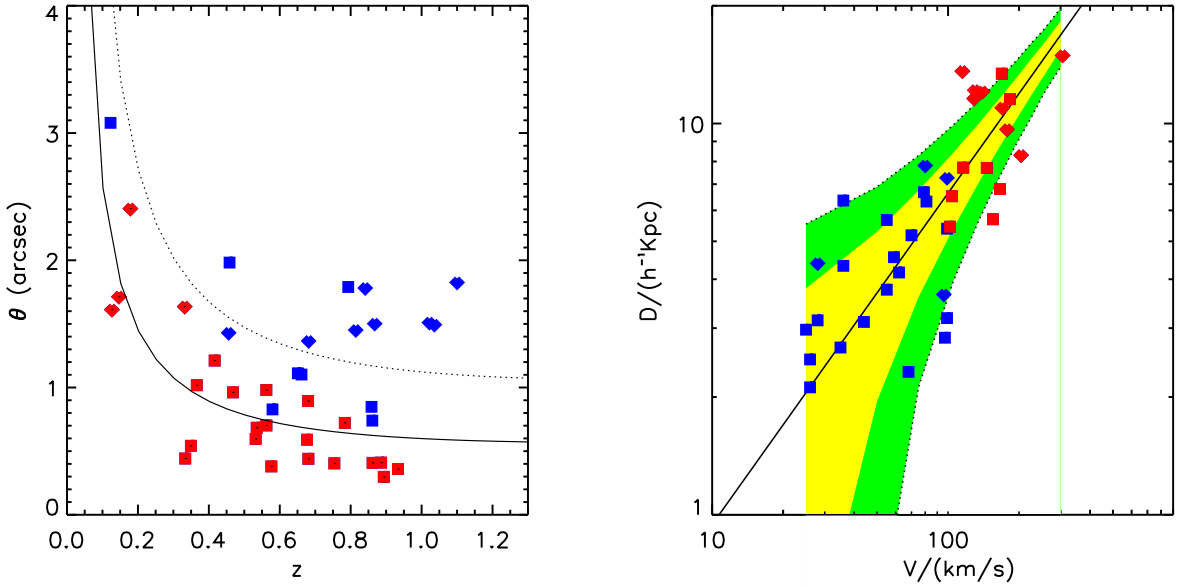

Fig. 2. *Left:* angular diameter-redshift diagram for galaxies with $0 < v < 100$km s^{-1} (red points) and $100 < v < 200$km s^{-1} (blue points). Galaxies for which HST images are available are indicated with a square. Diamonds represent galaxies with ground photometry (EIS catalog; Arnouts et al., 2001). The angular diameter scaling predicted in a flat, Λ-dominated cosmology ($\Omega_m = 0.3$,$\Omega_\Lambda = 0.7$) is shown. The theoretical expectation has been derived assuming as standard rods the locally ($z = 0$) calibrated half-light diameters of galaxies (see Table 2) at the characteristic velocity corresponding to the mean of the observed velocity distribution of galaxies in the two velocity ranges considered. These values are $D(z = 0, v = 60$ km s$^{-1}) = 4.3h_{70}^{-1}$kpc for the S_{60} sample (solid line) and $D(z = 0, v = 143$ km s$^{-1}) = 9h_{70}^{-1}$ kpc for the S_{143} sample (dotted line). *Right:* The inferred half-light diameter D for the S_{60} (red) and S_{143} (blue) samples of galaxies is plotted as a function of the rotational velocity of galaxies. The same cosmology as before is assumed for converting angles into linear diameters. The local calibration for the diameter-velocity relationship (see Eq. 3 of paper II) is overplotted together with 1σ and 2σ uncertainties in the zero-point calibration (shaded area).

3.2. Velocity selection of rotators: proof of concept

After checking the consistency of the strategy to select rotators based on the use of different spectral emission lines and different velocity indicators at different redshifts, we now show that, by selecting low/high velocity rotators, we effectively identify distinct classes of small/big disc galaxies which can be used for cosmological studies.

In the right panel of Figure 2 we plot the intrinsic linear diameter of the high redshift rotators recovered by assuming a flat, lambda-dominated cosmology ($\Omega_m = 0.3$, $\Omega_\Lambda = 0.7$, $h_{70} = 1$). The relative scatter at a given velocity is comparable to what is found locally. In particular we observe a tighter relationship for big rotators and a looser one for smaller discs. We are however comparing samples of systematically different richness. As a matter of fact, because of the specific form of the galaxy mass function, the number density of rotators decreases as a function of velocity (e.g. White & Frenk 1991, Marinoni & Hudson 2002). This plot confirms that a tight selection in rotational velocity space translates into a tight selection in diameters, even at high redshift.

In Figure 2 (left panel), we also show the angular diameter-redshift diagram for our sample of high redshift objects. While no obvious relation seems to exist between the apparent angular dimension and its redshift, by separating the sample into rotational velocity classes (S_{60} and S_{143}) evidence for this relation starts to appear; the angle subtended by galaxies in the low-velocity sample are systematically lower, at any redshift, with respect to those of faster rotators. The tightness of the relation becomes even clearer when the theoretically expected θ *vs.* z scaling relations are overplotted (the theoretical $\theta(z)$ relation assumes the intrinsic size of the galaxies given in Table 2 and a flat, Λ-dominated cosmology).

4. Cosmology-Evolution diagram at $z = 1$

As shown in Paper I, if we assume that the evolution of discs is linear with redshift (or can be linearly approximated in the redshift range of interest) and mild (less then 30% at $z = 1.5$), then one can use the angular diameter-redshift test to detect in a direct way the eventual presence of a dark energy component. Since our data are still too sparse for placing any meaningful constraint onto this cosmological parameter, we here use our sample to construct the cosmology-evolution plane (see §6.2 of Paper I).

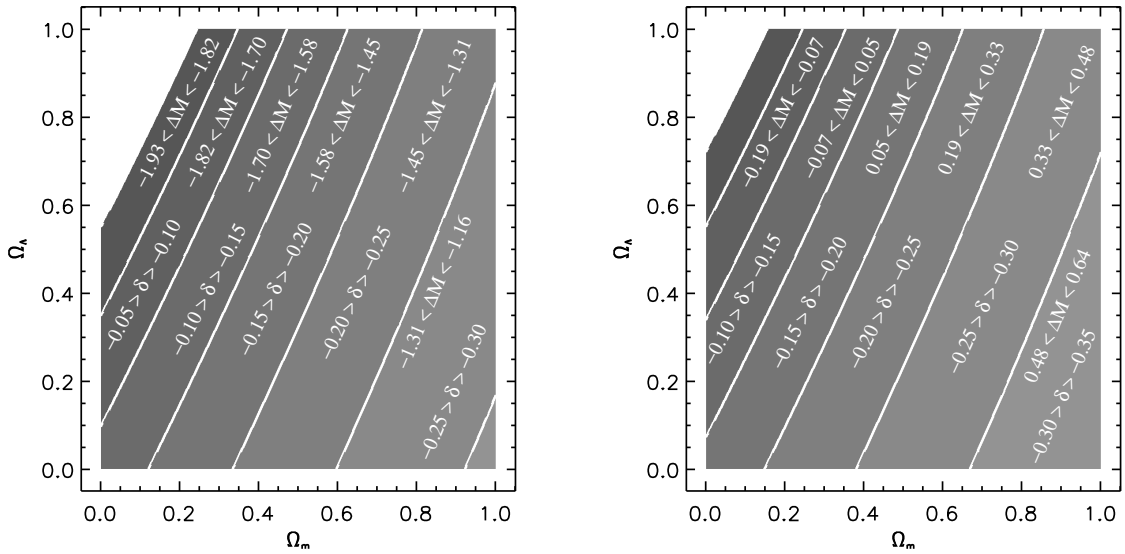

Fig. 3. *Left:* Cosmology-evolution diagram for the S_{60} sample at $z = 1$. The cosmological plane is partitioned with different boundaries obtained by solving equation 10 for different values of δ, i.e. of the relative evolution in disc size at $z = 1$. Boundaries corresponding to different relative disc evolutions from $\delta = 0$ to $\delta = -30\%$ in steps of 5% intervals are shown. We also show the set of possible absolute luminosity evolutions at $z = 1$ which are compatible with a given set of cosmological models. These upper/lower limits in luminosity evolution have been derived by using Eq. 6. Boundaries in disc relative evolution (δ) are uncertain by a 23% factor, while luminosity evolution boundaries are uncertain by 0.27mag. *Right:* the same but for the S_{143} sample of higher mass objects.
Disc relative evolution boundaries are uncertain by a 20% factor, while luminosity evolution boundaries are uncertain by 0.2mag.

This diagram allows us to visualize the set of cosmological parameters which are compatible with a given interval of disc/luminosity evolution, and *vice versa* how much evolution is expected given a specific cosmology. It establishes a one-to-one correspondence between cosmology and the amount of evolution in disc or luminosity at a given redshift.

Given the local calibration for diameters and magnitudes of galaxies within a particular velocity interval, we construct the angular diameter-redshift and Hubble diagrams in any possible cosmological model $\boldsymbol{p}$ spanning the range $p_1 = \Omega_m = (0, 1)$ and $p_2 = \Omega_\Lambda = (0, 1)$. We then solve for the set of points $\boldsymbol{p}$ of the parameter space which satisfy the condition

$$\delta_l(\bar{z}) < \frac{\epsilon_D(\bar{z}, \boldsymbol{p})}{D(0)} < \delta_u(\bar{z}) \qquad (10)$$

where δ_l and δ_u are the lower and upper limits in relative disc evolution at redshift $z = \bar{z}$. For consistency, we thus require that the amount of evolution having to be introduced in order for both sizes ($\epsilon_D(z, \boldsymbol{p}) = D_v(z, \boldsymbol{p}) - D_v(0)$) and luminosities ($\epsilon_M(z, \boldsymbol{p}) = M_v(z, \boldsymbol{p}) - M_v(0)$) to fit observations, be compatible with Eq. 6 which describes the *observed* evolution of the intrinsic mean surface brightness within the HLD of the objects, a cosmology-independent observable.

Solving for eqs. 6 and 10 we can thus construct a self-consistent cosmology-evolution plane, where to any given upper/lower limit for the evolution of diameters or luminosity at $z = \bar{z}$ corresponds in a unique way a specific region of the cosmological parameter space. In Figure 3 we show the cosmology-evolution diagram for both the S_{60} and S_{143} samples at redshift $z = 1$. This plot establishes a direct link between global properties of the cosmological background, such as curvature, dark matter and dark energy content, and the local structural parameters of rotators.

Let's assume that the luminosity of $v = 200$ km s^{-1} rotators cannot be fainter at $z = 1$, which means that the light output of high redshift rotators hosted in dark matter halos of $v = 200$ km s^{-1} cannot be smaller than that emitted by present day galaxies hosted in such halos. This can be expressed as the following boundary condition for the luminosity evolution of the fast rotators: $\Delta M(z = 1) \leq 0$. Therefore, we assume that the luminosity produced per unit mass is declining (or at most constant) since $z = 1$, and since we are considering halos of similar mass, that galaxies as a whole have been fading away. By inspecting the cosmology-evolution diagram for the S_{143} sample we can conclude, using this *a-priori* constraint, that a flat, matter-dominated cosmology ($\Omega_m = 1$) is excluded at a confidence level of $\sim 3\sigma$. Even more interestingly, the $\Delta M(z) \leq 0$ constraint allows us to conclude that an open cosmology with low mass density ($\Omega_m \sim 0.3$) and with no

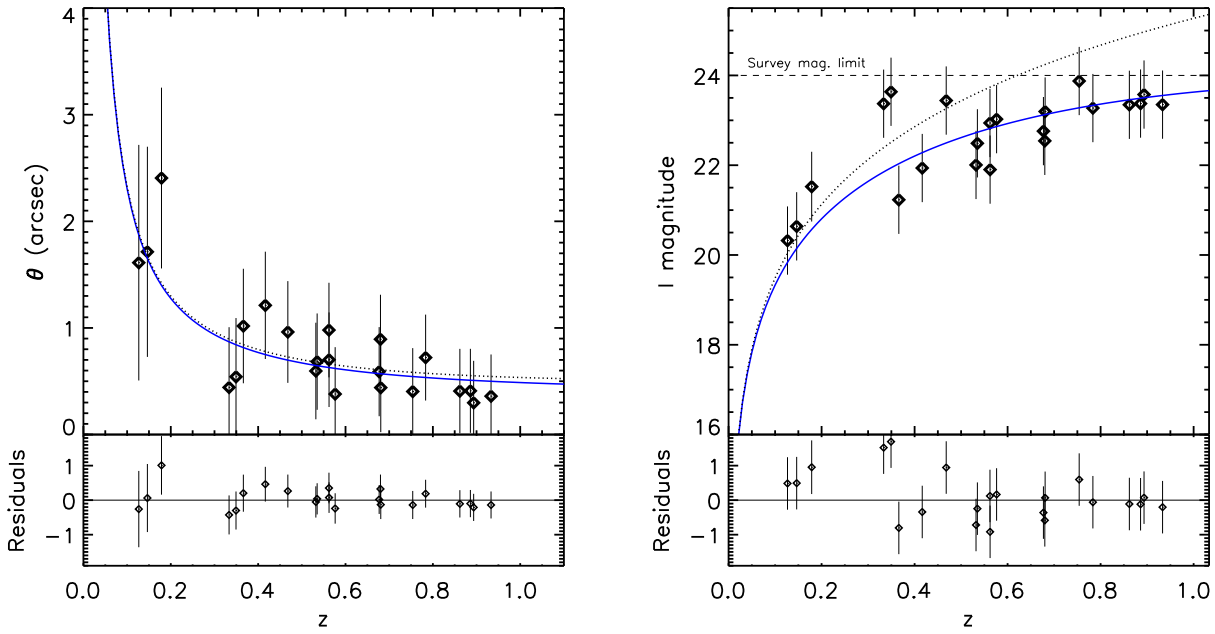

Fig. 4. *Left :* Angular diameters versus redshift for the S_{60} sample. The dotted line represents the theoretical scaling (Eq. 6) predicted assuming a standard rod of size $D_{60}(z = 0) = 4.3h_{70}^{-1}$kpc and a ΛCDM background cosmological model with parameters $(\Omega_m = 0.3, \Omega_\Lambda = 0.7)$. The solid line represent the best fitting linear evolutionary model obtained by assuming $\epsilon_D = \alpha z$ in Eq. 4. Errorbars represent the uncertainties in the calibration of the local standard rod (see Table 2) $\sigma_D/D \sim 0.6$. *Right :* Hubble diagram for the S_{60} rotators. The dotted line represent the theoretical scaling predicted assuming a standard candle of absolute luminosity $M_{60}(z = 0) = -18.80 + 5\log h_{70}$ and the same cosmology as before. The solid line represents the best fitting linear evolutionary model for luminosities obtained by using $\epsilon_M = \beta z$ in Eq. 1. Errorbars represent the uncertainties in the calibration of the local standard candle (see Table 2) $\sigma_m = 0.75$.

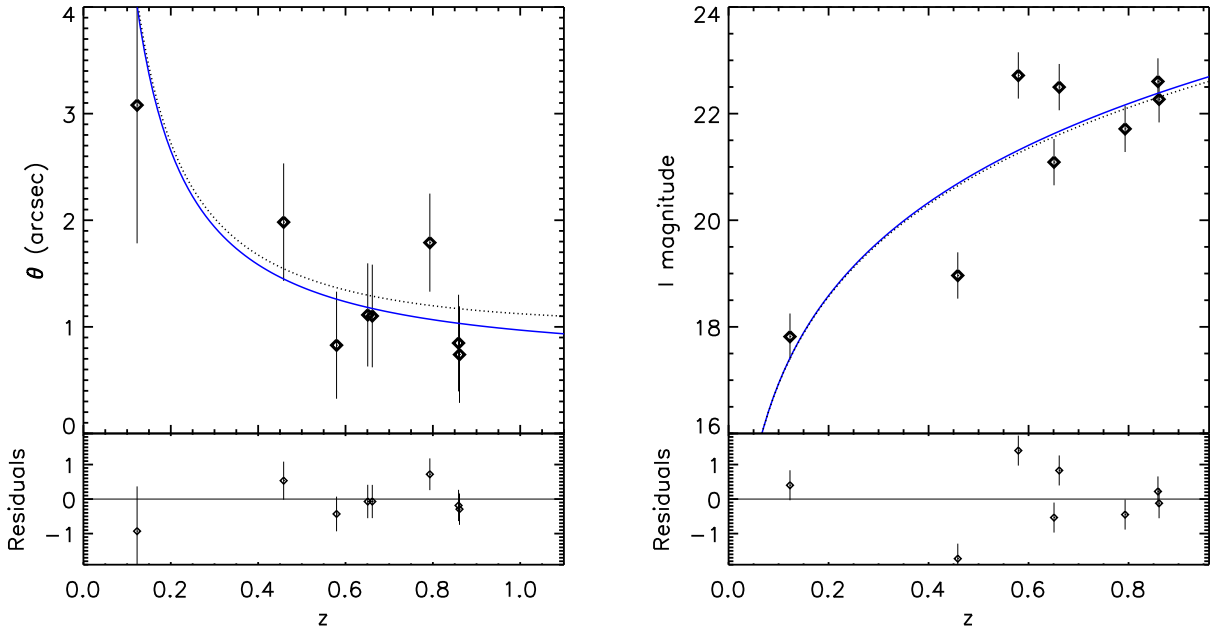

Fig. 5. The same as in Figure 4 but for the S_{143} sample of rotators.
Errorbars in the angular diameter-redshift diagram (*left*) represent the uncertainties in the calibration of the local standard rod (see Table 2) $\sigma_D/D \sim 0.3$. Errorbars in the Hubble-diagram (*right*) represent the uncertainties in the calibration of the local standard candle (see Table 2) $\sigma_m = 0.2$.

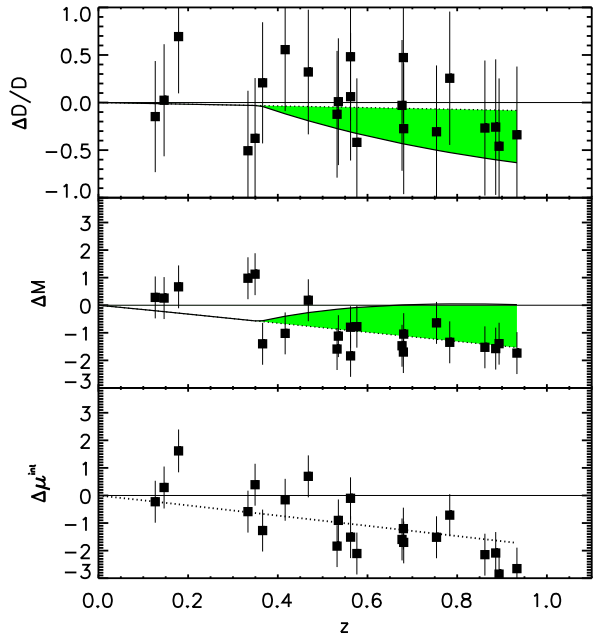

Fig. 6. *Top:* relative evolution in the diameter size for the S_{60} sample of low velocity rotators. We assume the zeropoint diameter normalization quoted in Table 2 and a a ΛCDM cosmological framework. Errorbars represent 1σ scatter in the calibration of the local standard rod. The dotted line represent the best fitting linear evolutionary model for diameters obtained by assuming $\epsilon_D = \alpha z$ in Eq. 4. The solid line represents the upper limit on relative disc evolution estimated by correcting for the Malmquist bias affecting the data. *Center:* Evolution of the absolute magnitude of galaxies in the S_{60} sample and in a ΛCDM cosmological framework. We assume as standard luminosity the mean absolute magnitude of a sample of similar rotators at $z \sim 0$ (see Table 2). Errorbars represent 1σ scatter in the calibration of the local standard candle. The dotted line represent the best fitting linear evolutionary model for luminosities obtained by using $\epsilon_M = \beta z$ in Eq. 1. The solid line represents the inferior limit on absolute magnitude evolution estimated by correcting for the Malmquist bias affecting the data. *Bottom:* evolution in the intrinsic surface brightness within the half-light diameter. This evolution is independent of the particular cosmological background. The dotted line represents the combination (Eq. 6) of the best fitting diameter and luminosity evolution functions.

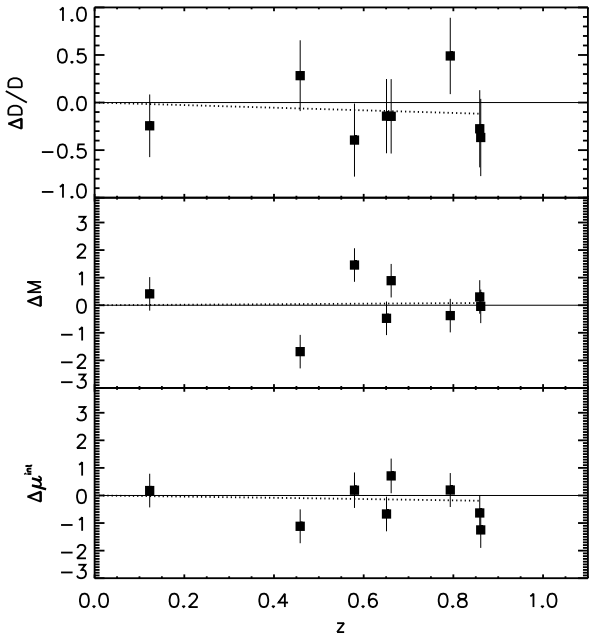

Fig. 7. Same as Figure 6 but for the S_{143} sample.

dark energy contribution (Ω_Λ) is excluded at a confidence level greater than 1σ.

We stress that these cosmological conclusions are drawn by assuming that, whatever the strength of the luminosity evolution of galaxies with redshift, this evolution cannot lead to the brightening $v = 200$ km s^{-1} rotators from $z = 1$ to the present time. We include evolution in our analysis from the beginning, and we only reject *a-posteriori* cosmological models that are associated at a particular cosmic epoch ($z = 1$ in our case) with unlikely galaxy evolutionary models.

5. Diameter and Luminosity evolution in a ΛCDM cosmological model

Insights into the mechanisms of galaxy evolution are traditionally accessible through the study of disc galaxy scaling relations, such as the investigation of the time-dependent change in the magnitude-velocity (Tully-Fisher) relation (e.g., Vogt et al (1996); Böhm et al. (2004); Bamford et al. (2006)), of the magnitude-size relations (e.g., Lilly et al. (1998); Simard et al. (1999); Bouwens & Silk (2002); Barden et al. (2005)), or of the disc "thickness" (Reshetnikov et al., 2003; Elmegreen et al., 2005). Yet owing to sample selection effects, and differences in analysis techniques, these studies have come to widely divergent conclusions. In this study, we have explored and adopted a different approach: we infer information about size and luminosity evolution of galaxies by constructing their respective angular diameter-redshift and Hubble diagrams in a fixed reference cosmology.

In Figure 4 and 5 we show the angular diameter-redshift and Hubble diagrams for the S_{60} and S_{143} samples, respectively. The expected scaling in the flat, Λ-dominated cosmology with $\Omega_m = 0.3$ and $\Omega_\Lambda = 0.7$ is shown together with the best fitting function obtained by assuming a simple linear redshift evolution for both diameters and absolute magnitudes. Both diameters and angles for the 2 velocity samples are normalized at $z = 0$ by using the values derived in Paper II and shown in Table 2.

The disc and luminosity evolution in a ΛCDM cosmology for both small and large rotators is shown in Figure 6 and 7, respectively. In these figures, we also show how these theoretically-derived evolutionary patterns combine together to give the evolution of the intrinsic surface

brightness (see Eq. 5), and how this last quantity compares to the observed one, which as stated earlier does not depend on the adopted cosmological model.

As stressed in Paper I, the test should be performed with big rotators i.e. using bright candles whose selection is unbiased in a flux-limited spectroscopic survey. Our sample of $v = 200$ km s^{-1} meets this criteria. However, because of the specific form of the galaxy luminosity function, our preliminary sample is dominated by small rotators, whose magnitude distribution could be affected by the Malmquist bias: the observed distribution of galaxies might not include the fainter tail of members having a rotation velocity satisfying our selection criteria ($0 < v < 100$). Even though he GOODs catalog is virtually unbiased in surface brightness selection for the magnitude range considered in this paper, our measurements of surface brightness evolution could be biased simply because of the flux cut at I=24 characterizing our sample. One could in principle miss low surface brightness galaxies of the same size as those observed, simply because their magnitudes are fainter then the survey limit. However, using the low redshift SFI++ sample we have checked that galaxies that are on the faint end tail of the magnitude distribution also tend to be the smaller discs. Therefore, no Malmquist effect is expected to contaminate the observed intrinsic surface brightness evolution.

The spectroscopic survey in the CDFS region is flux-limited at $I < 24$. Since the standard candle of the S_{60} sample has an absolute luminosity $M_{60} = -18.8 + 5 \log h_{70}$ while the brighter luminosity sampled at $z = 1$ is $M = -20.2 + 5 \log h_{70}$, we could be overestimating the observed evolution in luminosity. The fact that we see in our I=24 magnitude-limited sample rotators with $v = 100$ km s^{-1} at $z = 1$ can be interpreted in two different ways: i) these rotators were effectively much brighter in the past, or ii) we only sample the brightest objects, scattered around the standard absolute value. To address the latter, we correct our results for any possible Malmquist bias.

Let's consider the difference between the survey flux limit and the theoretically-predicted best fitting function to the observed magnitude distribution, $\Delta = 24 - m^{bfit}$. A simple estimate of the Malmquist bias is obtained by assuming that the best fitted apparent magnitude is systematically overestimated as a function of distance by the additive quantity $3\sigma - \Delta(z)$, where we assume that the scatter in the standard candle calibration is constant as a function of redshift. In other words, we assume that the galaxies we see are the brighter subset of standard rods whose luminosity scatters around M_{60}.

We have implemented this correction consistently both for galaxy luminosities and diameters. The incidence of the Malmquist bias on our conclusions is graphically shown in Figure 6. Due to the strong influence of the Malmquist correction term, the observed disc and luminosity evolution for the slow rotators sample S_{60} is compatible with the following diametrically opposite interpretations: i) data are affected by the Malmquist bias and therefore small discs have undergone almost no luminosity evolution but a strong size evolution (they were nearly 50 % smaller at $z = 1$ than at present epoch), or ii) data are unaffected by the Malmquist bias and the small discs have undergone strong luminosity evolution but not much size evolution since $z \sim 1$.

Since there is marginal evidence that the scatter around the expected disc and luminosity evolution is decreasing as redshift increases (see Figure 6), we take a conservative position and assume, in the following, that our S_{60} sample is affected by the Malmquist bias. Only a sample of small rotators selected in a magnitude-limited survey deeper than the CDFS will allow to unambiguously resolve the issue by differentiating between the two opposite scenarios. However, we stress again that the large rotators sample S_{143} does not suffer from Malmquist bias selection effects.

6. Discussion on the Evolution of Structural Parameters

Assuming a ΛCDM cosmology, several conclusions can be reached about the evolution of the structural parameters of fixed-velocity rotators.

1. The surface brightness evolution of discs is significantly different for the two populations, S_{60} and S_{143}: $\Delta\mu = -1.90 \pm 0.35$ mag/arcsec^2 for the slow rotators (S_{60}) and $\Delta\mu = -0.25 \pm 0.27$ mag/arcsec^2 for the fast rotators (S_{143}).
2. The fast rotators show neither significant size nor luminosity evolution since $z = 1$.
3. Under the conservative assumption that most of the luminosity difference over redshift for the small rotators is due to the Malmquist bias, they appear to have gone through a significant size evolution and no luminosity evolution since $z = 1$. (however the opposite is true in the limiting case in which Malmquist bias minimally affects our low-velocity data. In this case, small discs have undergone strong luminosity evolution but not much size evolution since $z \sim 1$.)

The results presented in the previous section highlight the potential of the geometrical tests, not only to constrain cosmological parameters, but also to derive information about the evolution of galaxy structural parameters. However, the extent of the analysis that can be performed at this point is significantly reduced by the small sample of galaxies available with deep photometry and high resolution spectroscopic measurements, and by the limiting magnitude of the CDFS. This magnitude limit introduces a potentially very strong Malmquist bias for the sample of small discs, S_{60}, which prevents us from determining if the surface brightness increase of ~ 1.9 mag/arcsec^2 of these galaxies at $z = 1$ is due to a strong luminosity or size evolution (or a combination of both). This distinction has not been made by most previous studies either, but could be achieved in the future using the strategy proposed here and a deeper, more complete galaxy sample.

Because at the limiting magnitude of I=24 of the VIMOS spectroscopic survey the GOODs photometric catalog is unbiased in surface brightness selection, conclusions can however be reached about the surface brightness evolution of discs. While we find strong evolution for the small rotators, the large rotators seem to have retained a constant surface brightness since $z = 1$. The evolution of more than one mag/arcsec^2 at $z = 1$ for the small discs is consistent with results of previous studies of the magnitude-size relation (e.g. Schade et al. (1996); Forbes et al. (1996); Lilly et al. (1998); Roche et al. (1998); Saintonge et al. (2005); Barden et al. (2005)), or of the magnitude-velocity (Tully-Fisher) relation (e.g. Milvang-Jensen et al. (2003); Böhm et al. (2004); Bamford et al. (2006)). While others report very little or no surface brightness evolution (e.g. Simard et al. (1999); Ravindranath et al. (2004)), Barden et al. (2005) reconciles this discrepancy by considering the different data analysis techniques. It also seems likely that some of these results are affected by the selection criteria applied. For example, some authors selected their samples on the basis of blue colors (Rix et al., 1997), strong emission line equivalent widths (Simard & Pritchet, 1998), or large disc sizes (Vogt et al, 1996). The two former criteria prefer late-type spirals, whereas the latter criterion leads to the overrepresentation of large, early-type spirals. With our strategy, based on a spectroscopic follow-up of objects with OII emission-lines selected from a purely flux-limited redshift survey, biases are largely reduced.

In §3.1, we have shown that the two classes of galaxies at high redshift with rotation velocity estimated on the basis of their OII linewidths represent in an unbiased way the progenitors of local discs whose velocity is inferred using the $H\alpha$ rotation curves. We stress that this statement does not imply that every high redshift galaxy with the same rotational velocity as a local galaxy is its direct progenitor. Due to the prevalence of mergers, interactions and accretion phenomena in the past, this is actually an unlikely scenario. What the η-test guarantees is that the high- and low-z samples represent the same populations of rotators with nearly the same mass. While interactions were more frequent in the past, are known to lead to the onset of star formation events and could therefore provide an explanation of the excess in luminosity of the small discs at high z, all the ACS images were examined and show that all the galaxies in the sample are not undergoing merger events.

Under the hierarchical scenario for the growth of structure, the following scaling relation for the disc scalelength, R_d, of dark matter systems is predicted (Mo, Mao & White, 1998):

$$R_d \approx 8.8 h^{-1}\mathrm{kpc} \left(\frac{\lambda}{0.05}\right) \left(\frac{V_c}{250\mathrm{kms}^{-1}}\right) \left(\frac{H(z)}{H_0}\right)^{-1} \left(\frac{j_d}{m_d}\right)$$

where λ is the disc spin parameter, V_c the circular velocity, j_d the angular momentum of the disc as a fraction of that of the halo, and m_d is the disc mass as a fraction of that of the halo. Since there is no dependency of λ on redshift and since $j_d/m_d = 1$ if discs are formed while conserving specific angular momentum, the disc scalelength of dark matter systems having a given circular velocity scales as

$$R_d \propto H^{-1}(z), \tag{11}$$

where z corresponds to the redshift of formation of the galactic discs. Under the fairly safe assumption that the diameter of the stellar disc of a galaxy scales with the scalelength of its dark matter halo, the diameter of our velocity-selected standard rods should also evolve as $D \propto H^{-1}(z)$. This relation therefore predicts that discs forming at the present epoch should be larger by a factor of 1.8 than those that formed at $z = 1$. This estimate agrees with our most pessimistic scenario for the Malmquist bias, which asks for the small discs to be larger by a factor of two at $z = 0$.

Interestingly, the fact that no size evolution is seen for the large rotators may tell us something about the time of formation of these systems. In Eq. 11, the dependency of the radius R_d is on the value of the Hubble constant *at the epoch of last assembly of the discs*. This corresponds to the last time when there was a significant reshuffling of the disc (i.e. the last incidence of a major merger). Since the discs in our S_{60} sample show size evolution that is consistent with Eq. 11, the redshifts at which we observe them probably coincide with the epochs at which these systems are still forming. Due to the paucity of the galaxy sample at hand, no firm conclusion can be reached at this point, but there are some hints that the large discs were already in place by $z = 1$ while most of the small discs have assembled since then. There is tantalizing evidence of a similar effect in the scaling relation between disc scalelength and rotation velocity observed for nearby galaxies, where the smallest discs appear to be consistent with an epoch of last formation at $z < 0.5$ while this is pushed back at $0.5 < z < 1.0$ for the larger systems (Spekkens, 2005).

Note that a relation similar to Eq. 11 also exists for the disc surface density, Σ_0. However, it is not as straightforward to extend that relation to predict the behavior of surface brightness, because of its dependency on the stellar mass-to-light ratio. Therefore, a similar interpretation can not be made for the observed surface brightness evolution of the discs, as it is not possible to disentangle the combined effects of redshift and mass-to-light ratio evolution.

Finally we note that fast rotators cannot have stopped forming stars at least over the epochs explored in this study. The constancy of their luminosity up to $z = 1$ can be explained in terms of star-formation activity continuously on-going for a Hubble time.

7. Conclusions

The goal of this pilot observational program is to investigate the relationship between global properties of the universe (geometric curvature, dark matter and dark energy content) and local structural parameters of disc galaxies (disc linear size and absolute luminosity). To this purpose

we apply the angular size-redshift test and the Hubble diagram at the same time to the same class of standard objects, namely, velocity-selected disc galaxies. As such, it presents one of the first attempts to investigate if specific subsamples of high redshift galaxies can be used as cosmological tracers complementary to SNIa and CMB observations. This approach allows us to construct a cosmology-evolution diagram at redshift $z = 1$, the chart that allows for the mapping of the cosmological parameter space onto the disc galaxy structural parameter space (diameter, luminosity and surface brightness). Assuming prior knowledge about disc evolution, this diagram allows us to draw some interesting cosmological conclusions. If we assume that the absolute magnitude evolution is constrained to be negative at $z = 1$ (i.e. it is impossible that $v = 200$ km s^{-1} rotators were fainter at $z = 1$ than at the present time, which means that their luminosity per unit mass was higher in the past), we find with the data at hand that:

1. a flat matter-dominated cosmology ($\Omega_m = 1$) is excluded at a confidence level of 2σ.
2. an open cosmology with low mass density ($\Omega_m \sim 0.3$) and no dark energy contribution (Ω_Λ) is excluded by present data at a confidence level of 1σ.

On the other hand, by fixing the background cosmological model, the cosmology-evolution diagram allows us to investigate the evolution in the structural parameters of disc galaxies which are hosted in dark matter halos of *similar mass*. Assuming a ΛCDM model, we find that:

1. while small mass galaxies go through a strong surface brightness evolution of -1.90 ± 0.35 mag/arcsec^2 since $z = 1$, larger discs only evolve by -0.25 ± 0.27 mag/arcsec^2,
2. under the assumption that our sample of small discs is affected by the Malmquist bias, this surface brightness evolution is caused by an increase in the size of the fixed-velocity rods by a factor of two from $z = 1$ to the present epoch,
3. discs hosted in more massive halos, which are not affected by the Malmquist bias, show neither size nor luminosity evolution, suggesting that they finished assembling before $z = 1$, unlike the smaller discs that are still undergoing formation at $z < 0.5$.

We conclude that the luminosity evolution observed is coherent with the emerging picture of a differential star formation history for galaxies of different masses (Juneau et al., 2005). These results are also consistent with the growth of structure predicted in the universe described by the concordance cosmological model (Mo, Mao & White, 1998; Bower et al., 2006).

In this preliminary study we are still limited by the small number statistics affecting our sparse sample. While with a larger sample of high resolution spectra and images one can detect in a direct way the eventual presence of a dark energy component (see Paper I), it was not possible to apply the angular diameter-redshift test and put a constraint on its amplitude and on its equation of state parameter w with the amount of data currently available. For the same reason, galaxies were separated in only two velocity bins to construct the cosmology-evolution diagram. This limits the class of mass-selected objects for which we can trace evolution across different cosmic epochs. The availability of a larger sample will allow finer velocity bins, and therefore less scatter in the results.

To conclude, we reiterate that the rotational velocity of distant galaxies, when interpreted as a size (luminosity) indicator, may be used as an interesting tool to select high redshift standard rods (candles). Though the power of geometrical tests to constrain fundamental cosmological parameters has long been recognized, only with the recent large, deep redshift surveys have their implementation been made possible. With only a limited amount of data but a novel and physically justified technique to select standard rods/candles, we have shown that these tests can give useful insights not only on the value of fundamental cosmological parameters, but also the time evolution of fundamental galaxy observables in mass-selected disc rotators.

Acknowledgments

We wish to thank the referee for many useful comments and suggestions. This work has been partially supported by NSF grants AST-0307661 and AST-0307396 and was done while AS was receiving a fellowship from the *Fonds de recherche sur la Nature et les Technologies du Québec*. CJW is supported by the MAGPOP Marie Curie EU Research and Training Network. KLM is supported by the NSF grant AST-0406906. The VLT-VIMOS observations have been carried out on guaranteed time (GTO) allocated by the European Southern Observatory (ESO) to the VIRMOS consortium, under a contractual agreement between the Centre National de la Recherche Scientifique of France, heading a consortium of French and Italian institutes, and ESO, to design, manufacture and test the VIMOS instrument.

References

Arnouts, S., et al. 2001, A&A, 379, 740
Bamford, S. P., Aragón-Salamanca, A., & Milvang-Jensen, B. 2006, MNRAS, 366, 308
Barden, M., et al. 2005, ApJ, 635, 959
Böhm, A. et al. 2004, A&A, 420, 97
Bottini, D. et al. 2005, PASP, 117, 996
Bouwens, R., & Silk, J. 2002, ApJ, 568, 522
Bower, R. G., Benson, A. J., Malbon, R., Helly, J. C., Frenk, C. S., Baugh, C. M., Cole, S., & Lacey, C. G. 2006, MNRAS, 370, 645
de Jong, R. S. 1996, A&A, 313, 377
Elmegreen, D. M., Elmegreen, B. G., Rubin, D. S., & Schaffer, M. A. 2005, ApJ, 631, 85
Ferguson, H. C., et al. 2004, ApJ, 600, L107
Forbes, D.A., et al. 1996, ApJ, 462, 89

Giavalisco, M., et al. 2004, ApJ, 600, L93
Ilbert, O. et al. 2005 A&A, 439, 863
Juneau, S., et al. 2005, ApJ, 619, L135
Le Fèvre O., et al. 2004, A&A, 428, 1043
Le Fèvre O., et al. 2005, A&A, 439, 845
Lilly, S. J., et al. 1998, ApJ, 500, 75
Lilly, S. J., et al. 2006, ApJS, in press (astro-ph/0612291)
Lima, J. A. S., & Alcaniz, J. S. 2001, A&A, 566, 15L
Madau, P., Ferguson, H. C., Dickinson, M. E., Giavalisco, M., Steidel, C. C., & Fletcher, A. 1996, MNRAS, 283, 1388
Marinoni, C., & Hudson M., 2002, ApJ, 569, 101
Marinoni, C., et al. 2004, Ap&SS, 290, 195
Marinoni, C., Saintonge, A., Giovanelli, R., Haynes, M.P., Masters, K.L., Le Fèvre, O., Mazure, A., Taxil, P., & Virey, J. M. 2007, A&A, in press (Paper I)
Milvang-Jensen, B. et al. 2003, MNRAS, 339, L1
Mo, H. J., Mao, S., & White, S. D. M. 1998, MNRAS, 295, 319
Oke, J. B., & Gunn, J. E. 1983, ApJ, 266, 713
Ravindranath, S., et al. 2004, ApJ, 604, L9
Reshetnikov, V. P., Dettmar, R.-J., & Combes, F. 2003, A&A, 399, 879
Rix, H.-W., Guhathakurta, P., Colless, M., & Ing, K. 1997, MNRAS, 285, 779
Roche, N., Ratnatunga, K., Griffiths, R. E., Im, M., & Naim, A. 1998, MNRAS, 293, 157
Saintonge, A., Masters, K.L., Marinoni, C., Giovanelli, R., & Haynes, M.P. 2007, A&A, submitted (Paper II)
Saintonge, A., Schade, D., Ellingson, E., Yee, H. K. C., & Carlberg, R. G. 2005, ApJS, 157, 228
Sandage, A. 1988, ARA&A, 26, 561
Sandage, A., & Perelmuter, J.-M. 1990, ApJ, 350, 481
Sandage, A., Kron, R.G. & Longair, M.S. /it The Deep Universe, Saas-Fee Advanced Course 23. Lecture Notes 1993. Swiss Society for Astrophysics and Astronomy, ed. B. Bingelli & R. Buser (Springer-Verlag, Berlin, 1995)
Schade, D., Carlberg, R. G., Yee, H. K. C., Lopez-Cruz, O., & Ellingson, E. 1996, ApJ, 465, L103
Schlegel, D. J., Finkbeiner, D. P., & Davis, M. 1998, ApJ, 500, 525
Simard, L. et al. 1999, ApJ, 519, 563
Simard, L., & Pritchet, C. J. 1998, ApJ, 505, 96
Spekkens, K. 2005, Ph.D. Thesis, Cornell University
Springob, C. M., Masters, K. L., Haynes, M. P., Giovanelli, R., & Marinoni, C. 2007, ApJS in press, astro-ph/07050647
Stoughton, C., et al. 2002, AJ, 123, 485
Tresse L., et al. 2006, A&A 472, 403
Tully, R. B., & Fisher, J. R. 1977, A&A, 54, 661
Tully, R. B., Pierce, M. J., Huang, J.-S., Saunders, W., Verheijen, M. A. W., & Witchalls, P. L. 1998, AJ, 115, 2264
Vogt, N. P., Forbes, D. A., Phillips, A. C., Gronwall, C., Faber, S. M., Illingworth, G. D., & Koo, D. C. 1996, ApJ, 465, L15
White, S. D. M., & Frenk, C. S., 1991, ApJ, 379, 52

Bibliography

[1] M. Sher, Phys. Rep. **179** (1989) 273; B.A. Kniehl, Phys. Rep. **240** (1994) 211; pour une discussion récente voir C.T. Hill et E.H. Simmons, Phys. Rep. **381** (2003) 235, Erratum Phys. Rep. **390** (2004) 553; G. Burdman arXiv hep-ph/0703194.

[2] T. Hambye et K. Riesslmann, Phys. Rev. **D55** (1997) 7255.

[3] U. Baur et al., Snowmass working group on precision electroweak measurements, Snowmass, Colorado, USA, Juillet 2001, arXiv hep-ph/0202001.

[4] D. Charlton, International Europhysics Conference on High Energy Physics, Budapest, Hongrie, Juillet 2001, arXiv hep-ex/0110086.

[5] LEP Higgs Working Group for Higgs boson searches, arXiv:hep-ex/0107029.

[6] A. Ealet, Habilitation à Diriger des Recherches 2004.

[7] A. Freitas, M. Awramik et M. Czakon, International Linear Collider Workshop, Stanford, USA, 2005, arXiv hep-ph/0507159.

[8] J.-M. Virey, Thèse de doctorat (1997).

[9] E. Eichten, K. Lane et M. E. Peskin, Phys. Rev. Lett. **50** (1983) 811; E. Eichten et al., Rev. Mod. Phys. **56** (1984) 579.

[10] H. Saltz, dans *Proc. of the Joint International Symposium and Europhysics Conference on High Energy Physics, Geneva, Suisse*, (1991) eds. S. Hegarty et al., (World Scientific 1992).

[11] RSC Annual Meeting, Marseille, France (1996), G. Bunce communication privée.

[12] R. M. Woloshyn, Nucl. Phys. **A496** (1989) 749.

[13] G. Bunce, N. Saito,J. Soffer, W. Vogelsang, Annu. Rev. Nucl. Part. Sci. **50** (2000) 525.

[14] J. Soffer, J.-M. Virey, Nucl. Phys. **B509** (1998) 297.

[15] E.W. Hughes et R. Voss, Ann. Rev. Nucl. Part. Sci. **49** (1999) 303; B.W. Filippone et X. Ji, Adv. Nucl. Phys. **26** (2001) 1; S.D. Bass, Rev. Mod. Phys. **77** (2005) 1257.

[16] M. Stratmann et W. Vogelsang, arXiv:hep-ph/0702083.

[17] R.L. Jaffe et A. Manohar, Nucl. Phys. **B337** (1990) 509.

[18] G. Altarelli et G.G. Ross, Phys. Lett. **B212** (1988) 391.

[19] EMC, J. Ashman et al., Nucl. Phys. **B238** (1990) 1; Phys. Lett. **B206** (1988) 364 .

[20] G. Altarelli et W.J. Stirling, Part. World **1** (1989) 40; R.D. Carlitz, J.C. Collins et A.H. Mueller, Phys. Lett. **B214** (1988) 229.

[21] R.L. Jaffe, Phys. Lett. **B365** (1996) 359.

[22] V. Barone, T. Calarco et A. Drago, Phys. Lett. **B431** (1998) 405; H.J. Lee et al., Phys. Lett. **B491** (2000) 257.

[23] P. Chen et X.D. Ji, arXiv:hep-ph/0612174.

[24] S. Adler *et al.* [PHENIX Collaboration], Phys. Rev. Lett. **93** (2004) 202002; Phys. Rev. **D73** (2006) 091102; K. Boyle [PHENIX Collaboration] arXiv:nucl-ex/0606008.

[25] B. Abelev *et al.* [STAR Collaboration], Phys. Rev. Lett. **97** (2006) 252001.

[26] M. Glück, E. Reya, M. Stratmann, W. Vogelsang, Phys. Rev. **D63** (2001) 094005.

[27] C. Bourrely et J. Soffer, Phys. Lett. **B314** (1993) 132 .

[28] J.-M. Virey, Eur. Phys. J. **C8** (1999) 283.

[29] J.-M. Virey, Nucl. Phys. Proc. Suppl. **105** (2002) 150, ArXiv hep-ph/0109194.

[30] J.-M. Virey, Parity Violation in Jet Production, Workshops "Predictions and Uncertainties for RHIC Spin Physics" et "Event Generator for RHIC Spin Physics III", RIKEN-BNL Research Center, New-York, USA, Mars 2000, Editeurs J. Qiu et W. Vogelsang.

[31] S. Moretti, M.R. Nolten et D.A. Ross, Phys. Lett. **B643** (2006) 86 .

[32] S. Moretti, M.R. Nolten et D.A. Ross, Nucl. Phys. **B759** (2006) 50.

[33] J. Ellis, S. Moretti et D.A. Ross, JHEP **0106** (2001) 043.

[34] T. Gehrmann et W. J. Stirling, Phys. Rev. **D53** (1996) 6100.

[35] T. Stelzer, Z. Sullivan et S. Willenbrock, Phys. Rev. **D58** (1998) 094021.

[36] N. Kidonakis, Phys. Rev. **D75** (2007) 071501 et références internes.

[37] S. Dodelson, "Modern Cosmology" (2003) New York Academic Press.

[38] T. Padmanabhan, "Structure Formation in the Universe" (1993) Cambridge University Press.

[39] J. Peebles, "Principles of Physical Cosmology" (1993) Princeton University Press.

[40] G. Huey et al., Phys. Rev. **D59** (1999) 063005.

[41] Dark Energy Task Force report, arXiv astro-ph/0609591.

[42] P.J.E. Peebles and B. Ratra, Rev. Mod. Phys. **75**, 559 (2003).

[43] D. Huterer and M.S. Turner, Phys. Rev. **D64** (2001) 123527.

[44] P. Astier et al., Collaboration SNLS, Astronomy and Astrophysics **447** (2006) 31.

[45] T.M. Davis et al. [ESSENCE Collaboration], arXiv astro-ph/0701510.

[46] E. V. Linder, Phys. Rev. Lett. **90**, 091301 (2003).

[47] M. Chevallier and D. Polarski, Int.J.Mod.Phys. **D10**, 213 (2001).

[48] Obtenue par André Tilquin et Diane Talon en Septembre 2007, à partir des données de SNIa[45], du CMB[49] et des BAO[50], en utilisant le kosmoshow[51].

[49] D.N. Spergel *et al.* [WMAP Collaboration], arXiv:astro-ph/0603449.

[50] D.J. Eisenstein *et al.*, Astrophys. J. **633**, 560 (2005).

[51] Notre outil de simulation, le "kosmoshow", a été développé par André Tilquin et est disponible sur
http://marwww.in2p3.fr/renoir/Kosmoshow.html.

[52] W. Hu, Phys. Rev. D **71**, 047301 (2005); R.R. Caldwell et M. Doran, Phys. Rev. D **72**, 043527 (2005); G.B. Zhao et al., arXiv:astro-ph/0507482.

[53] A.G. Riess et al., arXiv astro-ph/0611572.

[54] E. Copeland, M. Sami et S. Tsujikawa, Int. J. Mod. Phys. **D15** (2006) 1753.

[55] E.V. Linder, arXiv 0704.2064.

[56] T. Padmanabhan, Phys. Rept. **380**, 235 (2003); T. Padmanabhan, Current Science, **88**, 1057 (2005) [arXiv:astro-ph/0510492].

[57] S.M. Carroll, Living Rev. Rel. **4**, 1 (2001).

[58] S. Weinberg, Rev. Mod. Phys. **61**, 1 (1989).

[59] B. Ratra and J. Peebles, Phys. Rev **D37**, 321 (1988).

[60] C. Wetterich, Nucl. Phys. **B302**, 668 (1988).

[61] R.R. Caldwell et E.V. Linder, Phys. Rev. Lett. **x** (2004) x.

[62] P. Brax, et J. Martin, Phys. Lett. **B468**, 40-45 (1999); Phys. Rev. **D61**, 103502 (2000); Phys. Rev. **D71** (2005) 063530; J.C.A.P. **0611** (2006) 008.

[63] R.R. Caldwell, R. Dave et P. J. Steinhardt, Phys. Rev. Lett. **80**, 1582 (1998); I. Zlatev, L.M. Wang et P.J. Steinhardt, Phys. Rev. Lett. **82**, 896 (1999); P.J. Steinhardt, L.M. Wang et I. Zlatev, Phys. Rev. D **59**, 123504 (1999).

[64] D. Huterer et H.V. Peiris, Phys. Rev. **D75** (2007) 083503.

[65] T. Chiba, T. Okabe et M. Yamaguchi, Phys. Rev. **D62**, 023511 (2000); C. Armendáriz-Picón, V. Mukhanov, et P.J. Steinhardt, Phys. Rev. Lett. **85**, 4438 (2000); C. Armendáriz-Picón, V. Mukhanov, et P.J. Steinhardt, Phys. Rev. **D63**, 103510 (2001).

[66] E.V. Linder, arXiv 0705.0400.

[67] R. R. Caldwell, Phys. Lett. B **545**, 23-29 (2002).

[68] P.Q. Hung, arXiv hep-ph/0010126; M. Li et al., Phys. Rev. **D65**, 103511 (2002); R. Fardon, A.E. Nelson et N. Weiner, JCAP **0410**, 005 (2004); D.B. Kaplhan, A.E. Nelson et N. Weiner, Phys. Rev. Lett. **93**, 091801 (2004); R.D. Peccei, Phys. Rev. D **71** 023527 (2005); H. Li, B. Feng, J.Q. Xia et X. Zhang, arXiv:astro-ph/0509272.

[69] E.W. Kolb, S. Matarrese, A. Notari et A. Riotto, arXiv hep-th/0503117; E.W. Kolb, S. Matarrese et A. Riotto, arXiv astro-ph/0506534; arXiv astro-ph/0511073; arXiv astro-ph/0511124.

[70] T. Buchert, J. Larena et J. M. Alimi, arXiv gr-qc/0606020.

[71] T. Buchert, arXiv:0707.2153; S. Räsänen, arXiv astro-ph/0607626.

[72] E.E. Flanagan, Phys. Rev. **D71**, 103521 (2005); C.M. Hirata et U. Seljak, Phys. Rev. **D72**, 083501 (2005); E.R. Siegel et J.N. Fry, Astrophys. J. **628**, L1 (2005); A. Ishibashi et R.M. Wald, Class. Quant. Grav. **23**, 235-250 (2006).

[73] K. Freese et M. Lewis, Phys. Lett. **B540**, 1 (2002); Z.-H. Zhu, M.K. Fujimoto et X.T. He, Astrophys. J.**603**, 365 (2004); Z.-H. Zhu et M.K. Fujimoto, Astrophys. J. **602**, 12 (2004); Z.-H. Zhu et M.K. Fujimoto, Astrophys. J.**58** , 1 (2002); E.V. Linder, Phys. Rev. **D73** (2006) 063010.

[74] G. Dvali et M.S. Turner, arXiv astro-ph/0301510;

[75] B. Boisseau, G. Esposito-Farese, D. Polarski et A. A. Starobinsky, Phys. Rev. Lett. **85**, 2236 (2000); G. Esposito-Farese et D. Polarski, Phys. Rev. **D63**, 063504 (2001); A. Riazuelo et J. P. Uzan, Phys. Rev. **D66**, 023525 (2002); C. Schimd, J. P. Uzan et A. Riazuelo, Phys. Rev. **D71**, 083512 (2005).

[76] S.M. Carroll et al., Phys. Rev. **D71** (2005) 063513.

[77] S. Nojiri et S.D. Odintsov, Phys. Rev. **D70**, 103522 (2004). S. Nojiri, S.D. Odintsov et M. Sasaki, Phys. Rev. **D71**, 123509 (2005); S. Nojiri, S.D. Odintsov et M. Sami, arXiv hep-th/0605039; T. Koivisto and D. F. Mota, arXiv astro-ph/0606078;

[78] G. R. Dvali, G. Gabadadze et M. Porrati, Phys. Lett. **B485**, 208 (2000).

[79] C. Deffayet, Phys. Lett. **B502**, 199 (2001); C. Deffayet, G.R. Dvali et G. Gabadadze, Phys. Rev. **D65**, 044023 (2002).

[80] E.V. Linder et D. Huterer, Phys. Rev. **D72**, 043509 (2005).

[81] S. Nesseris et L. Perivolaropoulos, Phys. Rev. **D70**, 043531 (2004);

[82] A. Upadhye, M. Ishak et P.J. Steinhardt, Phys. Rev. **D72**, 063501 (2005).

[83] D. Huterer et G. Starkman, Phys. Rev. Lett. **90** (2003) 031301; D. Huterer et A. Cooray, Phys. Rev. **D71** (2005) 023506.

[84] R.A. Daly et S.G. Djorgovski, Astrophys. J. **597** (2003) 9; Astrophys. J. **612** (2004) 652.

[85] A. Shafieloo et al., Mon. Not. Roy. Astron. Soc. **366** (2006) 1081.

[86] Y. Wang et M. Tegmark, Phys. Rev. **D71** (2005) 103513.

[87] G. Efsthatiou and J.R. Bond, Mon. Not. R. Astron Soc. **304**, 75 (1999).

[88] I. Maor, R. Brustein et P.J. Steinhardt, Phys. Rev. Lett. **86**, 6 (2001); I. Maor et al., Phys. Rev. **D65**, 123003 (2002).

[89] E.V. Linder et R.N. Cahn, arXiv astro-ph/0701317.

[90] R. Bean, S. Carroll et M. Trodden, white paper submitted to Dark Energy Task Force, arXiv astro-ph/0510059.

[91] J.-P. Uzan, Gen. Rel. Grav. **39** (2007) 307; arXiv astro-ph/0605313.

[92] J.R. Bond, G. Efsthatiou and M. Tegmark, Mon. Not. R. Astron Soc. **291**, L33 (1997).

[93] M. Zaldarriaga, D.N. Spergel and U. Seljak, Astrophys. J. **488**, 1 (1997).

[94] Y. Wung and P. Mukherjee, Astrophys. J. **650**, 1 (2006).

[95] O. Elgaroy and T. Mutamaki, astro-ph/0702343.

[96] J. Weller et A.M. Lewis, Mon. Not. Roy. Astron. Soc. **346**, 987 (2003).

[97] A.G. Riess et al., Astrophys.J. **607**, 665 (2004).

[98] C.A. Shapiro et M.S. Turner, arXiv astro-ph/0512586.

[99] R.B. Tully et J.R. Fisher, Astronomy and Astrophysics **54** (1977) 661.

[100] L. Bottinelli, L. Gouguenheim, G. Paturel et G. de Vaucouleurs, Astrophys. J. **242** (1980) L153.

[101] H.J. Mo, S. Mao et S.D.M. White, Mon. Not. Roy. Astron. Soc. **295** (1998) 319.

[102] O. Le Fèvre et al., Astronomy and Astrophysics **439** (2005) 845.

[103] S.J. Lilly et al., arXiv astro-ph/0612291.